POLITECNICO DI TORINO

Department of Mechanical, Aerospace, and Automotive Engineering

Master’s Degree Thesis in Mechanical Engineering
AY 2023/2024

Long-term Predictive Analysis and Control Strategies Development for μ-CHP SOFC System

Supervisors:
Prof. Massimo Santarelli
Prof. Jan Van Herle
Eng. Hangyu Yu

Candidate:
Dante Fronterotta

October 2024

Acknowledgements

I remember the first day I arrived in Turin; I was uncertain and scared. Today, I am here at the end of my university journey, writing the acknowledgements for my master's thesis, much more confident in myself and ready to take the next step. Before proceeding with the discussion, I would like to dedicate a thought to all who have accompanied me along this path.

A heartfelt thank you to my supervisors: Professor Santarelli for his great availability and kindness, and Professor Van Herle for welcoming me into his lab, for his excellent and kind guidance, and for all his help over the past year. A due and sincere thank you also goes to Hangyu, who, over the past year, has not only been an invaluable tutor but also a great friend.

I thank all the members and staff of the GEM lab for warmly welcoming me and sharing these last few months with me.

I would also like to thank Collegio Einaudi for welcoming me and helping me grow, as well as all the friends, from those who have already left to those who are still here today.

A thought goes out to my grandparents, who I know would have been proud.

A sincere thank you goes to Enea, Antonio, and Stefano for putting up with me and always being by my side, as well as to all my lifelong friends like the Serano group and the Stempione group for sharing so many moments of happiness and carefreeness.

I would especially like to thank my parents, my sister, Marco, Emanuela, and my entire family for their constant support, which has shaped me into the person I am today, I truly wouldn't be here without their encouragement, love, and belief in me.

Thank you all from the bottom of my heart.

Abstract

Global warming and the urgent need for renewable energy necessitate advancements in efficient and durable energy systems. Solid oxide fuel cells (SOFCs) offer a promising solution due to their high efficiency and flexibility. However, managing SOFC degradation to ensure prolonged life and optimal performance remains a critical challenge. This thesis addresses these issues through several steps. First, it integrates a degradation model and a techno-economic model into an existing 0-D model for catalytic partial oxidation (CPOX)-based SOFC system. Various end-of-life (EoL) criteria were tested using three health indicators: power, voltage, and cumulative energy, optimized under different control strategies. Three control strategies were analyzed: fixing power, voltage, or stack temperature over time. Predictive analysis through single-objective optimization revealed that: fixing power maintained stable performance but required frequent voltage adjustments, leading to high energy production and significant degradation. Fixing voltage provided the longest life expectancy, effectively minimizing degradation. Fixing temperature showed high efficiency but less stability due to a lack of direct constraints on voltage, current, or power. A multi-objective optimization (MOO) approach assessed trade-offs between minimizing degradation and maximizing electrical efficiency with fixed system inputs over time. The best trade-off was found by balancing each system variable, revealing interesting trends in CPOX air flow rate and current over time. Dynamic operation analysis confirmed the robustness of the predictive model under real-world conditions. The techno-economic optimization demonstrated profitability, while the degradation minimization scenario extended life expectancy threefold compared to others. This thesis introduces a comprehensive predictive analysis. The integration of detailed modeling, optimization, and control strategies offers a solid foundation for future research, providing valuable tools to enhance the performance, efficiency, and durability of SOFC systems in sustainable energy applications.

Keywords: Solid oxide fuel cell, degradation,control strategies, optimization

Contents

List of Figures

List of Tables

List of abbreviations

AFC	alkaline fuel cell
ASC	anode-supported cell
ASR	area specific resistance
AU	air utilization ratio
BoP	balance of plant
CAPEX	capital expenditures
CHP	combined heat and power
CPOX	catalytic partial oxidation reactor
CSTR	continuous stirred-tank reactor
DMFC	direct methanol fuel cell
DOE	U.S. Department of Energy
DOF	degrees of freedom
DRT	distribution of relaxation times
ECM	equivalent circuit model
EIS	electrochemical impedance spectroscopy
EoL	end of life
ESC	electrolyte-supported cell
FIB	focused ion beam
FU	fuel utilization ratio
GA	genetic algorithm
GDC	gadolinium doped ceria
GDL	gas diffusion layer
LCOE	levelized cost of electricity
LHV	low heating value
LSCF	$La_{0.6}Sr_{0.4}Co_{0.2}Fe_{0.8}O_3$
MCFC	molten carbonate fuel cell
MHE	moving horizon estimation
MIC	metal interconnector
MOO	multi-objective optimization
MSC	metal-supported cell
NMPC	Nonlinear model predictive control
NTU	number of transfer units
OCV	open circuit voltage
OI	operating income
OPEX	operational expenditures
PAFC	phosphoric acid fuel cell
PEMFC	proton exchange membrane fuel cell
PI	proportional integral
PID	proportional integral derivative
RoW	rest of the world
rSOFC	reversible solid oxide fuel cell
RTO	real-time optimization
RUL	remaining useful life
SEM	scanning electrode microscopy
SMA	simple moving average
SOEC	solid oxide electrolyzer cell
SOFC	solid oxide fuel cell
SoH	state of health
SQP	sequential quadratic programming
SR	steam reforming
TEM	transmission electron microscopy
TPB	triple phase boundary
WGS	water gas shift
YSZ	yttria-stabilized zirconia

1 Introduction

In the current era of globalization, world emissions of greenhouse gas carbon dioxide have increased significantly with respect to the past: today more than ever the aim for a clean environment remains a crucial factor for the health of the population and the planet. Improving air quality is a major focus of environmental policies, as it affects all aspects of nature, including humans [1]. For these reasons, it is appropriate to consider the health risks posed by greenhouse gas (GHG) emissions released into the atmosphere and its related impact on climate change.

The urgency of combating global climate change has prompted nations worldwide to set ambitious targets for achieving carbon neutrality. On December 12, 2015, in Paris, 195 governments agreed to the text of the most significant global climate agreement in history. Known as the Paris Agreement [2], the international deal commits nearly every country in the world to lowering greenhouse gas emissions to curb the dangerous effects of climate change. This agreement aimed to prevent global temperatures from rising above pre-Industrial Revolution temperatures by 2°C. Ideally, the Paris Agreement strives to limit global temperature increases to 1.5°C.

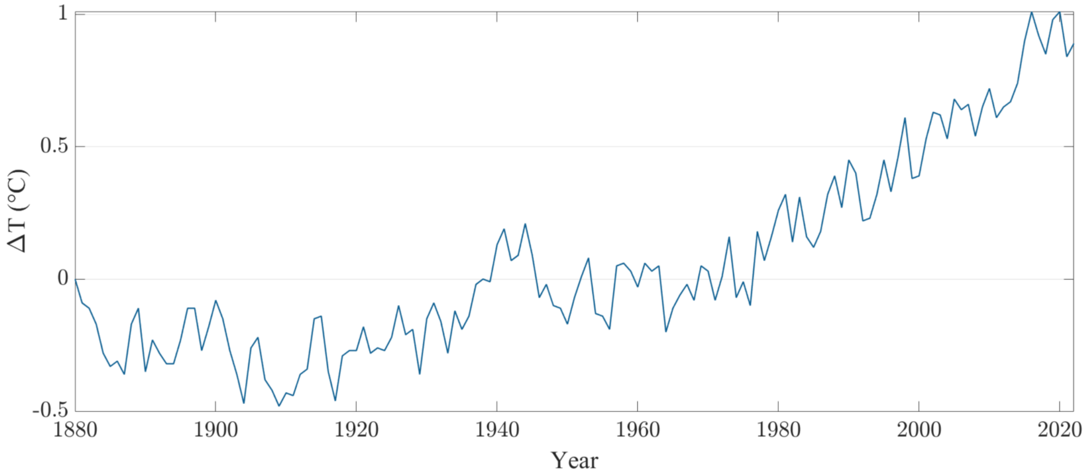

Figure 1.1: Global annual average surface air temperature compared to 1880, data from Potsdam Institute For Climate Impact Research via Climate Watch [3]

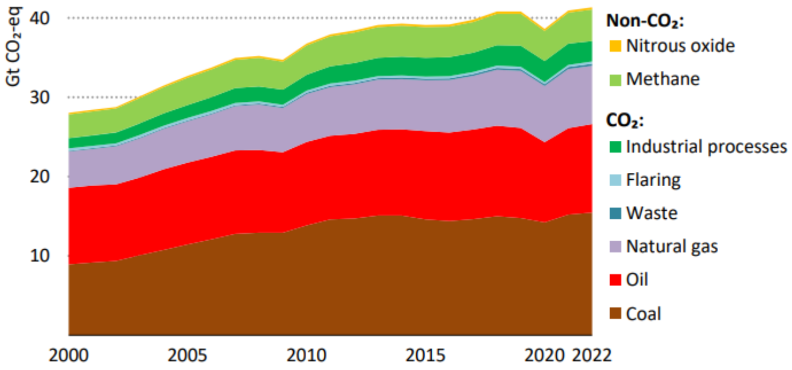

Figure 1.2: Global energy-related greenhouse gas emissions, 2000-2022 [4]

In the quest for a sustainable energy future, the transition to renewable sources like wind and solar presents significant challenges, notably the fact that they are not stationary and dependant on weather conditions, with low energy density and efficiency-related problems (Table 1.1).

Table 1.1: Energy density and efficiency of renewable energy sources [5]

	Energy Density
Fuels	Natural Gas: About 55 MJ/kg Gasoline: Around 46 MJ/kg
Solar PV Panels	About 0.36-0.72 MJ/m^2/day
Wind Turbines	Typically 1.44-2.16 MJ/m^2/day
	Efficiency
Solar Panels	Average efficiency: 15-20% Best commercially available: 22-23%
Wind Turbines	Capacity factor: 30-40% 2 MW turbine output: 0.6-0.8 MW on average

In this last decade, hydrogen has acquired a lot of interest as a renewable resource since it is clean and can be produced from a variety of other resources, such as natural gas, nuclear power, biogas, and renewable power. In the evolving landscape of renewable energy technologies, fuel cells have emerged as a pivotal area of research, attracting increasing interest due to their hydrogen applications and their potential to contribute significantly to a sustainable energy future.

1.1 Motivation

Hydrogen fuel offers several significant benefits that make it a promising alternative energy source. These benefits are crucial for achieving a sustainable and environmentally friendly energy future. One of the primary advantages of hydrogen fuel is its potential for zero emissions at the point of use. When hydrogen is used in fuel cells, it combines with oxygen from the air to produce electricity, with water vapor as the only by-product. This process eliminates the release of harmful greenhouse gases and pollutants, such as CO_2, NO_x, and particulate matter, which are typically associated with traditional fossil fuel combustion. As a result, hydrogen fuel can play a critical role in reducing air pollution and mitigating climate change. Hydrogen is also an abundant and versatile energy carrier and its energy density is another notable benefit. Hydrogen contains more energy per unit of weight than conventional fuels (120-142 MJ/kg), such as gasoline and diesel (Table 1.1). This high energy density makes hydrogen an attractive option for applications requiring high energy output, including transportation and industrial processes.

In addition to its environmental and performance benefits, hydrogen fuel also offers energy security and economic opportunities. Hydrogen can be produced domestically, reducing dependence on imported fossil fuels and enhancing energy security. The International Energy Agency (IEA) Renewables report on January 31, 2024, stated that Hydrogen-dedicated renewable energy capacity is expected to grow by 45 GW between 2022 and 2028 [6]. This heightened focus is underscored by the findings of the Fuel Cell Industry Review 2021 [7], which provides compelling insights into the state of the fuel cell sector, despite the publication delays and without speculating on future developments. Fuel cells are considered a promising technology for a variety of applications, including in transportation, stationary power generation, and portable electronics. The report's revelations from 2021, coupled with the acknowledgment of the impact of events in 2022 on the energy markets, present a robust case for the ongoing and future significance of fuel cell technology. The industry's achievement of surpassing 2.3 GW of fuel cell capacity shipped in 2021, meeting its goal from 2019 albeit a year late, and the increase in total units to nearly 86,000, underscores the technological advancements and growing market acceptance of fuel

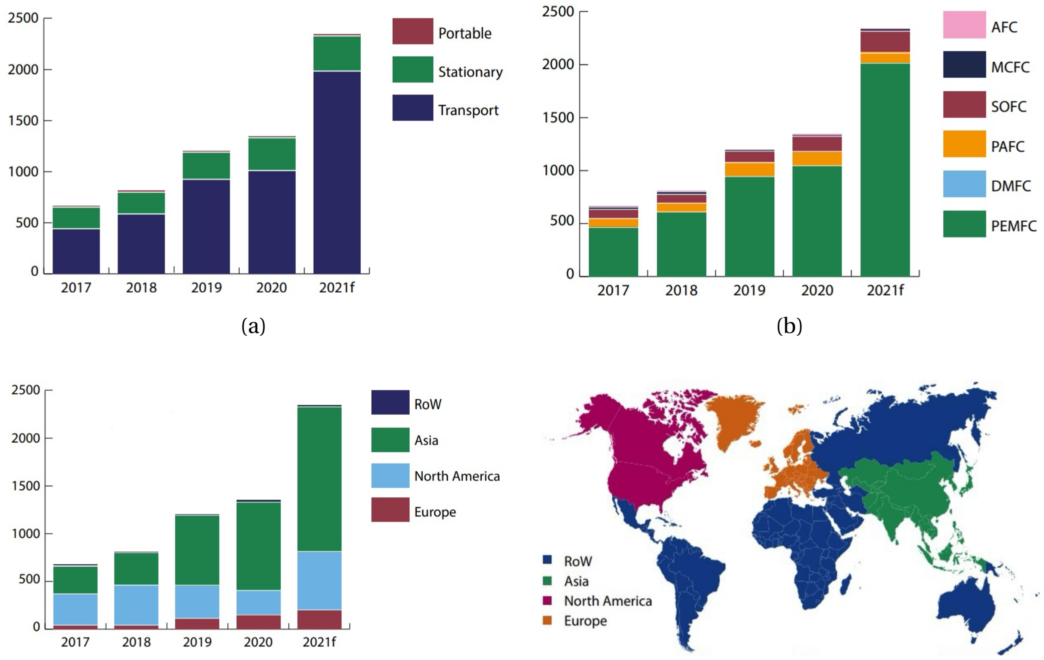

(a) (b)

(c) (d)

Figure 1.3: Total fuel cells produced megawatts 2017-2021 by application (a), by fuel cell type (b), by region of adoption (c-d) [7]

cells. Leading companies like Hyundai and Toyota continue to demonstrate the power of fuel cells in mobility, signifying a diverse and expanding market presence. Notably, the adoption of proton-exchange membrane (PEM) fuel cells, especially in mobility applications where they comprise 86% of the megawatt capacity, highlights the technology's versatility and increasing efficiency. However, solid oxide fuel cells (SOFC) are also garnering growing interest due to their high efficiency and fuel flexibility. SOFCs operate at higher temperatures, which allows them to use a wider range of fuels, including natural gas and biogas, without requiring expensive catalysts. This capability makes them particularly attractive for stationary power generation and combined heat and power (CHP) applications. Additionally, their ability to achieve higher electrical efficiencies and lower emissions contributes to their increasing appeal in various energy markets Nonetheless, the wide span of SOFC technology brings several new challenges, such as possible degradation mechanisms, material costs, and lifetime durability that currently hinder the broader application of fuel cells. Understanding and addressing these issues is key to advancing commercialization and their role in future energy systems, necessitating in-depth analysis of failure modes, performance impacts, and degradation mechanisms for technological improvements. Addressing this issue requires a deep understanding of the balance between system performance, degradation rates, and operational costs.

1.2 Scope of the thesis

To address the various new challenges associated with SOFC technology, this thesis, starting from an existing zero-dimensional (0-D) model for a CPOX-based SOFC system, integrates a degradation model to assess the operational lifespan of the fuel cell stack and a techno-economic analysis to connect the results to financial assessments. The primary focus is on implementing novel control strategies to manage the end-of-life (EoL) of the SOFC stack, thereby optimizing system performance under various operating conditions. The main scope is to develop a comprehensive approach for predictive control optimization of complex SOFC systems.

This project encompasses several key objectives:

1. **Comprehensive Review:** Conduct an extensive literature review of existing SOFC technologies, emphasizing their operational efficiencies, degradation mechanisms, and current strategies for extending lifespan and reducing costs. Investigate the fundamental degradation processes of SOFCs under various operating conditions and explore end-of-life detection methods in complex SOFC systems during dynamic operations.

2. **Refinement of SOFC Model:** Refinement of an existing detailed 0-D model of a CPOX-based SOFC system that accurately reflects its performance characteristics and degradation behaviors under different operating scenarios. Integration of an existing degradation model that can be used for optimization analysis.

3. **Optimization Strategy Formulation:** Formulate and test various control strategies, using single-objective optimization and multi-objective optimization (MOO), with both fixed and dynamic mission profiles to find an optimal balance between maximizing system

performance (electrical and combined heat and power efficiencies) and life expectancy, thereby reducing overall operating costs.

1.3 Thesis structure

The remainder of this project is structured as follows:

- **Chapter 2 - Fundamentals:** This chapter provides an in-depth review of the current state of SOFC technology, including its advantages, challenges, and the various approaches taken to mitigate degradation and enhance system longevity.
- **Chapter 3 - Model of CPOX-based SOFC system:** Describes the analytical methods and modeling techniques employed in this study to understand SOFC degradation mechanisms and develop the optimization algorithm to perform predictive analysis.
- **Chapter 4 - Long-Term Prognostic Analysis with Control Strategies:** Discusses the application of predictive control to SOFC systems, and evaluates performances and state of health (SoH) of the SOFC system after single-objective optimization.
- **Chapter 5 - Operating Map Development through Multi-Objective Optimization:** Explores the development of operating maps and the analysis of Pareto fronts obtained using multi-objective optimization for different operational scenarios with fixed input operations.
- **Chapter 6 - Dynamic Mission Profile for a Real-Case Application:** Analyzes the application of dynamic profile operations to a real-world case study.
- **Chapter 7 - Conclusion:** Summarizes the findings of the study, discusses its implications for SOFC technology deployment, and outlines directions for future research.

Through this structured approach, the project aims to contribute to the advancement of SOFC technology, making it a more viable and cost-effective solution for clean energy generation in the fight against climate change.

2 Fundamentals of SOFCs

Fuel cells are devices that convert chemical energy directly into electrical energy through an electrochemical reaction, bypassing the need for combustion. This process involves the combination of hydrogen (or another fuel) and oxygen (from the air) across an electrolyte. Unlike traditional batteries, which store a finite amount of energy, fuel cells can continuously produce electricity if supplied with fuel and oxygen. Several fuel cell types are categorized primarily based on the kind of electrolyte they use. These include SOFCs, PEMFCs, alkaline fuel cells (AFCs), molten carbonate fuel cells (MCFCs), and phosphoric acid fuel cells (PAFCs), among others. Each type has its unique advantages, operating temperatures, and applications ranging from portable power generation to large-scale energy production in power plants. PEMFCs have lower efficiency, are sensitive to fuel purity, and require complex water management. AFCs are highly sensitive to carbon dioxide, which can degrade the electrolyte and are limited to pure hydrogen and oxygen, reducing their flexibility. MCFCs operate at very high temperatures, leading to material degradation and increased maintenance, and their electrolyte is corrosive. PAFCs have moderate efficiency, slow startup times due to their operating temperature, and require careful handling of the corrosive phosphoric acid electrolyte.

SOFCs emerge among the others for their high electrical efficiency, often exceeding 60%, and up to 80% with heat recovery systems. They can operate on various fuels, including natural gas, biogas, hydrogen, and liquid hydrocarbons, offering versatility. The solid ceramic electrolyte in SOFCs is durable and tolerates high temperatures, resulting in longer lifespans and lower maintenance costs. SOFCs also produce fewer pollutants, contributing to better air quality, and can be scaled for different power needs, from small distributed systems to large power plants.

This chapter delves into the core principles and technological underpinnings of SOFCs, which are the object of the project's analysis. SOFCs are an innovative class of fuel cells that have garnered significant attention for their potential in highly efficient, sustainable energy conversion. SOFCs are notable for their high operating temperatures, fuel flexibility, and potential for integration into various energy systems, ranging from portable power sources to large-scale electricity generation.

2.1 SOFC operating principles

SOFCs have garnered significant attention due to their high efficiency, cost-effectiveness, fuel flexibility [8, 9, 10, 11] and pollution-free operation [12]. Recent advancements in SOFC technology, including the development of proton conducting electrolyte [13] and direct carbon SOFCs [14], highlight their potential inefficient energy conversion using diverse alternative fuels[15].

A solid oxide cell (Fig 2.1) can operate in dual modes: as a fuel cell and an electrolyzer. This device consists of two porous electrodes and a solid electrolyte. The fuel electrode, made of a Ni-YSZ composite, provides structural support. The electrolyte, composed of Yttria Stabilized Zirconia (YSZ), conducts oxygen ions at high temperatures (> 550 °C). On top of this electrolyte is the air electrode, made of Lanthanum Strontium Cobalt Iron Oxide (LSCF), which prevents chemical interactions with the electrolyte. The Gadolinium-Doped Ceria (GDC) layer is placed between the LSCF and YSZ as an ionic conductor barrier. The Ni-based fuel electrode facilitates the internal reforming of hydrocarbons (e.g., CH_4, C_2H_6), improving thermal management and potentially eliminating the need for an external reforming unit. In electrolyzer mode, solid oxide electrolysis cells (SOECs) are used for hydrogen and oxygen production, fuel generation, carbon dioxide recycling, and chemical synthesis [16]. The most common structures are electrolyte-supported cells (ESC), anode-supported cells (ASC), and metal-supported cells (MSC).

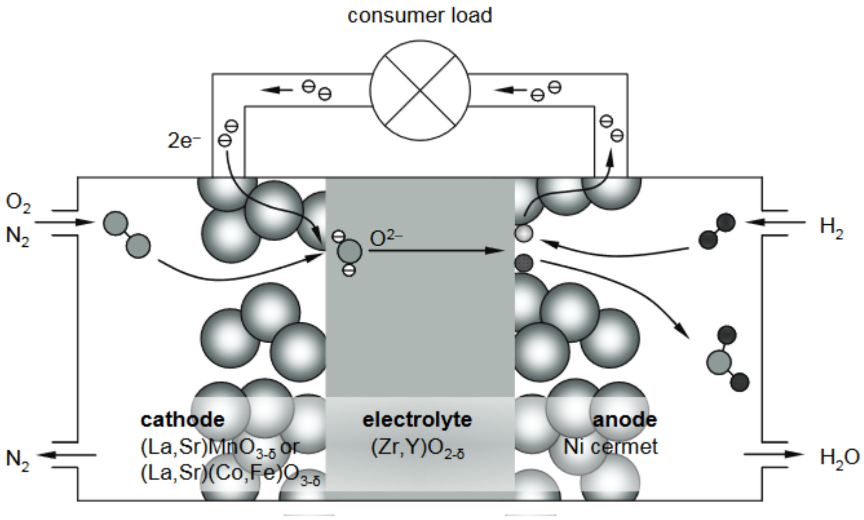

Figure 2.1: Structure of a SOFC [17]

In fuel cell mode, fuel is consistently delivered to the anode and undergoes oxidation by oxygen ions from the electrolyte, generating H_2O (CO_2) and electrons. The anodic reaction occurring at the triple phase boundary (TPB) is indicated schematically by the red dot in Figure 2.2. TPB is a critical region where three different phases coexist and interact: the ionic conductor (electrolyte), the electronic conductor (electrode), and the gas phase (fuel or oxidant). Efficient SOFC operation depends significantly on the effective management and optimization of the TPB, as it directly influences the reaction kinetics and overall performance of the fuel cell. Concurrently, the air is supplied to the cathode, where oxygen molecules are adsorbed and

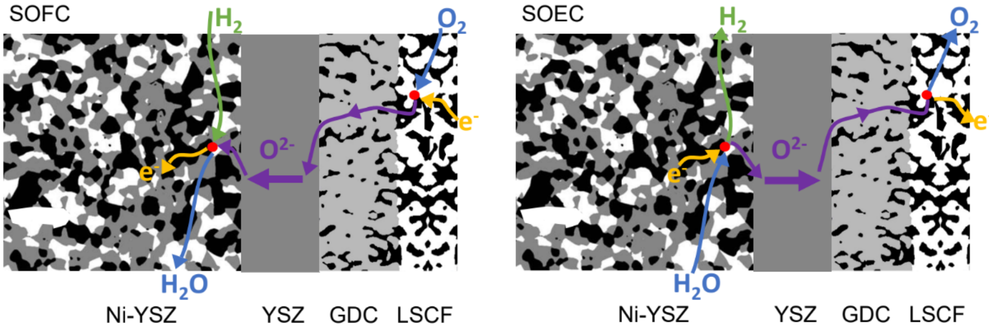

Figure 2.2: Working principle and half-reactions in SOC [18]

reduced to oxygen ions (O^{2-}) upon accepting electrons. These ions migrate to the anode-electrolyte interface through the cathode's ionic conductor phase and the electrolyte.

In the electrolysis mode, the reactions are reversed: water is reduced at the cathode, producing H_2 and O^{2-}. The oxygen ions then travel through the electrolyte to the cathode, releasing electrons to form oxygen molecules. A resume of the main reactions in SOFC and SOEC is proposed in Fig 2.1.

Table 2.1: Comparison of reactions in SOFC and SOEC

SOFC Reactions	**SOEC Reactions**
Fuel electrode:	Fuel electrode:
$\mathrm{H_2 + O^{2-} \rightarrow H_2O + 2e^-}$	$\mathrm{H_2O + 2e^- \rightarrow H_2 + O^{2-}}$
Oxygen electrode:	Oxygen electrode:
$\mathrm{\frac{1}{2}O_2 + 2e^- \rightarrow O^{2-}}$	$\mathrm{O^{2-} \rightarrow \frac{1}{2}O_2 + 2e^-}$
Total reaction:	Total reaction:
$\mathrm{H_2 + \frac{1}{2}O_2 \rightarrow H_2O}$	$\mathrm{H_2O \rightarrow \frac{1}{2}O_2 + H_2}$

Oxygen and fuel (H_2) react via a dense, oxide ion-conducting electrolyte (YSZ); the spatial separation of reduction and oxidation reaction enables the utilization of the electrons involved in the redox process; in fact, electrochemical redox reactions induce an electrical potential due to varying oxygen partial pressures across the electrolyte.

Knowing that for a generic chemical reaction:

$$\sum_{\text{reactants}} \nu_{\mathrm{A,B,...}}\mathrm{A,B,...} \rightarrow \sum_{\text{products}} \nu_{\mathrm{X,Y,...}}\mathrm{X,Y,...} \tag{2.1}$$

The reaction's standard enthalpy change, ΔH^0, crucial for understanding the electrochemistry of solid oxide cells, is determined as:

$$\Delta H^0(T) = \sum_i \nu_{\mathrm{st},i} \Delta_f H^0(T) \tag{2.2}$$

Here, $\nu_{\mathrm{st},i}$ are the stoichiometric coefficients, with products assumed positive and reactants negative. The term $\Delta_f H_i^0$ represents the standard formation enthalpy of species i, under standard conditions (STP, $T^0 = 25C$, $p^0 = 1$ atm). Importantly, the reaction enthalpy primarily depends on temperature. The temperature dependence of reaction enthalpy and the derivation of standard reaction entropy, $\varDelta S^0$, incorporating the species' standard entropies and their variations with temperature and pressure, follow as:

$$\varDelta H(T) = \varDelta_r H^0(T) + \sum_i \nu_{\mathrm{st},i} \int_{T^0}^{T} c_{p,i}(T) dT \tag{2.3}$$

$$\varDelta_r S^0(T,p) = \sum_i \nu_{\mathrm{st},i} S_i^0(T,p) \tag{2.4}$$

Expanding on the entropy's dependency, it is possible to find:

$$\varDelta S(T,p) = \varDelta S^0(T,p) + \sum_i \nu_{\mathrm{st},i} \left(\int_{T^0}^{T} \frac{c_{p,i}(T)}{T} dT - R \ln \frac{p_i}{p^0} \right) \tag{2.5}$$

The distinction between reaction enthalpy, $\varDelta H$, and Gibbs free energy, $\varDelta G$, highlights the thermodynamic limits of reaction work, W, in terms of electrical energy:

$$\varDelta_r G(T,p) = \varDelta_r H(T) - T\varDelta_r S(T,p) = -W \tag{2.6}$$

$$W = neFE^0 \tag{2.7}$$

Here, W denotes the work associated with an endothermic or exothermic reaction under isothermal and isobaric conditions, further refined to represent the electrical energy via Faraday's laws, with E^0 denoting cell reversible potential at STP, F the Faraday constant (96485.332 Cmol^{-1}) and n the electron count in the reaction (e.g. 2 in the case of H_2).

The reversible standard cell voltage [16] is then determined using the reaction's Gibbs free energy ($\varDelta G^0$):

$$E^0(T) = -\frac{\varDelta G^0(T)}{nF} \tag{2.8}$$

It's important to mention that the cell voltage depends on operating temperature and gas partial pressures and can be correlated to the Nerst voltage through the Nerst equation:

$$E = E^0(T) + \frac{RT}{2F} ln \left(\frac{\frac{p_{H_2}}{p} (\frac{p_{O_2}}{p})^{0.5}}{\frac{p_{H_2O}}{p}} \right) \tag{2.9}$$

In the typical operation range (600-950 °C) of a SOFC operated on hydrogen (with 1 % H_2O) and air as oxidant Equation 2.9 gives values of E between 1.18 and 1.13 V.

2.2 Loss mechanisms

SOFCs, like all technologies, are prone to various loss and degradation mechanisms that can impair their performance over time [19]. Various factors contributing to the observed voltage drop are detailed in Equation 2.10:

$$U(i) = E_0 - \eta_{\mathrm{ohm}} - \eta_{\mathrm{act,a/c}} - \eta_{\mathrm{con,a/c}} \tag{2.10}$$

where $U(i)$ represents the cell voltage under load, E_0 the open circuit potential, η_{ohm} the ohmic resistance losses, $\eta_{\mathrm{act,a/c}}$ the activation overpotentials for the anode/cathode, and $\eta_{\mathrm{con,a/c}}$ the concentration overpotentials at the anode and cathode, respectively. This equation summarizes the main factors that cause the voltage drop in electrochemical systems.

Ohmic losses

Ohmic losses are encountered during the transport of electrons or ions through electrodes and electrolytes. The total ohmic resistance is a cumulative function of the individual ohmic resistances denoted by R_k. According to Ohm's law, the ohmic overpotential, η_{ohm}, exhibits a linear relationship with the current density, j, expressed as:

$$\eta_{\mathrm{ohm}} = j \sum_{k}^{tot} R_k = j \cdot R_{ohm} \tag{2.11}$$

Absolute measures like resistance (Ω) and current (A) lack comparability across varying system sizes. Instead, area-normalized metrics, namely current density (A/cm^2) and area-specific ohmic resistance ($\Omega \cdot cm^2$), offer a standardized basis for analysis. These adjustments account for differences in active surface areas, particularly using the smallest layer in multi-layered systems like ASCs for normalization. This approach ensures consistency in comparing electrochemical performance across diverse configurations. The calculation of ohmic resistance (R_{ohm}) in fuel cells involves the specific resistivity of the membrane (ρ_{ohm}), the active area of the cell (A), and the thickness of the polymer membrane (l), which acts as the cell's electrolyte. The formula for determining R_m is expressed as:

$$R_{ohm} = \frac{\rho_{ohm} \cdot l}{A} \tag{2.12}$$

In the context of planar cells, a significant portion of ohmic losses is attributed to the solid electrolyte component. Notably, 8 mol% yttria-stabilized zirconia (8YSZ) remains the benchmark material in this domain, exhibiting an ionic conductivity of $\sigma = 5\,\mathrm{S/m}$ at 800 °C. Contrary to electrolyte-supported cells, which may have electrolyte thicknesses up to 200 μm, anode-supported cells typically feature a much thinner electrolyte layer, around 10 μm. Consequently, at 800 °C, the ohmic resistance in anode-supported cells can theoretically be reduced to $0.020\,\Omega \cdot \mathrm{cm}^2$, and even at 600 °C, a resistance of $0.176\,\Omega \cdot \mathrm{cm}^2$ is achievable, facilitating cell operation [20].

Activation loss

Activation loss refers to the electrochemical degradation processes primarily occurring at the TPB, where the phases of ionic conduction, electronic conduction, and gas meet. To initiate a reaction, an activation energy is requisite to surmount the energy barrier inhibiting spontaneous reactions. The activation overpotential must be applied to every half-cell reaction. Typically, in fuel cells, the hydrogen oxidation reaction is much faster than the oxygen reduction reaction, which is why the activation overpotential of the oxygen electrode dominates. Elevated temperatures increase the likelihood that reactants acquire the essential activation energy, thereby diminishing overpotentials. The main equation in describing the impact of activation overpotential on current density is the renowned Butler-Volmer equation [21]:

$$\eta_{\mathrm{act,el}} = \frac{RT}{n_{\mathrm{e}}F}\left(\alpha_{\mathrm{el}}\ln\left(\frac{j}{j_{0,\mathrm{el}}}\right) - (1-\alpha_{\mathrm{el}})\ln\left(1-\frac{j}{j_{0,\mathrm{el}}}\right)\right) \tag{2.13}$$

In this formula, $j_{0,\mathrm{el}}$ denotes the exchange current density for the anode or cathode, which is dependent on partial pressure and temperature. The term n_{e} represents the number of electrons transferred (for this study, $n_{\mathrm{e}} = 2$), α_{el} signifies the apparent charge transfer coefficient, and $\eta_{\mathrm{act,el}}$ indicates the activation overpotential for the specified electrode (either anode or cathode). The charge transfer coefficient offers insights into the symmetry of the activation energy barrier under the influence of either a positive or negative overpotential. Activation overpotentials for both the anode and cathode are calculated separately using the Butler-Volmer equation (Eq. 2.13). The required parameters, $j_{0,\mathrm{el}}$ and α_{el}, are determined through impedance spectroscopy conducted both at open circuit conditions and under applied current load.

Diffusion overpotential loss

Diffusion overpotential, denoted as $\eta_{\mathrm{conc,a/c}}$, is caused by mass transfer kinetics that govern the transport of reactants to the electrode surface for redox reactions. Concentration overpotential within electrochemical cells is due to two primary sources: the electrode and the Gas Diffusion Layer (GDL). The GDL, serving as a critical intermediary between the electrode and the interconnect, plays a crucial role in ensuring a consistent and efficient supply of reactants, facilitating the removal of products, and maintaining electrical connectivity. The electrochemical potential variation, attributed to reactant depletion and product accumulation, contributes significantly to the concentration overpotential observed. Efforts to mitigate concentration overpotential focus on optimizing the GDL's design for enhanced convective mass transport and creating electrodes with optimal thinness and gas permeability. Strategic modifications, such as adding macropores within the electrode, aim to improve gas diffusion to the active layer, thereby enhancing overall cell efficiency. While the concentration overpotential can be evaluated for each side of the cell, it is mainly influenced by the fuel electrode due to the excess air during operation. This effect becomes significant when current extraction causes reactants to diffuse through both the gas layer and the porous structure of the electrode to reach the active reaction sites. As a result, there is a difference in composition between the electrode surface and the bulk gas stream, leading to a voltage difference. The mathematical expression for the concentration overpotential at the anode and cathode is given by:

$$\eta_{\text{conc,a}} = \frac{RT}{2F} \ln\left(\frac{p_{\text{bulk},H_2} p_{\text{TPB},H_2O}}{p_{\text{TPB},H_2} p_{\text{bulk},H_2O}}\right) \tag{2.14}$$

$$\eta_{\text{conc,c}} = \frac{RT}{2F} \ln\left(\left(\frac{p_{\text{bulk},O_2}}{p_{\text{TPB},O_2}}\right)^{1/2}\right) \tag{2.15}$$

Quantifying these overpotentials is challenging due to the difficulty in measuring local reactant partial pressures at the electrode's active sites. These partial pressures can be calculated by applying Fick's first law, assuming a linear concentration gradient directly related to the current density, j. This approach yields the following equations for the anode and cathode, which correlate the diffusion-based voltage drop, $\eta_{\text{conc,a/c}}$, to the current density j [22].

ASR model

In the context of this project, the previous loss mechanisms have been sinthetized in a simplified area-specific resistance (ASR) model, that is a measure of the overall resistance of the cell and is expressed in ohm-square centimeters ($\Omega \cdot \text{cm}^2$). In an SOFC, the ASR encapsulates the various resistances mentioned before and it is influenced by several factors, including temperature, cell design, material properties, and the operating conditions of the SOFC. Lowering the ASR is a primary objective in SOFC development because it directly correlates with higher cell efficiency and power output. Mathematically, the ASR can be represented as:

$$\text{ASR} = \frac{\eta}{j}$$

where η is the overpotential (the deviation from the equilibrium potential due to resistance losses) and j is the current density. This equation highlights that ASR is a function of the electrochemical characteristics of the SOFC. Furthermore, ASR can be described as the sum of ohmic resistance (R_{ohm}) and polarization resistance (R_{pol}):

$$ASR = R_{ohm} + R_{pol} \tag{2.16}$$

2.3 Degradation mechanisms

Failures within electrochemical cells can be categorized into two main types:

- **Physical failures**: These affect cell efficacy, electrical resistance, and energy dissipation.
- **Morphological failures**: These lead to structural damage and permanent changes in cell morphology.

Morphological failures often lead to physical failures, resulting in a decline in cell performance. These failures depend on two primary factors: the materials used in cell construction and the environmental conditions during operation [23].

Material-related degradation worsens with prolonged operation and is irreversible. To mitigate this, advanced materials must be developed, or operational parameters optimized. Key operational conditions such as impurity levels, steam concentration, carbonaceous compounds, and temperature are crucial. Impurities like sulfur, phosphine, and chlorine, even in parts per billion, can significantly impair cell functionality. These contaminants increase energy losses in both SOFCs and SOECs, reduce catalytically active sites, and block gas channels, decreasing electrode porosity. Removing these impurities from the fuel supply is essential for maintaining long-term cell operation. Additionally, carbonaceous materials in the fuel stream can lead to carbon formation and deposition on nickel-based electrodes, reducing efficiency. Preventing nickel reoxidation and agglomeration is also important. Thermal cycling is a significant stressor that accelerates degradation. Reversible operation shows mixed results; some studies suggest it harms SOC performance, while others indicate it can help reduce or eliminate degradation in SOE configurations. Besides cell-level degradation, system components like reformers, heat exchangers, and steam generators also degrade, affecting overall system stability.

In Table 2.2 all main degradation mechanisms discovered and analyzed are summarized.

2.4 Diagnostic tools

A variety of diagnostic instruments are available for detecting degradation in its early stages, helping to prevent permanent damage. These techniques are broadly categorized into two groups: in-situ and ex-situ methods, each providing unique insights into the cell's operation and structure.

In-situ techniques are used to assess the cell's functionality during operation, making them "online" tools. These methods allow real-time analysis of the cell, enabling continuous monitoring of operational parameters, sensitivity assessments, and evaluation of both steady-state and dynamic behaviors. Additionally, in-situ techniques are very useful for tracking the evolution of cell performance over time. The primary advantage of in-situ methods is their ability to provide immediate data without compromising the cell's operational integrity or availability.

Ex-situ characterization allows for a detailed investigation into the material composition, structural integrity, and properties influencing a cell's performance. By examining components outside their operational context, researchers can identify degradation mechanisms, evaluate material compatibility, and develop strategies to enhance cell longevity and efficiency. The choice between in-situ and ex-situ characterization methods depends on the study's objectives. In-situ methods offer a dynamic view of the cell under operational conditions, while ex-situ techniques provide a detailed examination of structural and material characteristics. Combined, these methods offer a comprehensive understanding of fuel cell behavior. The instruments used, along with the parameters they can detect and the data they yield, include temperature monitoring via thermocouples and thermography, light imaging, gas analysis through gas chromatography and mass spectrometry, spectrochronopotentiometry, raman vibrational spectrometry voltage, and current monitoring systems, polarization curve analysis, electrochemical

Phenomenon	Degradation Effect
FE1: Ni redox cycling	Deactivation/mechanical damage: Ni is deactivated when it is oxidized at very low H2 contents; When reduced again, the Ni undergoes a redox cycle that could compromise the mechanical integrity of the electrode after several cycles [24, 25].
FE2: Ni coarsening	Deactivation [26, 27, 28]
FE3: Carbon deposition and Ni dusting	Deactivation [29]
FE4: Sulfur Poisoning	Deactivation
FE5: Phosphorus poisoning	Deactivation
FE6: Silicon poisoning	Deactivation
FE7: Other Poisoning/-contaminations	Deactivation [30, 31, 32]
OE1: Silicon poisoning	Deactivation
OE2: Boron poisoning from the sealant	Deactivation by LaBO3 formation
OE3: Chromium poisoning	Deactivation by SrCrO4 or Cr2O3 Formation [33, 34, 35, 36]
OE4: Chlorine poisoning	Deactivation, electrode delamination
EY1: Cracks and Embrittlement	Loss of electrolyte tightness; gas mixing; Hot spot creation due to gas crossover; Delamination and grain boundary embrittlement, pore formation near the oxygen electrode.
EY2: Conductivity loss	Ionic conductivity loss
IC1: Corrosion/Growth of insulating oxide layers	Loss of electric conductivity by poorly conducting scale formation; Electrode poisoning (Cr, Si)
IC2: Scale spallation	Ohmic losses
IC3: Mechanical deformation	Decrease of contact area with the cell; change in electrical current pathways between the MIC and the cell
IC4: Depositions on interface with electrodes	Gas channel blocking
SL1: Mechanical failure: Leakage	Loss of contact pressure in the case of compressible seals or thermodynamically induced cracking of glass-ceramic seals; A secondary effect is fuel combustion on the leak location leading to a hot spot and further degradation of stack components; Increased humidity from combustion may also increase corrosion of MICs, and increased chromium evaporation from MICs leading to poisoning of O2-electrode; devitrification of glass ceramics
SL2: Chemical instability: Reactivity & Poisoning	Causes or increases corrosion at its' interfaces; released species from sealing poisoning cell components; BaCrO4 formation; seal porosity

Table 2.2: Degradation effects in SOFC, FE is fuel electrode-related degradation, OE is oxygen electrode-related degradation, EY is electrolyte-related degradation, IC is interconnection-related degradation, SL is sealing-related degradation.

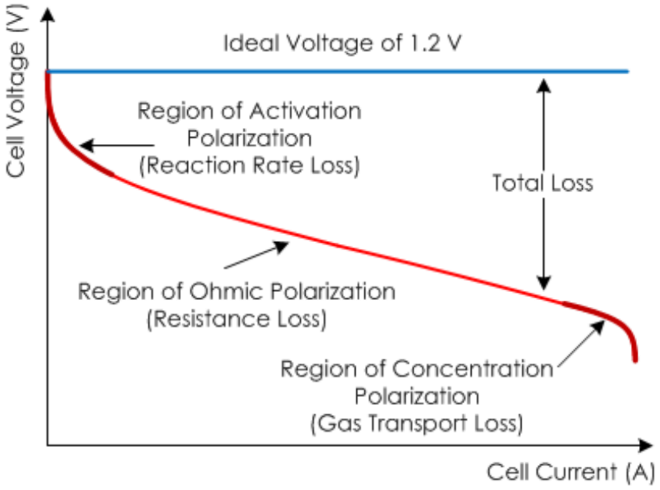

Figure 2.3: Schematic plot of current-voltage curve principle and half-reactions in SOC [41]

impedance spectroscopy (EIS) analyzer, scanning electron microscopy (SEM), equivalent circuit model analysis.

Other methods can be found in the literature, but the majority of these methods involve economic analysis through "Life Cycle Assessments" [37, 38, 39]. For the scope of this research only iV curves are presented in detail.

Current/Voltage characteristics (iV curves)

The impact of various loss mechanisms on the voltage output of a SOFC during operation is qualitatively depicted in Figure 2.3. Notably, even under open circuit conditions (OCV), the cell voltage falls short of the thermodynamically predicted Nernst voltage. This discrepancy, termed "Overpotential", may result from parasitic losses such as undesired electron leaks across the electrolyte or imperfections in the electrolyte's gas tightness. These factors cause fuel utilization even at an open circuit, which reduces the Nernst voltage. Figure 2.3 shows the relationship between current density (j) and different types of polarization. At low current densities, activation polarization is the main factor. At high current densities, diffusion polarization becomes dominant because the transport of reactive species to the electrolyte/electrode interface becomes a limiting factor [40]. Another significant voltage drop comes from gas conversion loss due to fuel utilization. As current density increases, more fuel and oxidant gases are consumed, changing the hydrogen and oxygen partial pressures. This change lowers the Nernst voltage, which is the electromotive force driving the overall cell reaction. Furthermore, impedance spectroscopy reveals the nonlinear nature of voltage drops across different operating regimes: activation losses are prominent at low current densities due to processes occurring at the TPB of the electrodes. In the medium current range, ohmic overpotential loss predominates, exhibiting a nearly linear decline in cell voltage with increasing current density. At high current densities, the fuel cell's voltage output experiences a sharp decrease, attributed to mass-transport limitations (gas diffusion polarization) at the electrodes.

Since current and fuel utilization (FU) are linked by Faraday's Law 2.17, the current-voltage characteristics can be converted into FU-voltage curves:

$$FU = \frac{i}{i_{max}} = \frac{i \cdot N_{cell}}{n_e \cdot F \cdot \dot{n}_{fuel}} \tag{2.17}$$

where $\dot{n}_{fuel}$ denotes the specific molar flow rate (in $\mathrm{mol} \cdot \mathrm{s}^{-1} \cdot \mathrm{cm}^{-2}$), n_e represents the electrons involved in the redox reactions, and F is the Faraday constant. The term N_{cell}, included for stack configurations, is the total number of cells within the stack. Despite this characterization method being straightforward and quick, it often lacks in providing insights into the system's dynamics. ASR can be derived from the IV curves. It is calculated as follows:

$$ASR = \frac{U - OCV}{j} \tag{2.18}$$

The local ASR at a specific current density (j^*) can be determined by the derivative of voltage concerning current, evaluated at j^* [18]:

$$ASR_{local}(j^*) = \left.\frac{dU}{dj}\right|_{j=j^*} = \frac{U(j^* + \Delta j) - U(j^*)}{\Delta j} \tag{2.19}$$

Typically, the ASR value is extracted from the linear portion of the IV curve, providing a quantifiable measure of the electrochemical system's resistance properties.

2.5 SOFCs physical modelling

Over recent years, significant advancements are made in the field of SOFC modeling, focusing on the simulation of internal processes grounded on the fundamentals of physics. Researchers have effectively utilized both physical and analytical equations to encapsulate the dynamics of electrochemical reactions, alongside the electronic and ionic characteristics of materials, and the kinetics of gas flow, into comprehensive physical models. The scope of these models extends from the simplistic zero-dimensional (0-D) approaches to the more complex three-dimensional (3-D) models, each tailored to address distinct investigative goals as highlighted by K. Wang et al. [42]: the 0-D models are the simplest, treating the SOFC as a continuously stirred tank reactor (CSTR) without spatial variations, ideal for quick performance estimates and initial design studies; 1-D models add complexity by considering variations along the flow direction of the fuel or air, useful for understanding gradients in temperature, concentration, and potential. Among these models its meaningful for this thesis to cite the work of Zaccaria et al [43, 44], who have used a real-time 1-D model to simulate the effects of voltage degradation in the cell, where different mechanisms are summarized in simple empirical expressions that relate degradation rate to operating conditions (current density, fuel utilization, and temperature) on a localized basis; 2-D models incorporate variations in two dimensions, providing detailed insights into the distribution of variables across the cell, including edge effects and channel-to-channel variations; 3-D models consider all three spatial dimensions, capturing complex interactions within the cell and offering a detailed understanding essential for optimizing cell design and performance. In the context of developing online diagnostic tools, models with lower dimensions

(0-D and 1-D [45, 46, 47, 48, 49, 50]) are preferred owing to their reduced computational demands compared with their higher-dimensional counterparts (2-D and 3-D). Despite this, models of higher dimensions are invaluable for understanding the operational dynamics of fuel cells across various geometric configurations and are instrumental in generating training datasets for non-transparent (black-box) modeling approaches or neural networks algorithms [51, 52, 53, 54].

For the scope of this thesis, only 0-D dimensional models are discussed, since the primary focus of the thesis is the optimization analysis considering a 0-D model case.

2.5.1 0-D modelling

Among the spectrum of models utilized for SOFC analysis, the 0-D model stands out for its simplicity. It operates under the principle that dimensions and spatial variations are disregarded. This model fundamentally transforms input variables into output variables without considering spatial differentiation. The simplification of 0-D models is achieved through the adoption of theoretical assumptions and the integration of empirical data. Within the framework of a SOFC system, the discrete components such as compressors, heat exchangers, valves, partial oxidizers, and systems for the removal of contaminants are represented using distinct 'black box models'. These models function independently, each simulating the specific element it represents without accounting for spatial dimensions. This approach allows for the modular analysis of the SOFC system, facilitating the understanding and optimization of each component's performance in isolation.

From the literature there are many 0-D model proposed for monitoring stack performance: Costamagna et al. [55] proposed macroscopic finite equations that expressed a balance between inlet and outlet flows of mass and energy in each component of the group; under suitable assumptions, they allowed the evaluation of the average values of the physical-chemical variables of each components and the electrochemical performance of the group itself; Peters et al. assumed constant temperature and approximated the overall cell resistance from experimental measurements [56]; Becker et al.'s model [57] added deviation of an equilibrium potential and implemented an analytical expression for an activation overpotential, an empirical area specific resistance for an ohmic overpotential, and a limiting current density for a concentration overpotential; Torii et al. came up with a model which assumed internal reforming at equilibrium under the supposed operating temperature [58]; Campanari [59] and Park et al. [60] adopted empirical current–voltage data from experiments; Ni et al. also applied analytical expression-based electrochemistry, and the cell geometry is especially considered during activation overpotential calculation [61]; Fallah et al. assumed constant operating temperature and equilibrium for internal reforming [62]; Rokni worked on a dynamic network analysis tool given with fixed inlet and outlet gas temperature [63]; Chitsaz et al. introduced equations for equilibrium internal reforming and externally given temperature difference [64].

2.5.2 Degradation modelling

When dealing with SOFC modeling, also a model for the degradation mechanisms should be carefully built to address performance decreases over time. This modeling analysis can be done both at the system and at the stack levels.

Stack level degradation takes into account all the stressors and operating parameters that have a direct and indirect influence on the degradation and performance reduction, often in conjunction with the interaction between each of them. Peng et al. [65] have resumed some of the most relevant prediction models that are built to predict degradation performance, Table 2.3 shows a list based on his work. There are mainly four different approaches that are currently used to predict future degradation trends:

- Model-based approaches: The model-based approach characterizes the progression of SOFC performance through the development of a physical model. This model forecasts the system's degradation by emulating the microscopic parameters and material properties intrinsic to the SOFC. Employing this model-based prediction methodology enables the identification of voltage degradation trends over extended periods. Nevertheless, the efficacy of this prediction technique is influenced by two primary factors. Initially, the accuracy of mechanism models is compromised by an incomplete comprehension of the degradation processes occurring within electrodes, electrolytes, interconnects, and seals. Additionally, there is a challenge in accurately replicating the complex connection associated with the materials, their fabrication, operational conditions, and subsequent degradation. Constructing these models necessitates the establishment of numerous presuppositions, which may render the predicted degradation overly idealized.
- Data-based approaches: data-based prediction uses black-box models to understand system behavior through analysis of sensor monitoring data, aiming to forecast future system states. This approach does not need a physical comprehension of the system's operations. Thanks to its superior adaptability and precision, the data-based prediction technique offers a practical solution for real-time analysis and forecasting and is swiftly advancing. Nevertheless, these approaches encounter specific limitations: the precision of data-driven models is contingent upon the volume of training data, the acquisition of which can be both costly and time-intensive. Secondly, the integrity of the training data significantly influences the algorithm's accuracy; ideal training datasets should encapsulate the system's degradation trends. Another issue is that the efficacy of data-driven algorithms is around the judicious selection of suitable algorithmic structures and parameters, which in turn impacts the feasibility of employing data-based strategies in practical scenarios.
- Image-based approaches: Image analysis methods offer a robust and accurate means for predicting performance degradation in SOFC systems. This technique adeptly captures the microscopic characteristics, mechanical attributes, and thermal properties of SOFCs, utilizing performance parameters derived from images to quantify degradation phenomena. Initially, this approach uses advanced techniques such as SEM, Transmission Electron Microscopy (TEM), and Focused Ion Beam (FIB) methods to capture images of

SOFC microstructure. Subsequent processing and quantitative analysis of these images yields detailed insights, including phase fractions, grain and particle sizes, compositional shapes, spatial phase arrangements, and other descriptive characteristics. This information facilitates a comprehensive analysis of SOFC degradation by examining the internal microstructure. With respect to the model-based and data-based prediction methods, image analysis stands out for its simplicity and efficacy and is often used as a validation of previously mentioned approaches. The primary limitation of the image-based strategy lies in the high cost of the requisite equipment, which can significantly inflate the expenses associated with system performance evaluations. Moreover, this method predominantly allows for the analysis of system interiors post-shutdown, thereby relegating its application to offline assessments of SOFC performance degradation.

- EIS-based approaches: EIS operates through the introduction of a sinusoidal current into the SOFC system and the measurement of the resultant voltage response. The relationship between the observed voltage and the input current delineates the system's electrochemical impedance, a metric that can inform predictions about the system's performance variations. However, employing EIS for SOFC degradation forecasting comes with notable drawbacks: firstly, the EIS process itself can influence SOFC performance during its operation. Secondly, it necessitates extra equipment, thereby elevating the overall system costs.

System level degradation takes into account also the performance decrease of other units that are present in the BoP of the SOFC stack, such as fuel processing units, air supply systems, heat exchangers, inverters and power conditioning units, water management systems, control systems, and thermal insulation. Different analyses are made in the literature at the system level [26, 66, 67].

2.6 SOFC performance optimization

Nowadays, given the significant capital costs associated with fuel cell stacks, computational modeling has emerged as a crucial tool for the analysis of SOFCs in terms of dynamics and control. Studies on hybrid systems, in particular, have shown high performance and flexibility under both full-load and part-load conditions, as well as during transitional phases, when compared to standalone fuel cell systems. Optimizing SOFC performance needs to achieve various goals, including the harmonization of components, temperature management, and load adaptation. It's important to distinguish between dynamic controls and supervisory controls, with the latter often utilizing optimization techniques for better performance. It's also important to mention that in this section, performance optimization does not take into account any improvement that can be made at the design level since the focus of the thesis is to develop an online strategy to control and optimize system performances.

In the literature, emphasis has often been placed on basic control mechanisms for SOFC systems. Key objectives for effective performance control include robust load adaptation, high efficiency under varying operational conditions, and extended component lifespan through minimized

Table 2.3: Different studies on SOFC degradation prediction, adapted from [65]

Prediction Method	**Predicted Objects**	**Models / Algorithm**	**Ref.**
Model-based	Predicting future degradation trends and remaining service life of SOFC stack.	Nonlinear SOFC power stack integration model	[68]
Model-based	Predicting the long-term performance degradation process of SOFC stack under accelerated operating conditions.	SOFC multi-physics field degradation model	[69]
Model-based	Predicting the effect of operating parameters on SOFC output voltage in the presence of degradation.	1D real-time SOFC model	[43, 44]
Model-based	Predicting the effect of Ni coarsening on SOFC performance.	Transient multi-physics field model for SOFC	[70]
Data-based	Predicting the degradation performance of SOFC systems.	Double-layer LSTM model	[71]
Data-based	Predicting the SOFC performance degradation caused by Cr poisoning.	Machine learning combined with relaxation time (DRT) distribution	[72]
Data-based	Predicting the output voltage trajectory of SOFC.	Neural network (NN) algorithm	[54]
Data-based	Predicting the impact of uncertainty in SOFC during degradation.	An approximate randomized algorithm based on Taylor series expansion	[73]
Image-based	Detecting the degradation of SOFC system performance due to chromium poisoning and nickel agglomeration.	Image line autocorrelation function analysis	[74]
Image-based	Predicting the degradation of Ni/YSZ anodes in SOFCs are related to the aggregation of metal particles.	Developed image analysis technique	[75]
EIS-based	Quantification of the particle size, phase ratio, and TPB point distribution of the anodes	EIS with SEM and two-dimensional image analysis technique	[76]
EIS-based	Prediction of the performance degradation of a single cell when operating under predetermined conditions	EIS with DRT and ECM	[77]

degradation. Critical control variables identified in the literature include fuel cell temperature and fuel flow. For basic level controls, a combination of proportional-integral-derivative (PID) controllers and feedforward strategies is commonly employed to mitigate temperature and fuel utilization fluctuations, thereby ensuring quick responses to load changes [78, 79]. Performance control has expanded to include the regulation of SOFC power output, fuel efficiency, cell temperature, and gas turbine operations. Innovative approaches, such as reversible operations to prevent degradation, offer promising methods for enhancing durability and potentially decoupling cell temperature from current density variations [80], [81]. Furthermore, various control architectures are explored to prevent fuel starvation and excessive temperature changes during load transitions. Aguiar et al. introduced a dual-loop control system comprising a supervisory controller that sets air and fuel flows based on power demand, and a PID controller that adjusts the airflow to maintain constant exhaust gas temperature, demonstrating a sophisticated approach to dynamic power demand management and operational stability [82]. Multi-variable model predictive control is used to minimize thermal stresses in an SOFC and improve lifetime [83, 84]. Zaccaria et al. [85] compared several different operating strategies to offset or mitigate cell degradation in a standalone SOFC stack and a hybrid system (with a gas turbine), discussing the benefits and limitations of such strategies in terms of fuel cell durability. This control mechanism is applied to a real-time, dynamic SOFC model for hardware-based hybrid system simulations. The fuel cell is tested under constant current, voltage, or stack power, and the gas turbine under off-design or constant power modes. The hybrid system provided greater control flexibility and extended lifespan compared to the standalone SOFC. Maintaining constant cell voltage in the hybrid system at constant power could extend operational life beyond 100,000 hours, offering superior performance. Allowing power degradation in the standalone system could extend its life by 70% but reduce electrical power output.

2.6.1 Non-Linear Model Predictive Control

The Non-Linear Model Predictive Control (NMPC) theory introduction is essential for the predictive analysis in Chapter 4. NMPC is a sophisticated technique for managing systems with nonlinear behaviors and constraints, differing from linear methods by solving an optimization problem that predicts future system outputs. This is particularly beneficial for SOFC systems due to their nonlinear interactions and operational constraints [86].

NMPC operates by controlling processes at distinct intervals, measuring the system state $x(n)$ and applying control inputs $u(n)$ to influence future states. The aim is to align $x(n)$ with a reference state $x_{ref}(n)$, minimizing deviations and maintaining proximity to the desired state. Control input $u(n)$ is often a feedback function $u(n) = \mu(x(n))$, mapping the state x into the control space U. Predictive control models the system as $x^+ = f(x,u)$, constructing a predicted trajectory of the state using control inputs from $u(0)$ to $u(N-1)$ over a prediction horizon N. The goal is to adjust $u(0),...,u(N-1)$ to minimize the deviation from the reference x^* using a cost function penalizing state deviation and control effort. The solution to this optimization provides the control inputs applied in practice. This iterative online approach updates control inputs based on new measurements, adapting to the latest state. Known also as receding horizon control, this method continuously adjusts the prediction horizon with new data, reflecting its dynamic and predictive capabilities. "Nonlinear" in NMPC indicates that the model $f(x,u)$ can handle complex, dynamic systems, distinguishing it from linear predictive control.

In this project, NMPC theory is utilized to develop a prognostic algorithm that focuses solely on future predictions. Unlike a traditional "online" controller algorithm, which continuously adjusts control actions in real-time, this approach is designed to evaluate and compare the outcomes of various control strategies. The main goal is to predict and analyze the potential results of different control methods rather than actively controlling the system in real-time.

2.6.2 Peak power conditions

The dynamic behavior of SOFCs under varying operating voltages is characterized by an initial increase in current from zero as the voltage decreases from the OCV. This variation leads to a power output that first escalates to a maximum value before diminishing. The voltage or current at which this maximum power output occurs is identified as the peak power point. This point is crucial, as it marks the optimal balance among various operational conditions, such as fuel flow rate, furnace temperature, and air supply, to achieve peak performance. Efficiency in this context is defined as the quotient of the electrical power output (P_{el}) and the lower heating value (LHV) input rate of the fuel (P_{fuel}), a parameter significantly influenced by the fuel's composition and flow rate. The relationship between electrical power and fuel efficiency is direct, with efficiency (η) being directly proportional to the ratio of P_{el} to P_{fuel}. Consequently, the cell's efficiency mirrors the power output behavior, peaking concurrently with it at the peak power point. This point, therefore, represents the most energy-efficient operational condition.

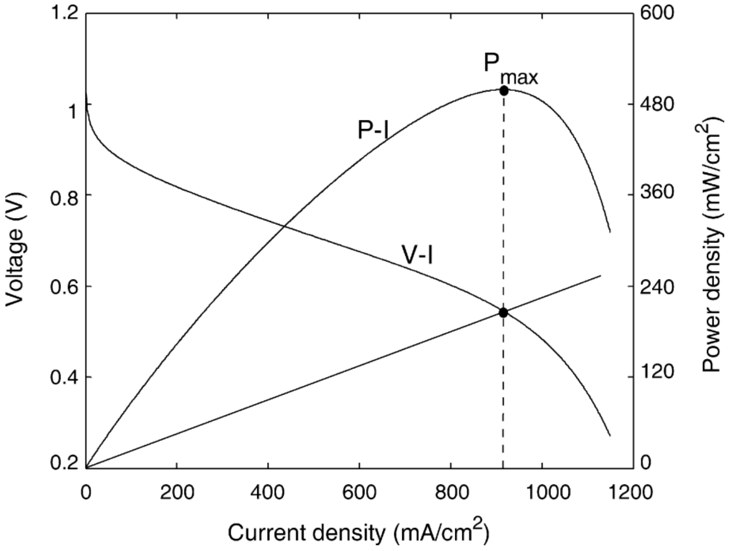

Figure 2.4: Typical fuel cell polarization and power curves [87]

Notably, the ideal long-term operating condition might deviate towards lower currents than those at the peak power point to mitigate degradation rates, which are intricately linked to the operating environment. Thus, the peak power point also functions as a critical benchmark for control strategies managing operating parameters. As discussed by Li et al. [51]:

- peak power of a generic SOFC at 800 °C is higher than at 720 °C regardless of fuel flow-rate or ohmic resistance value;
- voltage at peak power point is higher at higher temperatures and H_2 flowrates, and lower ohmic resistances;
- efficiency at peak power, is higher at higher temperatures but lower H_2 flowrates and lower ohmic resistances;
- fuel utilization at peak power displays similar trends as efficiency.

This demonstrates the highly complex interplay of each operating factor in managing SOFC performance: to optimize SOFC performances one should consider not only each factor's impact but also their interaction with each other. There might be not a single best control strategy but several different possibilities have to be taken into account.

2.6.3 Online control strategies

Control strategies in SOFC systems are crucial for optimizing performance, enhancing efficiency, and ensuring longevity minimizing the degradation mechanism's impact. These strategies must carefully balance power output, fuel utilization, and thermal management. This section outlines six different control strategies: fixed power, maximum power/efficiency, fixed voltage, reversible cycling, fixed current, and extended lifetime each serving different operational goals. Each of these strategies has its advantages and applications, and the choice among them depends on the specific requirements of the SOFC system, including its integration into broader energy systems, operational flexibility, and efficiency goals.

It's important to mention that control strategies here do not take into account any design-onset approach, but only "online" ones. When dealing with this kind of approach the optimization is not that simple and has to take into consideration each lower and upper constraint of the operating variables and possibly the fact that these constraints are not fixed and should be carefully tuned to each operating point.

Fixed power output operations

The fixed power strategy aims to maintain a constant power output from the SOFC system. This is a common scenario since in real applications the power demand is usually fixed. This approach is often used in applications where the energy demand is stable or predictable [79, 85]. The control system would simultaneously adjust H_2 flowrate and operating voltage to keep the actual power to the set value while maintaining suitable H_2 fuel flowrate so that the cell operates at a peak power point. This strategy prioritizes meeting energy demand but requires sophisticated control algorithms to manage the complex interplay of factors affecting SOFC performance. Other possible variations of this strategy are also possible since one can maintain a constant current voltage and let other operating factors vary or can maintain a constant temperature of the cell and let other operating factors vary depending on the operating environment and objectives.

Fixed input current operations

Under a fixed current strategy, the SOFC operates at a constant current. This method is beneficial for applications requiring a steady current supply, such as in certain types of electrochemical processes or in integration with other energy systems where current stability is paramount. The fixed current operation simplifies the control system but necessitates close monitoring of voltage and temperature to prevent conditions that could lead to accelerated degradation or thermal stress within the SOFC.

Fixed output voltage operations

The fixed voltage strategy involves maintaining a constant voltage across the SOFC. This approach is ideal for maximizing efficiency and is particularly relevant when the SOFC is used in conjunction with power electronics that require a stable voltage input. Operating at a fixed voltage can optimize fuel utilization and reduce the risk of damaging overpotentials. However, this strategy demands precise control over the fuel input and air supply to adapt to changes in power demand and to mitigate the effects of cell degradation over time. A common scenario when this strategy is adopted is to increase the current density and so the temperature of the cell during SOFC operation, to contrast degradation mechanisms. At the same time, it should be noted that this is a very simplified approach that does not take into account degradation mechanisms. Several analyses are conducted in the literature that proved that temperature is highly impacting the degradation ratio, more than the current density increase itself [88]. Temperature should be regulated across the cell and system to ensure uniform heat distribution and prevent thermal gradients that can lead to mechanical stresses and damage.

Minimized degradation rate operations

Optimizing the system to minimize degradation rate at stack or at system level is equivalent to maximize its life-expectancy: this operating approach is centered on enhancing the operational longevity of SOFC systems by adapting operational parameters in response to real-time performance and degradation data [89, 90, 91, 68]. With this approach it is possible to integrate continuous monitoring of critical performance metrics, such as cell voltage, temperature profiles, and electrochemical impedance, to identify signs of wear or degradation at their onset. Using predictive analytics and machine learning techniques, the system anticipates potential degradation scenarios and dynamically modifies operational parameters to counteract these effects. Adjustments may include the optimization of fuel and air flows, modification of the temperature set points, or alterations in the load distribution, all aimed at mitigating stressors that accelerate degradation, such as thermal cycling, electrode deterioration, or contaminant buildup. Combined with robust computational models, this strategy enables the SOFC system to proactively adapt to changing conditions and internal wear, thereby maximizing the cell's useful life while maintaining optimal efficiency and performance.

Maximum power operations

The maximum power operation approach is designed to ensure that the SOFC system or SOFC stack operates at its peak power output point under given conditions. This strategy dynamically adjusts the operating parameters, such as fuel flow rate and air supply, to align with the SOFC's peak power point. This operating mode is particularly advantageous in scenarios where the power demand is variable, and the system needs to adapt efficiently to these changes without compromising on performance or fuel efficiency. In maximum power operation, the control system uses real-time monitoring and predictive models to forecast the optimal operating conditions that will yield the highest power output. This involves a complex balance between maintaining high efficiency and avoiding conditions that may accelerate degradation or reduce the lifespan of the SOFC. The strategy is complex, as it must account for the nonlinear characteristics of SOFC performance and the varying external demands placed on the system.

Maximum efficiency operations

The maximum efficiency operation approach aims to maximize the efficiency of the SOFC system or SOFC stack. This involves optimizing the operating parameters to ensure the best possible fuel utilization and minimal energy losses. It is important to note that peak power conditions do not necessarily coincide with peak efficiency conditions at the system level; in fact, maximizing efficiency often requires operating at conditions that do not produce the highest power output. This can include lower fuel flow rates and different air supply configurations that are optimized for efficiency rather than power. This approach ensures that the SOFC system operates more sustainably, with reduced fuel consumption and lower emissions, but may not always meet the peak power demands.

Reversible cycling operations

The reversible cycling strategy is relevant to reversible SOFCs (rSOFCs), functioning as fuel cells to generate electricity from hydrogen and as electrolyzers to produce hydrogen from water using electricity. This dual role allows flexible energy management, enabling power generation during high demand and hydrogen storage when surplus electricity is available from renewables. This method mitigates temperature fluctuations and reduces degradation from impurities and nickel migration. Alternating between electrolysis and brief fuel cell modes maintains a stable thermal profile. Skafte et al. showed that rapid reverse pulses to the direct current can decouple hydrogen production rate from cell temperature [81]. Graves et al. demonstrated this method can eliminate degradation, likening it to battery recharging [80]. This strategy needs advanced management systems to switch modes based on real-time energy prices and demand forecasts. Transitions must be controlled to maintain efficiency, reduce SOFC wear, and respond to energy changes.

3 Model of CPOX-based SOFC system

In this chapter the main model of the CPOX-based SOFC system is given and discussed in detail. This chapter aims to bridge the fundamentals insights gained from the previous chapter, with the practical outcomes and analyses presented in Chapters 4,5, and 6.

This chapter is divided into several key sections, each focusing on a specific aspect of the study:

- A first general overview of the system with a degree of freedom analysis evidencing the operating parameters that are relevant to SUNFIRE system.
- The analytical techniques employed to model the system behavior, encompassing each subsystem.
- A detailed exposition of the degradation model employed together with the explanation of its parameter estimation process.
- A detailed techno-economic analysis of the SUNFIRE system aims to evaluate its profitability, providing the base equations for subsequent optimization analysis.

3.1 Introduction

As depicted in Figure 3.1, the SOFC system developed primarily consists of the following components:

1. A 57-active-cell SOFC stack with an electroactive area of 127.8 cm^2, which generates between 650 to 850 W of power under nominal conditions.
2. A catalytic partial oxidation reactor (CPOX).
3. An afterburner to combust the unreacted fuel.
4. A startup burner for temperature regulation inside the stack.
5. An air heat exchanger designed to heat up the sweep air for the stack.

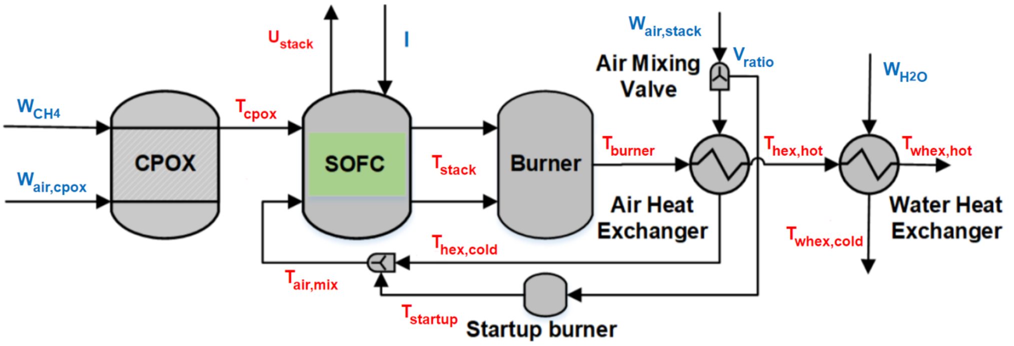

Figure 3.1: Simple flowsheet diagram of the Sunfire Home 750 SOFC system, developed by Sunfire Fuel Cells GmbH [92].

6. An air mixing valve to control the ratio of not superheated air.
7. A water heat exchanger for waste heat recovery.

In the figure blue variables represent the system inputs (manipulated variables) and red variables denote the output measurements (measured variables), $W_{\mathrm{CH_4}}$ is the methane blower workload (%), $W_{\mathrm{air,cpox}}$ is the CPOX air blower workload (%), $W_{\mathrm{air,stack}}$ is the stack air blower workload (%), V_{ratio} is the air mixing ratio indicating the ratio of air bypassing the air heat exchanger, and $W_{\mathrm{H_2}O}$ is the water pump workload (%). The V_{ratio} represents the portion of the input cathode blower air flow rate that is directed to the startup burner, while the remaining air flows through the air HEX.

Given the complexity of the Sunfire H750 module, where electrical and CHP (Combined Heat and Power) efficiencies serve as the target metrics, the system incorporates six adjustable inputs or manipulated variables. These include the flow rates of methane, air to the CPOX process, air to the stack cathode, water, the stack current, and the valve opening ratio. The control setpoints for these variables, managed by low-level Proportional-Integral (PI) controllers, act as the decision variables or degrees of freedom for optimization efforts. Rather than directly measuring water and gas flow rates, the model simplify the flow rate calculation with linear conversion from the work load of the blowers pumps:

$$\begin{aligned} \dot{q}_{\mathrm{CH_4}} &= W_{\mathrm{CH_4}} \times 4.5\,[\mathrm{NL/min}] \\ \dot{q}_{\mathrm{air,cpox}} &= W_{\mathrm{air,cpox}} \times 16\,[\mathrm{NL/min}] \\ \dot{q}_{\mathrm{air,stack}} &= W_{\mathrm{air,stack}} \times 342\,[\mathrm{NL/min}] \\ \dot{q}_{\mathrm{H_2O}} &= W_{\mathrm{H_2O}} \times 5\,[\mathrm{NL/min}] \end{aligned} \tag{3.1}$$

$\dot{q}_{\mathrm{CH_4}}$ is the methane flow rate in NL/min, $\dot{q}_{\mathrm{air,cpox}}$ is the airflow rate for the CPOX in NL/min, $\dot{q}_{\mathrm{air,stack}}$ is the air flow rate for the stack in NL/min, and $\dot{q}_{\mathrm{H_2}O}$ is the liquid water flow rate for waste heat recovery in NL/min. The system's outputs are the CPOX outlet temperature, superheated air temperature (at the air heat exchanger outlet), stack voltage (which includes power consumption by the blowers and pumps), stack outlet temperature, burner outlet temperature, and water outlet temperature. Calculations of air and fuel utilization rates, electric power output, and

Table 3.1: Set of manipulated and measured variables for the CPOX-SOFC system in Fig. 3.1

Measured variables	Manipulated variables
CPOX temperature (T_{cpox})	Natural gas blower workload (W_{CH_4})
SOFC stack voltage (U_{stack})	CPOX air blower workload ($W_{air,cpox}$)
SOFC stack temperature (T_{stack})	Electrical current (I)
Burner outlet temperature (T_{burner})	Cathode air blower workload ($W_{air,stack}$)
HEX temperatures ($T_{hex,hot}$,$T_{hex,cold}$)	Air-mixing valve ratio (V_{ratio})
WHEX temperatures ($T_{whex,hot}$, $T_{whex,cold}$)	Water pump workload ($W_{\mathrm{H_2O}}$)
Startup burner temperature ($T_{startup}$)	Time (t)
Mixed air temperature ($T_{air,mix}$)	
Carbon-to-oxygen ratio (CO)	
Air utilization (AU)	
Fuel utilization (FU)	

efficiencies (both electrical and CHP) derive from these input and output measures. Detailed system modeling is elaborated upon subsequently.

3.2 DoF analysis

This section is written based on the investigation conducted by Colombo et al. [93], tailored to the specifics of the SUNFIRE system. Degradation and failure mechanisms are significantly influenced by constraints imposed at the system, component, or part levels due to design choices or operational policies. These constraints are considered to be rigid, which are inflexible and can not be exceeded. The system's high degree of freedom results in a limited set of manipulated variables available for adjusting setpoints to regulate the operational output parameters. Table 3.1 presents the array of manipulated and measured variables identified for the SOFC system. Notably, the manipulated variables correspond to the system's independent variables, or DoF. This means that 7 distinct values uniquely define the system's operating conditions. However, the high number of degrees of freedom is limited by the complex interactions among these variables and their respective constraints.

The constraints are given by the operational and material limitations specific to each component of the SOFC system, resumed in Table 3.2. The breach of these constraints can precipitate irreversible damage, including operating under conditions that exceed these bounds for extended periods or even briefly, potentially compromising system safety and performance.

3.3 System modelling

To develop a control strategy and optimize it to find the best operating point, the CPOX-based SOFC system is modeled with a simplified 0-D approach. A pre-made model is used, built by Yu H. for the RUBY project [92] and it is described in the following paragraphs. This approach involves the modelization of each one of the single units: CPOX reactor, SOFC stack, burner, air heat exchanger, and water heat exchanger which are characterized at least by both mass and energy balances. This phase is fully managed using a code developed with MATLAB software [94].

Table 3.2: Operational constraints for process units of the CPOX-SOFC system in Fig. 3.1 (* are system manipulated variables).

Process Unit	**Constraint**	**Min. Value**	**Max. Value**	**Potential Effect**
CPOX	Temperature	650 °C	850 °C	Safety of operation
	Air CPOX blower workload*	-	80%	Avoiding non-linear relationship between workload and air flow rate
SOFC	Temperature	650 °C	865 °C	Performance loss, failure due to thermo-mechanical stresses and chemical interaction
	Voltage	40 V	60 V	Nominal operation limit
	FU	-	80%	Fuel starvation, efficiency loss
	AU	-	25%	Performance loss due to air diffusion in the cathode deterioration
	CO	-	95%	Performance loss due to carbon deposition
	Current*	-	24 A	Higher concentration polarization, faster cell degradation
	Air temperature	650 °C	850 °C	Safety of operation
	Air stack blower workload*	-	80%	Avoiding air cooling down stack temperature
Burner	Outlet temperature	700 °C	1050 °C	Safety of operation
St-Burner	Temperature	25 °C	700 °C	Safety of operation
Air HEX	Outlet temperature (hot)	100 °C	700 °C	Safety of operation
	Outlet temperature (cold)	650 °C	860 °C	Safety of operation
	Valve opening ratio*	-	45 %	Safety of operation
Water HEX	Outlet air temperature	25 °C	320 °C	Safety of operation
	Outlet water temperature	25 °C	60 °C	Safety of operation

3.3.1 CPOX reactor

Both mass balance and energy balance within the CPOX reactor are considered, in line with established literature [95]. Distinct from the conventional methane steam reforming reactions, the partial oxidation of methane within CPOX involves four principal reactions: methane combustion, steam reforming of methane-producing carbon monoxide and hydrogen, and dry reforming of methane-yielding hydrogen and carbon monoxide. The reactions can be resumed as follows:
Methane combustion

$$CH_4 + 2O_2 \Rightarrow CO_2 + 2H_2O \quad (\Delta H_{(298K)} = -802\ kJ/mol) \tag{3.2}$$

Methane steam reforming

$$CH_4 + H_2O \rightleftharpoons CO + 3H_2 \quad (\Delta H_{(298K)} = 206\ kJ/mol) \tag{3.3}$$

Methane dry reforming

$$CH_4 + CO_2 \rightleftharpoons 2CO + 2H_2 \quad (\Delta H_{(298K)} = 247\ kJ/mol) \tag{3.4}$$

CPOX is assumed to behave as an ideal continuous stirred-tank reactor (CSTR), characterized by uniform composition and temperature, indicative of a single thermal body with consistent internal and outlet conditions.

The mass balance accounts for all component flow rates entering CPOX, specifically methane, oxygen, and nitrogen. Based on empirical data from Sunfire, the outlet gas composition is predominantly hydrogen and carbon monoxide, with no residual oxygen. Assumptions made to simplify the mass balance include steady-state conditions at the transition between operating states and complete reaction conversions. If excess oxygen is present after the primary reactions, it is consumed by further combustion to produce steam, represented as:

$$H_2 + 0.5O_2 \rightarrow H_2O. \tag{3.5}$$

The mass balance, therefore, considers two scenarios: surplus O_2 and insufficient O_2, with the inlet flows delineated as follows:

$$n_{in,cpox}^{CH_4} = \frac{q_{CH_4}}{22.4 \cdot 60}\ \text{(mol/s)} \tag{3.6}$$

$$n_{in,cpox}^{O_2} = \frac{q_{air,cpox} \cdot 21\%}{22.4 \cdot 60}\ \text{(mol/s)} \tag{3.7}$$

$$n_{in,cpox}^{N_2} = \cdot \frac{q_{air,cpox} \cdot 79\%}{22.4 \cdot 60}\ \text{(mol/s)} \tag{3.8}$$

When the amount of O_2 is not enough to convert CH_4 into CO and H_2, there will be CH_4 left and the mass balance can be expressed as below:

$$\begin{pmatrix} n_{out,cpox}^{H_2O} \\ n_{out,cpox}^{CH_4} \\ n_{out,cpox}^{CO} \\ n_{out,cpox}^{H_2} \\ n_{out,cpox}^{CO_2} \\ n_{out,cpox}^{O_2} \\ n_{out,cpox}^{N_2} \end{pmatrix} = \begin{pmatrix} 0 & 0 & 0 \\ 1 & -2 & 0 \\ 0 & 2 & 0 \\ 0 & 4 & 0 \\ 0 & 0 & 0 \\ 0 & 0 & 0 \\ 0 & 0 & 1 \end{pmatrix} \begin{pmatrix} n_{in,cpox}^{CH_4} \\ n_{in,cpox}^{O_2} \\ n_{in,cpox}^{N_2} \end{pmatrix} \tag{3.9}$$

When the amount of O_2 is enough to convert CH_4 into CO and H_2, the mass balance can be expressed as below:

$$\begin{pmatrix} n_{out,cpox}^{H_2O} \\ n_{out,cpox}^{CH_4} \\ n_{out,cpox}^{CO} \\ n_{out,cpox}^{H_2} \\ n_{out,cpox}^{CO_2} \\ n_{out,cpox}^{O_2} \\ n_{out,cpox}^{N_2} \end{pmatrix} = \begin{pmatrix} -1 & 2 & 0 \\ 0 & 0 & 0 \\ 2 & 0 & 0 \\ 3 & -2 & 0 \\ 0 & 0 & 0 \\ 0 & 0 & 0 \\ 0 & 0 & 1 \end{pmatrix} \begin{pmatrix} n_{in,cpox}^{CH_4} \\ n_{in,cpox}^{O_2} \\ n_{in,cpox}^{N_2} \end{pmatrix} \tag{3.10}$$

It's important to note that, in the context of this project, CO is capped at an upper limit of 0.95, which ensures an excess of oxygen (since the condition CO < 1 is always met). Consequently, the initial mass balance presented is primarily intended to enhance the model's robustness. Regarding the energy balance equations, thanks to the hypothesis of CSTR, the CPOX's interior temperature is considered to be equal to the outlet temperature. The design and placement of CPOX within the system enclosure necessitate the consideration of heat losses through convection to both the stack and the surrounding environment. These convective losses are evaluated based on empirical data from Sunfire and UNISA, where the ambient conditions are inferred from the temperature readings of the system's internal printed circuit board (PCB). Thermodynamic data calculation function, `Gas_Energy`, is designed for gas-phase species with the capability to determine the change in enthalpy, standard formation enthalpy, standard entropy, and Gibbs energy for a specified gas at a given temperature. Polynomial coefficients for the heat capacity as a function of temperature are utilized, in the format $Cpo = A + Bt + Ct^2 + Dt^3 + E/t^2$. These coefficients are sourced from the NIST Chemistry WebBook [96]. The resulting enthalpy is expressed as $\Delta H_{298.15K} = At + Bt^2/2 + Ct^3/3 + Dt^4/4 - E/t + F - H$, and the standard entropy is calculated via $S = A\ln(t) + Bt + Dt^3/3 - E/(2t^2) + G$, where t is the temperature in kelvin divided by 1000. The function accounts for different temperature intervals and utilizes a persistent storage mechanism for the coefficients to enhance computational efficiency.

The energy balance equation encapsulates the net energy flux within the CPOX, accounting for both the enthalpic contributions of the inlet and outlet streams and the thermal losses through convection to the stack and ambient. This energy balance is articulated as follows:

$$
\begin{aligned}
m_{\text{cpox}} C_{p,\text{cpox}} \frac{dT_{\text{cpox}}}{dt} =& \sum_i n^i_{\text{in,cpox}} H^i_{\text{in,cpox}}(T_{\text{in}}) \\
& - \sum_j n^j_{\text{out,cpox}} H^j_{\text{out,cpox}}(T_{\text{cpox}}) \\
& + Q_{\text{loss,cpox}} \\
Q_{\text{loss,cpox}} =& F^{\text{cpox}}_{\text{conv,stack}} \times (T_{\text{cpox}} - T_{\text{stack}}) \\
& + F^{\text{cpox}}_{\text{conv,pcb}} \times (T_{\text{cpox}} - T_{\text{pcb}}) \ (\text{W})
\end{aligned} \tag{3.11}
$$

where $Q_{loss,cpox}$ is the sum of heat losses due to convection, calculated as the product of the estimated convection coefficients with the temperature differentials between the CPOX, the stack, and the PCB, indicative of the ambient temperature. Here, m_{cpox} denotes the mass of the CPOX, $C_{p,cpox}$ its heat capacity, T_{cpox} the temperature, $H_{in,cpox,i}(T_{in})$ the enthalpy of each inlet gas species i, $H_{out,cpox,j}(T_{cpox})$ the enthalpy of each outlet gas species j, with $n_{in,cpox,i}$ and $n_{out,cpox,j}$ representing the molar flow rates of the inlet and outlet gases, respectively.

3.3.2 SOFC

The modeling of SOFC encompasses three main aspects: the electrical output of the stack, the conservation of mass, and the thermal energy management. Mirroring the approach taken with the CPOX reactor, the SOFC stack is conceptualized as a CSTR.

The primary electrochemical reactions within the stack, which are integral to its functionality, are represented as follows:

$$
\begin{aligned}
H_2 + \frac{1}{2} O_2 &\rightarrow H_2O \\
CO + H_2O &\rightarrow CO_2 + H_2, \\
CH_4 + 2H_2O &\rightarrow CO_2 + 4H_2
\end{aligned} \tag{3.12}
$$

In terms of mass balance, the model accounts for the flow rates of all constituents entering and exiting the stack. The anode inlet stream is the direct continuation of the CPOX outlet, while the cathode inlet and the consumed hydrogen are characterized by the following expressions:

$$
\begin{aligned}
n^{\text{H}_2}_{\text{react}} &= \frac{N_{\text{cell}}}{2F} I \ (\text{mol/s}) \\
n^{\text{O}_2}_{\text{in,cath,hex}} &= \frac{q_{\text{air,stack}} \times 21\% \times (1 - V_{\text{air}})}{22.4 \times 60} \ (\text{mol/s}) \ (\text{mol/s}) \\
n^{\text{N}_2}_{\text{in,cath,hex}} &= \frac{q_{\text{air,stack}} \times 79\% \times (1 - V_{\text{air}})}{22.4 \times 60} \ (\text{mol/s}) \\
n^{\text{O}_2}_{\text{in,cath,valve}} &= \frac{q_{\text{air,stack}} \times 79\% \times V_{\text{air}}}{22.4 \times 60} \ (\text{mol/s}) \\
n^{\text{N}_2}_{\text{in,cath,valve}} &= \frac{q_{\text{air,stack}} \times 79\% \times V_{\text{air}}}{22.4 \times 60} \ (\text{mol/s})
\end{aligned} \tag{3.13}
$$

where $n_{\text{react}}^{\text{H}_2}$ is the amount of hydrogen that has undergone reaction, N_{cell} represents the total number of cells within the stack, and F stands for the Faraday constant. The term $n_{\text{in,cath,hex}}^{\text{O}_2}$ specifies the molar flow rate of oxygen as it enters the cathode from the air heat exchanger, while $n_{\text{in,cath,hex}}^{\text{N}_2}$ pertains to the analogous molar flow rate for nitrogen. Furthermore, $n_{\text{in,cath,valve}}^{\text{O}_2}$ and $n_{\text{in,cath,valve}}^{\text{N}_2}$ correspond to the molar flow rates for oxygen and nitrogen, respectively, that bypasses the usual path and are directed through the startup burner. Given the intricate composition of the exhaust gas from CPOX and the swift nature of the electrochemical reaction, several simplifications are introduced as follows:

- The system achieves a steady-state mass balance during the shift between varying operational states due to the rapid kinetics of the electrochemical processes, which adjust within a second upon any change in operational conditions. This implies an almost immediate alteration in the chemical quantities, with the system's behavior primarily influenced by the thermal balance and the related temperature shifts.
- CH_4 and CO are transformed into H_2 and CO_2 through steam reforming (SR) and water-gas shift (WGS) reactions before reaching the stack. Based on the electric current and the steam input rate, three scenarios are delineated, with cases 2 and 3 being a way to increase the robustness of the model preventing simulation crashes in extreme conditions of operation:

    1. When the total steam generated by the electrochemical reactions combined with the steam entering the anode exceeds the steam demand for both SR and WGS reactions, i.e., $n_{\text{react}}^{H_2} + n_{\text{in,an}}^{H_2O} > n_{\text{in,an}}^{CO} + 2n_{\text{in,an}}^{CH_4}$. This indicates the complete conversion of CO and CH_4 into H_2 and CO_2, allowing for the mass balance to be articulated as follows:

$$\begin{pmatrix} 1 & 1 & -2 & -1 & 0 & 0 & 0 & 0 & 0 & 0 \\ 0 & 0 & 0 & 0 & 0 & 0 & 0 & 0 & 0 & 0 \\ 0 & 0 & 0 & 0 & 0 & 0 & 0 & 0 & 0 & 0 \\ -1 & 0 & 4 & 1 & 1 & 0 & 0 & 0 & 0 & 0 \\ 0 & 0 & 1 & 1 & 0 & 1 & 0 & 0 & 0 & 0 \\ 0 & 0 & 0 & 0 & 0 & 0 & 1 & 0 & 0 & 0 \\ 0 & 0 & 0 & 0 & 0 & 0 & 0 & 1 & 0 & 0 \\ -0.5 & 0 & 0 & 0 & 0 & 0 & 0 & 0 & 1 & 0 \\ 0 & 0 & 0 & 0 & 0 & 0 & 0 & 0 & 0 & 1 \end{pmatrix} \begin{pmatrix} n_{\text{react}}^{H_2} \\ n_{\text{in,an}}^{H_2O} \\ n_{\text{in,an}}^{CH_4} \\ n_{\text{in,an}}^{CO} \\ n_{\text{in,an}}^{H_2} \\ n_{\text{in,an}}^{CO_2} \\ n_{\text{in,an}}^{O_2} \\ n_{\text{in,an}}^{N_2} \\ n_{\text{in,cath}}^{O_2} \\ n_{\text{in,cath}}^{N_2} \end{pmatrix} = \begin{pmatrix} n_{\text{out,an}}^{H_2O} \\ n_{\text{out,an}}^{CH_4} \\ n_{\text{out,an}}^{CO} \\ n_{\text{out,an}}^{H_2} \\ n_{\text{out,an}}^{CO_2} \\ n_{\text{out,an}}^{O_2} \\ n_{\text{out,an}}^{N_2} \\ n_{\text{out,cath}}^{O_2} \\ n_{\text{out,cath}}^{N_2} \end{pmatrix} \tag{3.14}$$

    2. The second scenario outlines when the combined steam generation from electrochemical reactions and the anode inlet steam rate surpasses the demand for the WGS reaction yet falls short for both the WGS and SR reactions,i.e., $n_{\text{react}}^{H_2} + n_{\text{in,an}}^{H_2O} > n_{\text{in,an}}^{CO}$ and $n_{\text{react}}^{H_2} + n_{\text{in,an}}^{H_2O} - n_{\text{in,an}}^{CO} < 2n_{\text{in,an}}^{CH_4}$. The outlet steam flow, crucial for the Nernst

equation, is maintained at 10^{-6} mol/s.

$$\begin{pmatrix} 10^{-6} \\ 0 \\ 0 \\ 0 \\ 0 \\ 0 \\ 0 \\ 0 \\ 0 \\ 0 \end{pmatrix} + \begin{pmatrix} 0 & 0 & 0 & 0 & 0 & 0 & 0 & 0 & 0 & 0 \\ -0.5 & -0.5 & 1 & -0.5 & 0 & 0 & 0 & 0 & 0 & 0 \\ 0 & 0 & 0 & 0 & 0 & 0 & 0 & 0 & 0 & 0 \\ 1 & 2 & 0 & -1 & 1 & 0 & 0 & 0 & 0 & 0 \\ 0.5 & 0.5 & 0 & 0.5 & 0 & 1 & 0 & 0 & 0 & 0 \\ 0 & 0 & 0 & 0 & 0 & 0 & 1 & 0 & 0 & 0 \\ 0 & 0 & 0 & 0 & 0 & 0 & 0 & 1 & 0 & 0 \\ -0.5 & 0 & 0 & 0 & 0 & 0 & 0 & 0 & 1 & 0 \\ 0 & 0 & 0 & 0 & 0 & 0 & 0 & 0 & 0 & 1 \end{pmatrix} \begin{pmatrix} n_{\text{react}}^{H_2} \\ n_{\text{in,an}}^{H_2O} \\ n_{\text{in,an}}^{CH_4} \\ n_{\text{in,an}}^{CO} \\ n_{\text{in,an}}^{H_2} \\ n_{\text{in,an}}^{CO_2} \\ n_{\text{in,an}}^{O_2} \\ n_{\text{in,an}}^{N_2} \\ n_{\text{in,cath}}^{O_2} \\ n_{\text{in,cath}}^{N_2} \end{pmatrix} = \begin{pmatrix} n_{\text{out,an}}^{H_2O} \\ n_{\text{out,an}}^{CH_4} \\ n_{\text{out,an}}^{CO} \\ n_{\text{out,an}}^{H_2} \\ n_{\text{out,an}}^{CO_2} \\ n_{\text{out,an}}^{O_2} \\ n_{\text{out,an}}^{N_2} \\ n_{\text{out,cath}}^{O_2} \\ n_{\text{out,cath}}^{N_2} \end{pmatrix} \tag{3.15}$$

3. In the third scenario, the combined steam generation is inadequate for the WGS reaction, indicating incomplete conversion of CO. The outlet steam rate is again set at 10^{-6} mol/s for application in the Nernst equation and the overall system of equation is described as follows:

$$\begin{pmatrix} 10^{-6} \\ 0 \\ 0 \\ 0 \\ 0 \\ 0 \\ 0 \\ 0 \\ 0 \\ 0 \end{pmatrix} + \begin{pmatrix} 0 & 0 & 0 & 0 & 0 & 0 & 0 & 0 & 0 & 0 \\ 0 & 0 & 1 & 0 & 0 & 0 & 0 & 0 & 0 & 0 \\ -1 & -1 & 0 & 1 & 0 & 0 & 0 & 0 & 0 & 0 \\ 0 & 0 & 0 & 0 & 1 & 0 & 0 & 0 & 0 & 0 \\ 1 & 1 & 0 & 0 & 0 & 1 & 0 & 0 & 0 & 0 \\ 0 & 0 & 0 & 0 & 0 & 0 & 1 & 0 & 0 & 0 \\ 0 & 0 & 0 & 0 & 0 & 0 & 0 & 1 & 0 & 0 \\ -0.5 & 0 & 0 & 0 & 0 & 0 & 0 & 0 & 1 & 0 \\ 0 & 0 & 0 & 0 & 0 & 0 & 0 & 0 & 0 & 1 \end{pmatrix} \begin{pmatrix} n_{\text{react}}^{H_2} \\ n_{\text{in,an}}^{H_2O} \\ n_{\text{in,an}}^{CH_4} \\ n_{\text{in,an}}^{CO} \\ n_{\text{in,an}}^{H_2} \\ n_{\text{in,an}}^{CO_2} \\ n_{\text{in,an}}^{O_2} \\ n_{\text{in,an}}^{N_2} \\ n_{\text{in,cath}}^{O_2} \\ n_{\text{in,cath}}^{N_2} \end{pmatrix} = \begin{pmatrix} n_{\text{out,an}}^{H_2O} \\ n_{\text{out,an}}^{CH_4} \\ n_{\text{out,an}}^{CO} \\ n_{\text{out,an}}^{H_2} \\ n_{\text{out,an}}^{CO_2} \\ n_{\text{out,an}}^{O_2} \\ n_{\text{out,an}}^{N_2} \\ n_{\text{out,cath}}^{O_2} \\ n_{\text{out,cath}}^{N_2} \end{pmatrix} \tag{3.16}$$

It is important to note that due to the constraints on CO, FU, and current, the mass balance consistently aligns with the first case. The second and third cases are included to enhance the model's robustness during the optimization process. Regarding the energy balance and taking into account the assumption of CSTR, the temperature at the stack's outlet is assumed to be homogenized with the internal reactor temperature. Considering the stack's placement within the system enclosure, three primary heat loss mechanisms are accounted for (1) convection heat transfer from the CPOX process, (2) convection heat transfer due to the environmental conditions, and (3) radiative heat loss from the afterburner. Thus, the energy balance is established by summing the energy inputs and outputs associated with the fluid streams, in addition to the thermal losses attributable to convection and radiation. The energy balance is formulated as follows:

$$
\begin{aligned}
m_{\text{stack}} C_{p,\text{stack}} \frac{dT_{\text{stack}}}{dt} =& \sum_i n^i_{\text{in,an}} H^i_{\text{in,an}}(T_{\text{cpox}}) \\
&+ n^{O_2}_{\text{in,cath,hex}} H^{O_2}_{\text{in,cath,hex}}(T_{\text{air}}) \\
&+ n^{N_2}_{\text{in,cath,hex}} H^{N_2}_{\text{in,cath,hex}}(T_{\text{air}}) \\
&+ n^{O_2}_{\text{in,cath,valve}} H^{O_2}_{\text{in,cath,valve}}(T_{\text{stburn}}) \\
&+ n^{N_2}_{\text{in,cath,valve}} H^{N_2}_{\text{in,cath,valve}}(T_{\text{stburn}}) \\
&- \sum_j n^j_{\text{out,stack}} H^j_{\text{out,stack}}(T_{\text{stack}}) \\
&- P_{\text{stack}} \\
&- Q_{\text{loss,stack}} \qquad (3.17) \\
Q_{\text{loss,stack}} =& F_{\text{stack,conv,cpox}}(T_{\text{stack}} - T_{\text{cpox}}) \\
&+ F_{\text{stack,conv,pcb}}(T_{\text{stack}} - T_{\text{pcb}}) \\
&+ F_{\text{stack,rad,burn}}(T^4_{\text{stack}} - T^4_{\text{burn}}) \ \text{(W)}
\end{aligned}
$$

where m_{stack} represents the mass of the stack, while $C_{p,\text{stack}}$ denotes its specific heat capacity. The term $Q_{\text{loss,stack}}$ encompasses the thermal losses experienced by the stack, which include convective heat losses from both the Catalytic Partial Oxidation (CPOX) process and the surrounding environment, as well as radiative heat losses from the afterburner system. The specific enthalpy of the inflowing gases from the CPOX, denoted by $H^i_{\text{in,an}}(T_{\text{cpox}})$, contributes to the internal energy of the system. Additionally, $H^{O_2}_{\text{in,cath,hex}}(T_{\text{air}})$ and $H^{N_2}_{\text{in,cath,hex}}(T_{\text{air}})$ represent the enthalpies of oxygen and nitrogen, respectively, coming from the air heat exchanger. The enthalpies of oxygen and nitrogen from the air bypass valve are indicated by $H^{O_2}_{\text{in,cath,valve}}(T_{\text{stburn}})$ and $H^{N_2}_{\text{in,cath,valve}}(T_{\text{stburn}})$, where T_{stburn} is the operational temperature of the startup burner. The term $H^j_{\text{out,stack}}(T_{\text{stack}})$ reflects the enthalpy of the stack's outlet gases. Molar flow rates are denoted by $n^i_{\text{in,an}}$ for the inflow and $n^j_{\text{out,stack}}$ for the outflow, with i and j indexing the respective species of gases at the stack's inlet and outlet. The coefficients $F^{\text{stack}}_{\text{conv,cpox}}$, $F^{\text{stack}}_{\text{conv,pcb}}$, and $F^{\text{stack}}_{\text{rad,burn}}$ quantify the convective and radiative heat transfer interactions between the stack and the CPOX, the ambient environment, and the afterburner, respectively.

In evaluating the stacking potential, it is necessary to consider both the Nernst equation, which accounts for gas concentration and stack temperature, and the current flowing through the system. The losses in the system are attributed to two primary factors: (1) overpotentials, which encompass activation overpotentials, oxygen dissociation, electrolyte ohmic losses, gas diffusion, and ohmic losses from metal interconnectors (MIC), and (2) power losses stemming from internal electronic devices, air blowers for the CPOX and SOFC, natural gas blower, water pump, and conversion inefficiencies of the inverter. Rather than individually assessing each component of overpotential losses, a comprehensive ASR model developed by Sunfire is employed. This model encapsulates the losses into a single expression, simplifying the computation of the stacking potential. The formula for determining the stack potential is as follows:

$$\begin{aligned}
ASR &= A_0 \exp\left(-\frac{E_a}{RT_{\text{stack}}}\right) \;(\Omega \cdot cm^2)\\
U_{\text{stack}} &= \left(U_{\text{nernst}} - \frac{I}{A_{\text{active}}} \times ASR\right) \times N_{\text{cell}} \;(\text{V})\\
U_{\text{system}} &= U_{\text{stack}} - U_{\text{loss,dev}} \;(\text{V})\\
U_{\text{loss,dev}} &= \frac{P_{\text{inv}} + \sum_{\text{dev}} \left(P_{\text{dev}}^{\text{max}} \times W_{\text{dev}}\right)}{I} \;(\text{V})
\end{aligned} \tag{3.18}$$

where ASR is the area-specific resistance, U_{nernst} is the Nerst voltage, from which the stack voltage, U_{stack}, is computed. To speed up the computation, outlet gas compositions are utilized, which may introduce some level of approximation into the model voltage output. Therefore, a chosen constant correction factor, k_{nernst}, is introduced to adjust for potential deviations in the gas concentration terms. The electroactive area of the cell, A_{active}, is specified as 127.8 cm^2, and the parameters $A_0 = 2.6 \times 10^{-4}\ \Omega \cdot cm^2$ and $E_A = 72900$ J/mol are derived from the fitted ASR model. The ideal gas constant is denoted by $R = 8.314$ J·K^{-1}·mol^{-1}. The power loss due to inverters is represented by P_{inv}, while $P_{\text{dev}}^{\text{max}}$ indicates the maximum power consumption of various blowers and pumps, and W_{dev} denotes the workload of the electronic devices. The expression for the Nernst voltage is as follows:

$$U_{\text{nernst}} = U_s - dU_1 \times 75 - dU_2 \times (T_{\text{stack}} - 100) + \frac{RT_{\text{stack}}}{2F} \times \ln\left(\frac{x_{\text{out,an}}^{H_2}}{x_{\text{out,an}}^{H_2O}} \times \left(\frac{x_{\text{out,cath}}^{O_2}}{k_{\text{nernst}}}\right)^{0.5}\right) \tag{3.19}$$

where standard redox potential is denoted by U_s, while $dU_1 = 846\ \mu$V/K and $dU_2 = 230\ \mu$V/K represent the voltage drops due to temperature increases from room temperature (25 °C) to 100 °C, and from the stack temperature to the evaporation temperature at 1 bar, respectively. The molar fractions of H_2, O_2, and H_2O in the outlet gases of the anode and cathode are represented by $x_{\text{out,an}}^{H_2}$, $x_{\text{out,cath}}^{O_2}$, and $x_{\text{out,an}}^{H_2O}$, respectively.

In the analysis of fuel cell performance, two critical indices are the FU and the AU. The AU indicates the fraction of the oxygen that reacts compared to the total oxygen supplied. These ratios are essential for determining the efficiency of the fuel cell system. The expressions are as follows:

$$FU = \frac{n_{\text{reac}}^{CH_4}}{n_{\text{in,cpox}}^{CH_4}} = \frac{n_{\text{reac}}^{H_2}}{n_{\text{in,an}}^{H_2}} == \frac{N_{\text{cell}} \cdot I}{8F \cdot n_{\text{in,cpox}}^{CH_4}} \tag{3.20}$$

$$AU = \frac{N_{\text{cell}} \cdot 2I}{8F \cdot n_{\text{in,cath}}^{O_2}} \tag{3.21}$$

3.3.3 Burner

In the proposed thermal management system, unreacted fuel from the fuel cell stack is subjected to post-combustion using the excess air supplied to the cathode. The exothermic nature of the combustion process generates significant heat, which is subsequently harnessed to preheat the incoming air to the stack cathode beyond 750°C and to elevate the temperature of the water from ambient to approximately 60°C. These thermal integrations contribute to an enhanced CHP efficiency for the system. The primary reactions occurring within the combustion chamber can be described as follows:

$$
\begin{aligned}
&\mathrm{H_2} + \frac{1}{2}\mathrm{O_2} \rightarrow \mathrm{H_2O}\\
&\mathrm{CO} + \frac{1}{2}\mathrm{O_2} \rightarrow \mathrm{CO_2}\\
&\mathrm{CH_4} + 2\,\mathrm{O_2} \rightarrow \mathrm{CO_2} + 2\,\mathrm{H_2O}
\end{aligned}
\tag{3.22}
$$

The three reactions above are complete, in which case, the mass balance can be expressed as below:

$$
\begin{pmatrix}
2 & 0 & 0 & 0 & 0\\
0 & 0 & 0 & 0 & 0\\
0 & 0 & 0 & 0 & 0\\
0 & 0 & 0 & 0 & 0\\
1 & 0 & 0 & 0 & 0\\
-2 & 1 & 0 & 1 & 0\\
0 & 0 & 1 & 0 & 1
\end{pmatrix}
\begin{pmatrix}
n^{CH_4}_{\text{in,cpox}}\\
n^{O_2}_{\text{in,cpox}}\\
n^{N_2}_{\text{in,cpox}}\\
n^{O_2}_{\text{in,cath}}\\
n^{N_2}_{\text{in,cath}}
\end{pmatrix}
=
\begin{pmatrix}
n^{H_2O}_{\text{out,burn}}\\
n^{CH_4}_{\text{out,burn}}\\
n^{CO}_{\text{out,burn}}\\
n^{H_2}_{\text{out,burn}}\\
n^{CO_2}_{\text{out,burn}}\\
n^{O_2}_{\text{out,burn}}\\
n^{N_2}_{\text{out,burn}}
\end{pmatrix}
\tag{3.23}
$$

To model the thermal dynamics of the afterburner within the system, the CSTR assumption is adopted under constant pressure with ideal gas behavior, so the temperature at the outlet of the afterburner (T_{burn}) is representative of the internal temperature of the chamber. The energy balance equation, which accounts for the heat contributions and losses in the afterburner, is essential for understanding its impact on the overall system's CHP efficiency. The equation is given by:

$$
\begin{aligned}
m_{\text{burn}} C_{p,\text{burn}} \frac{dT_{\text{burn}}}{dt} =& \sum_i n^i_{\text{in,burn}} H^i_{\text{in,burn}}(T_{\text{stack}})\\
&- \sum_j n^j_{\text{out,burn}} H^j_{\text{out,burn}}(T_{\text{burn}})\\
&- Q_{\text{loss,burn}}\\
Q_{\text{loss,burn}} =& F_{\text{rad,stack–burn}}(T^4_{\text{burn}} - T^4_{\text{stack}})\\
&+ F_{\text{conv,stburn–burn}}(T_{\text{burn}} - T_{\text{stburn}})\\
&+ F_{\text{conv,hex–burn}}(T_{\text{burn}} - T_{\text{hex}}) \text{ (W)}
\end{aligned}
\tag{3.24}
$$

In these equations, m_{burn} represents the mass of the burner, and $C_{p,\text{burn}}$ is the specific heat capacity of the burner. The term $Q_{\text{loss,burn}}$ indicates the heat losses from the afterburner, including both radiative and convective contributions, denoted by $F_{\text{rad,stack–burn}}$ and $F_{\text{conv,stburn–burn}}$ and $F_{\text{conv,hex–burn}}$ respectively. $H^i_{\text{in,burn}}(T_{\text{stack}})$ signifies the enthalpy of the inflowing gases to the burner at the stack temperature, while $H^j_{\text{out,burn}}(T_{\text{burn}})$ denotes the enthalpy of the outflowing gases at the afterburner temperature. The variables $n^i_{\text{in,burn}}$ and $n^j_{\text{out,burn}}$ are the molar flow rates of gases entering and exiting the burner, with i and j indexing the specific gas species involved in the combustion process.

3.3.4 Start-up burner

The start-up burner incorporates the same reaction equations and mass balance considerations as the general burner, outlined previously. However, it introduces modifications to the energy balance equation to account for the specific thermal dynamics and heat losses associated with the start-up process. The primary reactions within the start-up burner's combustion chamber are identical to the burner ones, facilitating the same complete combustion process.

Similarly, the mass balance for the start-up burner can be represented by the same stoichiometry matrix as in Equation 3.23, given the consistent input and output streams within both burner systems. Therefore, the focus shifts primarily to the adaptations in the energy balance to accommodate the unique operational parameters of the start-up phase.

The energy balance equation for the start-up burner mirrors that of the general burner, with specific attention to the loss terms that characterize the initial operational conditions. It is expressed as follows, analogous to Equation 3.24, but with adjusted loss terms:

$$\begin{aligned} m_{\text{stburn}} C_{p,\text{stburn}} \frac{dT_{\text{stburn}}}{dt} = & \sum_i n^i_{\text{in,stburn}} H^i_{\text{in,stburn}}(T_{\text{stack}}) \\ & - \sum_j n^j_{\text{out,stburn}} H^j_{\text{out,stburn}}(T_{\text{stburn}}) \\ & - Q_{\text{loss,stburn}} \end{aligned}$$

$$\begin{aligned} Q_{\text{loss,stburn}} = & F_{\text{conv,burn–burn}}(T_{\text{stburn}} - T_{\text{stburn}}) \\ & + F_{\text{conv,stburn–pcb}}(T_{\text{stburn}} - T_{\text{pcb}}) \ \text{(W)} \end{aligned} \tag{3.25}$$

In this equation, m_{stburn} and $C_{p,\text{stburn}}$ denote the mass and specific heat capacity of the start-up burner, respectively. The term $Q_{\text{loss,stburn}}$ represents the heat losses from the start-up burner, which include convective losses to both the main burner ($F_{\text{conv,burn–burn}}$) and the printed circuit board ($F_{\text{conv,stburn–pcb}}$), assuming these are the predominant loss mechanisms during the start-up phase. The variables $n^i_{\text{in,stburn}}$ and $n^j_{\text{out,stburn}}$, alongside their associated enthalpies $H^i_{\text{in,stburn}}$ and $H^j_{\text{out,stburn}}$, follow the same definitions as in the general burner scenario, underscoring the consistent treatment of gas flows and thermal properties across both systems.

3.3.5 Air heat exchanger

A plate counterflow heat exchanger (HEX) is responsible for recuperating heat from the afterburner's exhaust gases and transferring it to the inlet air stream feeding the cathode. The configuration facilitates the transfer of heat via metal gaskets that direct the flow within the channels situated between the plates. It is postulated that the HEX can be approximated as a large plate, with an effective area determined by its specific layout. The thermal interaction between the furnace and the air is modeled by considering the radiative heat transfer indirectly influencing the air outlet temperature. The governing energy balance equations for the HEX, encompassing both the hot flow (exhaust from the afterburner) and the cold flow (inlet air), are expressed as follows, based on the use of the $\epsilon - NTU$ method [97], to fully describe the relations:

$$\begin{aligned}
m_{\text{hexh}} C_{p,\text{hexh}} \frac{dT_{\text{hexh}}}{dt} &= \sum_i n^i_{\text{in,hex}} H^i_{\text{in,hex}}(T_{\text{burn}}) \\
&\quad - \sum_j n^j_{\text{out,hex}} H^j_{\text{out,hex}}(T_{\text{hex}}) \\
&\quad - Q_t \\
m_{\text{hexc}} C_{p,\text{hexc}} \frac{dT_{\text{hexc}}}{dt} &= \sum_i n^i_{\text{in,hexc}} H^i_{\text{in,hexc}}(T_{\text{in}}) \\
&\quad - \sum_j n^j_{\text{out,hexc}} H^j_{\text{out,hexc}}(T_{\text{air}}) \\
&\quad + Q_t \\
mCp_{\text{NTU}} &= \min(m_{\text{hexh}} C_{p,\text{hexh}}, m_{\text{hexc}} C_{p,\text{hexc}}) \text{ (W/K)} \\
Q_{\max} &= mCp_{\text{NTU}} \cdot (T_{burn} - T_{air}) \text{ (W)} \\
Q_{\text{t}} &= Q_{\max} \cdot \varepsilon \text{ (W)}
\end{aligned} \tag{3.26}$$

where m_{hexc} and m_{hexh} are the flowing mass of the cold side and hot side, respectively, $C_{p,hexh}$ and $C_{p,hexh}$ are the relative heat capacities. $H^i_{\text{in,hexh}}(T_{\text{burn}})$ represents the enthalpy of the incoming hot flow gas, while $H^j_{\text{out,hexh}}(T_{\text{hexh}})$ indicates the enthalpy of the outgoing hot flow gas. Molar flow rates are denoted by $n^i_{\text{in,hexh}}$ for the hot flow inlet and $n^j_{\text{out,hexh}}$ for the hot flow outlet. Similarly, $H^i_{\text{in,hexc}}(T_{\text{in}})$ and $H^j_{\text{out,hexc}}(T_{\text{hexc}})$ refer to the enthalpies of the incoming and outgoing cold flow gases, with $n^i_{\text{in,hexc}}$ and $n^j_{\text{out,hexc}}$ as the respective molar flow rates. The variable i indexes the inlet species, while j indexes the outlet species.

3.3.6 Water heat exchanger

The Sunfire H750 system is capable of heating domestic water to approximately $60°C$ using a water heat exchanger. Analogous to the air heat exchanger, a plate counter-flow heat exchanger design is adopted, positioning the exhaust on the hot side and the liquid water on the cold side. The heat exchanger is modeled as a large plate, with an effective heat transfer area determined by its specific configuration, and the $\epsilon - NTU$ method is applied. Given the spatial arrangement of the internal components within the H750 system, the water heat exchanger is thermally insulated from the surrounding components. Consequently, it is presumed that the thermal influence on both the hot and cold sides of the water heat exchanger is primarily due to thermal radiation from a hypothetical furnace. The relevant equations for the hot exhaust flow and the cold water flow are articulated as follows:

$$\begin{aligned}
m_{\text{whexh}} C_{p,\text{whexh}} \frac{dT_{\text{whexh}}}{dt} =& \sum_i n^i_{\text{in,whexh}} H^i_{\text{in,whexh}} (T_{\text{hexh}}) \\
& - \sum_j n^j_{\text{out,whexh}} H^j_{\text{out,whexh}} (T_{\text{whexh}}) \\
& - Q_{\text{wt}} \\
m_{\text{whexc}} C_{p,\text{whexc}} \frac{dT_{\text{whexc}}}{dt} =& n^{H_2O}_{\text{in,whexc}} H^{H_2O}_{\text{in,whexc}} (T_{\text{in,H2O}}) \\
& - n^{H_2O}_{\text{out,whexc}} H^{H_2O}_{\text{out,whexc}} (T_{\text{out,H2O}}) \\
& + Q_{\text{wt}} \\
mCp_{\text{NTU}} =& \min(m_{\text{whexh}} C_{p,\text{whexh}}, m_{\text{whexc}} C_{p,\text{whexc}}) \text{ (W/K)} \\
Q_{\max} =& mCp_{\text{NTU}} \cdot (T_{burn} - T_{air}) \text{ (W)} \\
Q_{\text{wt}} =& Q_{\max} \cdot \varepsilon \text{ (W)} \\
n^{H_2O}_{\text{in,whexc}} =& \frac{\dot{Q}_{\text{H2O}} \times 1000}{18} \text{ (mol/s)}
\end{aligned} \tag{3.27}$$

where m_{whexh} and m_{whexc} are the flow mass of the hot and cold sides, respectively, $C_{p,whexh}$ and $C_{p,whexc}$ are the heat capacity of the hot side and cold side of the heat exchanger, which are calculated based on the literature, $H^j_{out,whexh}(T_{in})$ is the inlet gas enthalpy of the hot flow, $H^j_{in,whexh}(T_{whexh})$ is the outlet gas enthalpy of the hot flow, $n^j_{in,whexh}$ are the molar flow rates of the hot flow inlet gas, $n^j_{out,whexh}$ are the molar flow rates of the hot flow outlet gas, i denotes the inlet gas species, j denotes the outlet gas species, $H^{H_2O}_{in,whexc}(T_{in})$ is the enthalpy of inlet water, $H^{H_2O}_{out,whexc}(T_{out,H_2O})$ is the enthalpy of outlet water, $n^{H_2O}_{in,whexc}$ is the mole flow rates of the cold flow inlet gas, $n^{H_2O}_{out,whexc}$ is the mole flow rates of the cold flow outlet gas,

3.3.7 Degradation model integration

Incorporating a degradation model into the analysis is imperative to accurately predict fuel cells' long-term performance. Notably, for the scope of this project, the degradation model is applied at the stack level, so it only concerns the SOFC stack degradation without affecting other units of the BoP, considering them to have an ideal performance for the time. Following a comprehensive review of existing methodologies, the data-driven approach delineated by Zaccaria et al. [98] is selected as the foundation for the current model. This particular model is chosen due to its simplicity and effectiveness in capturing the effects of voltage degradation over time. Moreover, it is adept at incorporating the variation of critical operating parameters, such as FU, current density, and temperature, and is extremely useful for control purposes. The capability of this model to simultaneously account for these factors makes it an invaluable tool for optimization studies, enabling a more nuanced understanding of the operational dynamics of fuel cells under extended use. This integration facilitates the refinement of performance estimates and enhances the robustness of operational strategies designed to mitigate degradation effects. Zaccaria et al. demonstrated through data extrapolation and subsequent analysis that:

- The degradation rate (r_d) exhibits an exponential relationship with the current density (j). Mathematically, this is represented as:

  $$r_d = a(e^{bj} - 1) \tag{3.28}$$

  where a is a coefficient that scales the relationship, and b is a constant that shapes the exponential curve.

- The coefficient a demonstrates a dual dependency: a linear relationship with the fuel utilization (FU) and an exponential relationship with the operating temperature. This dependency reflects the increased rate of degradation observed at higher fuel utilization levels and elevated temperatures.

- The value of b is considered a constant within the model, signifying that the rate of increase in degradation rate with current density does not change with varying conditions of fuel utilization or temperature.

- At any specified level of current density and fuel utilization, the ordering of degradation rates concerning temperature is such that:

  $$r_{d,850} < r_{d,800} < r_{d,750} \tag{3.29}$$

  indicating higher degradation rates at lower temperatures. This relationship is consistent with the understanding that higher operating temperatures can accelerate degradation mechanisms.

These constraints serve as the foundational principles guiding the development of the regression model, allowing for the extrapolation of the degradation rates under various operations. The final equation is adjusted to account for time measured in seconds rather than Zaccaria's original measurement in hours. This change results in a denominator of 3600000 instead of 1000:

$$r_d = \frac{A \cdot FU + C}{1 + \exp\left(\frac{T-D}{E}\right)} \left(\exp\left(B \cdot j\right) - 1\right) \cdot \frac{t}{3600000} \tag{3.30}$$

where r_d is the degradation rate described as a percentage increase in ASR, j is the current density in A/cm^2, T is the temperature in K inside the stack, FU is the fuel utilization and t is the time in seconds. A, B, C, D, and E are the five missing parameters that must be found to describe the relationship mathematically. It's important to mention that, in the code, the degradation rate r_d is applied directly to the ASR:

$$ASR_{deg} = ASR \cdot (1 + r_d) \tag{3.31}$$

For the SUNFIRE system, a parameter estimation is applied to estimate each equation factor to have a more robust description of the system performance in time.

3.4 Parameter estimation

Sunfire provided around 13 months of experimental data, collected between 01 Oct 2021 to 13 Nov 2023, on which a general parameter estimation is run. The regulation of the inputs with time is depicted in Figure 3.2a. To demonstrate the robustness of the modeling equations the experimental data output of the controlled variables needs to be taken into account, depicted in Figure 3.2b. Regarding the parameter estimation discussion, only the one regarding the degradation model is presented in detail, since the estimation for model parameters has already been done by Yu et al. [92]

3.4.1 General problem formulation

Based on the determined inputs and outputs described in Section 3.4, it is possible to evaluate the model's fidelity by computing the weighted least squares of the differences between the predicted and observed data as follows:

$$\min_{\mathbf{p}_i} SQ = \sum_i k_{i,pe} \sum_j \left(y_j^i - \hat{y}_j^i(\mathbf{u}_i, \mathbf{p}_i) \right)^2 \tag{3.32}$$

subject to the constraints provided by the system model in Section 3.3, and the parameter bounds presented in Section 3.2:

$$\mathbf{p}_i^L \leq \mathbf{p}_i \leq \mathbf{p}_i^U \tag{3.33}$$

Here, SQ denotes the sum of squared discrepancies between the plant measurements and the model outputs. The term $k_{i,pe}$ is a normalizing factor that ensures uniform significance across all outputs. The variable y_j^i represents the observed plant data, while $\hat{y}_j^i$ signifies the model's predictions. The vector $\mathbf{u}_i$ is the input vector, and $\mathbf{p}_i$ is the parameter vector being estimated. The vectors $\mathbf{p}_i^L$ and $\mathbf{p}_i^U$ specify the lower and upper bounds, respectively. The index i corresponds to the outputs, and the index j refers to the temporal points selected for analysis. The parameter optimization is conducted on the MATLAB software using the nonlinear programming solver `fmincon`.

3.4.2 Degradation model - Moving horizon estimation

To estimate the different parameters proposed by Zaccaria et al. [98] in Equation 3.30, at least five different operating points should be needed. Since the number of points collected at the beginning of this project is not enough, a first move to estimate the parameter of the degradation model is conducted by fixing two less impacting parameters and solving the problem using interpolation with a subsequent sensitivity on the final parameter reported in the Appendix A.1. A second move, which resulted in more robust results, considered an additional second data set and an optimization approach, the moving horizon estimation (MHE) to fit the degradation

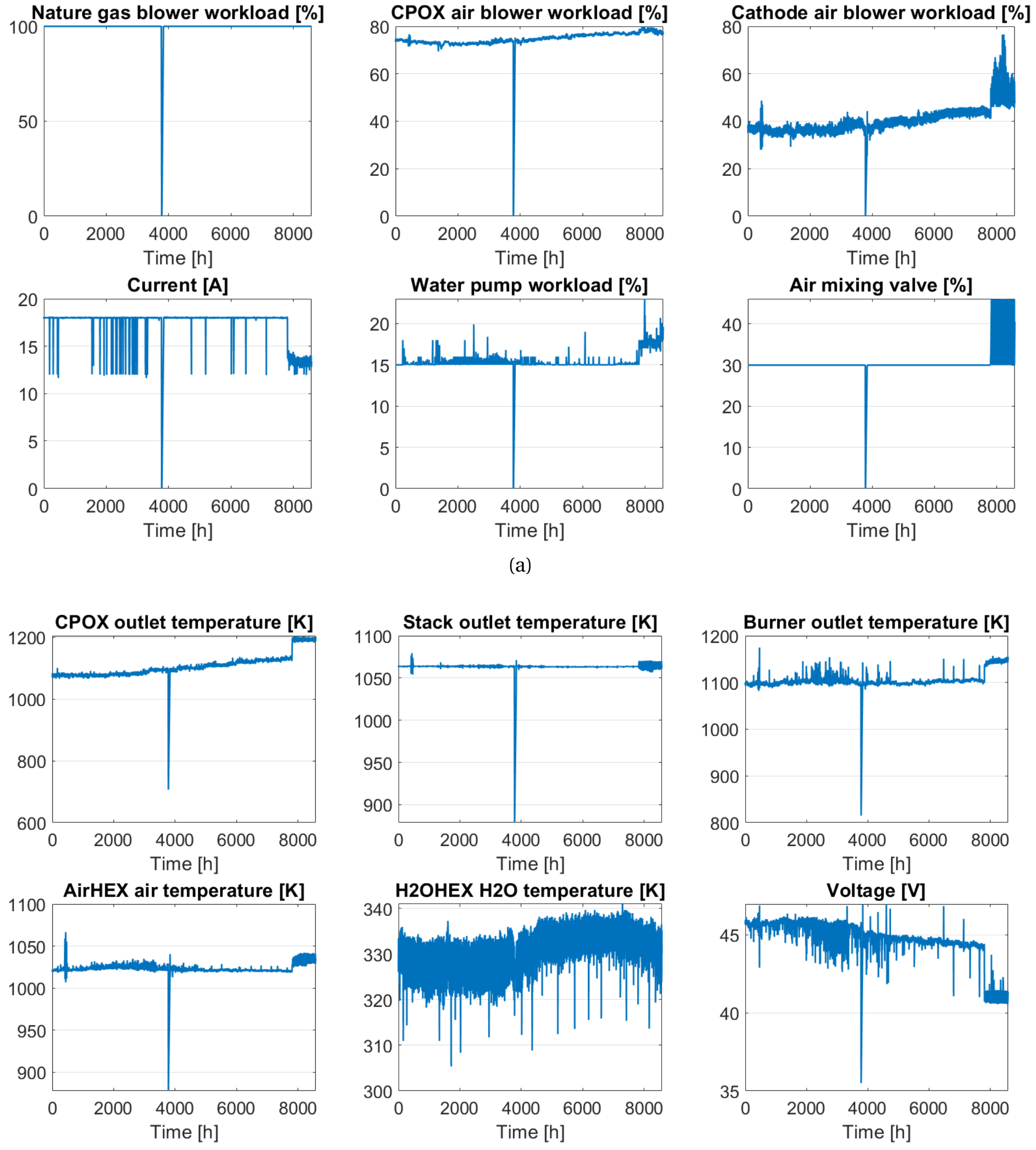

(a)

(b)

Figure 3.2: Experimental input (a) and output (b) data from Sunfire [92]

model to SUNFIRE data better.

The second data set is collected during current decreasing operations, a common control approach adopted to maintain an almost constant voltage in time. This means that the inputs in this data set vary in time, which is particularly useful to have a correct parameter estimation of the degradation model. Inputs and outputs from the data-set experimental results are shown more in detail in Appendix A.2. The optimization approach that is used to deal with this multitude of states varying with time to have a correct parameter estimation, is a MHE. MHE is an optimization technique that processes noisy and potentially imprecise measurements over time to derive estimates of unknown variables or parameters. Differing from deterministic methods, MHE utilizes an iterative strategy that depends on linear or nonlinear programming solvers to determine the estimates. To find the best parameters to fit the degradation model, only a part of the whole data set is taken into account (444 hours), in which the current decrease shows an almost linear behavior concerning time and in which it has a less noisy behavior.

In the pre-processing stage of the analysis, a critical step involved the application of a smoothing filter to the dataset. The primary rationale behind this technique is to mitigate the influence of noise and fluctuations inherent in the raw data, thereby enhancing the clarity and interpretability of underlying trends. For this purpose, a simple moving average (SMA) filter is employed. The simple moving average filter, a widely used method in time series analysis, computes the mean of a specified number of consecutive data points at various intervals throughout the dataset. By averaging the data points within a defined window, the SMA filter effectively dampens short-term variations and highlights more substantial, long-term trends. This attribute makes it particularly beneficial for datasets where the goal is to analyze or forecast underlying patterns obscured by noise. For the dataset in question, a moving average window of ten data points is selected. This window size is determined to be optimal based on preliminary data characteristics, including the level of noise and the frequency of data acquisition. The application of the SMA filter transforms each value in the dataset into the average of itself and the nine preceding values. Mathematically, the smoothed value S_t at time t is calculated as follows:

$$S_t = \frac{1}{10}\sum_{i=0}^{9} x_{t-i} \tag{3.34}$$

where x_t represents the original data point at time t. The efficacy of this method in reducing noise and revealing smoother trends is evaluated through visual inspection of plots before and after the application of the SMA filter (Figure 3.3).

After applying the SMA filter, data smoothing is applied to better interpolate the data. Data smoothing is a fundamental technique used in data preprocessing to remove noise and reveal underlying trends. With the filtered data in place, regression analysis is conducted using polynomial models of varying degrees to fit the data. Starting with a linear regression (applied in the case of air cpox workload), which posits a direct relationship between the independent and dependent variables through a simple equation involving a slope and an intercept, the process aimed to minimize the discrepancies between observed values and those predicted by the model. As complexities in data trends are identified, cubic regression is applied, too. This model, encompassing a third-degree polynomial, provided the flexibility required to closely match the data's nuances, leveraging four parameters to minimize the sum of squared residuals and ensure an optimal fit. The fitting process is conducted using the 'Polynomial.fit' method from the NumPy library with Python, which efficiently computes the least squares fit of polynomial models. The results of filtering and smoothing of the data are shown in Figure 3.3.

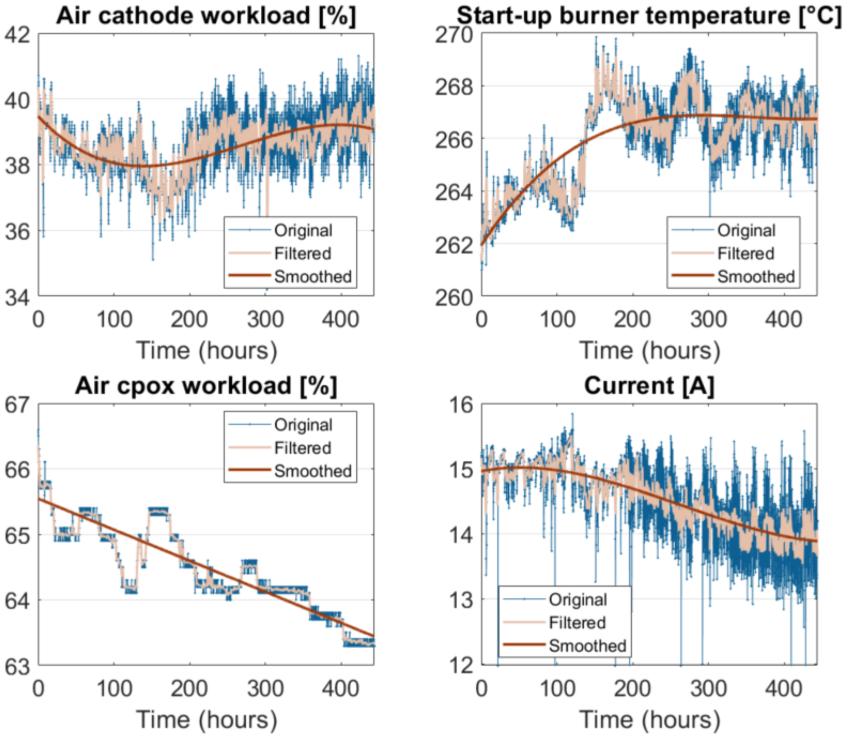

Figure 3.3: Second dataset's filtered and smoothed data inputs

Given the operational constraints detailed in Table 3.2, an MHE multivariable algorithm is developed using MATLAB to determine the best-fit parameters for the degradation model. The primary objective is to adjust the model parameters to minimize the variance of the stack voltage over time, thus ensuring its stability. The optimization process involves the five parameters, which are treated as variables. These parameters are adjusted to fit the second dataset operating point's extrapolated inputs into the model, under the assumption that the temperatures remain constant. This assumption is justified based on the observation that the duration of the linear voltage decrease is only 444 hours, which is likely to result in nearly constant temperature behavior. The optimization is executed using MATLAB's *fmincon* function, which is designed to find the minimum of a constrained nonlinear multivariable function. The function's goal is to minimize the time variance of the stack voltage, thereby maintaining its constancy. Additionally, to the constraints mentioned above, the algorithm ensures that the model parameters also fit the last time point of the first operating point dataset effectively. This dual fitting ensures that the parameters not only provide a good fit for the current operating point but also remain valid under previous operating conditions.

The formulation of the MHE multivariable estimation algorithm is as follows:

$$
\begin{aligned}
\underset{u}{arg\ \text{minimize}} \quad & var(U_{stack,m,t} - U_{stack,2^{nd},t}) \text{ in time} \\
\text{subject to} \quad & 650 \leq T_{cpox} \leq 850\,^{\circ}\mathrm{C} \\
& 650 \leq T_{stack} \leq 865\,^{\circ}\mathrm{C} \\
& 40 \leq U_{stack} \leq 60\,\mathrm{V} \\
& 700 \leq T_{burner} \leq 1050\,^{\circ}\mathrm{C} \\
& 25 \leq T_{startup} \leq 700\,^{\circ}\mathrm{C} \\
& 100 \leq T_{hex,hot} \leq 700\,^{\circ}\mathrm{C} \\
& 650 \leq T_{air,mix} \leq 850\,^{\circ}\mathrm{C} \\
& 650 \leq T_{hex,cold} \leq 860\,^{\circ}\mathrm{C} \\
& 25 \leq T_{whex,hot} \leq 320\,^{\circ}\mathrm{C} \\
& 25 \leq T_{whex,cold} \leq 60\,^{\circ}\mathrm{C} \\
& FU \leq 0.8 \\
& AU \leq 0.25 \\
& CO \leq 0.95 \\
& 0.1 \leq W_{CH_4} \leq 1 \\
& 0.1 \leq W_{air,cpox} \leq 0.8 \\
& 0.1 \leq W_{air,stack} \leq 0.8 \\
& 0.1 \leq W_{H_2O} \leq 1 \\
& 0.001 \leq V_{ratio} \leq 0.45 \\
& 0.1 \leq I \leq 24\,\mathrm{A} \\
& U_{stack,1^{st},model} - U_{stack,1^{st},real} = 0
\end{aligned}
$$

Where $U_{stack,m,t}$ is the voltage of the stack produced by the model per unit of time given by the collected variable inputs of the second dataset, $U_{stack,2^{nd},t}$ is the measured voltage of the second operating point per unit of time, $stack, 1^{st}, model$ is the modeled stack voltage with first operating point fixed inputs (single value taken from the last time point), and $U_{stack,1^{st},real}$ is the measured voltage of the first operating point (taken from the last time point). This new algorithm produced good fitting parameters for what concerns the first operating point (Figure 3.4a), but lacks accuracy for what concerns the fitting of the second one; in fact, the total range of variation of the voltage is still 1.63 V (Figure 3.4b). The results of this algorithm are shown in the new degradation formula:

$$
r_d = \frac{0.500 \cdot FU + 0.876}{1 + \exp\left(\frac{T-1089}{22.920}\right)} \left(\exp\left(0.3 \cdot j\right) - 1\right) \cdot \frac{t}{3600000} \tag{3.35}
$$

These results are considered because they perfectly match the voltage decrease in the first dataset, which is the project's primary objective, as the general parameter estimation is based on this dataset. It's important to note that the natural gas content can vary significantly within the system, and the presence of numerous PIDs introduces considerable uncertainty in the

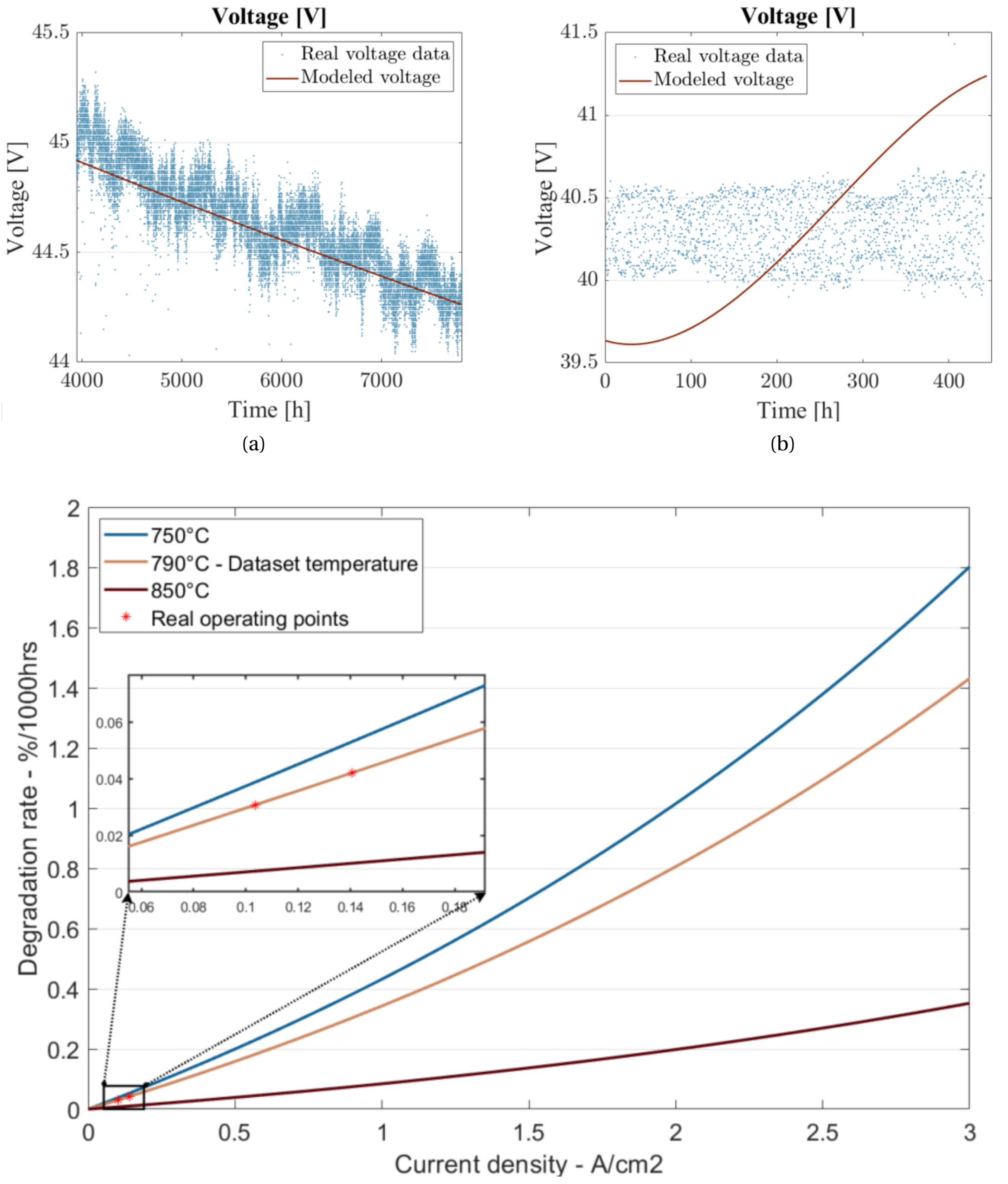

(a)

(b)

(c)

Figure 3.4: MHE degradation model fitting of the 1^{st} operating point (a), of the 3^{rd} operating point (b). Degradation ratio exponential dependency on current density with temperature effect [98] (c)

results. Therefore, the fit on the second dataset is acceptable, as it is derived from smoothed and filtered data. Additionally, this set of parameters preserves the exponential relationship between current density and degradation ratio, a crucial property identified by Zaccaria et al. in their degradation model, which is also upheld in this instance (Figure 3.4c). In this figure, the current density range is very large to demonstrate the exponential behavior. However, it is important to note that the nominal current density range in the SUNFIRE system is from 0 to 0.1875 A/cm^2.

It's also important to give two key definitions that will be used from now on:

- Degradation rate (%/1000hrs), a term that takes into account the impact on degradation on a specific time instant t, useful to assess the impact of degradation independently from the time of operations or the cumulative degradation in the cell:

  $$D_{rate} = \frac{0.500 \cdot FU + 0.876}{1 + \exp\left(\frac{T-1089}{22.920}\right)} \left(\exp\left(0.3 \cdot j\right) - 1\right) \tag{3.36}$$

- Performance degradation (r_d %) that is a cumulative factor of increase of ASR (linear) and so a non-linear factor of decrease of voltage, taking into account time:

  $$D_{performance} = r_d = \frac{0.500 \cdot FU + 0.876}{1 + \exp\left(\frac{T-1089}{22.920}\right)} \left(\exp\left(0.3 \cdot j\right) - 1\right) \cdot \frac{t}{3600000} \tag{3.37}$$

  Notably, the values obtained from the degradation rate and performance degradation in this project do not align with those commonly found in the literature. This discrepancy arises because there is currently no universal definition of degradation, as it depends on numerous factors. Therefore in this project, these values are used only as a relative reference and are not considered objectively. For example, in Figure 3.5, these parameters are related to the common degradation index used in the literature to define SoH achievements: voltage decrease % per 1000 hours, based on fixed inputs from the first dataset:

  $$D_{rate,volt} = \frac{(D_{rate} + 1) * U_{loss,ASR}}{U_{stack,i}} \tag{3.38}$$

  where $U_{loss,ASR}$ is the voltage loss due to ASR without degradation taken into account and $U_{stack,i}$ is the stack voltage at the beginning of the operation.

3.5 Techno-economic analysis of Sunfire system

This chapter presents a rough techno-economic analysis of the SUNFIRE system, in Switzerland. The analysis focuses on the cost implications of operating the system under varying conditions over its expected lifespan, modeling the cost factors in conjunction with the complex interplay of all operating costs. This has been done to integrate a profitability evaluation part into the current model, useful for Chapter 4 prognostic assessment. At the end of this analysis, a code for simulating model behavior over time is developed, integrating the `ode15s` function from MATLAB. This configuration allows for the simulation of system dynamics at a fixed

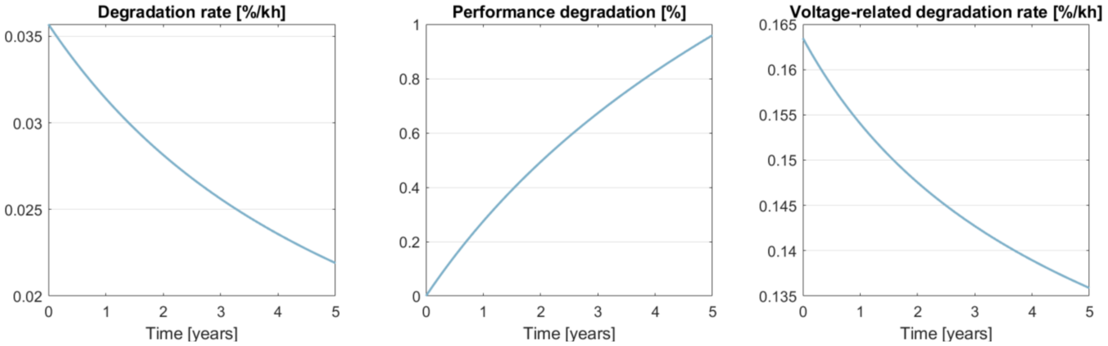

Figure 3.5: Degradation plots of operating condition given by the 1^{st} dataset

initial operating point without accounting for degradation, demonstrating the capability of the economic model to explore the economic breakpoints where operating income balances the cost of production, essentially where revenue equals expenses.

3.5.1 Capital cost

The capital costs for the SOFC stack can be estimated using the formula from DOE [99]:

$$C = C_0 \left(\frac{P}{P_0}\right)^{-\beta} \tag{3.39}$$

where C is the cost per unit power (\$/kW), C_0 is the reference cost per unit power at a reference power output P_0, P is the desired power output, and β is the scaling exponent. The parameter values are $C_0 = 1000$ \$/kW for a 100 kW system, $P_0 = 100$ kW, and $\beta = 0.7$, the formula for the Sunfire system, whose nominal power is 850 W (0.85 kW) becomes:

$$C = 1000 \left(\frac{0.85}{100}\right)^{-0.7} \approx \$6427.83 \text{ per kW} \tag{3.40}$$

Considering the 850 W SUNFIRE system, this results in a capital cost of $0.85 \times 6427.83 = \$5,463.66 \approx 4,960\text{CHF}$.

The capital cost for the entire system, excluding the SOFC stack, cannot be accurately estimated since there is no detailed market information about the SUNFIRE system costs.

Operational Expenditure (OPEX)

The cost factors for natural gas and electricity consumption are selected based on the prevailing market prices in Switzerland for the year 2019 to avoid the impact of market fluctuations due to the pandemic. According to HEV Schweiz [100], the average price of natural gas remained consistently around CHF 0.0958 per kWh throughout the year. This value is used to estimate the operational cost related to natural gas consumption with the following equation:

$$Cost_{CH_4}(t) = \frac{P_{CH_4,in}}{1000} \cdot k_m \text{ (CHF/hour)} \tag{3.41}$$

where $Cost_{CH_4}(t)$ is the methane consumption cost in CHF/hour, $P_{CH_4,in}$ is the input chemical power of CH_4 consumption in W, k_m is the methane cost factor of 0.0958 CHF/kWh In contrast, the price of electricity for households varied significantly depending on the municipality. Prices ranged from approximately 0.10 to over 0.50 CHF/kWh, with a median price of around 0.32 CHF/kWh as indicated by a comprehensive guide on electricity costs in Switzerland published by *Banken, Versicherungen & Telekom* [101], and the cost of electricity is computed as:

$$C_{auxiliaries}(t) = \frac{P_{auxiliaries}(t)}{1000} \cdot k_c \text{ (CHF/hour)} \tag{3.42}$$

where $C_{auxiliaries}$ is the cost of auxiliaries in CHF/hour, k_c is the current price of 32 CHF/kWh, and $P_{auxiliaries}$ is the auxiliaries' power consumption in W. However, in this analysis, this cost is not considered, assuming that the power required for the auxiliaries is supplied by the system itself.

An essential component in the financial model is the cost associated with CO_2 emissions. Since 2022, Switzerland has imposed a CO_2 tax on thermal fuels, aimed at reducing emissions and promoting cleaner energy sources. The tax rate is set at CHF 120 per ton of CO_2 emitted [102]. The cost of CO_2 emissions for the operational activities is calculated based on the emissions generated, converted to a cost per hour using the formula:

$$Cost_{CO_2}(t) = \dot{N}_{CO_2}(t) \cdot 3600 \cdot \frac{44.01}{1000000} \cdot k_t \text{ (CHF/hour)} \tag{3.43}$$

where $\dot{N}_{CO_2}(t)$ are the moles emitted per second, and the tax rate k_t is 120 CHF/ton.

The overall OPEX is computed summing up the three contributions of natural gas consumption, electricity consumption, and CO_2 taxation, adding interest of 2% to take into account other indirect costs (maintenance, manpower, etc... [103]):

$$OPEX(t) = (Cost_{CH_4}(t) + Cost_{CO_2}(t)) \cdot (1 + 0.02) \text{ (CHF/hour)} \tag{3.44}$$

Operating Income (OI)

The revenue model is based on the selling price of heat and electricity generated by the system. It is assumed that the selling price of generated heat is equivalent to the cost of natural gas adjusted for mean boiler efficiency.

For modeling, the electricity selling price is set at 0.266 CHF/kWh. This specific rate is taken from the 2024 projections published by *Oiken* [104], which reflects the anticipated cost of electricity supplied to the grid. The revenue made by selling electricity is computed with the equation:

$$I_{el}(t) = \frac{P_{system}(t)}{1000} \cdot r_e \text{ (CHF/hour)} \tag{3.45}$$

where $I_{el}(t)$ is the electricity selling revenue in CHF/hour, $P_{system}(t)$ is the power produced by the system in W, and r_e is the revenue selling price factor of 0.266 CHF/kWh.

Revenue generated from the production of heated water is calculated by considering the cost of methane and the efficiency of the boiler used to heat the water. The formula for calculating the revenue per hour is as follows:

$$I_{water}(t) = \frac{\mathrm{P}_{\mathrm{H_2O}}(t)}{1000} \cdot \left(\frac{r_m}{0.85}\right) \text{ (CHF/hour)} \tag{3.46}$$

where $I_{water}(t)$ is the revenue produced by the heated water selling in CHF/hour, P_{H_2O} is the power produced by the water heat exchanger in W, and r_m is the methane cost factor of 0.0958 CHF/kWh. The denominator, 0.85, represents the mean boiler efficiency. This efficiency factor is used as an assumption due to the lack of detailed information online regarding the selling price of heated water and is based on the common technology of boilers which are frequently used due to their low operational costs. This mean efficiency value is consistent with industry standards as reported in literature [105].

The overall OI is computed by summing up the two contributions of heated water and sold electricity:

$$OI(t) = I_{water}(t) + I_{el}(t) \text{ (CHF/hour)} \tag{3.47}$$

Cost analysis

The net operating income has then been computed by subtracting to the OI the OPEX costs:

$$OI_{net}(t) = OI(t) - OPEX(t) \text{ (CHF/hour)} \tag{3.48}$$

Then, to quantify the cash flows for a generic time instant T the integral of all the cost variables is computed concerning time, passing from CHF/year to CHF. The equation for the total operating expenditure is:

$$OPEX_{tot} = \int_{t=0}^{T} OPEX(t) \cdot dt \text{ (CHF)} \tag{3.49}$$

The equation for the total operating income is

$$OI_{tot} = \int_{t=0}^{T} OI(t) \cdot dt \text{ (CHF)} \tag{3.50}$$

The equation for the net total operating income is

$$OI_{net,tot} = \int_{t=0}^{T} OI_{net}(t) \cdot dt \text{ (CHF)} \tag{3.51}$$

Net total operating income computation aims to find after how many years it is possible to recover the initial investment, this defines the payback period. In MATLAB, this has been accomplished by discretizing the integral over a fixed time interval, defined by the time vector, and converting all the equations into cumulative sums.

Cost analysis of 1^{st} dataset This techno-economic analysis provides a comprehensive overview of the financial viability of the Sunfire system under specified operational conditions. An example simulation over 5 years aims to determine key financial outcomes, including net OI and the payback period. This is done using the input data of the 1^{st} dataset with fixed inputs in time, taking into account the degradation impact over time.

Figure 3.6 presents two pie charts detailing the distribution of operating income and costs for the system. The chart on the left (3.6) shows the operating income distribution, which comprises total electricity income and total heat income. A significant portion of the income is derived from electricity generation, with heat income representing a smaller share. On the right (3.6), the operating costs distribution is depicted, illustrating the contributions of CO_2 and CH_4 costs to the total operating expenses. Similar to the income distribution, the majority of the costs are associated with CH_4, while CO_2 costs form a lesser fraction of the total costs. The figure also presents a plot of the income vs operating expenditures of the system over the years, evidencing the operating income loss after 5 years to be 175 CHF/y due only to system degradation. This operating point is proven to be unprofitable. This outcome could be expected, given that the primary goal of the SUNFIRE system is not to achieve profitability. The primary aim of this analysis is not to emphasize the accuracy of economic profitability predictions. Instead, it highlights the crucial importance of optimizing system variables in real-world applications where profitability is a key objective.

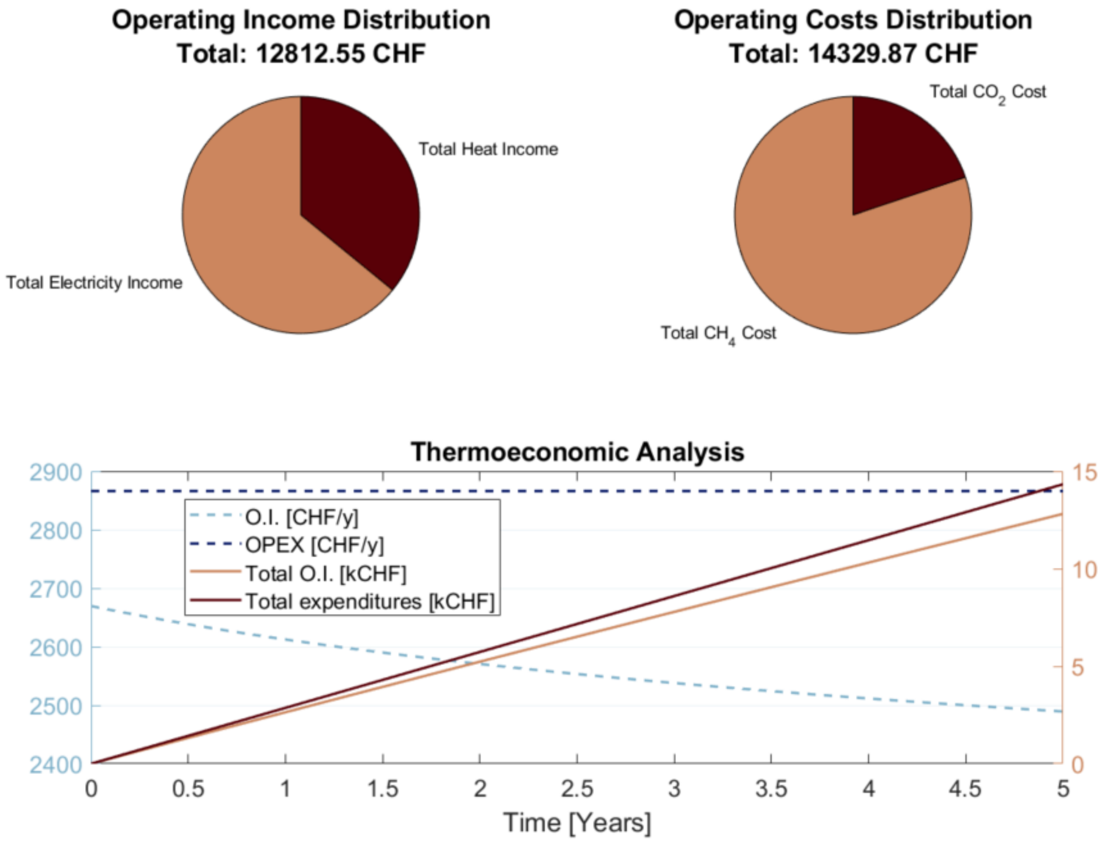

Figure 3.6: Techno-economic analysis of operating condition given by the 1^{st} dataset

4 Long-Term Prognostic Analysis with Control Strategies

This chapter explores the application of a method based on NMPC theory to the modeled CPOX-SOFC system. This advanced control strategy aims to enhance the performance and efficiency of the inherently complex and nonlinear SOFC systems. However, the primary focus of this chapter is on prognostics rather than control. It emphasizes predicting the dynamic system response over time to advance the field of predictive analysis for SOFC systems, providing deeper insights into their long-term performance behavior.

For SOFC systems, NMPC can be tailored to handle the fuel cell system's specific nonlinear characteristics and operational requirements. These include parameter workloads, fuel utilization rates, electrical demands, etc... By applying NMPC, it is possible to achieve several critical outcomes:

- Enhanced efficiency: optimal control of fuel input and operational parameters leads to improved efficiency of power generation
- Increased durability: by maintaining operations within safe limits, NMPC extends the life span of the SOFC system.
- Improved performance: NMPC helps in stabilizing the output despite the fluctuations in demand and supply conditions

In the context of SOFC systems, several studies are conducted in the literature with NMPC [106, 107, 108].

It's important to notice that, for this work, there is no physical online system control, but this NMPC approach is used only for predictive applications. Before diving deeper into the optimization analysis, firstly it is useful to introduce a more detailed overview of the state of health (SoH) of a SOFC stack and how this can be connected to detect its end of life (EoL).

4.1 Evaluation of the state of health of the SOFC system

The successful commercialization and sustained application of SOC-based systems in the future energy landscape hinge on enhancing their reliability and extending their lifetime. This is achievable through timely and accurate SoH assessments that detect early signs of potentially critical changes in system operation. U.S. Department of Energy (DOE) has set a long-term target for stationary power system lifetime equal to 130,000 hours (15 years) for SOFC stacks, reflecting requirements for data centers, where primary power systems must operate 24/7 for 365 days per year. Targets are technology-neutral and do not assume the type of fuel cell technology. While achievement of some of the individual targets has already been demonstrated for specific fuel cell technologies, concurrent achievement of all targets remains a challenge. Effective online SoH estimations allow for the optimal design of maintenance schedules and accurate end-of-life (EoL) predictions. This prevents equipment failure and reduces operational losses. Significant research in this area continues to advance understanding and capabilities. This section aims to assess the relationship between inputs and EoL to estimate the remaining useful life (RUL) and determine the target life expectancy of the stack.

The EoL criteria used in this analysis are introduced and discussed in detail in the following paragraph.

4.1.1 EoL criteria

Performance metrics monitoring serves as a foundational approach to assessing EoL for fuel cells. This involves various techniques that gauge the degradation and efficiency loss over time, crucial for maintaining system efficiency and safety.

Voltage decline is one significant indicator where the U.S. DOE has set specific performance targets [109]. For SOFCs, the target is maintaining less than 0.2% voltage degradation per 1,000 hours, whereas for PEM fuel cells, used predominantly in transportation, the goal is a more stringent less than 0.03% per 1,000 hours to maintain less than 10% voltage loss over their designed lifetime. Voltage monitoring involves the use of real-time sensors that record output continuously during operation, with advanced data analytics applied to predict future voltage trends based on historical data.

Another critical metric is power output, where DOE efficiency targets stipulate that stationary fuel cells like SOFCs should achieve more than 60% efficiency in combined heat and power (CHP) applications, with less than 10% degradation in efficiency before EoL. PEM fuel cells in automotive applications should maintain efficiency above 40% throughout the lifecycle. Regular performance testing under controlled load conditions helps in monitoring significant drops in efficiency.

Additional performance metrics include stack temperature and humidity controls, which are crucial for both SOFC and PEM fuel cells. Deviations from ideal operational temperatures and humidity levels can accelerate degradation. Integration of thermocouples and humidity sensors into the fuel cell system allows for continuous monitoring.

The issue with these metrics is that they are only valid if the inputs to the SOFC stack system remain constant. When inputs change over time, these metrics lose their validity. For example, a decreasing current can maintain a constant voltage over time, masking ongoing degradation in the stack and leading to undetected issues in voltage metrics. This is a common industry practice to keep voltage stable over time. Another approach is to increase the stack's temperature to maintain a fixed power output. Both methods can hide underlying degradation, making these metrics unreliable.

A very interesting paper by Jouin et al. [110] regarding PEMFC will be taken as a reference for this discussion, as they have made significant strides in better defining the problem. In their paper, Jouin et al. highlights that the literature lacks clear guidelines on how prognostics should be performed, which health indicators should be used, how to define the EoL of a PEMFC, and how to correctly evaluate prognostic performance, especially in the case of dynamic mission profiles. They propose several solutions to these issues. In the following paragraphs, the strategy proposed by Jouin et al. is adapted and discussed in the context of SOFC systems.

Health indicators A proper indicator is chosen according to the mission of the system. Several health indicators can be considered:

1. the voltage
2. the power (both at the stack and the system level)
3. efficiency
4. the cumulative energy
5. economic profitability

Indicators like voltage and power can be useful only when dealing with fixed power or voltage missions respectively; these are not monotonic indicators with variable mission profiles, they are not monotonic and they can lead to fixing a failure threshold.

Efficiency is a classical measure of an energetic system. In the case of SUNFIRE, two different efficiencies are taken into account: the one at the stack level, named electrical efficiency, and the one at the system level, named CHP efficiency. Both of them are a ratio between the power output and the chemical power input, for electrical the output considers stack power production in conjunction with power losses made by auxiliaries, while for CHP efficiency also the output power of the waste heat recovered is considered. Efficiency is strongly linked to the mission profile and the nominal conditions set for each current value. If the nominal conditions are maintained over time, guaranteeing fixed chemical power input, the efficiency should decrease with the stack power.

Cumulative energy is the most interesting approach since it relies on the polarization curve used to make a monotonic indicator useful to detect the EoL. Thanks to the voltage measurement U,

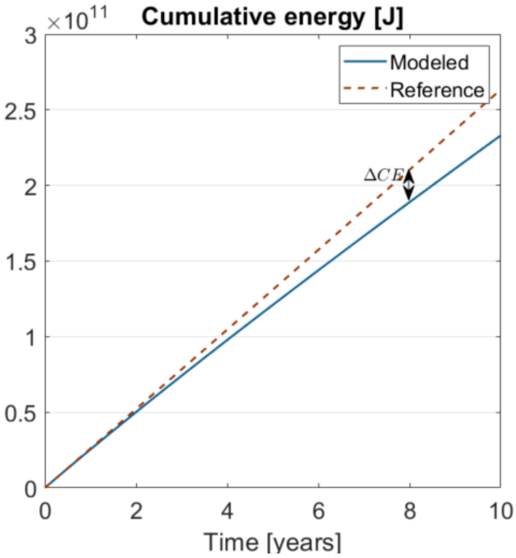

Figure 4.1: Comparison of measured cumulative energy and reference

knowing current profile i and the time of operation T, the cumulative energy can be defined as:

$$E(\text{t=0 : T}) = \int_0^T U(t)\cdot i(t)dt \tag{4.1}$$

This provides a quantitative indicator of performance and since it is monotonic independently from the system mission it makes the definition of a failure threshold easier to select. However, a reference states it is still needed. Join et al. [110] have proposed two different solutions to build the reference:

- The first solution requires a polarization curve of the first state of the SOFC stack that is assumed to have no degradation. Then the cumulative energy can be obtained in time using the voltages of that curve with the current made by the model.
- A second solution, which is the one used in this thesis, is to build the reference with a behavioral model that describes the evolution of the voltage or the power according to the current profile as if no degradation is occurring within the stack.

Once the reference is set, the collected data are used to build the cumulative energy and compare it to the reference. The difference between them (ΔCE) can be calculated at each time instant and converted into a percentage of energy loss to help estimate the EoL and RUL (Figure 4.1). The great advantage of this solution is that the indicator is monotonic and adaptable to any kind of mission.

Another possible health indicator could be the economic profitability of the system, especially for what concern a complex system such as the SUNFIRE one. This kind of system has a complex interplay of several factors to take into account, so reducing the analysis to just an economic assessment of the system's profitability could be enough to assess whether the system should be replaced or not (LCA).

EoL definition Two different thresholds can be defined for prognostics applications:

- a threshold of conformity to a mission
- a definitive EoL threshold

The first allows the engineer to a more flexible decision if the fuel cell stack can perform a given mission. The second one, more complex to define, guarantees more robustness to the analysis.

Defining the conformity is responsibility of the user. In the context of the SUNFIRE system, a conformity criterion could be for example the economic profitability of the system. In the context of a variable mission profile, a fixed threshold might not be suitable anymore. A possible solution for this can be considering cumulative energy indicator:

$$\Delta CE(t) = CE_{ref}(t) - CE_{real}(t) \tag{4.2}$$

where the related threshold value can be set to 10% of the reference cumulative energy according to DOE:

$$\Delta CE_{max}(t) = 5\% \cdot CE_{ref}(t) \tag{4.3}$$

Chen et al. [111], have proposed an economical lifetime EoL criterion where the PEM stack needs a replacement. This threshold takes into account stack capital cost Q_{stack}, the consumption of the system Q_{CH_4} (that increases with aging), and the CHP efficiency of the system Q_{ope} (auxiliaries power consumption):

$$Q_{total}(t) = Q_{stack} + \int_{t=0}^{T} Q_{CH_4} dt + \int_{t=0}^{T} Q_{ope} dt \tag{4.4}$$

The threshold is the point at which the Q_{total} function in time reaches its minimum. For the SUNFIRE system, this kind of model doesn't fit well, since with a fixed mission profile the function would be flat not exhibiting any minimum. This is due to a system assumption of no degradation in the system except the SOFC stack, which means that with fixed inputs, even if the stack power is decreasing in time, there is a fixed difference between stack and system power, given the fact that the system degradation coincides with stack's one. Due to this limitation, an alternative economic model is proposed using a techno-economic analysis to evaluate the system's economic profitability and suggest a new potential threshold, as discussed in Section 3.5. However, since model accuracy is not the primary focus of this project and the economic model may have inaccuracies leading to potential prediction errors, this model is considered only for optimizing profitability objectives. As EoL the approach used in this thesis is to put a definitive threshold in the case of voltage and power health indicator performances, and a threshold of conformity to the mission in the case of cumulative energy.

A possible definitive EoL can be the one proposed by DOE as a 10% loss of the initial performance. If the operating conditions are fixed with time, this is a very effective approach, easy and robust to apply. However, in the case of a variable mission profile, it lacks effectiveness making this kind of threshold closely linked to the application. It's useful to notice that in cases with fixed input operation, it would be possible to define a grade for each system state. As an example, one can define:

- From 0% to 5% of power loss: Good health;
- From 5% to 10% of power loss: Acceptable;
- Over 10% of power loss: Degraded SoH.

These thresholds are applied to the power or voltage difference in cases of fixed mission profile; for cumulative energy, a more strict rule is applied fixing the EoL at 95% of the relative difference to account for the possibility of prediction errors.

4.2 Optimization algorithm

NMPC uses an optimization algorithm to find what are the best inputs for each time point. In this case, several attempts are made to see what's the best approach also in fitting the scope of the project:

- Sequential Quadratic Programming (SQP)
- Genetic algorithm (GA)

Both SQP and GA have proven their effectiveness in various real-world applications, which supports their selection for this thesis project. Using both SQP and GA allows a comparative analysis of a gradient-based method and a non-gradient method, highlighting how each performs under various system conditions and constraints. This comparative study can provide insights into the robustness and reliability of different approaches under the specific scenarios encountered in the project. Evaluating both methods provides a comprehensive understanding of the trade-offs between solution quality (accuracy) and computational effort (convergence speed, resource usage).

Another attempt is making another code with "Model Predictive Control Toolbox" directly dealing with NMPC functions. This is done by re-writing the model to be compatible with NMPC object optimization. The algorithm resulted in being too slow concerning just using `fmincon` function, so this option has been discarded.

Sequential Quadratic Programming Algorithm

SQP is an iterative method used to solve nonlinear optimization problems, especially those involving both equality and inequality constraints. This optimization technique is widely regarded as one of the most powerful methods for nonlinear constrained optimization problems, and its effectiveness is due to its ability to rapidly converge to a solution near the optimal point under a variety of conditions. The fundamental approach of SQP is to model the nonlinear optimization problem at each iteration as a quadratic programming (QP) subproblem, whose solution provides a search direction for the next iteration. Each QP subproblem approximates the objective function by a quadratic model and the constraints by linear models. Formally, an optimization problem can be defined as:

$$\min f(\mathbf{x}) \quad \text{subject to} \quad \mathbf{g}(\mathbf{x}) = 0, \quad \mathbf{h}(\mathbf{x}) \leq 0, \tag{4.5}$$

where $f(\mathbf{x})$ is the objective function, $\mathbf{g}(\mathbf{x})$ and $\mathbf{h}(\mathbf{x})$ represent the equality and inequality constraints, respectively, then at each iteration, k, the SQP method solves the following QP subproblem:

$$\min \frac{1}{2}\mathbf{p}^\top \mathbf{B}_k \mathbf{p} + \nabla f(\mathbf{x}_k)^\top \mathbf{p} \tag{4.6}$$

$$\text{subject to} \quad \mathbf{A}_k \mathbf{p} = -\mathbf{g}(\mathbf{x}_k), \quad \mathbf{C}_k \mathbf{p} \leq -\mathbf{h}(\mathbf{x}_k), \tag{4.7}$$

where $\mathbf{p}$ is the step direction, $\mathbf{B}_k$ is an approximation to the Hessian of the Lagrangian (which can be updated using various strategies such as the BFGS method), $\mathbf{A}_k$ and $\mathbf{C}_k$ are the Jacobian matrices of the equality and inequality constraints, respectively. SQP is particularly valued for its superlinear convergence properties under mild assumptions, such as the regularity of the constraint Jacobians and sufficient second-order conditions at the solution. This method is also adaptable to large-scale problems, although its performance heavily depends on the quality of the Hessian approximation and the strategies used for constraint handling. Despite its robustness, one of the primary challenges in implementing SQP is ensuring the positive definiteness of the Hessian approximation, which is crucial for the algorithm's stability and convergence. Practical implementations of SQP often include modifications such as trust region strategies to maintain the step direction and size reliability. SQP has been successfully applied in numerous fuel cell fields. Its ability to efficiently handle complex models with multiple constraints makes it a preferred choice for many applications requiring high-precision solutions to challenging optimization problems.

This algorithm is successfully implemented in MATLAB using the "Optimization Toolbox" (Algorithm 1).

The MATLAB script configures and executes a constrained nonlinear optimization using the ‘fmincon‘ function. Initially, it sets solver options with ‘optimoptions‘, specifying the use of the SQP algorithm, detailed iteration display, and high limits for function evaluations and iterations to handle complex problems. The script initializes ‘input_sol‘, a cell array matching the length of ‘tspan‘, which represents the time vector. The core of the script is a loop over ‘tspan‘. In each iteration, ‘fmincon‘ is called with parameters including an objective function, initial variable guesses, constraint definitions, and variable bounds. The function solves for the optimum, storing results in ‘input_sol‘ and updating the guess for the next iteration to the current solution. This iterative updating is designed to refine the optimization across stages, improving both the speed and quality of convergence, especially in dynamic scenarios where optimal conditions

Algorithm 1: SQP algorithm implementation using fmincon

Data: Initial guess `input0`, constraint matrices `A`, `b`, bounds `lb`, `ub`, time span `tspan`

Result: Optimized solutions `input_sol` for each time point in `tspan`

```
options ← optimoptions('fmincon', 'Algorithm', 'sqp', 'Display',
 'iter','MaxFunctionEvaluations',100000,'MaxIterations',100000)
input_sol ← cell(length(tspan), 1)
for t ← 1 to length(tspan) do
    [sol, fval, exitflag, output] ← fmincon(@objectiveFunction, input0,
     A, b, [], [], lb, ub, @constr, options)
    input_sol{t} ← sol
    input0 ← sol
end
```

evolve.

Genetic Algorithm

GA is a stochastic search and optimization technique inspired by the natural selection process as described in evolutionary biology. GAs are particularly well-suited for solving complex optimization problems that are otherwise challenging for traditional, deterministic algorithms. They are characterized by their ability to explore a large search space searching for the global optima. The essence of a GA lies in its simulation of the evolutionary process, where potential solutions to an optimization problem are encoded as a set of individuals in a population. These individuals undergo processes analogous to biological evolution, including selection, crossover (recombination), and mutation. The algorithm proceeds as follows:

1. **Initialization:** Generate an initial population of random solutions.
2. **Evaluation:** Assess the fitness of each individual in the population.
3. **Selection:** Select individuals based on their fitness levels to participate in breeding the next generation.
4. **Crossover:** Combine pairs of individuals to produce new offspring, promoting the exchange of genetic material.
5. **Mutation:** Apply random changes to new offspring, aiming to introduce variability into the population.
6. **Replacement:** Replace some of the older generation with the new generation of offspring.
7. **Termination:** Repeat the process until a termination criterion is met, such as a maximum number of generations or a satisfactory fitness level.

One of the key advantages of GA is their robustness and ability to escape local optima, making them highly effective for problems where other optimization techniques fail. They are also inherently parallel, which allows for efficient implementations on modern multi-core processors or distributed systems. However, GAs also have limitations. Their stochastic nature means that convergence to the optimal solution cannot be guaranteed. The performance of a GA can be highly sensitive to its parameter settings, including population size, mutation rate, and crossover rate. Additionally, GAs may require a large number of function evaluations to find a sufficiently good solution, which can be computationally expensive.

This algorithm is successfully implemented in MATLAB using the "Global Optimization Toolbox". A genetic algorithm is implemented moving all the constraints to be a nonlinear inequivalent one in @constr, all the equivalent and linear constraints are not accepted (A,b,ceq) in the case of the system model optimization. The `optimoptions` function is utilized to set options for the GA, such as a large `PopulationSize` of 100,000 to enhance genetic diversity and a `MaxGenerations` limit of 10,000 to define the search depth. The display is set to 'iter' for detailed generation updates, no plotting function is employed to simplify output, and parallel execution is enabled to speed up computations by leveraging multi-core or distributed systems. The GA solves the optimization by defining the objective function inline to include parameters like `tspan` (time vector), and specifying the number of variables (`nvars=14`). It also sets lower (`lb`) and upper bounds (`ub`) from Table 3.2, and applies a custom constraint function (`constr`). The optimization process yields the best solution (`sol`), its value (`fval`), an exit flag (`exitflag`), and detailed output about the algorithm's execution. This approach is particularly effective for complex, potentially multi-modal optimization challenges where traditional methods might be inadequate. Despite the higher robustness, this algorithm is very much slower than the SQP one, so to increase its speed "Parallel Computing Toolbox" is implemented to make the processors run the algorithm more efficiently. This is done by adding the code snippet «`'UseParallel',true`» in `optimoptions`. Notably, parallel computing could not be applied using the SQP algorithm because each solution is updated iteratively with the initial guess (`input0`) from the previous solution's time point. A potential workaround would be to implement SQP without iteratively updating the solutions. However, this modification led to a decrease in robustness. Specifically, the algorithm required more function evaluations, which compromised its efficiency. Despite enhancements to the GA within the Toolbox to improve its speed, it remained significantly slower compared to SQP. Additionally, the number of evaluations required for the objective function in GA is still higher than those required by SQP.

Algorithm 2: GA algorithm implementation using ga

```
Data: Objective function objectiveFunction, number of variables nvars, bounds lb, ub,
      tspan
Result: Optimized solution sol, function value fval, exit condition exitflag, and
        algorithm output output
options ← optimoptions('ga', 'PopulationSize', 100000, 'MaxGenerations',
 10000, 'Display', 'iter', 'PlotFcn', [], 'UseParallel', true)
[sol, fval, exitflag, output] ← ga(@objectiveFunction, nvars, [], [],
 [], [], lb, ub, @constr, options)
```

For the scope of this thesis, both of the algorithms have been used: SQP which is used in this chapter and Chapter 6 for iterative first guess-dependant optimization in time, and GA is used in Chapter 5 for multi-objective optimization analysis with fixed inputs in time. The chosen simulation period is 5 years of operations, corresponding to the real expected lifetime of the system. The primary objective is not to achieve pinpoint accuracy in predictions but rather to understand how the system behaves over time. By simulating over this 5-year horizon, long-term trends, performance, and potential issues can be observed, providing valuable insights into the system's dynamics and robustness.

4.3 Predictive analysis

This section presents an analysis of three different control strategies: fixed power, fixed voltage, and fixed temperature with values taken from the first operating condition steady state operation (Table 4.1) taken into account as non-linear quadratic objective functions to the algorithm shown below. The initial guess for the `fmincon` algorithm follows also the conditions of 1^{st} operating point, ensuring that the optimization starts from the first operating point conditions. Different analyses are done in the following paragraphs:

Table 4.1: Fixed operations target values for optimization algorithm, taken from the 1^{st} operating conditions

Target Voltage	45.71 V
Target Power	758.27 W
Target Temperature	1078.47 K

1. Standard operations: control strategies applied without optimization;
2. Degradation rate minimization analysis;
3. Electrical efficiency maximization analysis;
4. CHP efficiency maximization analysis;
5. Net operating income maximization analysis.

Notably, the aforementioned objective optimizations could be considered as control strategies on their own. However, due to the limitations of the SQP algorithm, which is highly dependent on the initial system guess, the system simulation cannot be analyzed using only these optimizations. To ensure reliable results, the analysis is conducted under fixed operational conditions, avoiding the complications of finding a global optimum with SQP algorithm. It is also important to mention that the system simulation and optimization are always conducted under the condition of **safety of operation**, ensuring that each variable remains within the constraint limits presented in Table 3.2.

4.3.1 Standard operations analysis

The results are visualized through a series of plots (Figure 4.2), providing insights into the behavior of various system parameters over a simulated period of 5 years with 50000 points in total taken into account by `fmincon` algorithm:

$$
\begin{array}{ll}
\underset{u}{arg\ \text{minimize}} & (Variable - Target)^2_{U_{stack}/T_{stack}/P_{sys}} \text{ per each t in time} \\
\text{subject to} & 650 \leq T_{cpox} \leq 850\,^{\circ}\text{C} \\
 & 650 \leq T_{stack} \leq 865\,^{\circ}\text{C} \\
 & 40 \leq U_{stack} \leq 60\,\text{V} \\
 & 700 \leq T_{burner} \leq 1050\,^{\circ}\text{C} \\
 & 25 \leq T_{startup} \leq 700\,^{\circ}\text{C} \\
 & 100 \leq T_{hex,hot} \leq 700\,^{\circ}\text{C} \\
 & 650 \leq T_{air,mix} \leq 850\,^{\circ}\text{C} \\
 & 650 \leq T_{hex,cold} \leq 860\,^{\circ}\text{C} \\
 & 25 \leq T_{whex,hot} \leq 320\,^{\circ}\text{C} \\
 & 25 \leq T_{whex,cold} \leq 60\,^{\circ}\text{C} \\
 & FU \leq 0.8 \\
 & AU \leq 0.25 \\
 & CO \leq 0.95 \\
 & 0.1 \leq W_{CH_4} \leq 1 \\
 & 0.1 \leq W_{air,cpox} \leq 0.8 \\
 & 0.1 \leq W_{air,stack} \leq 0.8 \\
 & 0.1 \leq W_{H_2O} \leq 1 \\
 & 0.001 \leq V_{ratio} \leq 0.45 \\
 & 0.1 \leq I \leq 24\,\text{A}
\end{array}
$$

Fixed power control strategy

In this section, the metrics obtained by fixed power control strategy are analyzed, based on Figures 4.2a-d.

This kind of strategy involves three different main phases, that can be distinguished by two different points in which the slope of each variable plot in time drastically changes. These drastic changes in behavior are due to system constraints bound touching and algorithm re-adaptation escaping local minimum; in fact, the SQP algorithm is occasionally trapped in local minima, as illustrated in Figure 4.3. This occurs due to the non-convex nature of the objective function. The SQP algorithm in `fmincon` is a local optimizer that refines the solution based on local gradients. Consequently, depending on the starting point, it may converge to nearby local minima. In the context of this strategy, this algorithm re-adaptation happens after 1.5 and 2.7 years of

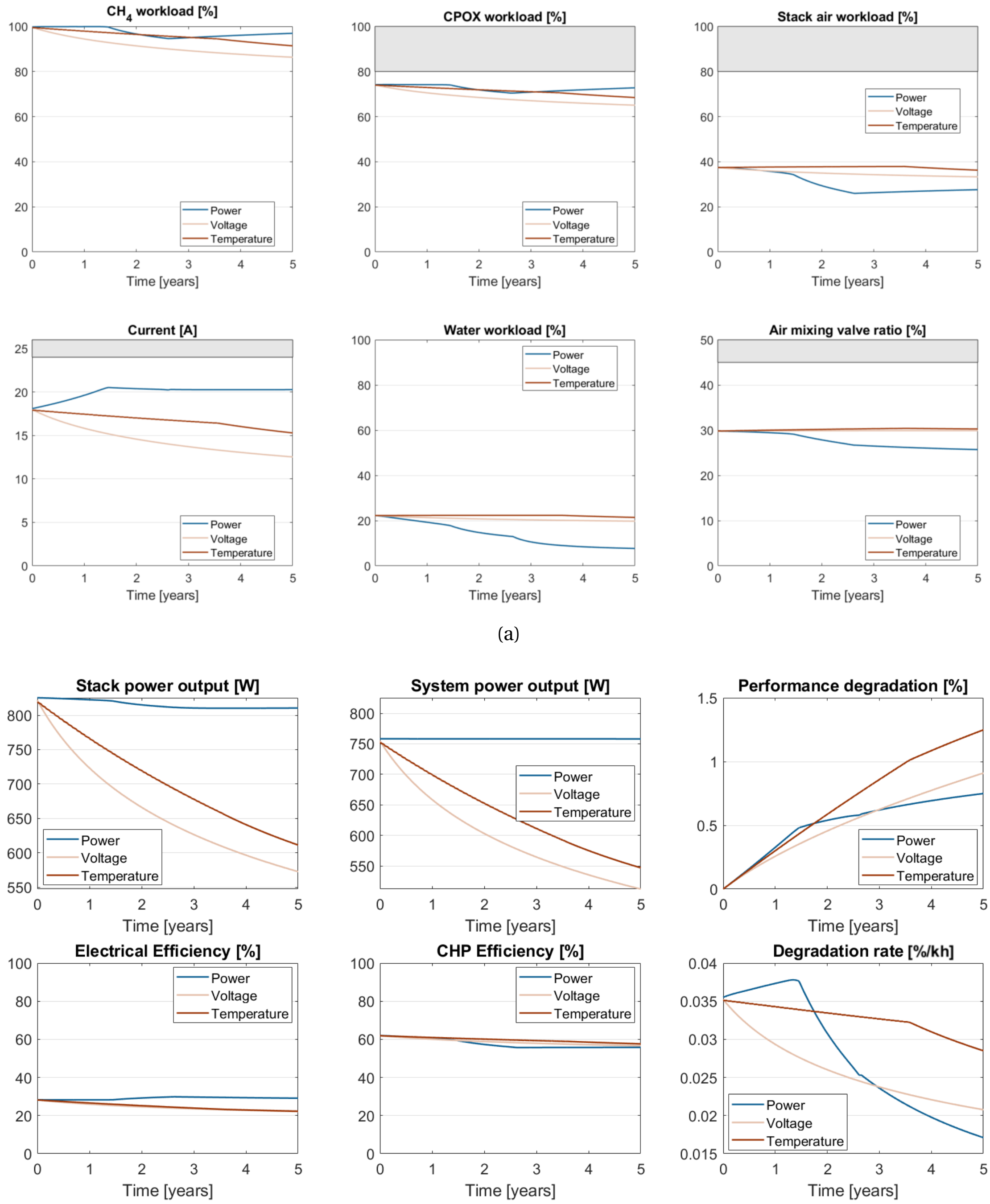

(a)

(b)

Figure 4.2: Optimization analysis results of the variation of the inputs (a), key indicators variation (b) with three different control strategies (fixed power,fixed voltage, fixed temperature)

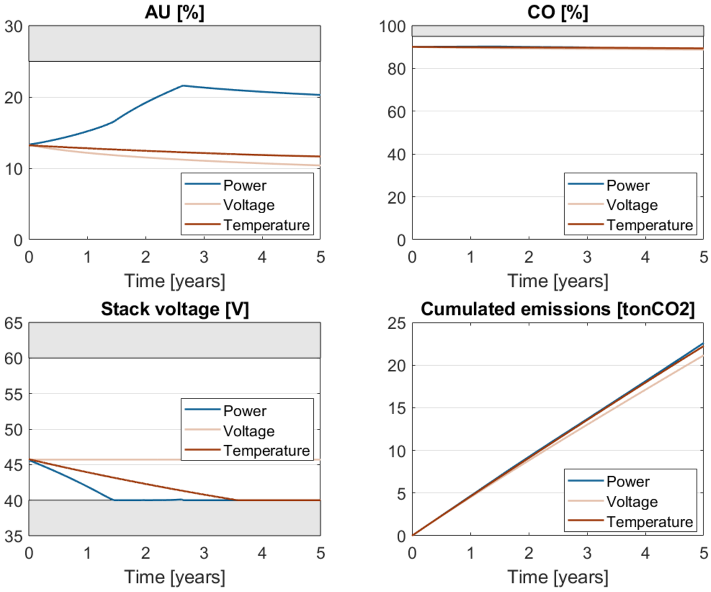

(c)

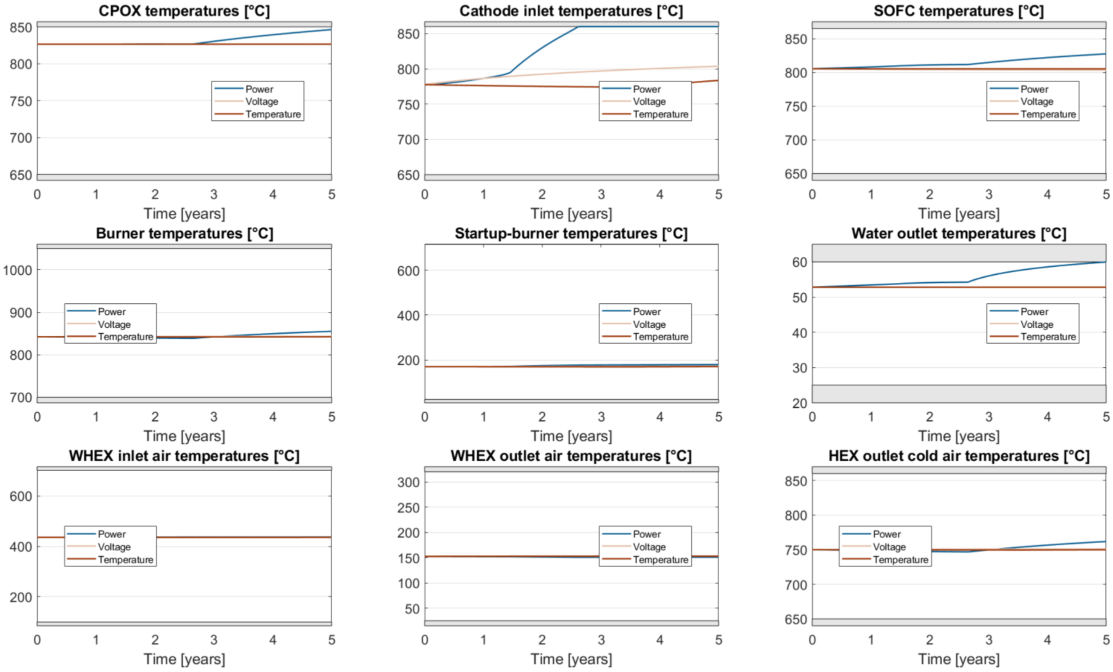

(d)

Figure 4.2: Optimization analysis key indicators variation (c), temperature variation (d) with three different control strategies (fixed power,fixed voltage, fixed temperature)

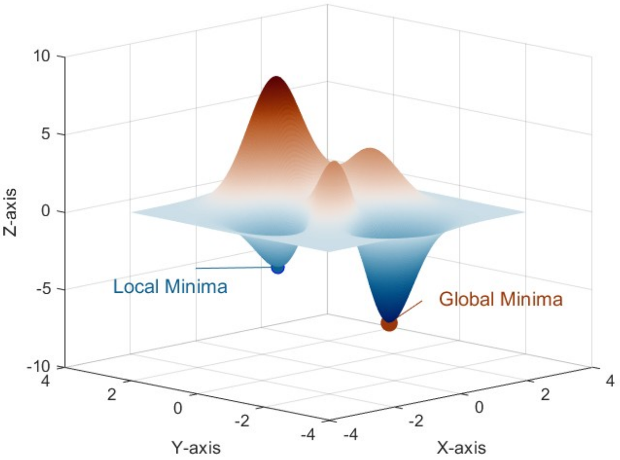

Figure 4.3: Local minima SQP algorithm problem

operations.

In the first phase of operation (from 0 to 1.5 years), the methane blower workload is fixed to the maximum from initial guess conditions, implying a constant fuel flow rate inside the CPOX reactor to maintain fixed system power, crucial for steady-state operation. The same consideration is valid for the CPOX air blower workload and so the temperature of the CPOX (825°C) and the CO (90%) remain unchanged in this phase. The current profile is increasing over time, from a target value above 20 A to compensate for the decrease in the voltage of the cell (from target to 40 V). This leads to an increase in degradation rate passing from 0.035 to 0.0375 %/kh which is the highest obtained in these years of operations among the three strategies and a decrease in the stack power output due to the higher losses. Degradation also leads to a slight increase in stack temperature. The stack air blower workload instead, is slightly decreasing, together with the air mixing valve ratio, ensuring less air mass flow rate and slightly increasing cathode inlet temperature inside the stack. Therefore, AU is increasing over time reaching 17%, also thanks to the increased current that leads to higher H_2 reacted and lower oxygen moles at the cathode outlet. FU is also increasing due to the increasing current reaching 65%. Water workload is slightly decreasing over time, causing a slight increase in water outlet temperature to reduce its power consumption. The unmentioned temperatures remained constant over time.

In the second phase of operation (from 1.5 to 2.7 years), the lower bound of voltage is touched, which causes an algorithm re-adaptation. This consists of a sudden decrease in methane blower workload, and CPOX blower workload, and the current to stop increasing and start a very slight decrease over time. This is caused by the degradation impact on voltage, which has reached the lower bound and cannot decrease more: at equal conditions, degradation decreases stack voltage, so to compensate for this decrease the system starts to increase the temperature inside the stack to decrease both the ASR and degradation rate while slightly increasing the OCV voltage. This double action prevents the voltage from decreasing more fixing it to 40 V. The stack temperature is increased mainly thanks to the cathode inlet air temperature increase given the lower workload of the air blower decrease useful also from the point of view of power consumption reduction. The valve opening ratio is still decreasing, to better control the temperature avoiding a too-hard increase. Notably, the electrical efficiency is increasing, and CHP efficiency is slightly decreased, due to the lower heat exchanged in WHEX. FU is slightly increasing, due to the lower methane flow rate and constant current, AU is also increasing due to the lower air flow rate in the cathode.

In the last phase of operation (2.7 to 5 years) the upper bound of CPOX temperature is touched, causing another algorithm re-adaptation. The major difference from now on is the increasing behavior of methane blower workload, and cpox air blower workload, stack air blower workload with a still constant current to accomplish the system target power. This is done to both maintain a constant cathode inlet temperature thanks to an almost fixed valve opening ratio, indirectly decreasing AU and maintaining a constant FU, and to increase CPOX temperature to still increase the stack temperature in such a way to increase OCV voltage and decrease ASR and degradation rate impact on performances. Water workload is reduced even more, increasing the water outlet temperature in order to further reduce the power consumption.

The performance degradation thanks to this strategy reaches is minimum among the others. Notably, the cumulated emissions in this strategy are the highest among the three scenarios.

Fixed voltage control strategy

The fixed voltage control strategy demonstrates stability, with no changes in slope or boundary violations. In this scenario, the applied current tends to decrease over time to maintain a fixed voltage. This decrease is exponential rather than linear, primarily due to the dual effect of current on both the ASR and the degradation rate, which together reduce voltage losses. The water pump workload remains nearly constant and is set to an initial value, as it is relatively independent of this analysis. Similarly, the air mixing valve ratio is fixed. The workloads for the methane blower, CPOX air blower, and cathode air blower all decrease over time. These three variables directly impact the SOFC mass balance, thereby influencing the OCV. For example, if constant flow rates are maintained while the current decreases exponentially, the amount of hydrogen reacting also decreases exponentially. This reduces the oxygen concentration at the cathode outlet and the hydrogen concentration at the anode inlet, leading to a decrease in OCV voltage. All these inputs decrease cause an exponential decrease also in stack and system power output and a slight decrease in both stack and CHP efficiency, the latter mainly due to the stack efficiency decrease. The degradation rate with current is exponentially decreasing but the overall performance at the end of the 5-year operations appears to be more degraded concerning the fixed power control strategy, despite having less CO_2 emissions. Regarding temperatures they are all constant except for the cathode inlet one which is increasing due to the air flow rate decrease in time, reaching a maximum of 800 °C.

Fixed temperature control strategy

The fixed temperature control strategy has an overall behavior similar to the fixed voltage one. There are two main phases in the shape of each variable's plot in time due to voltage lower bound touching after 3.5 years of operations.

The primary distinction of this strategy from others lies in maintaining nearly constant valve opening ratios and stack air workload, which stabilizes the cathode inlet temperature over time. Unlike other strategies, there is no need to adjust for degradation impacts because the temperature is mainly influenced by energy balance management. All system temperatures are kept constant, except for the cathode inlet temperature, which starts to rise after 3.5 years due to a reduced workload of the stack air blower. As time progresses, the workload for the current, methane blower and cpox air blower decreases. This is due to the SOFC's energy balance, which causes an increase in the total enthalpy difference between the inlet and outlet. This enthalpy difference compensates for the reduced power output, as all temperatures remain constant. This is the only way to make the system maintain a constant temperature inside the stack to compensate for degradation behavior.

In the second phase, there is a slight decrease of stack air blower to increase cathode inlet temperature that numerically has an impact on the stack inlet temperature, without affecting the outlet one that is maintained constant in this optimization. Increasing the inside temperature is useful to reduce the ASR and degradation rate to compensate for the voltage decrease.

The degradation rate, as expected, linearly decreases according to the current profile. However, the degradation of performance experienced in this case results in the highest among the three strategies. The total emissions are in between the ones of the other two cases. CHP efficiency is the highest among the three cases, while electrical efficiency is the lowest one due to the worst stack current-voltage management among the three strategies. AU slightly decreases, and FU is almost constant except for the last phase after 3.5 years by which starts decreasing and CO is set to 90&.

EoL Metrics

In this section, the EoL metrics of the system are analyzed based on Figures 4.4a-c. These figures illustrate the stack power output, voltage, cumulative energy, and system power over time under fixed power, fixed voltage, and fixed temperature conditions.

Across all conditions—fixed power, fixed voltage, and fixed temperature—the cumulative energy EoL threshold is never reached, indicating that the system continues to produce energy efficiently over the 5 years. In the fixed power condition (Figure 4.4a), the cumulative energy continues to increase steadily over time, demonstrating the system's ability to generate energy efficiently despite degradation. In the fixed voltage condition (Figure 4.4b), the cumulative energy increases consistently, indicating continuous energy production capability. In the fixed temperature condition (Figure 4.4c), the cumulative energy increases steadily, reflecting sustained energy production over time. Comparing the final cumulative energy values under these conditions, the fixed voltage condition shows the highest final cumulative energy value at around 34,000 kWh, followed closely by the fixed temperature condition with slightly over 32,000 kWh, and the fixed power condition at approximately 32,000 kWh.

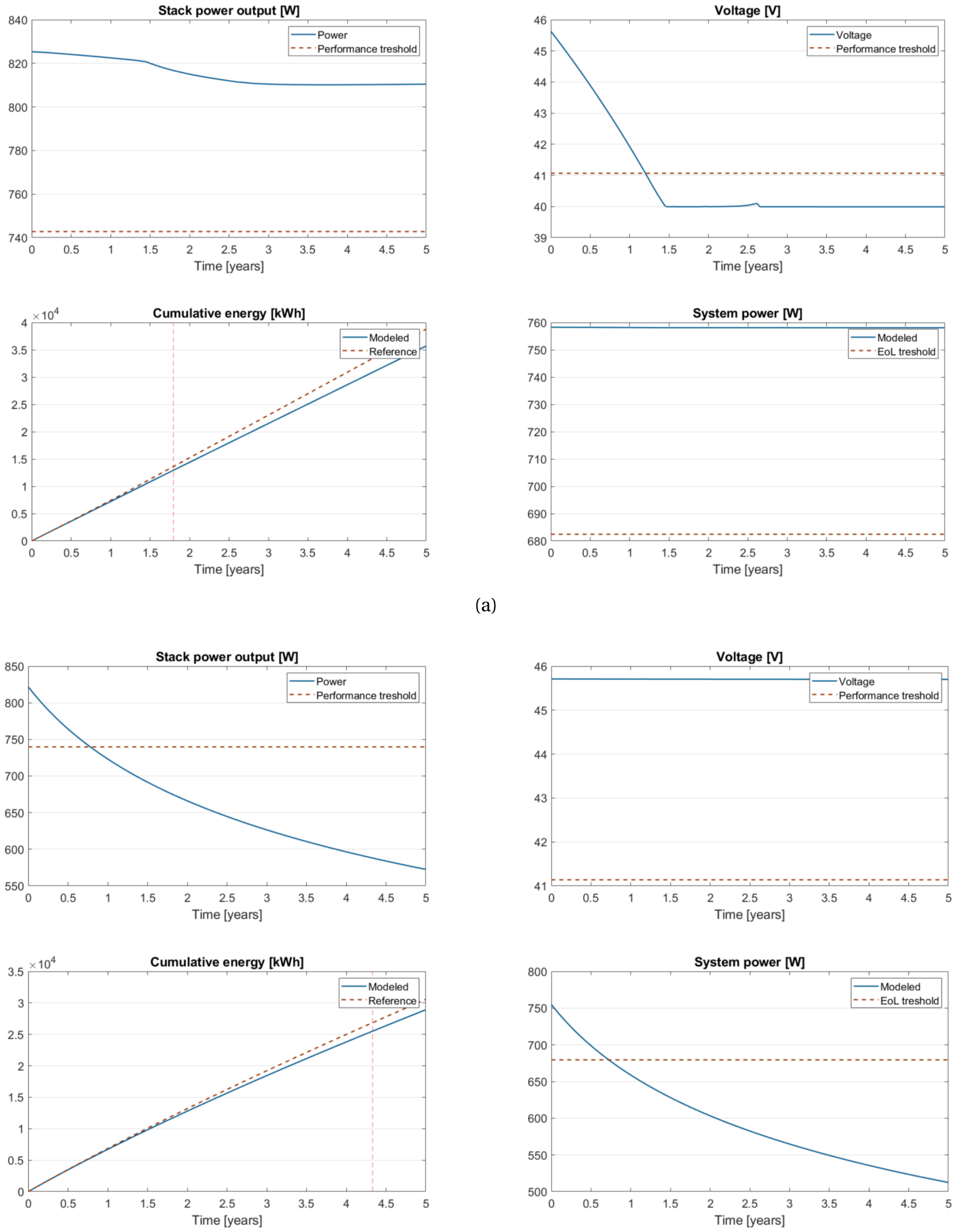

(a)

(b)

Figure 4.4: Optimization analysis EoL evaluation, with fixed power (a) and fixed voltage (b)

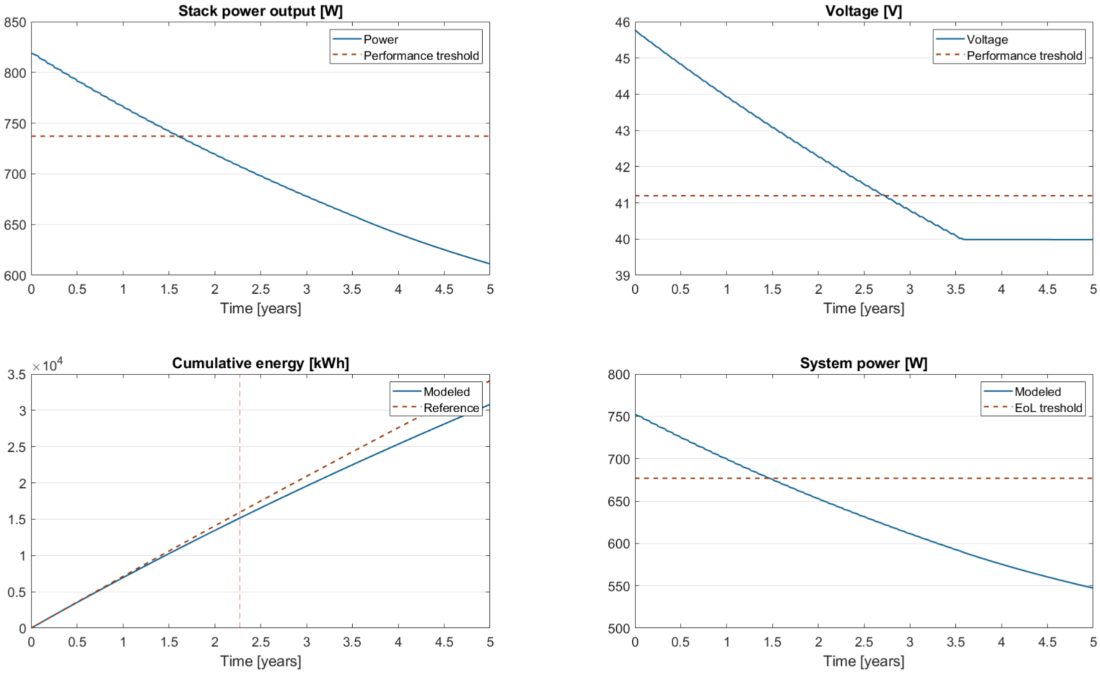

(c)

Figure 4.4: Optimization analysis EoL evaluation, with fixed temperature (c)

The actual hours of EoL thresholds for different conditions are summarized in Table 4.2. The EoL thresholds indicate distinct performance and longevity characteristics for each condition. The fixed temperature condition shows the highest EoL thresholds overall, indicating a longer life expectancy under stable thermal conditions. The fixed voltage condition, despite having the highest cumulative energy threshold (37,919 hours), has a shorter life expectancy for other metrics due to the accelerated degradation of system components. The fixed power condition falls between the other two, offering a balanced approach with moderate EoL thresholds but the lowest cumulative energy threshold of 15,712 hours. Overall, while fixed temperature conditions provide the longest lifespan in terms of voltage and power, the fixed voltage condition excels in cumulative energy output.

Table 4.2: EoL thresholds for fixed power, voltage, and temperature conditions.

Condition	EoL Type	Hours
Fixed Power	Voltage loss	10,533
	Power loss	-
	System power loss	-
	Cumulative energy	15,712
Fixed Voltage	Voltage loss	-
	Power loss	6,846
	System power loss	6,408
	Cumulative energy	37,919
Fixed Temperature	Voltage loss	23,875
	Power loss	14,044
	System power loss	12,903
	Cumulative energy	19,925

4.3.2 Minimization of degradation rate analysis

This section presents a similar analysis to the first one, maintaining a largely unchanged algorithm structure. However, it now incorporates three different approaches: fixed power, fixed voltage, and fixed temperature. These parameters are shifted from the objective function to nonlinear equivalent constraints. The specific values for these fixed parameters are the same as those in Table 4.1. The goal of the new algorithm is to impose degradation minimization. This is done using the degradation rate that is the same as Formula 3.35 but without the time-dependency:

$$obj : D_{rate} = \frac{0.500 \cdot FU + 0.876}{1 + \exp\left(\frac{T-1089}{22.920}\right)} \left(\exp\left(0.3 \cdot j\right) - 1\right) \tag{4.8}$$

where FU is the fuel utilization, j is the current density in A/cm^2, and T is the mean logarithmic temperature inside the stack.

The results are visualized through a series of plots. For brevity, all the plots are shown in Appendix A.3. These plots provide insights into the behavior of various system parameters over a simulated period of 5 years, with 50,000 points in total considered by the `fmincon` algorithm. The following paragraphs are written with the same structure as already done in the previous analysis.

Fixed power control strategy

In this section, the metrics obtained by fixed power control strategy are analyzed. This strategy involves two different main phases, that can be distinguished by a single point in which the slope of each plotted variable in time drastically changes. In the context of this strategy, this algorithm re-adaptation happens after 2.9 years of operations.

In the first phase of operation (from 0 to 2.9 years), the methane blower workload is linearly increasing from 80% in conjunction with the CPOX air blower workload from 70%. This is done to minimize the degradation rate inside the stack, which from the start of the operations increases due also to the increase of the current profile. In this optimization, the cathode inlet temperature is fixed to the upper bound, thanks to the lower value of the stack air blower workload. Despite that, CPOX temperature which also has an impact on SOFC temperature increase and degradation minimization, is kept constant until 2.9 years. After that, the voltage lower bound is touched and so the voltage and current are kept constant by increasing CPOX temperature, directly affecting the degradation rate and reversing its profile that is now decreasing. The increase in CPOX temperature leads also to a drastic increase in SOFC stack temperature, burner temperature, and outlet HEX air cold side temperature. Also water pump workload starts to decrease to compensate the its power consumption, causing the increase of water outlet temperature. Notably, concerning standard operation here the degradation rate order of magnitude is 30% lower in each of the strategies. Another interesting fact is that a fixed power control strategy also has both the best electrical efficiency and CHP efficiency of the system, with good power production despite the highest degradation of performances in time. This strategy has the highest CO_2 emissions among the others.

Fixed voltage control strategy

The fixed voltage control strategy demonstrates stability, with no changes in slope or boundary violations and it is found to be very similar to the standard case with some little differences. In this scenario, the applied current tends to decrease over time to maintain a fixed voltage. This decrease is exponential rather than linear, primarily due to the dual effect of current on both the ASR and the degradation rate, which together reduce voltage losses. The water pump workload remains nearly constant and is set to an initial value, as it is relatively independent of this analysis. Similarly, the air mixing valve ratio is fixed. The workloads for the methane blower, and CPOX air blower all decrease over time. These two variables directly impact the SOFC mass balance, thereby influencing the OCV. For example, if constant flow rates are maintained while the current decreases exponentially, the amount of hydrogen reacting also decreases exponentially. This reduces the oxygen concentration at the cathode outlet and the hydrogen concentration at the anode inlet, leading to a decrease in OCV voltage. The main difference from the standard operation results is that the cathode air blower workload is very slightly increasing from a far lower value. This led to the optimization to fix the air cathode inlet temperature to be fixed to the upper bound while minimizing the degradation rate and achieving the same target voltage.

All the inputs decrease cause an exponential decrease also in stack and system power output and a slight decrease in both stack and CHP efficiency, the latter mainly due to the stack efficiency decrease. The degradation rate with current is exponentially decreasing and the overall performance at the end of the 5-year operations appears to be less degraded concerning the fixed power control strategy, with less CO_2 emissions. Regarding the unmentioned temperatures, they are all constant in time.

Fixed temperature control strategy

Fixed temperature control strategy has a very simple behavior fixing each variable in time. Due to the absence of any constraint on current and voltage besides the operational limits, the algorithm set the current to 7.5 A and the voltage fixed to 60 V with a very low power generated around 400 W. This ensures the algorithm minimizes the degradation rate, which reaches very its lowest values (0.007 %/kh) with almost no degradation of performances (0.35% ASR increase after 5 years). This is normally expected to happen on a system since it is always operating in part load, which for SOFC is more efficient. However, the low current makes the system losses very much impactant on the efficiency, due to the still high values of methane blower, air blowers, and water pump workloads, resulting in producing the lowest electrical and CHP efficiencies among the three cases.

EoL Metrics

In this section, the EoL metrics of the system are analyzed based on Figures in Appendix A.3. These figures illustrate the stack power output, voltage, cumulative energy, and system power over time under fixed power, fixed voltage, and fixed temperature conditions.

Table 4.3: EoL thresholds for fixed power, temperature, and voltage conditions minimizing degradation.

Condition	EoL Type	Hours
Fixed Power	Voltage loss	20,013
	Power loss	-
	System power loss	-
	Cumulative energy	28,790
Fixed Voltage	Voltage loss	-
	Power loss	11,235
	System power loss	10,445
	Cumulative energy	-
Fixed Temperature	Voltage loss	-
	Power loss	-
	System power loss	-
	Cumulative energy	-

Across conditions of fixed voltage and fixed temperature the cumulative energy EoL threshold is never reached, indicating that the system continues to produce energy efficiently over the 5 years. Comparing the final cumulative energy values under these conditions, the fixed power condition shows the highest final cumulative energy value at approximately 35,500 kWh, followed by the fixed voltage condition at around 31,000 kWh, and the fixed temperature condition at approximately 20,000 kWh.

The actual hours of EoL thresholds for different conditions are summarized in the table below: The fixed temperature condition shows the highest EoL thresholds, indicating a longer life expectancy under these conditions, mainly due to the part load operations. In contrast, the fixed voltage condition has the shortest life expectancy based on the EoL thresholds, likely due to the higher performance in terms of energy supplied. The fixed power condition falls in between, with an EoL threshold that is higher than that of the fixed voltage condition but lower than that of the fixed temperature condition. The differences between the Table 4.2 values and Table 4.3 values obtained from the algorithm that minimizes degradation, thus maximizing expected lifetime, are significant. The new values reflect an optimization in the system's operational parameters to reduce degradation and extend the lifespan. This optimization algorithm has increased the EoL thresholds substantially compared to the initial values, demonstrating its effectiveness in prolonging the system's life expectancy and maintaining efficient energy production over an extended period.

4.3.3 Maximization of electrical efficiency analysis

This section presents a similar analysis to the last one, using the same specific values for the fixed parameters Table 4.1. The goal of the new algorithm is to impose electrical efficiency maximization. This is done using the efficiency computed per each iteration as:

$$obj : \eta_{el} = \frac{P_{sys}}{P_{in}} \tag{4.9}$$

where η_{el} is the electrical efficiency, P_{sys} is the system power, and P_{in} is the introduced chemical power.

The results are visualized through a series of plots. For brevity, all the plots are shown in Appendix A.4. These plots provide insights into the behavior of various system parameters over a simulated period of 5 years. The `fmincon` algorithm considered 60,000 points in total, which is 10,000 more than the other algorithms, to increase resolution due to the more constrained optimization problem. The following paragraphs are written with the same structure as already done in the previous analysis.

Fixed power control strategy

In this section, the metrics obtained by the fixed power control strategy are analyzed. This strategy involves two different main phases, that can be distinguished by a single point in which the slope of each plotted variable in time drastically changes. In the context of this strategy, this algorithm re-adaptation happens after 2 years of operations. The main concern about electrical efficiency maximization is to minimize the power losses, given by cathode air blower, CPOX air blower, methane blower loss, and water pump.

In the first phase of operation (from 0 to 2 years), the methane blower workload is linearly increasing from 92% in conjunction with the CPOX air blower workload from 68%. This is done to maximize electrical efficiency increasing FU. Electrical efficiency from the start of the operations is kept almost constant during operation to 32 %. In this optimization, the cathode inlet temperature is fixed to the upper bound, thanks to the lower value of stack air blower workload maximizing its impact on degradation decrease. However, this is mainly due to reduce the power loss produced by the cathode air blower consumption. After the 2 years, the voltage lower bound is touched and so the voltage and current are kept constant by increasing CPOX temperature, directly affecting the degradation rate and reversing its profile that is now decreasing. The increase in CPOX temperature leads also to a drastic increase in SOFC stack temperature, burner temperature, and outlet HEX air cold side temperature. The water pump workload is always kept to a minimum to reduce power losses. Notably, the fixed power control strategy ensures the worst electrical efficiency and CHP efficiency of the system, despite its good power production and the half-way degradation of performances in time to the other two strategies. This strategy has the lowest CO_2 emissions among the others.

Fixed voltage control strategy

The fixed voltage control strategy in this optimization analysis presents two main changes in slope, due to local minima escaping from the SQP algorithm: the first one is experienced after 1-year operations, where the algorithm is struggling to maintain the voltage fixed in time and so it slightly changes the operating conditions to increase it a little recovering the 1-year voltage lost; the second change in slope is experienced after CPOX temperature upper bound touching.

In the first part from 0 to 1 year operations, the methane blower workload and the cpox air blower workload are decreasing slightly from 93% and 71% respectively. These two variables directly impact the SOFC mass balance, thereby slightly increasing the OCV. Also current is decreasing to compensate for the voltage ASR losses and degradation impact on performances. FU is below 60% which is the lowest one among the three strategies, AU is exponentially decreasing from 19 % and CO is fixed to 90%. Water workload and cathode air workload are very low, to minimize power losses, fixing cathode inlet air temperature and water outlet temperature to the upper bound. Other temperatures are only slightly increasing. After 1 year of operation, there is a step in almost all the variables plots in time: methane blower workload bounces to 99.95%, CPOX air blower workload bounces to 75% and it is maintained fixed in time, stack air blower workload bounces to 30%, current bounces to 18.5 A, air mixing valve drops down to 25%. This led to an overall increase in power production and a very drastic decrease in degradation rate, due to the high SOFC temperature bounce to 840°C, led by the CPOX temperature bounce increase to the upper bound. This increase in temperatures is also reflected by the burner, and HEX air outlet temperature from the cold side. After 1 year of operation the SQP algorithm, after struggling to maintain the voltage constraint fixed to the target, rearrange the variables changing the operating conditions, leading to another one with higher CO_2 emission and lower performance degradation. The last change in shape it is also considered as an operating conditions change due to local minimum escaping with the main result of fixing the methane blower workload to the upper bound.

Thanks to the first bounce in manipulated variables, the fixed voltage control strategy reaches values of degradation rate of 0.08% resulting to be the least degraded scenario among the others.

Fixed temperature control strategy

The fixed temperature control strategy shows significant variability in its variables, primarily due to the methane blower workload frequently reaching its upper bound. This challenge occurs within the first 0 to 0.7 years as the algorithm struggles to stay within limits. At the 1-year mark, the primary change in the slope of the variables is attributed to the voltage reaching its lower bound.

Overall, this strategy starts with very high current values that decrease over time, almost reproducing the same behavior of standard operations, while maintaining higher values and with some differences. After 1 year, there is a bounce to higher current values, but the overall decreasing trend continues. The cpox air blower workload exhibits a similar pattern. Voltage begins at very low values (around 42 V) and continues to decrease until the 1-year mark, after which it remains fixed. Initially, the methane blower workload is set to its maximum and starts decreasing after 1 year. The high initial values are intended to maintain a fixed stack temperature while minimizing the system's power consumption, especially for the water pump and cathode air blower, which are the most power-intensive components. The workloads of these components are minimized, except after 1 year when the water pump workload increases. This increase is offset by a significant jump in the valve opening ratio, which then reaches its upper bound.

In this case, the highest electrical efficiency is reached 37% and also the highest CHP efficiency is 68%, with still the lowest CO_2 emissions at the end of the 5 years of operation. However, the degradation of performance of this control strategy is the highest among the three cases.

Table 4.4: EoL thresholds for fixed power, temperature, and voltage conditions maximizing electrical efficiency.

Condition	EoL Type	Hours
Fixed Power	Voltage loss	14,332
	Power loss	-
	System power loss	-
	Cumulative energy	22,814
Fixed Voltage	Voltage loss	-
	Power loss	-
	System power loss	-
	Cumulative energy	-
Fixed Temperature	Voltage loss	-
	Power loss	16,087
	System power loss	15,282
	Cumulative energy	22,668

EoL Metrics

In this section, the EoL metrics of the system are analyzed based on Figures in Appendix A.4.

In fixed voltage conditions the cumulative energy EoL threshold is never reached, indicating that the system continues to produce energy efficiently over the 5 years. Comparing the final cumulative energy values under these conditions, the fixed power condition shows the lowest final cumulative energy value at approximately 35,000 kWh, followed by the fixed voltage condition at around 36,000 kWh, and the fixed temperature condition at approximately 36,000 kWh.

The actual hours of EoL thresholds for different conditions are summarized in Table 4.4. The fixed voltage condition shows the highest EoL thresholds, indicating a longer life expectancy under these conditions, that is a very interesting result since the cumulated energy is also quite high. In contrast, the fixed temperature condition has the shortest life expectancy based on the EoL thresholds, likely due to the higher performance in terms of energy supplied. The fixed power condition falls in between, with EoL thresholds higher than that of the fixed voltage condition but lower than that of the fixed temperature condition.

4.3.4 Maximization of CHP efficiency analysis

This section presents a similar analysis to the last one, using the same specific values for the fixed parameters Table 4.1. The goal of the new algorithm is to impose CHP efficiency maximization. This is done using the efficiency computed per each iteration as:

$$obj : \eta_{CHP} = \frac{P_{sys} + P_{H_2O}}{P_{in}} \tag{4.10}$$

where P_{sys} is the power produced at system level, P_{H_2O} is the power produced by the WHEX, P_{in} is the chemical power of the methane consumed.

The results are visualized through a series of plots. For brevity, all the plots are shown in Appendix A.5. These plots provide insights into the behavior of various system parameters over a simulated period of 5 years. The `fmincon` algorithm considered 100,000 points in total, which is 50,000 more than the other algorithms, to increase resolution due to the more constrained optimization problem. The following paragraphs are written with the same structure as already done in the previous analysis.

Fixed power control strategy

In this section, the metrics obtained from the fixed power control strategy are analyzed. This strategy involves three main algorithm bounces and re-adaptations to escape local minima. The first bounce occurs due to the voltage touching its lower bound, while the subsequent bounces are due to the fixed system power constraint. These bounces are reflected in most of the variables plotted over time.

The primary difference between this strategy and other optimizations is that the methane blower workload is consistently fixed at its upper bound. In contrast, the CPOX air blower workload is not at its maximum and increases over time. This approach ensures the achievement of target power over time by providing more flexibility in energy balances, thereby maximizing the heat exchanged in the water HEX. This is achieved by increasing the moles of hydrogen injected into the SOFC, with an almost constant FU over time, ensuring enough uncombusted fuel is burned in the afterburner. This increases the water HEX air temperatures and maximizes heat exchange. In this strategy, the water workload is slightly higher than in the other optimizations among the three strategies. This is due to its ability to both increase pump power losses and water heat exchange. Therefore, the algorithm finds a trade-off value. Meanwhile, the water outlet temperature is fixed to its upper bound, facilitated by a low cathode air blower workload. While the current is always increasing, the different bounces cause it to step down periodically. As a result, by the end of the 5-year operation, the current is almost at the same value as at the start-up. This current behavior is due to voltage and power corrections inside the SOFC. Notably, the bounces primarily affect temperatures: CPOX, cathode inlet, SOFC, burner, and HEX outlet (both cold and hot side) temperatures all increase with each bounce, with the cathode inlet and SOFC temperatures reaching their upper bounds. It is also notable that after the first bounce, the CO ratio reaches its upper bound. This occurs because the step-down bounce of the CPOX air blower workload results in less oxygen being injected.

In this case, electrical efficiency is the highest among the three cases, while the CHP efficiency is the lowest. Although the degradation rate starts at the highest value among the three strategies, it decreases significantly over time due to the different bounces. Consequently, the fixed power control strategy results in the least performance degradation.

Fixed voltage control strategy

The fixed voltage control strategy in this optimization analysis shows a minor change in slope at 0.6 years of operation, caused by the cathode inlet air temperature touching its lower bound. This strategy maximizes CHP efficiency by optimizing the water heat exchange while maintaining a fixed voltage over time. As expected, the current decreases exponentially over time to reduce

ASR losses and maintain the voltage target. The water pump workload is higher than in other cases, while the cathode inlet air blower workload increases slightly to keep the water outlet temperature at its upper bound. The methane blower workload is also fixed at its upper bound. In this strategy, the algorithm increases the number of total moles passing through the water heat exchanger to maximize heat exchange. However, this causes the cathode inlet air temperature to decrease until it reaches and stays at the lower bound. This decrease in cathode inlet air temperature could potentially lower the SOFC temperature, increasing degradation and making it harder to maintain a fixed voltage over time. Nonetheless, the SOFC temperature remains above 750°C due to the still high CPOX temperature, which slightly decreases over time.

In this analysis, the power output is not very high, decreasing from about 650 W to 450 W. This indicates that to maximize overall efficiency with a fixed voltage, it is best to utilize waste heat recovery. The degradation rate decreases exponentially according to the current profile, but it remains quite high. By the end of the 5-year operation, this strategy results in the most degraded performance. Electrical efficiency reaches its lowest value at 20%, while CHP efficiency is higher than in the fixed power case, reaching 73%.

Fixed temperature control strategy

Similarly to the degradation minimization objective, the fixed temperature control strategy also exhibits a simple behavior by maintaining each variable constant over time. With no constraints on current and voltage beyond operational limits, the algorithm sets the current to 11 A and fixes the voltage at 60 V, resulting in a low power generation of around 550 W, which is higher than 400 W in the minimized degradation case. The water pump workload is higher than in other cases, while the cathode inlet air blower workload increases slightly to keep the water outlet temperature at its upper bound. The methane blower workload is also fixed at its upper bound. This strategy maximizes CHP efficiency, which reaches its highest value at 74%, with a relatively low and constant degradation rate of 0.24%/kh. This is expected for a system operating in part load, as it is more efficient for SOFC. However, the low current makes system losses significantly impact stack efficiency (20%), due to the high workloads of the methane blower, air blowers, and water pump. CO2 emissions are almost the same across the three strategies, indicating that maximizing CHP efficiency results in relatively high emissions.

EoL Metrics

In this section, the EoL metrics of the system are analyzed based on the Figures in Appendix A.5. Across conditions of fixed voltage and fixed temperature, the cumulative energy EoL threshold is never reached, indicating that the system continues to produce energy efficiently over the 5 years, except for the fixed voltage case in which the EoL is reached after 16,853 hours. Comparing the final cumulative energy values under these conditions, the fixed power condition shows the highest final cumulative energy value at approximately 36,000 kWh, followed by the fixed temperature condition at approximately 27,500 kWh and the fixed voltage condition at around 24,000 kWh. The same considerations are valid also for other thresholds, except for voltage loss cases. The actual hours of EoL thresholds for different conditions are summarized in Table 4.5.

Table 4.5: EoL thresholds for fixed power, temperature, and voltage conditions maximizing CHP efficiency.

Condition	EoL Type	Hours
Fixed Power	Voltage loss	-
	Power loss	-
	System power loss	-
	Cumulative energy	-
Fixed Voltage	Voltage loss	-
	Power loss	4,389
	System power loss	3,687
	Cumulative energy	16,853
Fixed Temperature	Voltage loss	-
	Power loss	-
	System power loss	-
	Cumulative energy	-

Both fixed power and fixed temperature conditions show no EoL thresholds, indicating a longer life expectancy under these conditions, mainly due to the shallow current used for the fixed temperature scenario, showing that the best option, in this case, is to fix the power. In contrast, the fixed voltage condition has the shortest life expectancy based on the EoL thresholds, likely due to the higher average degradation rate looking at the energy supplied.

4.3.5 Maximization of Net Operating Income analysis

This section presents a similar analysis to the last one, using the same specific values for the fixed parameters Table 4.1. This paragraph uses an algorithm based on the previous ones that maximizes the system's net operating income, a parameter that is fully described in Section 3.5:

$$\text{obj: } OI_{net,tot} \text{ per each time iteration} \tag{4.11}$$

This choice is made to maximize the operating income of the system while minimizing its operating costs at the same time. The goal of developing this objective function is to assess whether this system operating point condition can be optimized to be profitable, which in Section 3.5 is found to be unprofitable for the operating conditions given by the first data set. The simulation is run over 10 years of operations, using 150,000-time points for high resolution due to the highly constrained level of the optimization problem. The simulation time here is doubled since the main aim of this chapter is to delve deeper into the profitability of the system regardless of the accuracy of prediction. The algorithm's results are presented in the plots in Appendix A.6.

General results discussion

When analyzing the input metrics, it is important to note that in each of the three cases, the algorithm initially shows a significant bounce as it escapes the local minima set by the initial operating condition parameters. Following this, the values of all input variables and their behaviors over time change significantly. For the fixed voltage and fixed temperature scenarios,

Table 4.6: EoL thresholds for fixed power, temperature, and voltage conditions maximizing net operating income.

Condition	EoL Type	Hours
Fixed Power	Voltage loss	3,771
	Power loss	-
	System power loss	-
	Cumulative energy	16,485
Fixed Voltage	Voltage loss	-
	Power loss	35,075
	System power loss	34,812
	Cumulative energy	-
Fixed Temperature	Voltage loss	-
	Power loss	5,963
	System power loss	5,700
	Cumulative energy	13,241

almost all input workloads decrease over time, including methane blower workload, air CPOX blower workload, current, and water pump workload. However, the stack air blower workload remains nearly constant at 35%, and the air mixing valve ratio stays at 45%. Notably, in the fixed temperature case, the current decreases from its upper bound, a point not reached in other optimizations, highlighting the significance of high current for this analysis. In the fixed power scenario, most parameters increase over time, except for the air mixing valve ratio, which remains fixed at 45%. Interestingly, the algorithm attempts to stabilize the current at around 20 A, which corresponds to achieving the minimum voltage of 40 V.

Regarding performance and temperature metrics, it is noteworthy that the algorithm aims to minimize voltage while maintaining the highest possible current. In each scenario, both electrical and CHP efficiencies decline over time, along with the stack and system power outputs. The fixed temperature case consistently exhibits the highest degradation rate. This is attributed to the relatively low temperature inside the stack compared to the fixed power case, even though the fixed power scenario maintains a higher current after five years of operation.

Regarding EoL metrics, the cumulative energy threshold is used to determine the stack's life expectancy for this analysis. These metrics align with the degradation rate results, indicating that the fixed voltage case has the highest life expectancy, followed by the fixed power case, and finally, the fixed temperature case (Table 4.6).

Profitability analysis

This analysis primarily examines the techno-economic aspects, as shown in Figure 4.5. The main finding is that it is possible to adjust the operating parameters from the initial dataset to achieve system profitability. Looking at Figure 4.5a after an initial adjustment to escape the local minimum, where costs exceed revenues, the net operating income becomes positive in each of the three scenarios, except for the fixed temperature scenario. The fixed temperature scenario remains consistently profitable from the beginning due to the high initial current input (24 A).

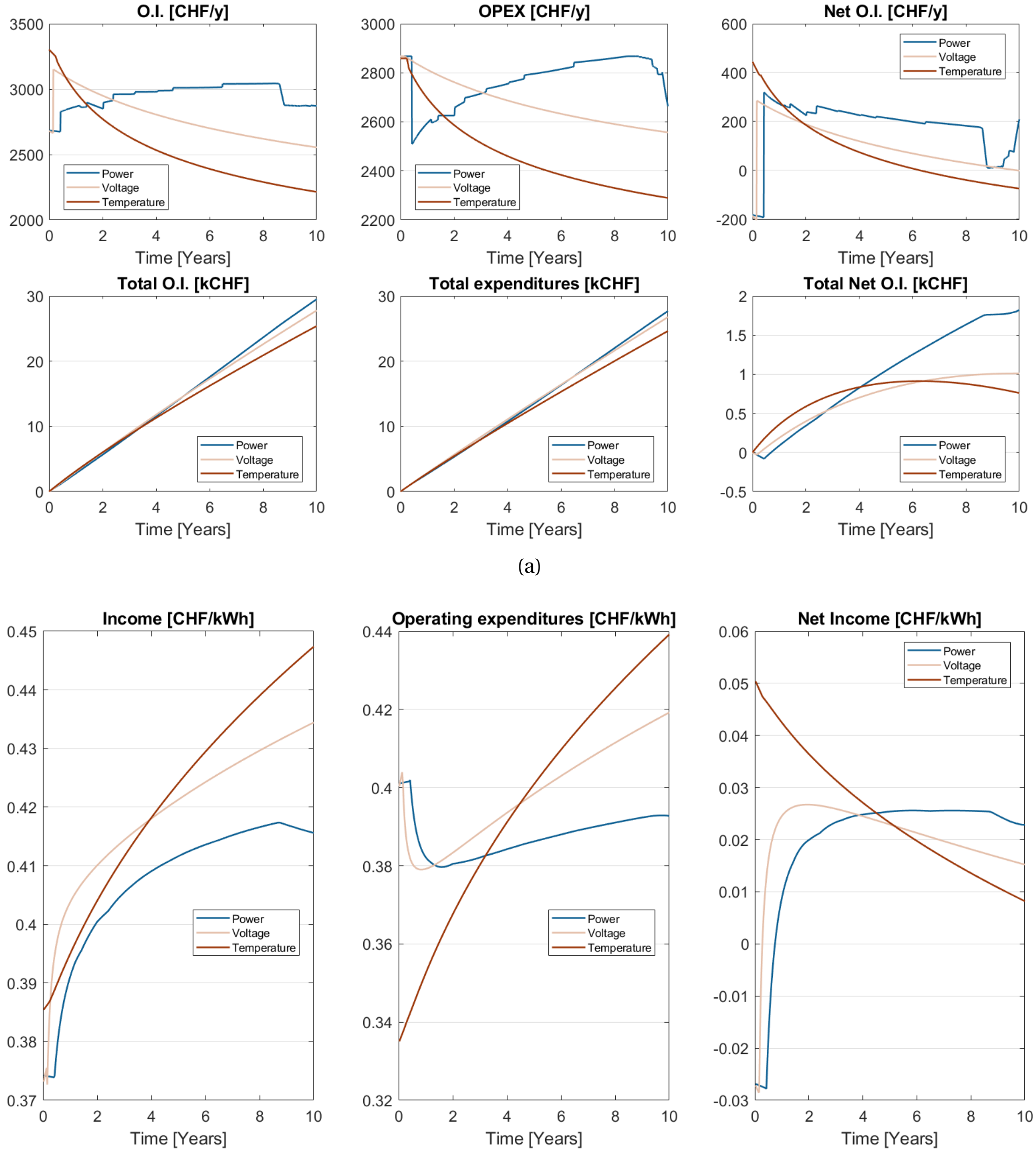

(a)

(b)

Figure 4.5: Optimization analysis maximizing Net Operating Income with fixed power, temperature, and voltage techno-economic results

In Figure 4.5b, the cumulative profitability indexes of the systems are presented, calculated by dividing the total cumulative values by the cumulative energy of the system in kWh. This results in income, operating expenditure, and net income indices expressed in CHF/kWh. These findings are valuable for assessing system performance and profitability. Notably, for the fixed power and voltage scenarios, there are two minima in the operating expenditure functions. In the fixed power scenario, these minima coincide with the cumulative energy detection at the EoL. Interestingly, the net income index for these scenarios starts negative, exhibiting a logarithmic behavior and stabilizing after two years at approximately 0.025 CHF/kWh. In contrast, the fixed temperature scenario shows a constant decrease in net income and a steady increase in operating expenditures, with no observed minima.

Thanks to this analysis, a final evaluation can be made regarding the Levelized Cost of Electricity (LCOE). The LCOE is a key metric for evaluating the economic viability of power generation technologies, representing the per-unit cost of building and operating a plant over its lifetime. LCOE helps compare the cost-effectiveness of different energy sources, considering all costs and energy output over the project's duration. It is essential for informed decision-making in energy investments and policy but can be complex due to various uncertainties and assumptions. In this analysis, the Levelized Cost of Energy (LCOE) primarily reflects the operating expenditure index. It is calculated as follows:

$$LCOE_{opt,stack} = \frac{\text{Stack Capital Cost + Operating Costs}}{\text{Total Energy Produced}} \approx 0.375 \text{ CHF/kWh} \tag{4.12}$$

Here, all cost and energy values are sourced from the EoL of the fixed power case, which demonstrates the highest energy production rate relative to the minimum operating expenditures within the system. The LCOE is calculated at the stack level because the total energy considered includes only the electrical energy produced by the stack. This can be considered a feasible result since another LCOE of another SOFC system in Switzerland is 0.285 CHF/kWh [112]. To put this in perspective, current LCOE values for various renewable energy technologies in Switzerland can be compared. According to recent data, the LCOE for utility-scale solar PV projects in Switzerland is approximately 0.10 CHF/kWh, and for onshore wind projects, it is about 0.08 CHF/kWh [113]. Notably, it's interesting to see that LCOE without optimization is:

$$LCOE_{st,stack} \approx 0.5734 \text{ CHF/kWh} \tag{4.13}$$

meaning that thanks to system optimization, the LCOE values are reduced in this case by 34%.

These values highlight the significant difference in LCOE between the SOFC system and other renewable energy technologies. This further reinforces the economic challenge that SOFC systems face in the current energy market, despite their potential technological benefits and advancements.

4.4 Discussion

This chapter explores the long-term prognostic analysis of a CPOX-SOFC system using the NMPC theory, focusing on enhancing the performance, efficiency, and longevity of SOFC systems.

The application of NMPC theory to this analysis demonstrates its effectiveness in managing nonlinear behaviors and operational constraints, which is crucial for optimizing temperature control, fuel utilization rates, and electrical load demands. The evaluation of the SoH of SOFC systems is emphasized as a critical aspect for ensuring reliability and extending the system's lifetime. Accurate SoH assessments enable early detection of degradation, facilitating optimal maintenance schedules and preventing critical failures. The chapter also discusses EoL criteria, with cumulative energy being a reliable indicator due to its monotonic behavior, particularly for dynamic mission profiles. Optimization algorithms, specifically SQP and GA, are evaluated for their ability to optimize the NMPC approach. Within the scope of this chapter, SQP is found to be more efficient and effective and thus is preferred. This last algorithm is applied to various scenarios, including fixed power, fixed voltage, and fixed temperature operations, to analyze their impact on system performance and longevity.

The results suggest that maintaining a fixed power generally results in higher degradation rates. However, it also leads to greater energy production and increased income. On the other hand, a fixed voltage approach is the most balanced, offering the highest life expectancy and optimal thermal balance. The fixed temperature method is the least balanced, with results varying significantly across different optimizations. This often results in very low degradation due to the application of very low current. More specifically, the analysis revealed:

- When no specific objectives are selected and the focus is solely on maintaining fixed values (power, temperature, and voltage), the results indicate that a **fixed voltage** approach yields the best life expectancy, followed by fixed temperature and fixed power approaches. Interestingly, the fixed power case exhibited the highest degradation rates in the short term but the lowest in the long term. Despite this, the overall energy produced by the fixed power approach is less than that of the fixed voltage approach, which also demonstrated a stable logarithmic degradation trend. Although this trend is slightly higher than that of the fixed power case, the average degradation value is lower. Additionally, the fixed voltage approach resulted in the lowest CO_2 emissions. Regarding efficiencies fixed power case showed the highest electrical one of about 2-3% difference, while the CHP efficiencies are almost the same across the scenarios.
- In the case of minimizing degradation, the fixed voltage approach demonstrated the highest life expectancy, followed by the fixed temperature and fixed power approaches. While the fixed temperature case exhibited the lowest degradation rate, its performance is also the lowest, primarily due to the very low current applied. The fixed power approach achieved the highest cumulative energy output. This analysis reveals that when minimizing degradation, a tradeoff must be made between maximizing cumulative energy and maximizing life expectancy. The **fixed power** approach achieves the former, while the **fixed voltage** approach achieves the latter which also achieves the lowest CO_2 emissions.
- In maximizing electrical efficiency, the fixed voltage approach demonstrated the best cumulative energy value over five years and the highest life expectancy, followed by fixed power and fixed temperature approaches. Interestingly, the fixed temperature approach achieved a cumulative energy value almost equal to the fixed voltage case. The fixed

voltage method also exhibited the best thermal balance and lowest CO_2 emissions. Regarding degradation, the fixed voltage case had the lowest value, followed by fixed power and fixed temperature. Notably, the fixed temperature approach achieved the highest CHP and electrical efficiencies. Ultimately, a tradeoff exists between degradation, energy production, and efficiencies. The **fixed temperature** approach emerged as the best overall, with high cumulative energy, good life expectancy, and the highest efficiencies.

- In maximizing CHP efficiency, the fixed power approach demonstrated the longest life expectancy, followed closely by the fixed temperature and then the fixed voltage approaches. In terms of cumulative energy, the fixed power approach led with the highest value, followed by fixed temperature and fixed voltage. The highest CHP efficiency is observed in the fixed temperature case at 76%, which also had the lowest electrical efficiency. The fixed power approach achieved the highest electrical efficiency at 32%, with a CHP efficiency of 70%. Regarding degradation, the fixed power approach had the lowest rate, followed by fixed temperature and fixed voltage. CO_2 emissions are similar across all conditions, while the fixed temperature approach provided the best thermal balance. Overall, the best trade-off is the **fixed power** approach, offering the lowest degradation, highest energy production, good CHP efficiency, and the highest electrical efficiency.
- In maximizing net operating income over 10 years, the fixed power approach achieved the highest cumulative energy, followed by fixed voltage and fixed temperature. The fixed voltage case had the highest life expectancy. Economic profitability analysis suggested that with proper optimization, SOFC systems can achieve competitive LCOE values, though initial capital costs remain critical. The best case in this optimization is the **fixed power** approach, which had the highest cumulative energy, highest net operating income, and good life expectancy.

In summary, this chapter demonstrates the efficacy of the proposed prognostic approach in optimizing CPOX-SOFC systems for performance, efficiency, and longevity. Key findings emphasize the importance of accurate SoH assessments and strategic optimization approaches for balancing energy production and system degradation.

5 Operating Map Development through Multi-Objective Optimization

This chapter aims to develop a comprehensive operating map that remains valid when the system operates with fixed inputs over time. This is achieved through a multi-objective optimization process with two distinct objectives: minimizing degradation to maximize the stack's life expectancy and increasing electrical efficiency to ensure optimal operation.

5.1 Introduction

The operating map of a SOFC system based on CPOX is crucial for understanding the performance boundaries and optimal operating conditions. A multi-objective optimization approach is employed to develop this map, balancing the trade-offs between minimizing degradation and maximizing electrical efficiency. The optimization process involves setting up a series of simulations over a defined period, during which the system's performance is evaluated against these objectives.

The simulation is conducted over a specific time interval, starting from an initial time and extending over a fraction of a year. This interval is discretized into a series of time points at which the system's state is evaluated.

The optimization problem is formulated by defining the decision variables, which include operational parameters such as fuel flow rates, air flow rates, and temperatures. The bounds for these variables are the ones described in the Table 3.2. Two primary objectives are considered in the optimization:

1. **Minimization of Degradation:** This objective aims to reduce the degradation impact on the SOFC system, thereby extending its operational life.
2. **Maximization of Electrical Efficiency:** This objective seeks to enhance the electrical efficiency of the system, ensuring that it operates at its best performance level.

The optimization process is carried out using a genetic algorithm for multi-objective optimization (`gamultiobj`) with the "Global Optimization Toolbox" of MATLAB software. The algorithm searches for the best trade-offs between the objectives by evolving a population of solutions over several generations. To ensure a robust and efficient optimization process, several options are configured for the `gamultiobj` function. First, the *PopulationSize* is set to 1000. This large population size helps to maintain a diverse set of solutions, which is crucial for effectively exploring the solution space and avoiding premature convergence on suboptimal solutions. Second, the *MaxGenerations* parameter is set to 1000, allowing the algorithm ample iterations to converge to the optimal solutions. Additionally, to ensure precision in the optimization, the *FunctionTolerance* is set to 1×10^{-6}. This tight tolerance ensures that the optimization process continues until the changes in the objective function values are negligible, indicating convergence. Similarly, the *ConstraintTolerance* is also set to 1×10^{-6} to enforce strict adherence to the constraints defined for the problem, ensuring that all solutions remain within feasible and realistic bounds. To expedite the optimization process, especially given the large population size and number of generations, the *UseParallel* option is enabled. This allows the algorithm to utilize multiple processors simultaneously thanks to the "Parallel Computing" Toolbox of MATLAB, significantly reducing computation time. Lastly, the *Display* option is set to 'diagnose', providing detailed information and diagnostics about the optimization progress, which can be invaluable for troubleshooting and refining the optimization setup.

Algorithm 3: Multi-objective optimization using `gamultiobj`

```
Data: Objective function multiObjective, number of variables nvars, bounds lb, ub, time
      span tspan
Result: Optimized solution sol, function value fval, exit condition exitflag, and
        algorithm output output
options ← optimoptions('gamultiobj', 'PopulationSize', 1000,
 'MaxGenerations', 1000, 'FunctionTolerance', 1e-6,
 'ConstraintTolerance', 1e-6, 'UseParallel', true, 'Display',
 'diagnose'); [sol, fval, exitflag, output] ← gamultiobj(@multiObjective,
 nvars, [], [], [], [], lb, ub, @constrGA, options);
```

It's important to note that all constraints for each parameter are moved to the @constGA function. This is done to treat them as non-linear inequality bounds, which is a requirement for the genetic algorithm. For equivalent constraints, an error margin of $\pm 10^{-6}$ is accounted for. Additionally, temperatures are no longer included as inputs but are instead calculated within the model function using the `fsolve` algorithm. This change reduces the system's DoF from 14 to 6, significantly improving the efficiency and speed of the genetic algorithm.

5.2 Pareto Front Analysis

The results of the optimization are analyzed to identify the Pareto front, which represents the set of optimal trade-off solutions between the objectives. The Pareto front is visualized to help in selecting the best compromise between minimizing degradation and maximizing efficiency. The MOO results at the start-up time can be visualized in Figure 5.1a. The three evidenced points are the best-trade-off solution, obtained minimized the sum between the two objective values, then there are the two best solutions concerning one single objective, so efficiency maximization and degradation rate minimization. The same results are obtained considering 1-year operations in

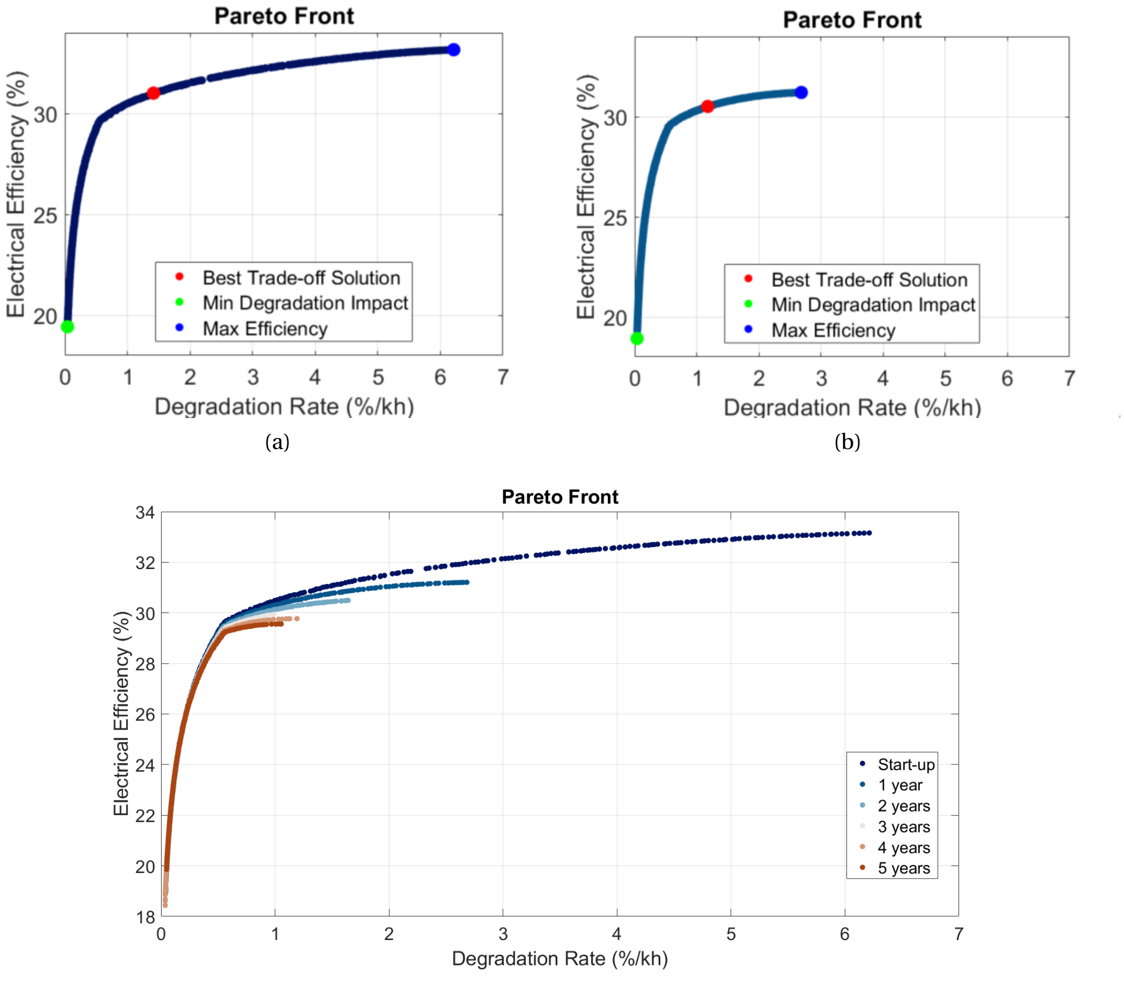

(a) (b)

(c)

Figure 5.1: Pareto fronts obtained using 2-objective optimization at start-up operations (a), 1-year operations (b), multiple-year operations (c)

Figure 5.1b. The approach is subsequently generalized to multiple time point considerations obtaining different Pareto fronts, plotted each in Figure 5.1c for comparison purposes. The results for the first 5 years of operations of the three possible different points: best trade-off, and best single objectives, where the best trade-off solution is typically found by minimizing the sum of the normalized objective functions. The process involves the following steps:

- Given a set of objective functions $f_1(x)$ and $f_2(x)$ for each solution x, the best trade-off solution is found by minimizing the sum of these functions:

  $$\text{Best Trade-Off Solution} = \arg\min_x \left(f_1(x) + f_2(x)\right)$$

  Where:

  - $f_1(x) = D_{rate}$ represents the first objective of degradation rate.
  - $f_2(x) = -\eta_{el}$ represents the second objective of electrical efficiency.

- Each objective function value is scaled to a common range, typically between 0 and 1, to ensure they are comparable. This is done using:

$$\text{Normalized } f_i(x) = \frac{f_i(x) - \min(f_i)}{\max(f_i) - \min(f_i)}$$

- The normalized objectives for each solution are summed. This aggregate measure represents the combined performance across all objectives. The solution that minimizes the combined normalized objectives is identified as the best trade-off solution.

All the results are resumed in Table 5.1:

- **Minimum Degradation**: The methane blower workload stabilizes around 0.9999 by the 5th year indicating no major impact from this variable. The CPOX air blower workload is fixed to 0.8000. The cathode air blower workload starts at nominal conditions (0.3883) and varies slightly. The current fluctuates more around 10-11 A, with the highest at 11.0366 A in the 2nd year and the lowest at 10.0114 A in the 4th year. The water pump workload varies, with notable spikes and drops just to accomplish the energy balances since it has no impact directly on degradation. The valve ratio also varies more significantly, ranging from 0.3213 to 0.3685, indicating adjustments in cathode inlet air temperature. This solution minimizes degradation rate in time mainly using current. There is a high FU utilization, and high CPOX temperature maintained thanks to the high CPOX air blower workload. However, the best factor to decrease the degradation rate in time is current; in fact in this case the system is operating in part load.
- **Maximum Efficiency**: The workload of the methane blower remains constant at 1.0000. The CPOX air blower workload shows an upward trend, increasing from 0.7054 at start-up to 0.7589, indicating improved efficiency optimization. The cathode air blower workload is stable at 0.3000, aligning with a valve ratio of around 0.1. The current decreases significantly from 23.6160 A at start-up to 19.7097 A after 5 years, indicating a substantial reduction in energy demand. The water pump workload remains steady at around 0.1000, primarily due to its high impact on power losses, which decreases efficiency. The system no longer operates at part load, reflecting the efficiency dependence on power production. With the aging of the SOFC, two trends become evident: an increasing CPOX air blower workload and a decreasing current. The former enhances FU from the start of operations, leading to higher SOFC temperature over time. Although it slightly increases degradation, higher FU ensures better fuel consumption, thereby improving the SOFC's performance. The latter trend helps mitigate the impact of degradation and reduces voltage ASR losses over time, which become more significant with prolonged operation.
- **Best Trade-off**: The best trade-off solution is derived from a normalized sum minimization, as previously explained. This approach ensures that each selected value represents the optimal compromise to optimize both objectives. If a value is closer to one objective's result, it has a greater impact on that objective rather than the other. Interestingly, the trends of efficiency maximization through increased CPOX air blower workload and decreased current over time are also evident in these results, though with slightly different

Table 5.1: Summary of operational parameters for different years of 2-objective optimization.

Year	CH4 %	CPOX %	Air cathode %	Current (A)	Water %	Valve %
Minimum degradation solution inputs						
Start-up	0.9991	0.8000	0.3883	10.4948	0.1035	0.3476
1 year	0.9977	0.8000	0.3887	10.2339	0.2217	0.3543
2 years	0.9976	0.8000	0.3863	11.0366	0.1424	0.3213
3 years	0.9998	0.8000	0.3832	10.6058	0.1238	0.3685
4 years	0.9999	0.8000	0.3900	10.0114	0.3767	0.3668
5 years	0.9999	0.8000	0.3812	10.9306	0.1454	0.3603
Maximum efficiency solution inputs						
Start-up	1.0000	0.7054	0.3000	23.6160	0.1008	0.1017
1 year	1.0000	0.7090	0.3001	20.9878	0.1015	0.1044
2 years	1.0000	0.7272	0.3000	20.0775	0.1001	0.1017
3 years	1.0000	0.7624	0.3002	19.2891	0.1001	0.1002
4 years	1.0000	0.7736	0.3001	19.9478	0.1006	0.1006
5 years	1.0000	0.7589	0.3000	19.7097	0.1005	0.1000
Best trade-off solution inputs						
Start-up	1.0000	0.7385	0.3001	19.3678	0.1012	0.1027
1 year	1.0000	0.7505	0.3001	19.2734	0.1020	0.1038
2 years	1.0000	0.7674	0.3000	19.0929	0.1009	0.1010
3 years	1.0000	0.7784	0.3002	19.0087	0.1008	0.1005
4 years	1.0000	0.7800	0.3001	19.0063	0.1010	0.1017
5 years	1.0000	0.7899	0.3000	18.8741	0.1025	0.1004

values. The CPOX air blower workload values are higher due to the fixed 0.8 value aimed at minimizing degradation. Similarly, the current values are lower to reduce voltage loss degradation and the impact of ASR on efficiency. The water pump workload remains stable at around 0.1, independent of degradation, to minimize water pump losses affecting efficiency. The air cathode blower workload is reduced along with the valve opening ratio to lower power losses, increase efficiency, and maintain good temperature management.

5.3 Operating maps

The same results are plotted in such a way as to build an operating map for each input of the system in Figures 5.2a-k (methane blower workload, cathode air blower workload, cpox air blower workload, valve ratio, water pump workload, and current) and for some outputs (voltage, stack temperature, chp efficiency, real electrical efficiency, system power). It's important here to notice the difference between real and normal electrical efficiency, the latter considers the overall methane consumption while the first one erases the part of methane that is not burned into the CPOX, to do so and taking into account the model equations in Section 3.3.1, the new molar flowrate of methane is taken into account as:

$$n_{in,real}^{CH_4} = n_{in,cpox}^{CH_4} - \frac{n_{in,cpox}^{O_2}}{2} \tag{5.1}$$

5.4 Discussion

According to Figure 5.1, the evolution of Pareto fronts for electrical efficiency against degradation rate over different periods is captured from the start-up phase to five years. This analysis highlights the trade-offs between electrical efficiency and degradation rate over time. Initially, the Pareto front for the start-up phase shows the highest electrical efficiency values with relatively low degradation rates, indicating that newly implemented systems perform optimally with minimal degradation rates. Over the first two years, the Pareto fronts demonstrate a slight shift towards higher degradation rates, with a minor decrease in electrical efficiency. This suggests that as the system ages, efficiency slightly drops while degradation becomes more pronounced. From the third year onwards, the Pareto fronts shift further, showing a more significant decrease in electrical efficiency and increased degradation rates. This indicates a trend where the system's efficiency is compromised more noticeably over time, and the degradation rate becomes a more critical factor. Another intriguing finding is that the optimal trade-off solution shifts over time toward the point of maximum electrical efficiency. This indicates that the degradation rate becomes a dominant factor as the system ages, significantly impacting efficiency maximization. It is also important to note that, over time, the maximum achievable efficiency decreases, while the minimum degradation rate increases slightly.

Looking at Table 5.1, in the SUNFIRE system, the optimal trade-off between two objectives is not always found exactly halfway between them. The analysis reveals that the CPOX air blower workload significantly impacts degradation minimization and decreases efficiency due to its power consumption, while the air cathode blower workload plays a more crucial role in enhancing electrical efficiency. Current affects both degradation and efficiency, with very good degradation rates still achievable at high currents (19A). The water pump workload is independent of the degradation objective, whereas it has a strong impact on electrical efficiency due to its high power losses. To further confirm this analysis, the operating maps of the Pareto Fronts are analyzed in the following lines.

Looking at Figures 5.2a-f, the operating maps offer a comprehensive view of how different variables impact degradation rate and electrical efficiency over time. Each map displays two perspectives: the relationship between degradation rate and the chosen variable, and the relationship between electrical efficiency and the chosen variable:

- Operating maps of the methane blower workload, appear to be almost independent of system efficiency and degradation. The workload remains consistently around the upper bound, ranging between 99% and 100% with no variation in each of the points. This result is expected since in both single objectives optimization the values found resulted to be around these values (Table 5.1).
- The operating maps for the CPOX air blower workload illustrate a clear relationship between the workload and both degradation rate and electrical efficiency over various periods. The main result is that with start-up operations, the range of variation of this variable is larger within a range from 70% to 80%. 70% values achieve high efficiency and high degradation, while for values near 80%, the efficiency decreases with degradation due

to power consumption and cpox (then SOFC) temperature-related impact as previously discussed. As time progresses, the degradation starts to impact on electrical efficiency, which to be maximized narrows progressively the range of variation of CPOX air blower workload to the upper bound.

- Air cathode blower workload is coherent maintaining a fixed range in time between 30 and 37%, with low values implying very high degradation and efficiency and the high values low degradation and efficiency. Good trade-off values are found in between. The shape of the plots means that the air blower workload in this MOO is independent of the aging process.
- The operating maps for current demonstrate a significant influence on degradation rate and efficiency. The current ranges from 10 to 24 A, with the minimum current yielding the lowest degradation rate and efficiency, and the maximum current resulting in the highest degradation rate and efficiency. Over time, the range of current narrows, with the maximum values steadily decreasing from 24 A to 20 A after 5 years of operation. This indicates that the current is a highly impactful parameter in managing system efficiency and degradation.
- The operating maps for the water pump workload show a significant impact on electrical efficiency. The majority of the Pareto front points fall within the 0% to 15% workload range. In this range regarding degradation rate, the points are dispersed without following a specific trend indicating no direct relationship. Concerning the electrical efficiency, an aging trend can be observed, in which the points are shifted to lower workload with time, to further reduce the water pump power consumption and enhance the total power produced.
- The operating maps for the air mixing valve ratio show how air mixing influences system performance. The ratio increases over time, ranging from 10% to 38%. At lower air mixing valve ratios, the system experiences a higher degradation rate but initially achieves the highest efficiency, which decreases over time. Conversely, higher valve ratios minimize the degradation rate but at the cost of reduced electrical efficiency. The aging process impacts the valve ratio Pareto fronts due to the valve's ability to increase the temperature inside the SOFC, which leads to lower degradation over time. The relationship with efficiency is indirect, as it depends on the cathode air blower workload that varies with the valve ratio. The algorithm commonly decreases both the air mixing valve ratio and the cathode air blower workload to maintain good efficiency and a manageable degradation rate over time.

Looking at Figures 5.2g-k, the operating maps outputs are discussed:

- The voltage behavior concerning the Pareto points is intriguing. The range of variation narrows over time, decreasing from 40-60 V to 43-60 V over 5 years of operation. This is primarily due to the degradation rate's impact on the ASR, which causes a voltage decrease. To manage this, the algorithm increases the current, which in turn raises the voltage over time. As a result, achieving lower voltage values becomes more difficult after several years of operation.

- Looking at the system power operating map is found that the maximum system power achievable decreases over time due to the degradation rate impact on performances. Minimizing the degradation rate to below 1% requires a significant reduction in system power that needs to operate in part load. The points that achieve this low degradation rate correspond to a higher CPOX air blower workload, lower current, higher valve ratios, and a higher air cathode blower workload.
- Looking at the SOFC temperature operating map, the stack minimum temperature rises from 800°C to 840°C, and eventually to 930°C over time. This increase is due to the impact of degradation on performance, which is counteracted by a rise in CPOX temperature, subsequently leading to a higher stack temperature. Interestingly, a significant number of data points cluster around 840°C. This temperature appears to be the optimal trade-off between the two objectives, achievable at any point during operations.
- The CHP efficiency operating map shows no direct connection with the two objectives or aging processes. Analysis of the Pareto fronts reveals that minimizing degradation results in the highest CHP efficiency values. However, maximizing CHP efficiency is inversely related to electrical efficiency. This is because achieving high CHP efficiency requires increased workloads on blowers and the water pump to maximize heat exchange in the water HEX. This increased workload significantly raises power consumption losses, which in turn reduces electrical efficiency.
- Real electrical efficiency showcases the true capabilities of the stack, resulting in overall efficiency values that are 10 to 15% higher than typical efficiencies. This efficiency ranges from 30% to 45%. The higher values, compared to electrical efficiency, are due to the exclusion of CPOX reaction efficiency. Electrical efficiency accounts for the CPOX efficiency in oxidation reactions, leading to a significant difference in fuel input.

It is important to note that the 2-objective optimization can be further complicated by adding more objectives. This leads to a much more complex analysis, requiring more computational time to run the algorithm and to get each result, which is beyond the scope of this thesis. Adding a third objective of net operating income maximization to the previous analysis, as shown in Figure 5.3 only for start-up operations, results in a 3-dimensional Pareto front with a stripe shape. The Curve Fitting Toolbox of MATLAB is used to interpolate the data for plotting this stripe. Notably, the color gradient in this figure is not meaningful. Looking at Table 5.2, it is interesting to note that the values generally reflect the previous analysis, with slight changes due to the inclusion of a new objective. The net operating income objective yields optimization results similar to those of maximizing electrical efficiency, with the main difference being the valve opening ratio, which is near the upper bound in this case. This difference is caused by an increase in the SOFC stack temperature, leading to higher temperatures in both the burner and the hot air side (inlet and outlet) of the heat exchangers. These latter temperature increases are significant for net operating income as they enhance the amount of heat exchanged in the water heat exchanger, thereby maximizing the waste heat recovered and sold by the system. A small conclusion can be made out of this analysis: the net operating income is an objective that takes into account both electrical efficiency objective and waste heat recovery maximization.

Table 5.2: 3-objectives optimization best points.

Objective	**CH_4 %**	**CPOX %**	**Air Cathode %**	**Current (A)**	**Water %**	**Valve %**
Minimum Degradation	0.9999	0.8000	0.3749	10.0807	0.1781	0.4481
Maximum Efficiency	0.9999	0.7051	0.3005	23.5835	0.1019	0.1066
Maximum Net O.I.	1.0000	0.7050	0.3003	22.0466	0.1002	0.4499
Best Trade-off	0.9999	0.8000	0.3749	10.0807	0.1781	0.4481

In summary, this chapter highlights the intricate balance between electrical efficiency and degradation rate in CPOX-SOFC systems over time. Key findings include the shifting Pareto fronts indicating aging effects, the significant impact of input parameters on system performance, and the complex relationships between operational variables. These insights emphasize the need for strategic optimization to enhance system longevity and efficiency.

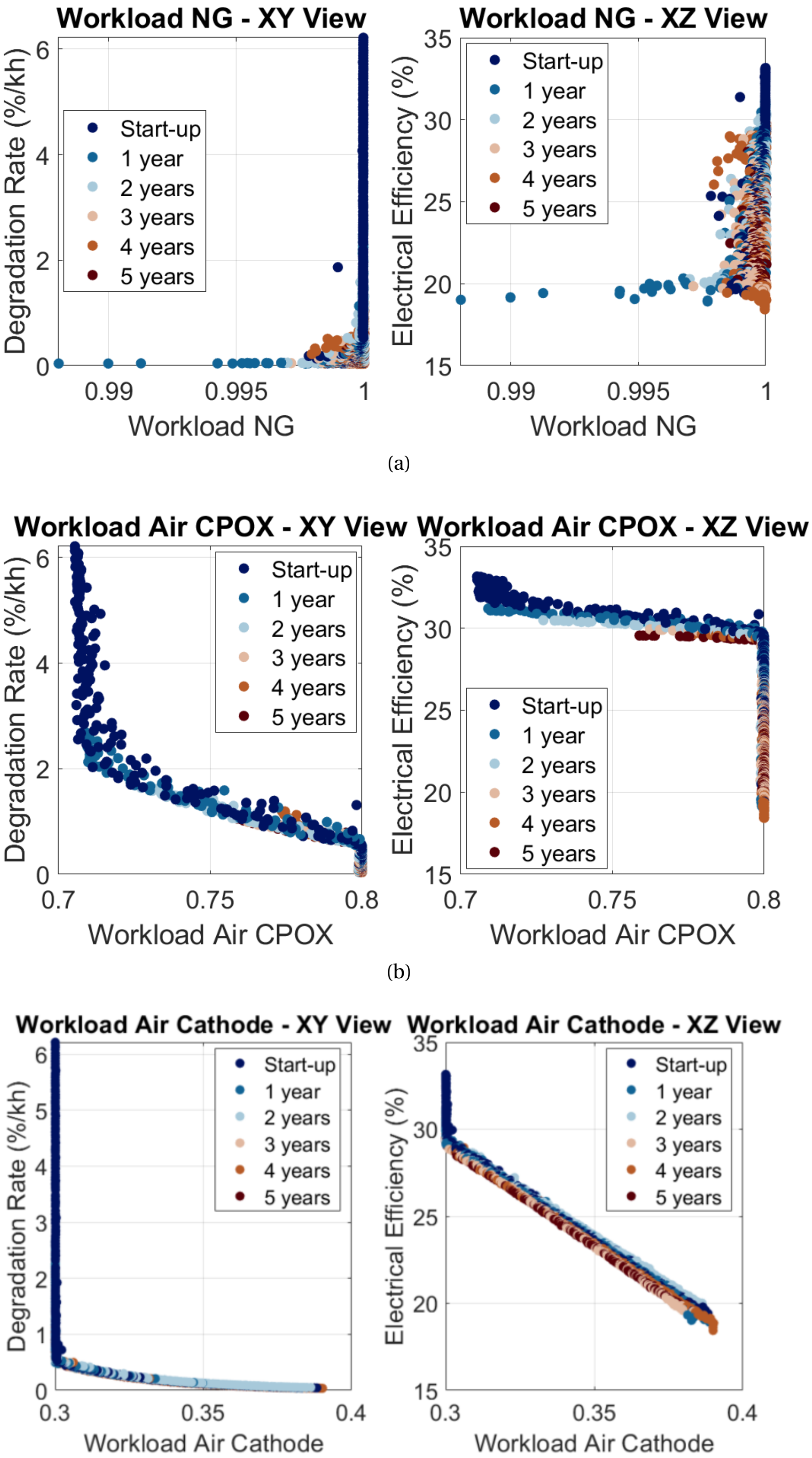

(a)

(b)

(c)

Figure 5.2: Operating maps of methane blower workload (a), CPOX air blower workload (b), and cathode air blower workload (c)

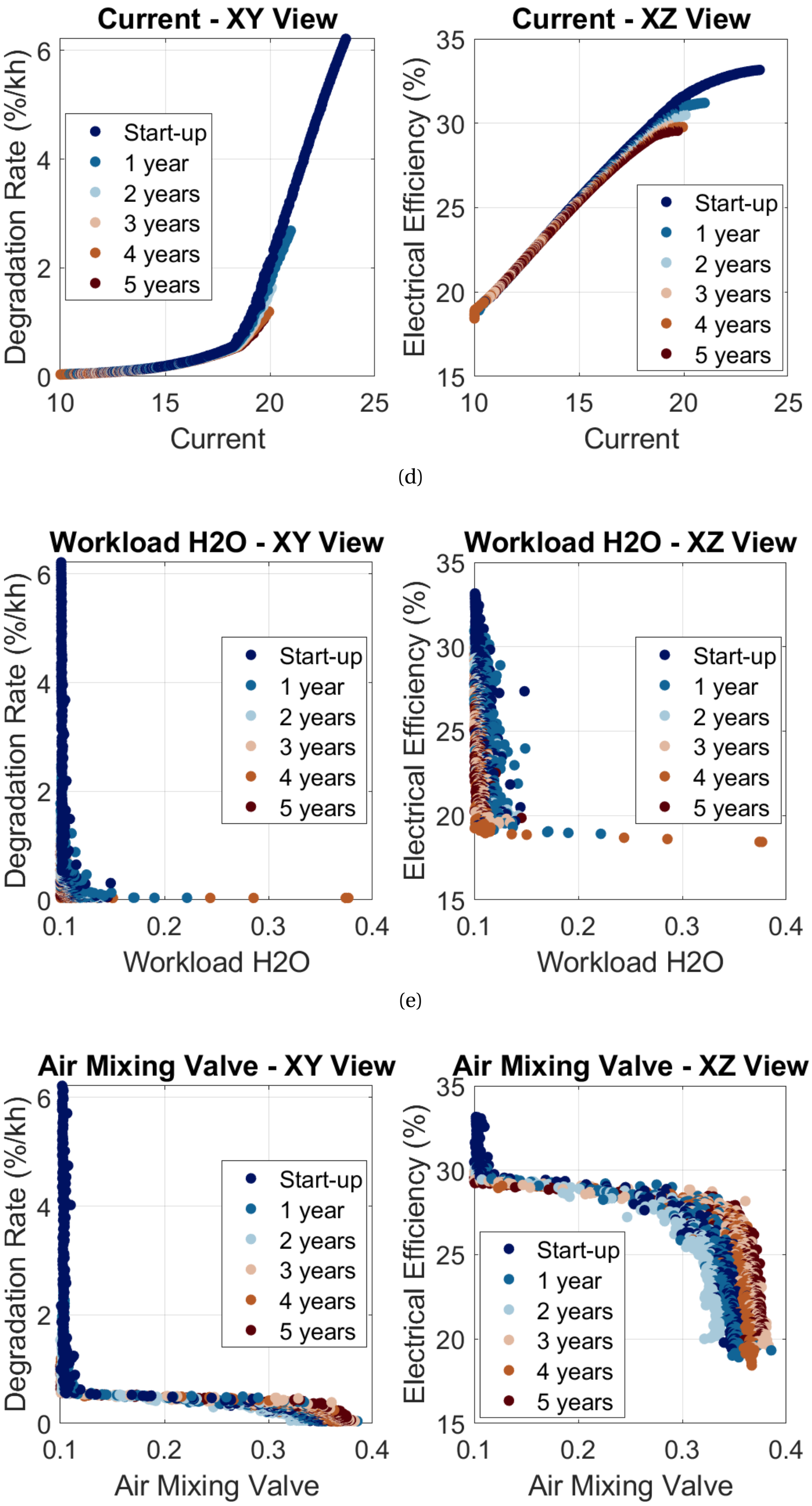

(d)

(e)

(f)

Figure 5.2: Operating maps of current (d), water pump workload (e), and valve ratio (f)

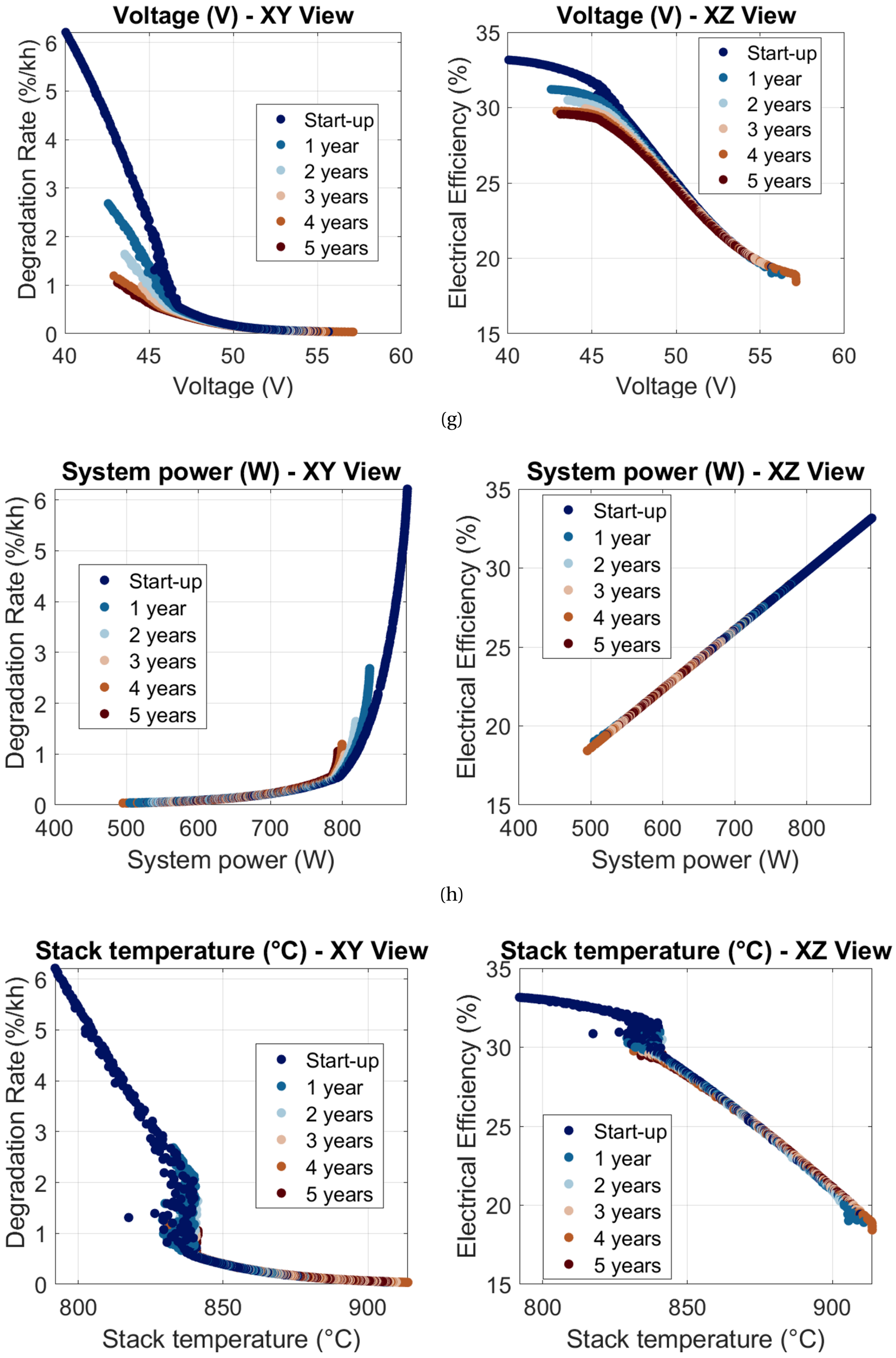

(g)

(h)

(i)

Figure 5.2: Operating maps of voltage (g), power (h), and stack temperature (i)

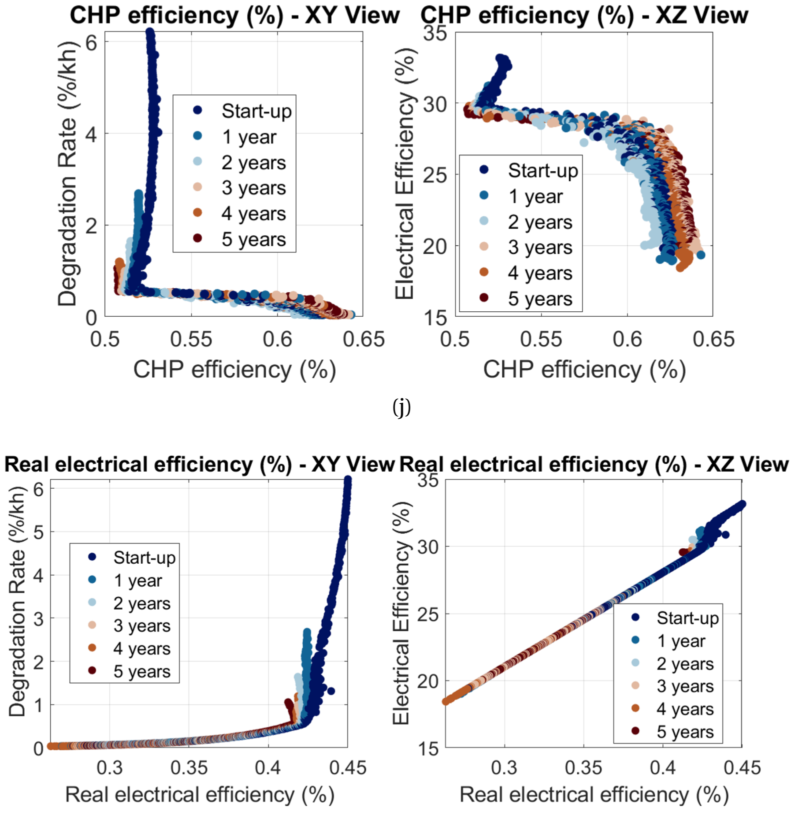

(j)

(k)

Figure 5.2: Operating maps of CHP efficiency (j), real electrical efficiency (k)

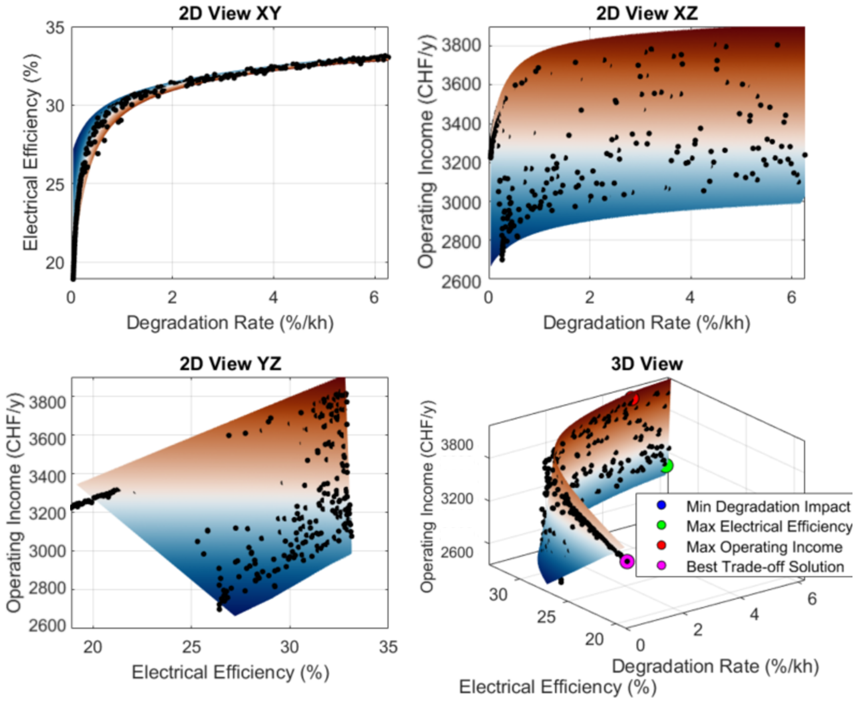

Figure 5.3: 3-objectives optimization results for start-up operations

6 Dynamic mission profile for a real-case application

7This chapter introduces a real-world case study involving the consumption data of buildings at the University of Applied Sciences and Arts Western Switzerland (HES-SO) in Sion, Switzerland. The objective is to apply the developed model optimization techniques to this real case scenario, demonstrating how dynamic mission profiles can impact the performance of a SOFC system over one year. The consumption data will be used to create a dynamic mission profile that will be integrated into the SOFC model to evaluate its performance and efficiency over time.

The used data contains detailed information on the electricity consumption at the HES-SO buildings. This dataset includes hourly data points over an entire year, providing a comprehensive view of the energy dynamics at the site. In this analysis, a new case in which the SOFC system completely replaces PV panels to satisfy the full building consumption is analyzed. By leveraging this data, the simulation aims to assess the SOFC system's response to real-world operational conditions and evaluate its long-term performance, degradation, and overall efficiency.

6.1 Methodology

Firstly, the data is extrapolated by considering 8,760 different time points, which represent each hour of the year. Each of these time points corresponds to a specific power consumption value. The ".csv" file contained information about building consumption (kW) and PV power production (kW), but only the first is taken into account. The extrapolated data is plotted in Figure 6.1a. Then, to adapt this high power consumption in kW to the SUNFIRE 850W SOFC system, the overall data is divided by the number of possible systems to fully satisfy the power need:

$$TargetPower_t = \frac{BuildingConsumption(kW)}{\frac{max(BuildingConsumption(kW))}{850W} \cdot 1000} \text{ per each t in time} \tag{6.1}$$

The result of the new variable TargetPower is shown in Figure 6.1b in a 3D plot to better visualize the daily operations. The presence of Figure 6.1b helps to further understand the behavior of a typical day operation; in fact, it is possible to see how during each day the power experiences two major peaks, around noon and around 18:00. It's also interesting to see how the power consumption drops to 200 W during the night from 20:00 to 7:00. A single-objective optimization

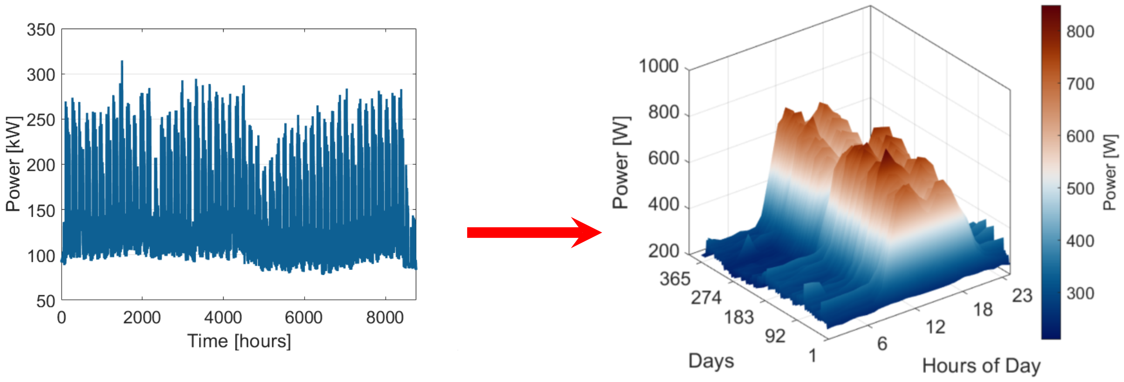

Figure 6.1: HESSO building consumption along a year of operations in 2D view (a), in 3D view (b)

is run with `fmincon` algorithm and SQP, considering all the system constraints presented in Table 3.2 in conjunction with a system power in time fixed to $TargetPower_t$ considered as an additional non-linear equivalent constraint.

Three different objectives are considered: degradation rate minimization, electrical efficiency maximization, and net operating income maximization, coming from a techno-economic assessment (Section 6.2).

6.2 Results

In this section, all the results given by the optimization with the three different objectives are shown in various figures and discussed in detail. It's important to notice that not all the figures are presented here and to have a complete and autonomous understanding of the analysis all the missing figures are available in Appendix A.7. One common result from the three scenarios is that almost all the variables follow the daily power profile of operation, diving the average power production in two different parts:

- Daily operations, from 8 to 20:00, where two power peaks are experienced around 14:00 and 17:00;
- Night operations, from 20 to 8:00, where the power production is constant and low (200 W) operating the system in part load.

Minimization of Degradation Rate

To minimize the degradation rate, the methane blower workload maintains a moderate level, ranging from 70% during the night to 100% during the day. The CPOX air blower workload is moderate, ranging from 50 to 75% between day and night. The stack air workload remains relatively stable, ranging from 20 to 60%, mirroring the target power profile. The current output is kept at a moderate level, ranging from 12 to 15A between day and night. The water pump workload operates at 100% during the night and reduces to 10-15% during the day. The air mixing valve ratio is the only value adjusted daily for temperature control, often set at 45% during night operations to maintain a good stack temperature.

What is interesting is how the optimization algorithm manages the daily power change: during the daytime, there are peak values for current around 16-17 A slightly increasing over time, methane blower workload, and other variables similar to the system nominal conditions; while during nighttime the extreme part-load conditions make the optimization struggle to achieve better performance: water workload normally independent from degradation rate is fixed to the upper bound to recover all the waste heat from the stack-cooling process due to the high power decrease and the burner temperature raise. Notably, during daytime a slight trend of current increase in time can be detected, given the voltage decrease in time. In terms of performance, the stack power output is equal to the building power consumption indicating a stable optimization, reflecting a balanced approach to sustaining performance while mitigating degradation. Electrical efficiency is moderate, ranging from 15 to 30% between day and night, while CHP efficiency shows higher peaks ranging from 60 to 80 % between day and night. Performance degradation and degradation rate are lowest, with performance degradation moving below 0.3% and a degradation rate averaging lower than 0.03%. Notably degradation rate is increasing over time quite slightly due to the higher current, while in performance degradation an upward trend in values is more visible, following the peak power profiles of power target. Voltage trends are similar across conditions, rising to 60V at night and dropping to 40-45V during the day. FU is at 70%, AU at 20%, and CO at 94%, showing the lowest fuel utilization rate. Also, temperatures inside the system follow the daily profile of operation with some differences: profiles of SOFC, cathode inlet, and HEX outlet (cold side) temperatures are shifted of around 1-hour operations due to the system's thermal inertia; in fact, after the power target start to decrease and with it also the mass flow rates, CPOX temperature raises reaching the upper bound of 850°C, and the system FU dropping down makes also burner temperature to experience an initial raise that causes the "shifting" phenomenon. This phenomenon is consequently experienced by cathode inlet air, WHEX inlet and outlet air temperatures. The system to mitigate the phenomenon acts on the inputs regulating the mass flow rates, increasing the water flow rate to the upper bound to maximize the waste heat recovery due to energy balance satisfaction. Doing so the water outlet temperature decreases in a narrow range from 60°C to 52°C.

Efficiency Maximization

In this scenario, there is an interesting phenomenon about the SQP algorithm's local minimum escaping, due to the cathode inlet upper bound touching, that around half-year operations slightly change the operating conditions. In this scenario, the methane blower workload increases significantly, ranging from 60 to 100% between day and night. The CPOX air blower workload is lowest in low-power operations, ranging from 45 to 80%. The stack air workload shows an overall increase after half-year operations, ranging from 20 to 80%, peaking during the night and lower during the day. The current output increases to boost power output, ranging from 14 to 20A, taking advantage of the improved efficiency. The water pump operates at full capacity (100%) during the night and significantly reduces its workload to less than 10%

during the day. This adjustment greatly lowers its average operating value with respect to the minimizing degradation scenario. The air mixing valve ratio is adjusted daily for temperature control, often set at 45% during night operations to maintain a good stack temperature. After local minimum escaping, there is a current drop and the system starts operating in part load during daily operations, indicating how the algorithm manages a strategy change due to cathode inlet temperature upper bound violation. From this point on, the degradation rate changes, decreasing due to the current decrease and AU is dropping to 10% due to the high cathode air blower workload. This drop in current is compensated by a voltage increase. The stack power output is satisfying the target, struggling in the operating point change, but maintaining values between 600 and 900 W. Electrical efficiency changes in the two operating conditions between the half-year operations, starting from an average of 38% during daily operations in the first half and reaching up to 41% in the second half, while CHP efficiency is slightly decreasing due to the less waste heat recovered in the second half. This electrical efficiency improvement in the second half of the year is mainly due to the part load operations and the lower water workload. During nighttime operations, the electrical efficiency drops down to 20% Performance degradation and degradation rate show the highest values during higher power operations, with performance degradation moving from 0 to 0.5% (between day and night) and a degradation rate averaging lower than 0.05%. Voltage trends mirror the current, rising to 60V at night and dropping to 40-45V during the day. FU, AU, and CO values are highest during most of the operating time, with FU at 80%, AU at 25%, and CO at 95%. Temperature considerations are equal to the ones of minimizing degradation case, with the only difference of cathode inlet temperature upper bound touching that makes the algorithm escape the local minimum. Only in those 50 days of operation, did the system cool down fixing CPOX, cathode inlet, SOFC, burner, start-up burner, hex outlet (cold side), and whex inlet air temperature to their lower bound. This is also reflected by the water outlet temperature which is always fixed to the upper bound these days.

Techno-economic optimization

For maximizing net operating income the considerations are almost the same as the minimizing degradation scenario but with different values. The methane blower workload fluctuates, ranging from 65 to 100% between day and night. The CPOX air blower workload is highest, ranging from 60 to 80% between day and night. The stack air workload shows an overall increase after half-year operations, ranging from 20 to 80% between day and night. The current output is dynamically adjusted, ranging from 10 to 17A, optimizing revenue from electricity generation while managing operating costs. The water pump workload operates at 100% during the night and reduces to 20% during the day. The air mixing valve ratio is adjusted daily for temperature control, often set at 45% during night operations to maintain a good stack temperature. The stack power output is lower and more stable, reflecting a balanced approach to sustaining performance while optimizing costs, with values between 600 and 900 W. Electrical efficiency fluctuates to balance cost and performance, rising after half-year operations. CHP efficiency is relatively stable but shows higher peaks. Performance degradation and degradation rate show high values during higher power operations, with performance degradation moving from 0 to 0.55% and a degradation rate averaging lower than 0.05%. Voltage trends are similar across conditions, rising to 60V at night and dropping to 40-45V during the day. FU is at 75%, AU at

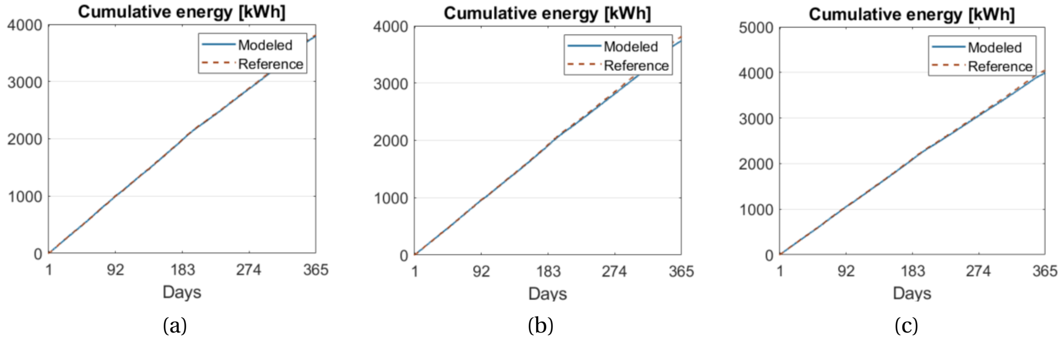

Figure 6.2: Cumulative energy results minimizing degradation rate (a), maximizing electrical efficiency (b), and maximizing net operating income (c).

18%, and CO at 94% during daytime operations. Temperature-wise, the CPOX and cathode inlet temperatures are fixed at 850°C on most days. The stack temperature follows the power profile, increasing from 650°C to 865°C. The burner temperature ranges from 700°C to 900°C, with the start-up burner temperature rising from 150°C to 170°C. The water outlet temperature increases from 48°C to 60°C. WHEX inlet and outlet air temperatures rise from 400°C to 520°C and from 150°C to 200°C, respectively. HEX outlet cold air temperature rises from 650°C to 800°C.

Interestingly in the last 30 days of operation, to avoid CPOX temperature upper bound violation the algorithm escaped the local minimum readapting to a new control approach to cool down the system: current drops to lower values 10-15 A, increasing voltage to maintain the target power fixing it to 60 V among day and night operations. This impacts the CHP efficiency which drops down to very low values of 30% also due to the lower methane and air blower workloads.

Cumulative energies comparison

In this paragraph, only the cumulative energy method for the EoL is analyzed. This approach is chosen because it is the only method to address system degradation under dynamic profile operation. As previously discussed, fixed thresholds relative to initial values are no longer valid under varying mission conditions. The cumulative energy results are shown in Figure 6.2. The values of cumulative energy are not yet enough degraded to detect the EoL of the cell, which is a reasonable result due to the relatively small time of operation, also considering most of the time the system is operated at 200W conditions. The performance degradation according to cumulative energy criterion (relative error difference between the final cumulative energy values to the reference) is presented in Table 6.1. It is interesting to note the change in the slope of cumulative energy over time, indicating that its dependency on dynamic power profile

Table 6.1: Performance degradation according to cumulative energy at the end of the year.

Objective	Value (%)
Degradation rate	0.57
Electrical efficiency	1.88
Net operating income	1.55

operations prevents it from being linear. Another notable point is that the cumulative energy values at the end of the 1-year operation are almost the same for both the minimization of degradation rate and the maximization of efficiency cases, each totaling 3700 kWh which is the amount of energy needed to satisfy the building consumption in the year. However, for the net operating income maximization case, the cumulative energy value is higher, reaching 4000 kWh, adding 3000 kWh of energy production. This is significant because the algorithm plays between the switch from daily to night operations to produce more energy and gain extra profit (detailed discussion in the following Section 6.2).

Thecno-economics metrics

This section provides a detailed analysis of the techno-economic results for the three different optimizations. The operating income, net operating income, and OPEX values mirror the pattern of the target power values. In this analysis, there are several points of evidence about techno-economic assessment:

- Operating income comes from the electricity savings, made by the buildings to not pay for the electricity grid price;
- Operating expenditures come from both methane consumption and CO_2 emissions, not taking into account the actual emissions produced today by the buildings to accomplish their heating needs, underestimating the potential revenues.
- Extra profits are generated only in the case of techno-economic optimization, in which the algorithm managed to produce 3000 kWh of extra energy that corresponds to 800 CHF of surplus electricity sold.

According to the performances discussed before, during night operations the SOFC system is less profitable, especially in the case of degradation rate minimization, where the net operating income is negative. All the average peak values are reported in Table 6.2.

Table 6.2: Average peaks values of economics metrics in 1-year of dynamic mission profile simulation

Objective:	**Degradation Rate**	**Electrical Efficiency**	**Techno-Economics**
Daily operations:			
O.I. (CHF/year)	3100	3100	3400
OPEX (CHF/year)	2700	2800	2800
Net Income (CHF/year)	400	300	600
Night operations:			
O.I. (CHF/year)	1400	1400	1900
OPEX (CHF/year)	1800	1700	2100
Net Income (CHF/year)	-400	-300	-200
Total Extra-Profit (CHF)	0	0	800
Total CO_2 Cost (CHF)	410	340	425
Total Net O.I. (CHF)	0	0	400

In conclusion, while each optimization objective leads to different profiles in terms of income, techno-economic optimization leads to the only profitable case in terms of operating costs saved. Further profit could be made by considering CO_2 emissions saved from the current building heating system.

6.3 Discussion

This chapter presents a comprehensive case study involving the dynamic mission profiles derived from real-world electricity consumption data of the HES-SO buildings in Sion, Switzerland. With the results of this chapter it is possible to validate the prognostic approach for real-case application: even with such a constrained system, due to the high complexity of the system, rearranging the operating parameters in a good way can lead to different outcomes, both maximizing the profitability of the operations or the life expectancy of the stack. The analysis aims to provide a detailed understanding of how varying operational conditions affect the 1-year performance, degradation, and efficiency of the SOFC system. By dividing the building's total power consumption by the number of SOFC systems required to meet this demand, the results are appropriately scaled.

The single-objective optimization strategies reveal distinct operational behaviors and trade-offs. Minimizing the degradation rate results in a moderate workload for components, effectively reducing thermal and electrochemical stresses, and prolonging the system's lifespan. Conversely, maximizing stack efficiency leads to higher workloads and power outputs, emphasizing fuel utilization and energy conversion efficiency. The net operating income optimization balances these aspects by adjusting component workloads dynamically to optimize revenue generation while managing costs. Performance metrics further elucidate these differences. The stack power output, electrical efficiency, and degradation rates vary significantly across the optimization strategies. Temperature metrics indicate that the system maintains consistent temperature according to the daily power profile, with CPOX and cathode inlet that mirror it decreasing during daily operations from their upper bound. The minimized degradation case shows more stable and higher temperature settings, while the efficiency and net operating income cases demonstrate more dynamic temperature adjustments, reflecting their respective optimization focuses.

The results outline highlighted the following key findings about the various optimization:

- Minimization of Degradation Rate: This scenario maintained system stability and balanced performance, ensuring low degradation rates and moderate efficiency, reflecting the system's resilience over prolonged use.
- Efficiency Maximization: This approach achieved the highest electrical efficiency, although it required significant system adjustments, particularly during half-year operations, to manage CPOX temperature constraints.
- Techno-economic optimization: This scenario demonstrated the most balanced approach, optimizing both performance and cost-efficiency. Notably, it generated additional profits

by producing surplus energy, reflecting the economic viability of integrating SOFC systems in similar real-world applications.

The cumulative energy analysis underscores the importance of considering system degradation under dynamic mission profiles employing this criterion. The relatively small operation time and predominant part-load conditions (200W) result in cumulative energy values that are not significantly degraded, indicating that the system's EoL threshold is not reached within the year. The non-linear relationship between cumulative energy and dynamic power profile operations highlights the complexity of accurately predicting system longevity under varying conditions. Nonetheless, the different optimization scenarios yield significantly varied results in terms of cumulative energy: these results indicated that the total energy required to meet the building's consumption needs was about 3700 kWh for both the degradation rate minimization and efficiency maximization scenarios. However, for the techno-economic optimization scenario, the cumulative energy reached 4000 kWh, with an additional 300 kWh of energy produced. This extra energy production highlights the system's capability to generate surplus electricity, contributing to the overall net operating income.

Techno-economic optimization is a critical metric for assessing the economic viability of the SOFC system. This optimization scenario emerged as the most profitable, with a total net operating income of 400 CHF per single system. This scenario benefited from the additional energy production, which was sold to generate extra revenue. The income was further enhanced by electricity savings from reduced reliance on grid power.

Overall, the integration of dynamic mission profiles into SOFC system modeling has proven effective in enhancing the understanding of its operational behavior under real-world conditions. The insights gained from this study can inform future strategies for optimizing SOFC systems in various applications, promoting sustainable and efficient energy solutions. The results underscore the potential for SOFC technology to contribute significantly to the energy needs of buildings, particularly when combined with comprehensive optimization strategies that balance performance, efficiency, and economic considerations.

7 Conclusion and Future Outlook

This thesis has undertaken a comprehensive exploration of the development and refinement of a 0-D model for a CPOX-based SOFC system, integrating a degradation model to enhance the fuel cell stack's predictive accuracy and operational lifespan. The primary focus is on implementing novel control strategies to manage the EoL of the SOFC stack, optimizing system performance under various operating conditions. By addressing the challenges of system degradation and efficiency, this work contributes significantly to the advancement of SOFC technology and its potential for sustainable energy applications.

Chapter 1 is the introduction of the thesis, while **Chapter 2** is describing the fundamentals behind SOFC technology.

In **Chapter 3**, a 0-D model of the SUNFIRE CPOX-based SOFC system is constructed to simulate the system's behavior accurately. To do that, a DoF analysis is done to classify the operational parameters that influence the SUNFIRE system. The model incorporates the CPOX reactor, SOFC stack, burner, start-up burner, and air and water heat exchangers. The added value is the integration of a degradation model, taken from an existing one, which enables the prediction of the SOFC stack's lifespan under different operational conditions:

$$r_d = \frac{0.500 \cdot FU + 0.876}{1 + \exp\left(\frac{T-1089}{22.920}\right)} \left(\exp\left(0.3 \cdot j\right) - 1\right) \cdot \frac{t}{3600000} \tag{7.1}$$

It's important to notice that the parameters present in the formula are estimated through an MHE approach, thanks to the existing operational dataset from the SUNFIRE real system. This model forms the foundation for subsequent analyses and optimization strategies.

Chapter 4 focused on evaluating the SoH of the SOFC system and employing various control strategies to balance system performance and longevity. A comprehensive literature review is conducted to identify suitable EoL criteria for dynamic system analysis and the cumulative energy criterion from PEM cells effectively integrated life-expectancy and RuL evaluations given the degradation model, allowing simulation of the degradation rate effect over time on stack performance. Subsequently, optimization algorithms with SQP are applied under nominal system conditions, using different output parameters over time to determine the best approach for real-case applications. The objectives included minimizing degradation rate, maximizing net operating income, and maximizing CHP/electrical efficiency, with fixed stack temperature, power, or voltage. In general, it has been evidenced how each strategy reacts in a specific way:

- Fixed power strategy: it is the most stable strategy. It tends to increase the current profile over time to compensate for the voltage decrease due to degradation impact on performances. It's interesting how this strategy leads the voltage decrease to touch the lower bound of the safety of operation, after which an algorithm re-adaptation is needed. One common solution found in this thesis is to maintain the voltage fixed to its minimum playing with methane blower and cpox air blower workloads increasing them in time to increase CPOX temperature and minimizing again the impact of degradation. It's meaningful to notice that since the water pump workload decreases the system power due to its power consumption, it is often minimized by the algorithm. This approach often leads to high-energy production, high CO_2 emissions, and quite high-performance degradation.
- Fixed voltage strategy: it tends to decrease exponentially the current to both act to ASR and degradation rate impact on performances over time. Depending on the objective of optimization, this strategy can vary. The common use for maintaining a fixed voltage over time is to play with current, but when it is not possible more than a certain range it starts to manipulate also temperatures increasing the SOFC one to decrease voltage losses. The degradation rate with this strategy is often minimal over time, leading this strategy to be best in terms of life expectancy maximization.
- Fixed temperature strategy: it is the most unstable control strategy among the other cases; in fact, it has no direct constraints on voltage, current, or power, meaning that when optimized, the system is often operated in part load. The common strategy for fixing the stack temperature is to maintain fixed the ones at the inlet, fixing the fuel and airflow rates.

Depending on the objective optimization these strategies slightly change: the main findings indicate **no universal best approach**, but rather specific strategies depending on the objectives:

- Regarding standard operation, with no optimization, the fixed voltage control strategy provided the longest life expectancy, followed by fixed temperature and power approaches. Fixed voltage case also results in the lowest CO2 emissions
- To minimize the degradation rate, the best strategy identified is maintaining a fixed voltage. This approach resulted in the highest life expectancy for the SOFC system and the lowest CO_2 emissions, as determined by the cumulative energy criterion. It's important to note that the fixed power approach achieved maximum energy production over time, providing a good trade-off for scenarios where the primary goal is to maximize energy production.
- For maximizing electrical efficiency, the fixed temperature approach yielded the highest energy production and efficiencies, with good life expectancy. The highest life expectancy according to the cumulative energy criterion is obtained by fixed voltage case.

- Maximizing CHP efficiency showed that the fixed power approach led to the lowest performance degradation, highest energy production, and highest electrical efficiency, though not the highest CHP efficiency compared to the fixed temperature scenario.
- Maximizing net operating income showed that the fixed power strategy led to the highest cumulative energy and net operating income over time. In contrast, the highest life expectancy was achieved with the fixed voltage approach, which, although less profitable, significantly reduced degradation. This demonstrates a trade-off between profitability and system longevity, depending on the chosen optimization strategy.

This analysis demonstrated the effectiveness of the predictive approach in optimizing SOFC systems for performance, efficiency, and longevity. Key findings highlighted the importance of accurate SoH assessments and strategic optimization approaches for balancing energy production and system degradation.

In **Chapter 5**, a comprehensive operating map is developed for the system functioning with fixed inputs over time. This map is created using a multi-objective optimization process with GA, balancing the trade-offs between minimizing degradation and maximizing electrical efficiency. More in particular the findings reveal that the methane blower workload remains consistently high (99%-100%) without significantly affecting efficiency or degradation. The CPOX air blower workload, however, influences both efficiency and degradation, with a trend towards higher workloads over time to manage these factors. The air cathode blower workload stays within a fixed range (30%-37%), balancing degradation and efficiency effectively and independently of aging. Current levels, ranging from 10 to 24 A, significantly affect both degradation and efficiency, with the range narrowing over time, indicating the need for careful management. The water pump workload impacts efficiency more than degradation, showing a trend towards lower workloads over time to enhance efficiency. The air mixing valve ratio balances initial efficiency with long-term degradation management, with a trend towards higher ratios over time. Voltage levels narrow over time due to increased degradation, necessitating careful current management. System power decreases over time to manage degradation, requiring adjustments in operational parameters. The SOFC temperature increases over time, with a key balance point at around 840°C. CHP efficiency achieves high values by managing degradation, though there is a trade-off with electrical efficiency. A 3 objectives optimization is also carried evidencing how the net operating income of the system is an objective that if optimized, takes into account both electrical efficiency and waste heat recovered maximization.

Chapter 6 highlighted the practical implications of the developed model and control strategies. By applying dynamic profile operations to real-world data, the study validated the model, and more in particular, validated the cumulative energy criterion as the most adaptable for studying degradation impact in dynamic system optimization. The analysis demonstrates how the model reacts to daily power profile targets, managing temperatures and workloads to efficiently maintain requested performances. More in detail the results highlight three key optimization scenarios for the SOFC system:

- Minimization of Degradation Rate: Maintains system stability with low degradation rates and moderate efficiency, reflecting long-term resilience.

- Efficiency Maximization: Achieves the highest electrical efficiency with peaks of 41%, but requires significant adjustments to manage temperature constraints.
- Techno-economic Optimization: Balances performance and cost-efficiency, generating surplus energy and demonstrating economic viability with a net operating income of 400 CHF per system which is the amount of money saved if a single SUNFIRE system would generate per year of operation instead of buying electricity from the grid.

Cumulative energy analysis shows that under dynamic mission profiles, the system's end-of-life threshold is not reached within a year due to short operation time and predominant part-load conditions. The non-linear relationship between cumulative energy and dynamic operations complicates longevity predictions. Techno-economic optimization is the only one that is found to be financially profitable, producing an extra 3000 kWh of energy, and enhancing income through surplus electricity sales and grid power savings.

Overall, the analysis demonstrates that the integration of detailed modeling, optimization, and control strategies can markedly enhance the performance and durability of SOFC systems. This research highlights that tailored control strategies can significantly improve the performance and lifespan of SOFC systems, offering a solid foundation for future experimental and computational studies aimed at advancing SOFC technology. The developed models and optimization frameworks are invaluable tools for ongoing research and development in the field of fuel cell technology, paving the way for more efficient and resilient energy systems.

To apply the proposed approach to a real system, it will involve the following steps:

1. Collecting experimental data under various operating conditions.
2. Analyzing the experimental data to obtain polarization curves at different temperatures and operating conditions at the beginning of operations, assuming no degradation. Another possibility is to build the reference with a behavioral model that describes the voltage or power evolution according to the current profile as if no degradation is occurring within the stack.
3. Developing a dynamic model of the entire system over time.
4. Creating a multi-objective optimization algorithm that can optimize performance across varying operating conditions, with one or more objectives.
5. Validating the prognostic algorithm results with real data to enhance predictive accuracy extends the estimation horizon from 5 years to more years.

In future work, several avenues can enhance the model's overall accuracy. One approach is transitioning from the current 0D model to higher-dimensional models, which, despite higher computational costs, capture full spatial variations for maximum accuracy. Another possibility is integrating additional instruments, such as EIS and DRT analysis, into the predictive strategy. Replacing the SQP algorithm with a GA for time-operating optimization can significantly enhance predictive accuracy, as its higher explorative capability improves prediction precision despite increased computational time. Another critical improvement is integrating a comprehensive degradation model that accounts for all potential negative influences on stack performance, including sulfur poisoning, carbon deposition, and thermal cycling. This will enable the model to more accurately reflect real-world conditions and their impact on system performance. The collection of extensive datasets under various operating conditions is also paramount. Such datasets will facilitate extremely accurate parameter estimation, grounded in real system performance, useful to enhance the reliability and applicability of the model. Exploring additional optimization strategies and constructing operating maps with high-dimensional objective optimizations is another promising direction. These strategies will provide deeper insights into system behavior under a wide array of conditions and objectives. This research can also be expanded to encompass other types of fuel cells, offering broader insights into the potential applications of these technologies within the energy sector. Such expansion could lead to innovations that enhance the versatility and effectiveness of fuel cell technologies, where the only limit is the data collection capability. Lastly, long-term field testing in diverse operational environments is essential for validating the findings of this study. These validations will refine the proposed solutions, ensuring they are robust and reliable. Moreover, this step is crucial for fostering the broader adoption and commercialization of SOFC technology, ultimately contributing to sustainable energy production.

A Appendix

A.1 Degradation model parameter estimation first move

A preliminary step involves treating the final segment of the collected data as a distinct operating point due to its differing inputs compared to the remainder of the dataset, considering it as an additional second dataset for the parameter estimation analysis. To extrapolate their value, the mean of the dataset concerning the chosen time range has been computed, and the results are shown in Tab. A.1.

Table A.1: Input variables from Sunfire dataset

Parameter	**Input 1**	**Input 2**
Workload_NG (%)	99.999	99.999
Workload_air_CPOX (%)	74.367	78.167
Workload_air_cathode (%)	38.098	51.361
Current (A)	17.993	13.231
Workload_H2O (%)	15.010	17.924
Air mixing valve (%)	29.995	37.989

Since the effect of temperature is negligible concerning the FU and current density variation in the scope of this thesis, the denominator unknown parameters are assumed to be the same as the one proposed by Zaccaria et al., so the new equation turns out to be:

$$r_d = \frac{A \cdot FU + C}{1 + \exp\left(\frac{T-1087}{22.92}\right)} \left(\exp\left(B \cdot j\right) - 1\right) \cdot \frac{t}{3600000} \tag{A.1}$$

Now to estimate these three missing parameters with only two operating condition sets of data given by Sunfire, an iterative approach is set based on MATLAB function `fsolve` used to solve the nonlinear system of equations to find the best A and B parameters in conjunction with conducting a sensitivity analysis on the third one (C) that is fixed per each iteration. The steps made by the algorithm can be described as:

1. Selection of C value that is fixed to have a determinate system of nonlinear equations to be solved (2 equations with 2 unknowns): this selection is made by setting up a range of

different values that span from -5 to +5, given the 0.74 value chosen by Zaccaria et al. [98].

2. Solving the non-linear system of equations using `fsolve`, that is using the 'trust-region-dogleg' algorithm, a type of trust-region method that is well-suited for solving medium-scale problems. Trust-region methods are iterative optimization algorithms that focus on finding a local minimum of a function within a specified region (the "trust region"). The 'dogleg' part refers to the path followed within the trust region to approach the minimum, which can resemble a dog's leg in its shape.

3. The new set of A, B, and C parameters is used in the degradation model described in Section 3.3.7 trying to see if it is correctly describing the actual system voltage decrease presented in Figure 3.2b. It's important to mention that, since during the first 4000h the data seems to be more noisy, the degradation is fitted only to the second part from 4000h to the end. If it does not correctly fit the data, a new C parameter value is chosen and the procedure is started again from point 1.

4. If the set of A, B, and C parameters is correctly describing the degradation of the Sunfire system, another validation step is made to be sure to correctly describe the system: degradation ratios are plotted concerning the current density at different temperature levels, and if the relationship is exponential as described in Section 3.3.7 the set of A, B, C parameter is considered good, otherwise the procedure is started again from point 1 selecting a new C parameter.

It's essential to evidence that this procedure will require future validation. However, within the context of this thesis, it suffices to construct an effective control strategy, which is our primary goal.

Now, the procedure is started with point 1 trying a different range of C parameters and a sensitivity analysis is carried out firstly with a range of values from -5 to 5 to find what is the best value to fit the degradation model equation. Since the `fsolve` function did not find any solution in the range of positive C values and from -3 to -4 and the resulting A and B values will be very high, the analysis is restricted to the range of C values between -1 and 0 which results are depicted in Figure A.1 - (a). To have a set of parameters the most similar to the ones of Zaccaria et al. [98], the parameter found at the end is -0.74. Using such parameters the A and B ones are found through `fsolve` algorithm to be respectively 1.515 and 2.667. The new equation to model degradation is:

$$r_d = \frac{1.515 \cdot FU - 0.740}{1 + \exp\left(\frac{T-1087}{22.920}\right)} \left(\exp\left(2.667 \cdot j\right) - 1\right) \cdot \frac{t}{3600000} \tag{A.2}$$

The results of the last two steps of the procedure that imply the validation of the chosen parameters are shown in Figure A.1.

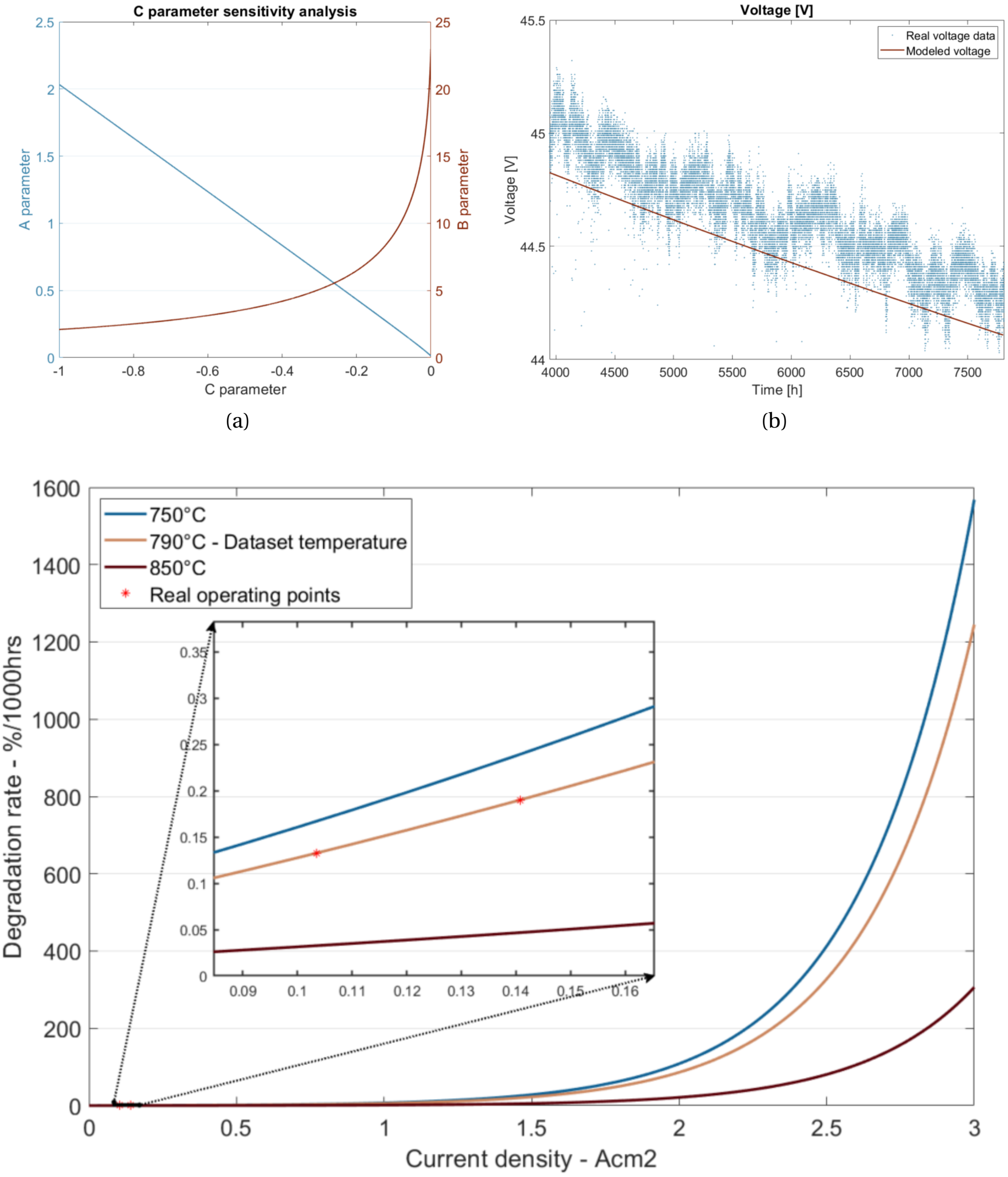

(a) (b)

(c)

Figure A.1: Sensitivity analysis of C parameter (a). Voltage degradation model fitting real data 4000h+ (b), degradation ratio exponential dependency on current density temperature effect [98] (c)

A.2 Second Sunfire data-set for CPOX-SOFC system

The second dataset given by Sunfire is shown in the following figures, collected from 01 Oct 2022 to 19 Jan 2023.

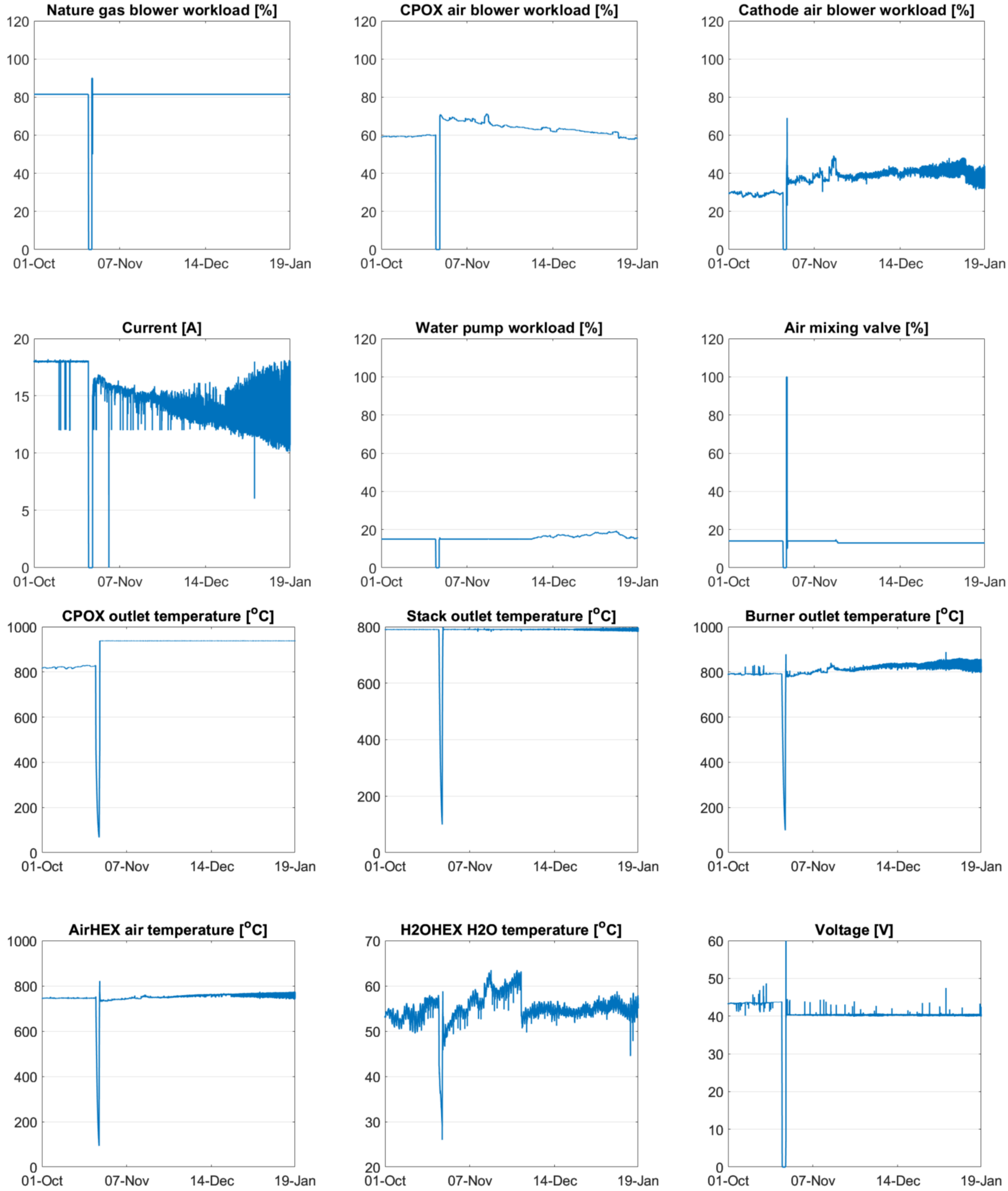

Figure A.2: Inputs (a) and outputs (b) experimental data results of second data-set

A.3 Minimization of degradation with fixed power, voltage, and temperature

The optimization results are shown in the following figures.

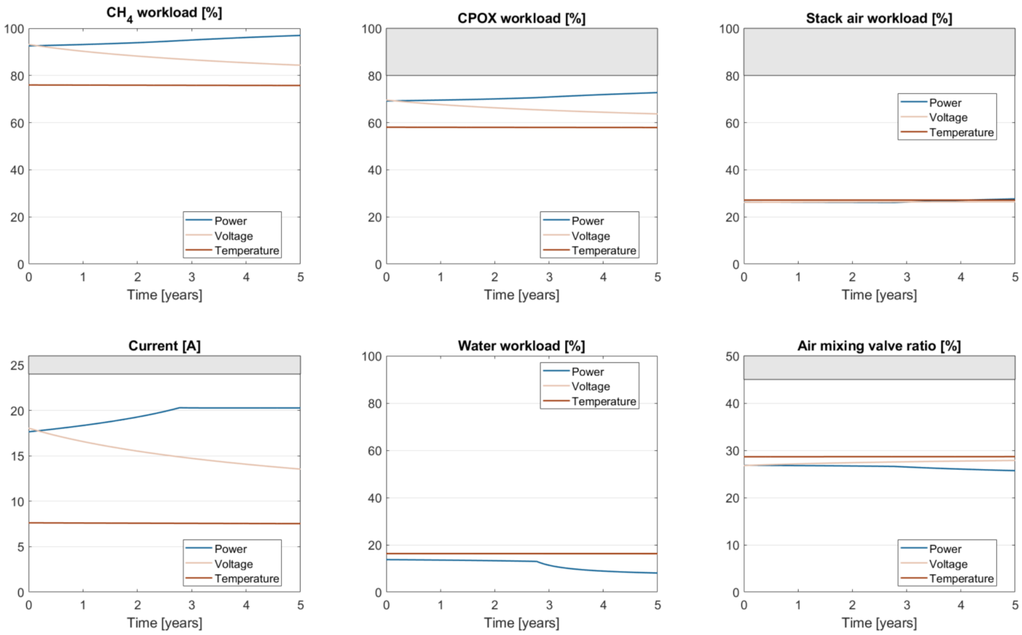

Figure A.3: Minimizing degradation with fixed outputs, inputs.

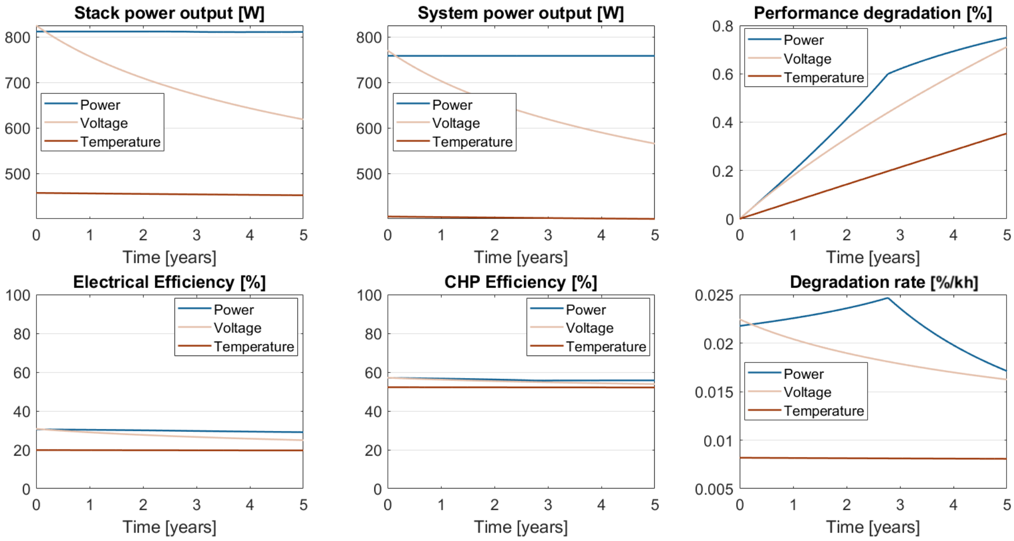

Figure A.4: Minimizing degradation with fixed outputs, key indicators part 1.

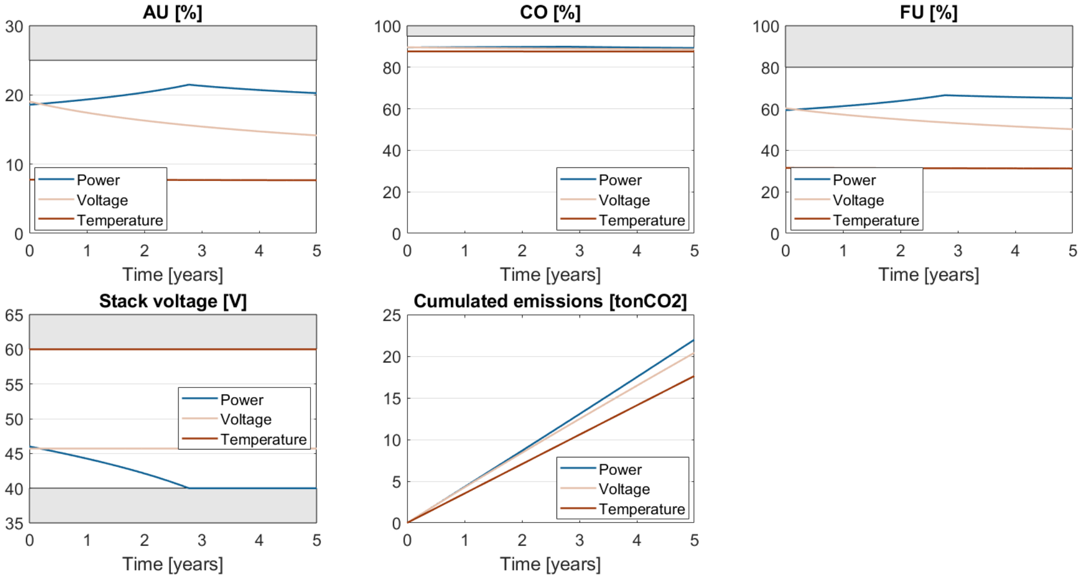

Figure A.5: Minimizing degradation with fixed outputs, key indicators part 2.

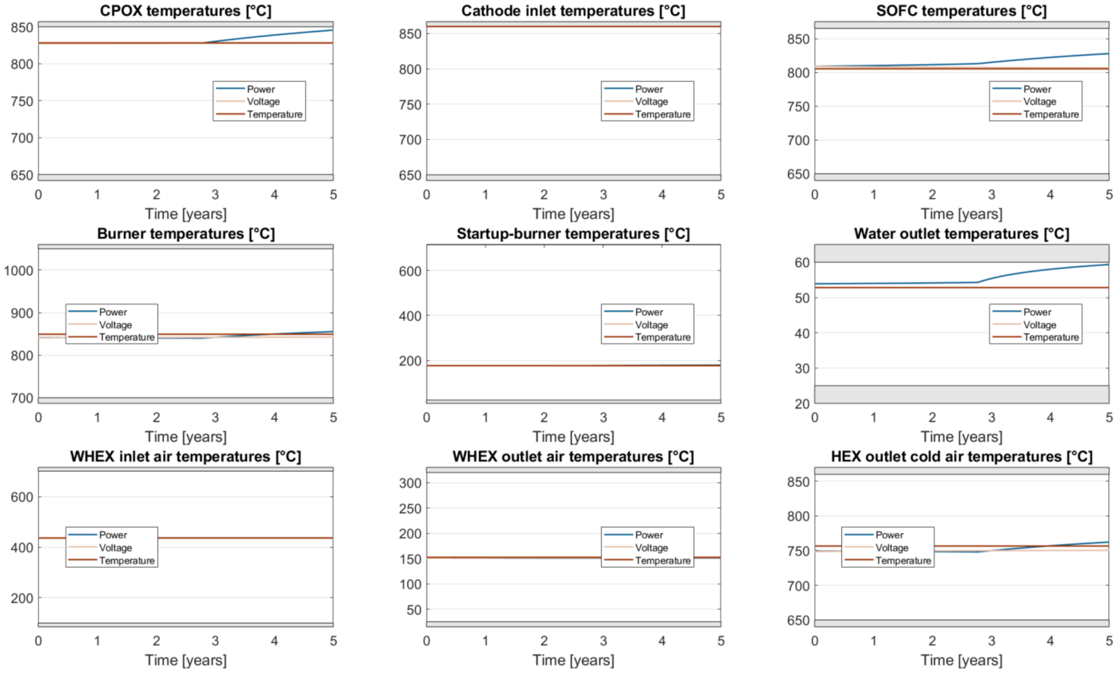

Figure A.6: Minimizing degradation with fixed outputs, temperatures.

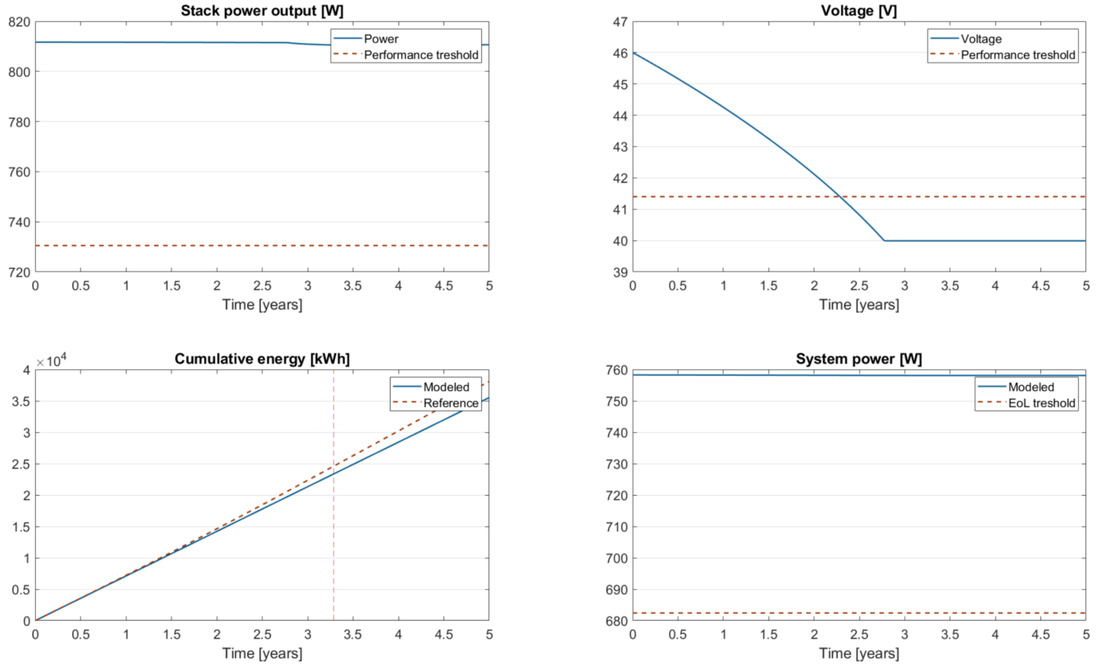

Figure A.7: Minimizing degradation with fixed power, EoL evaluation.

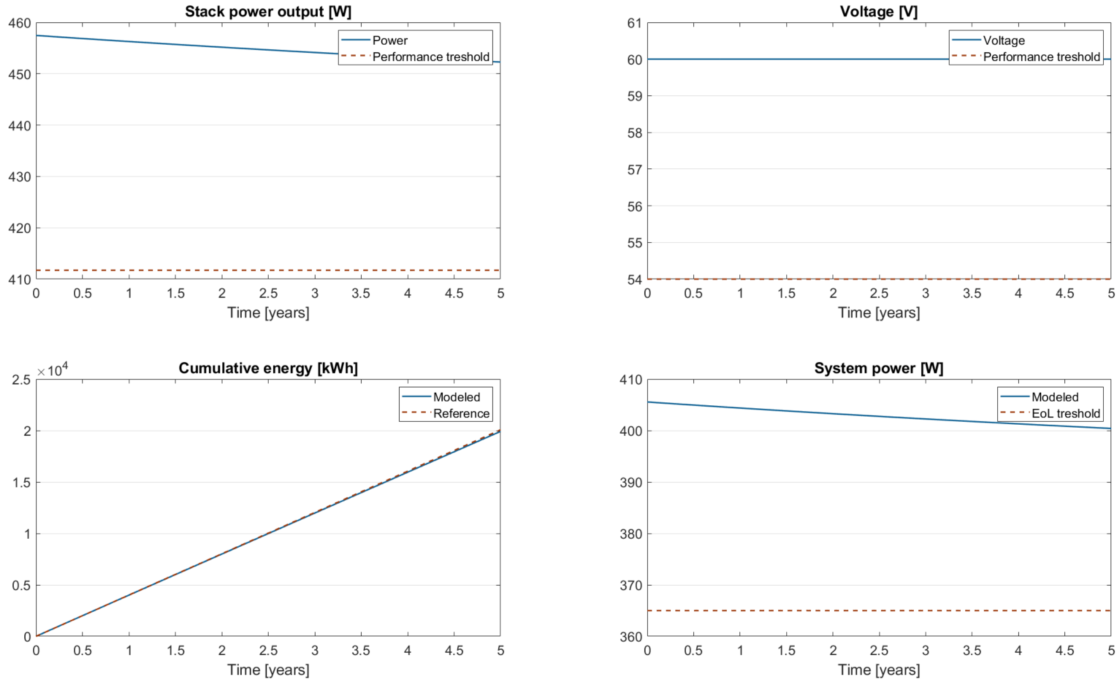

Figure A.8: Minimizing degradation with fixed voltage, EoL evaluation.

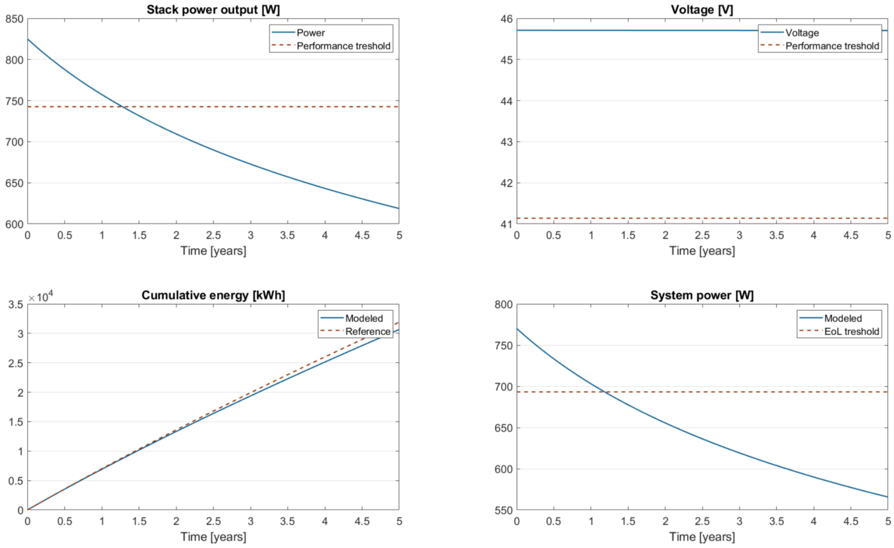

Figure A.9: Minimizing degradation with fixed temperature, EoL evaluation.

A.4 Maximization of electrical efficiency with fixed power, voltage, and temperature

The optimization results are shown in the following figures.

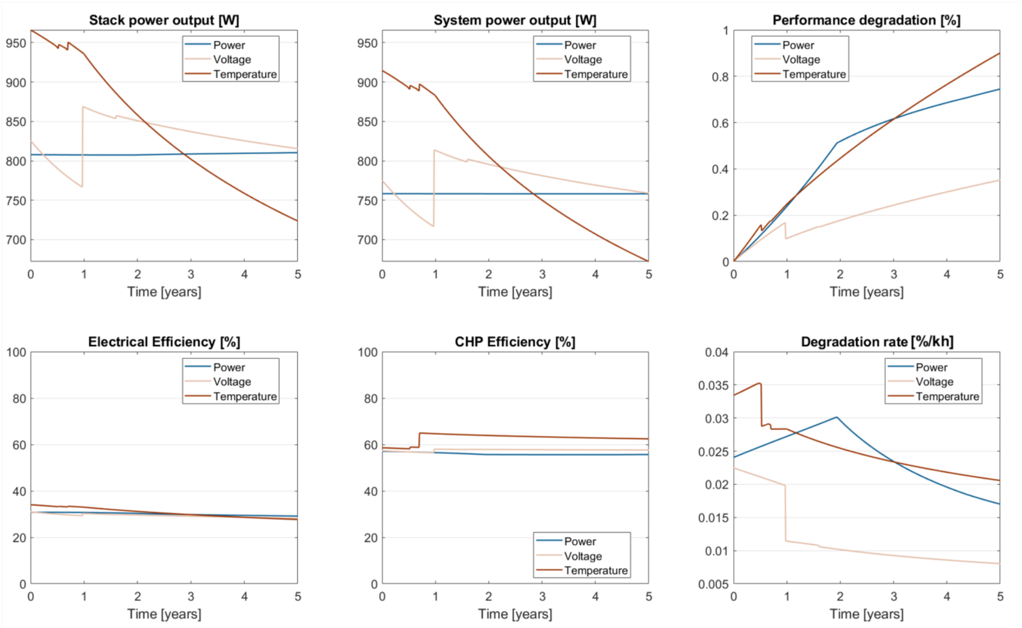

Figure A.10: Maximization of electrical efficiency with fixed outputs, key indicators part 1.

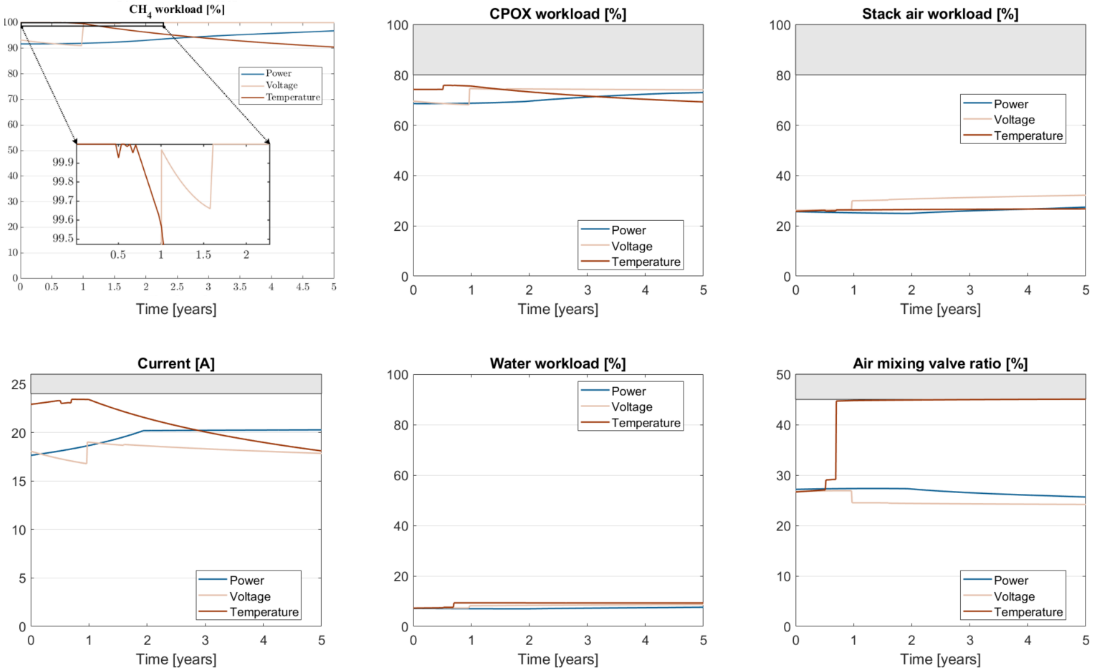

Figure A.11: Maximization of electrical efficiency with fixed outputs, inputs.

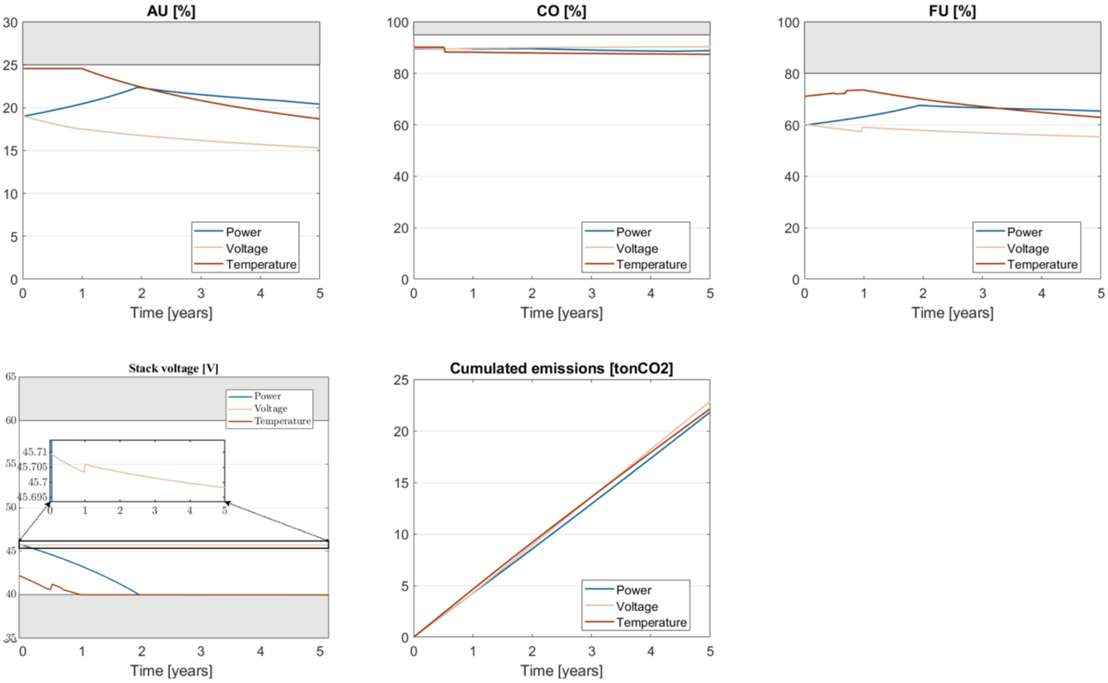

Figure A.12: Maximization of electrical efficiency with fixed outputs, key indicators part 2.

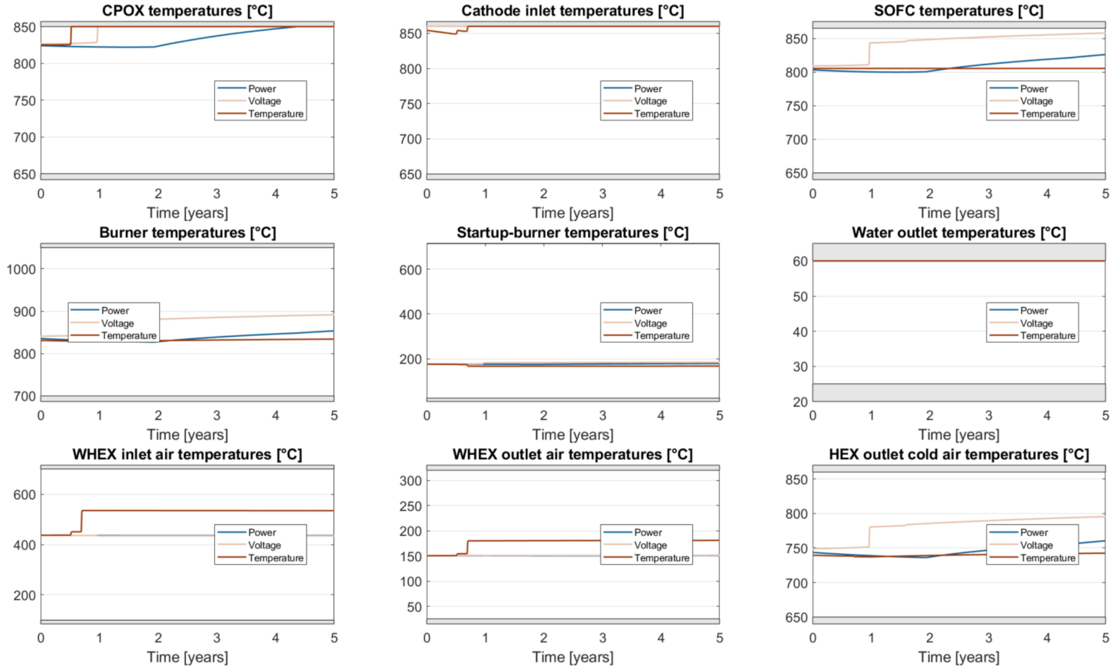

Figure A.13: Maximization of electrical efficiency with fixed outputs, temperatures.

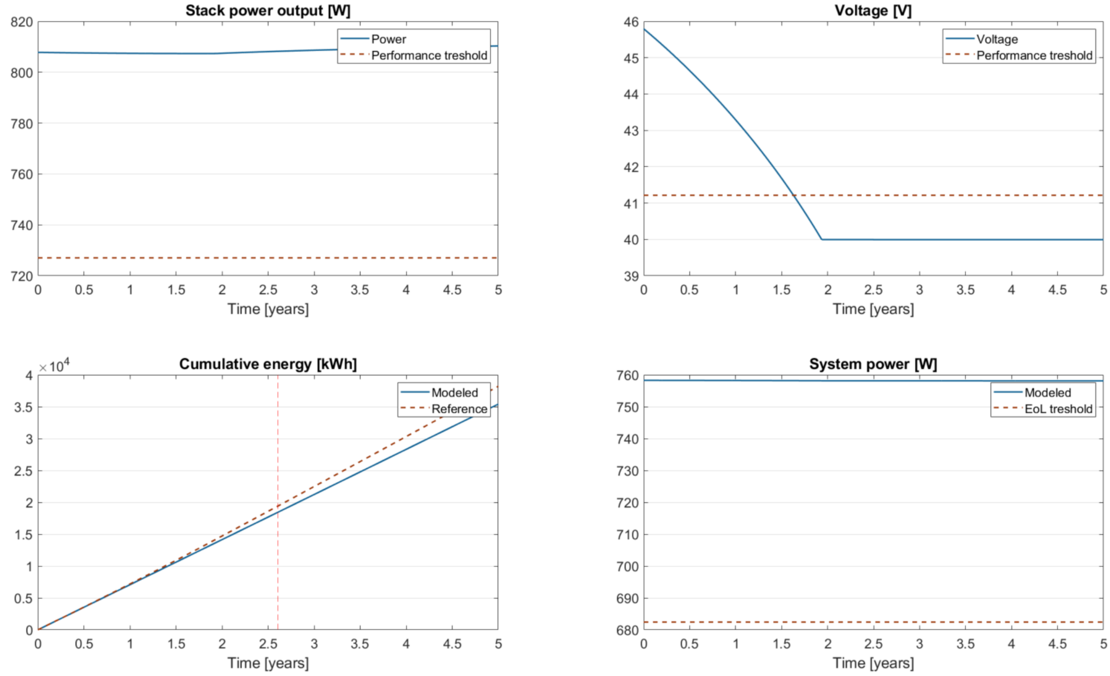

Figure A.14: Maximization of electrical efficiency with fixed power, EoL evaluation.

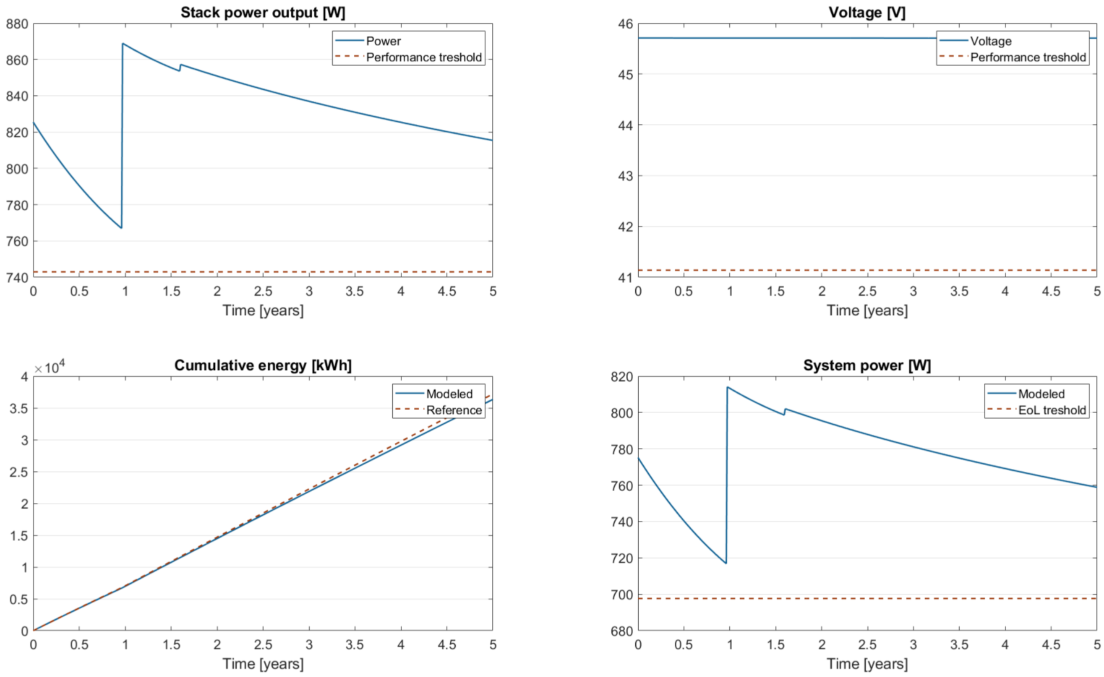

Figure A.15: Maximization of electrical efficiency with fixed voltage, EoL evaluation.

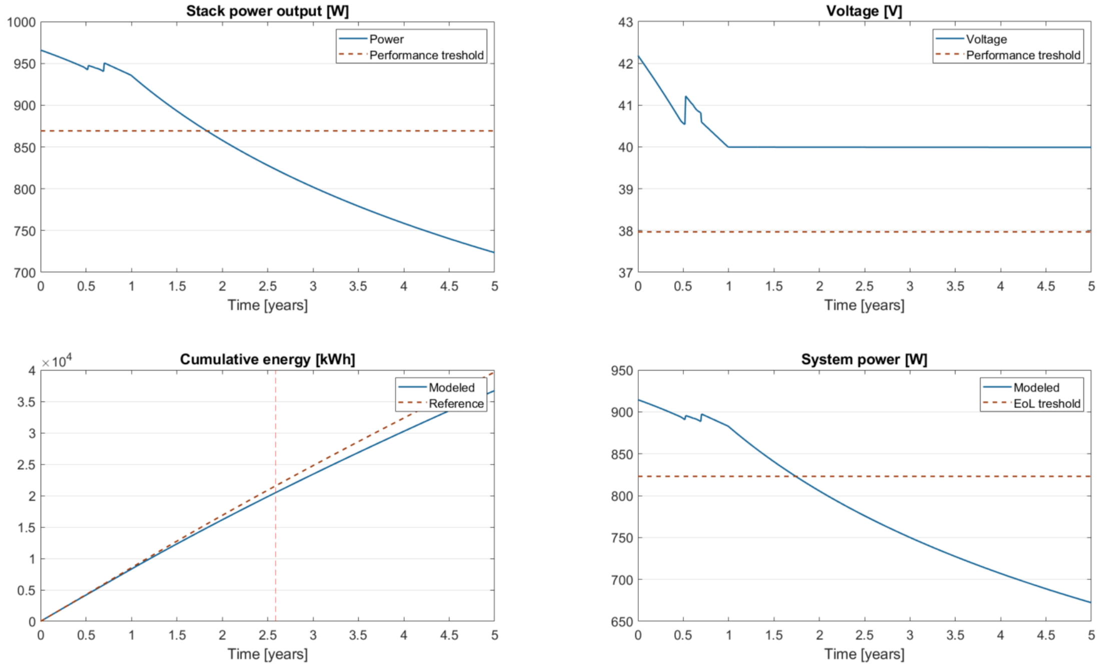

Figure A.16: Maximization of electrical efficiency with fixed temperature, EoL evaluation.

A.5 Maximization of CHP efficiency with fixed power, voltage, and temperature

The optimization results are shown in the following figures.

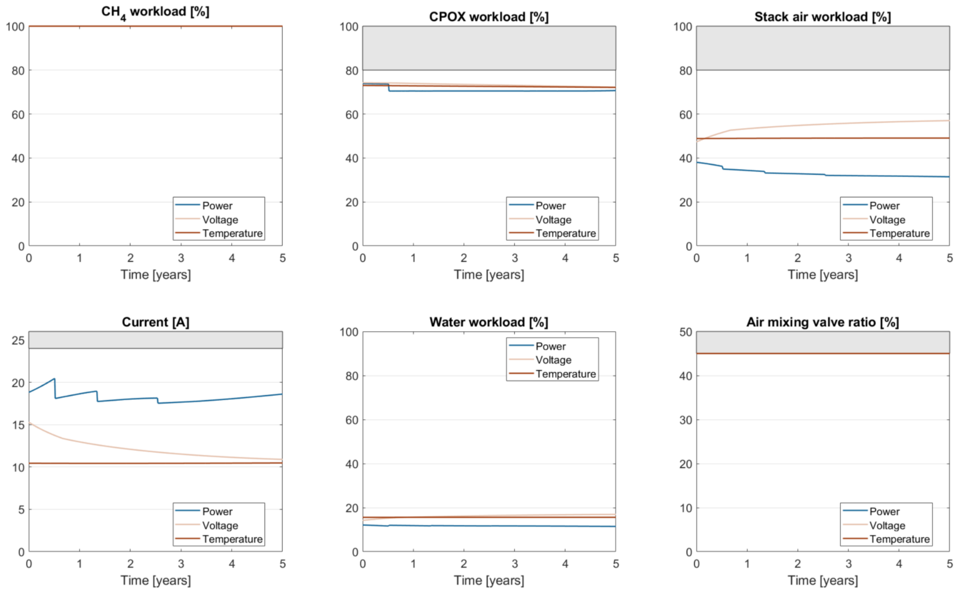

Figure A.17: Maximization of CHP efficiency with fixed outputs, inputs.

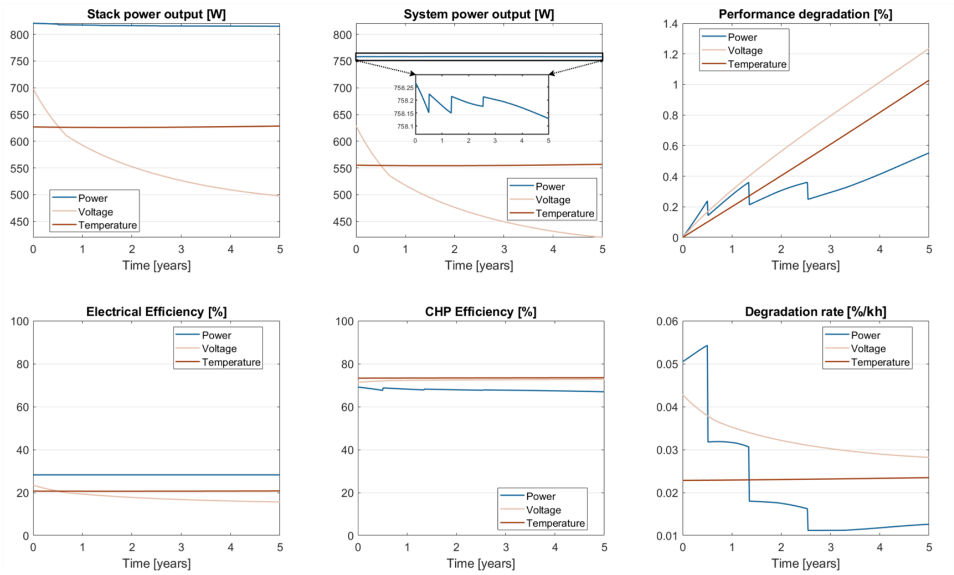

Figure A.18: Maximization of CHP efficiency with fixed outputs, key indicators part 1.

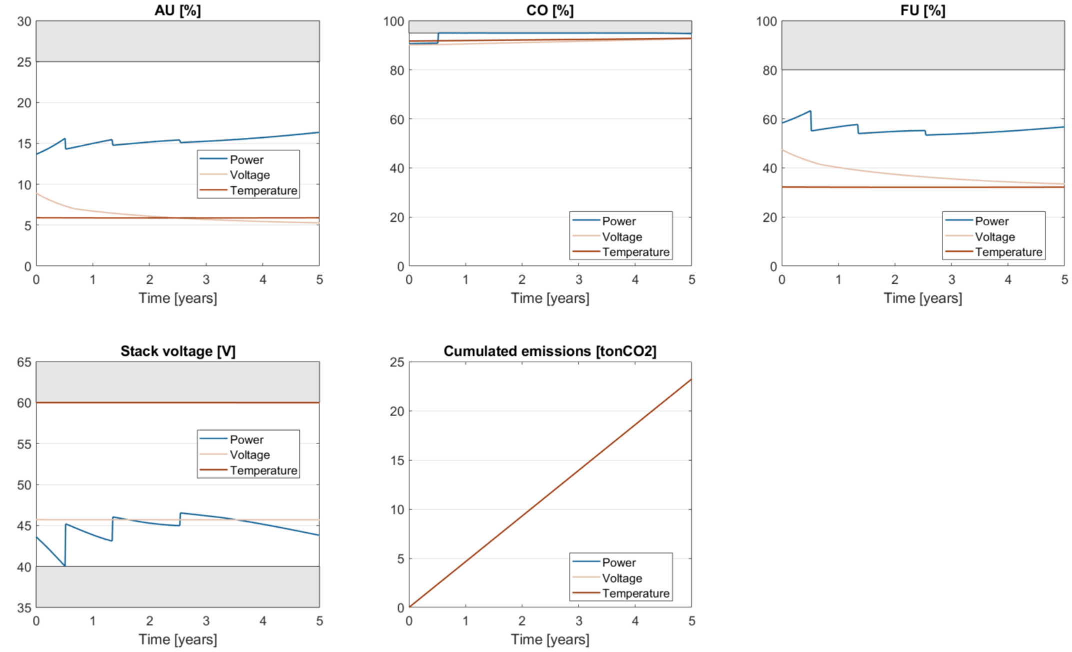

Figure A.19: Maximization of CHP efficiency with fixed outputs, key indicators part 2.

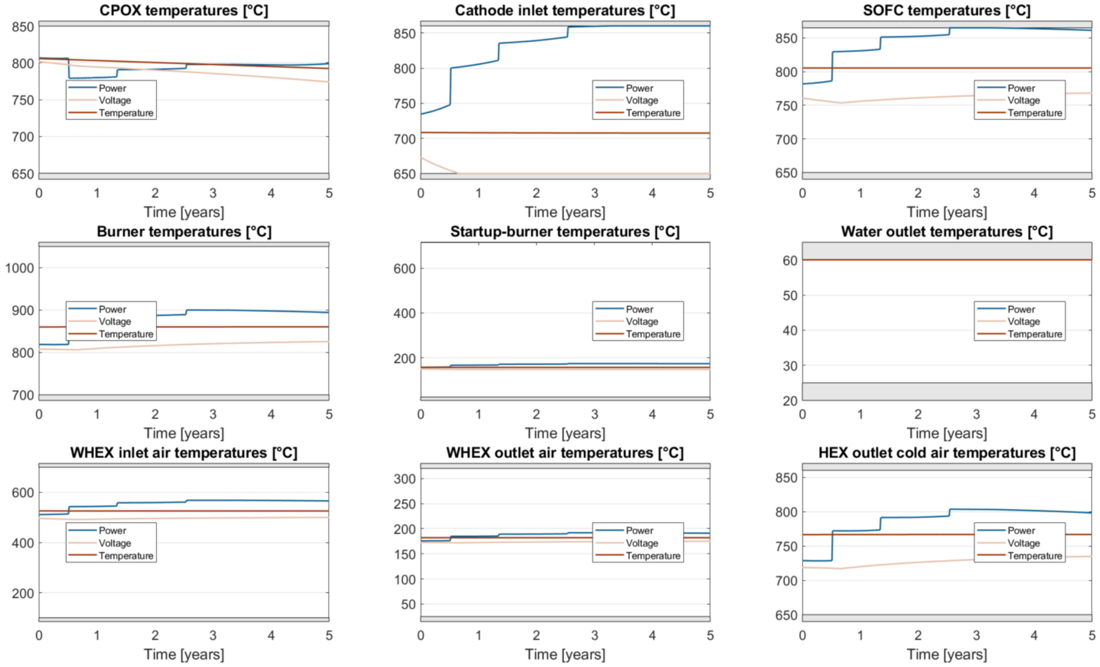

Figure A.20: Maximization of CHP efficiency with fixed outputs, temperatures.

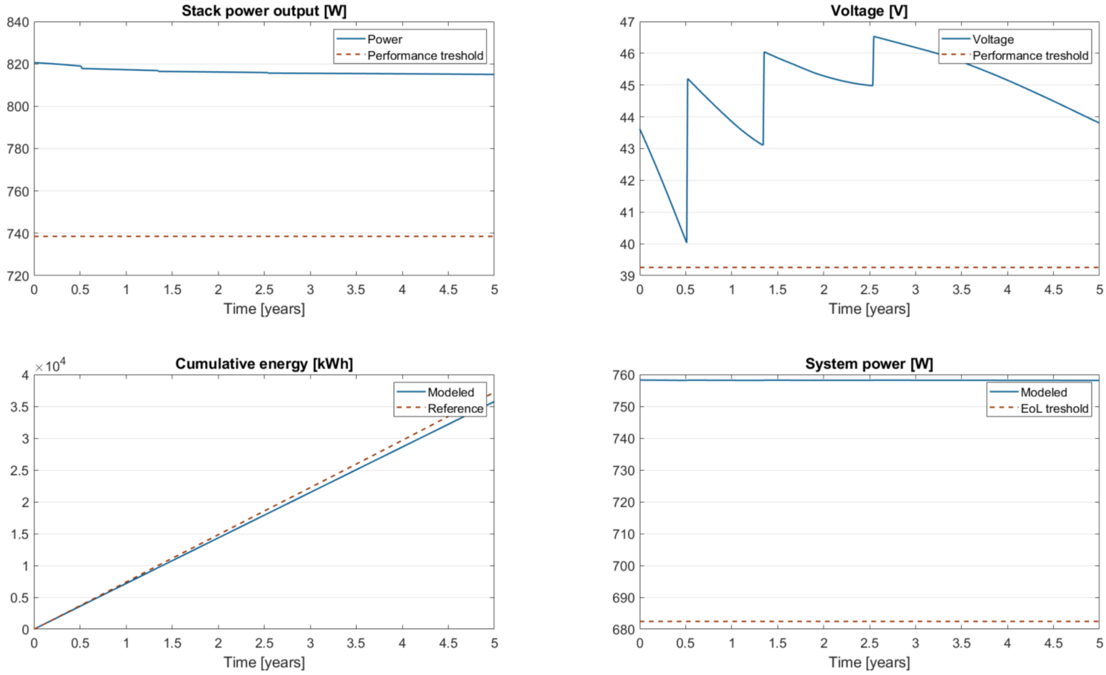

Figure A.21: Maximization of CHP efficiency with fixed power, EoL evaluation.

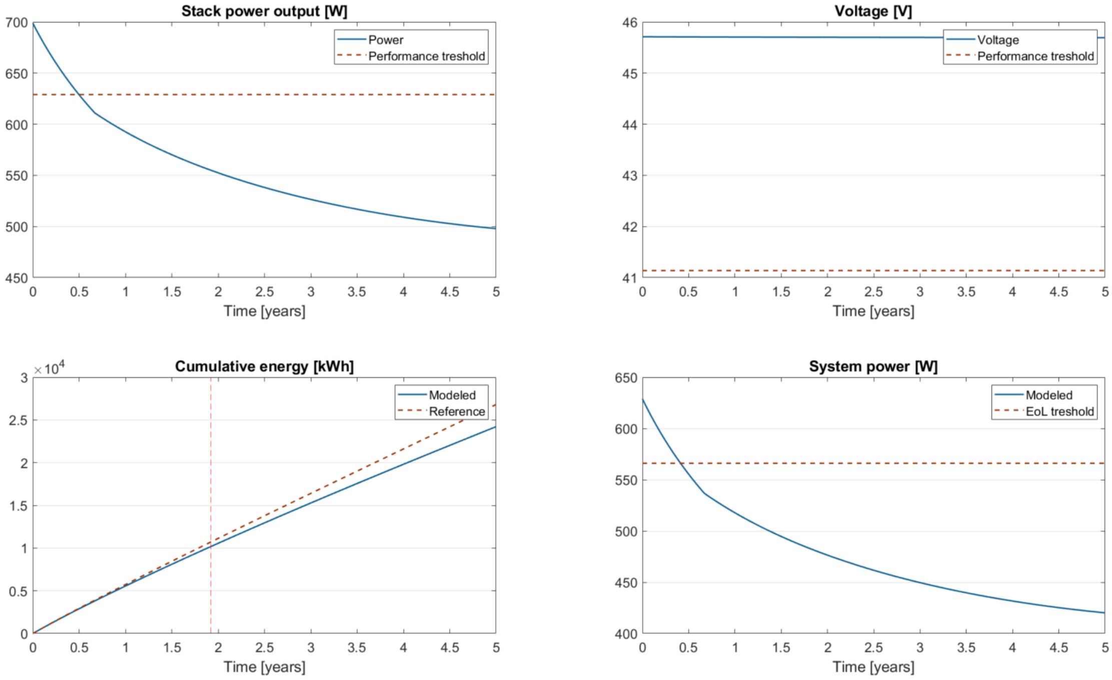

Figure A.22: Maximization of CHP efficiency with fixed voltage, EoL evaluation.

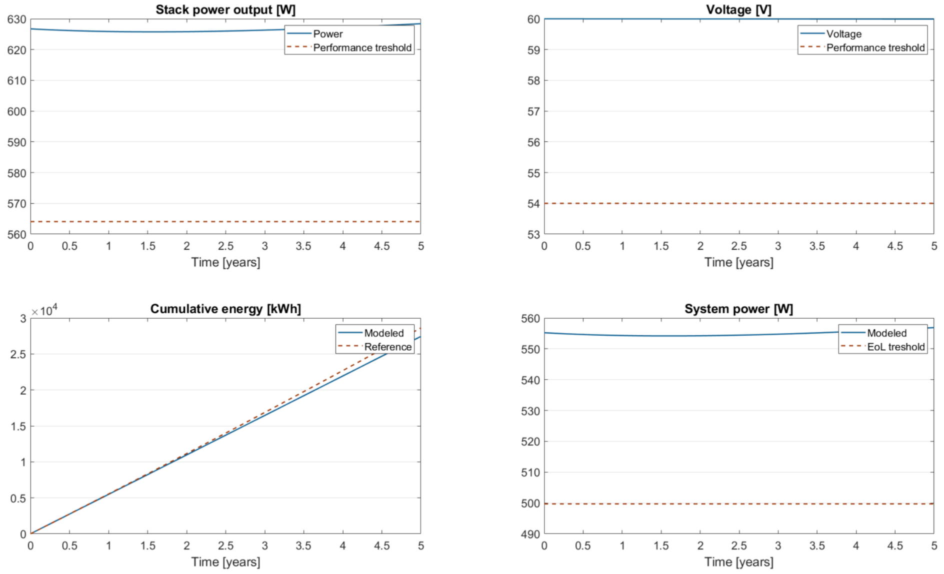

Figure A.23: Maximization of CHP efficiency with fixed temperatures, EoL evaluation.

A.6 Maximization Net Operating Income with fixed power, voltage, and temperature

The optimization results are shown in the following figures.

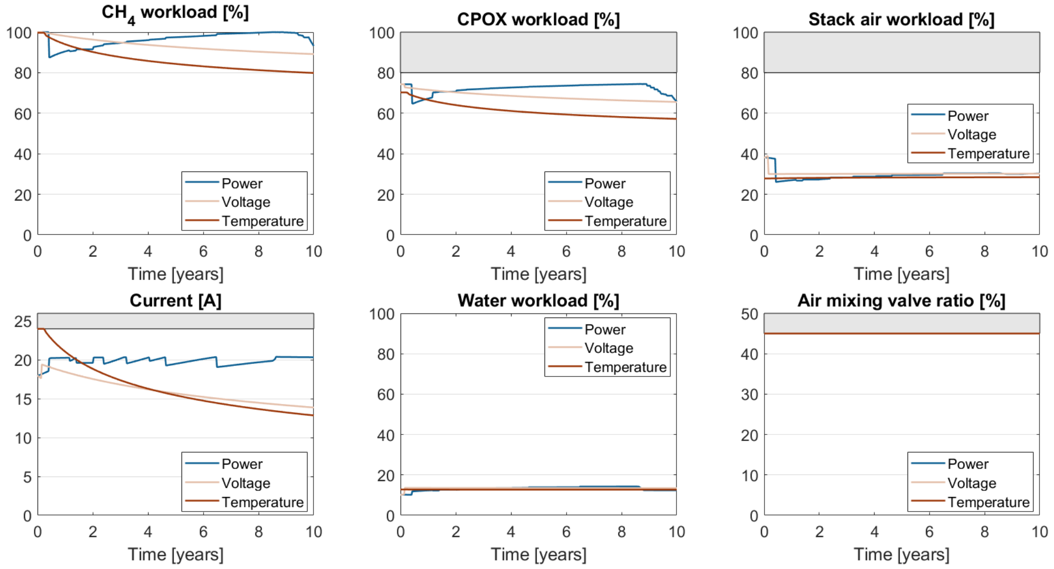

Figure A.24: Maximization of net operating income with fixed outputs, inputs.

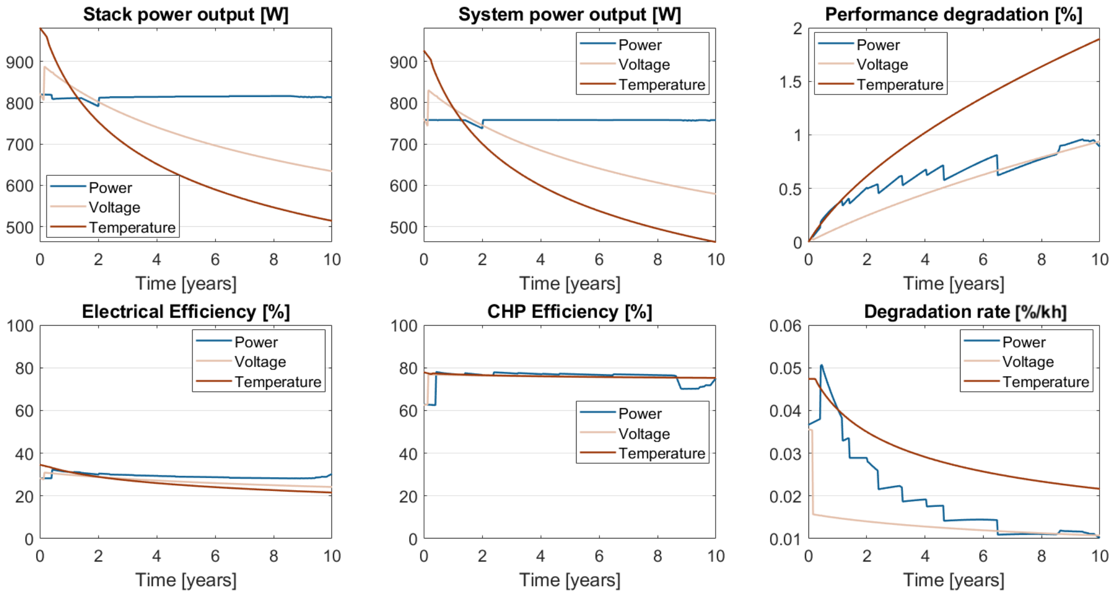

Figure A.25: Maximization of net operating income with fixed outputs, key indicators part 1.

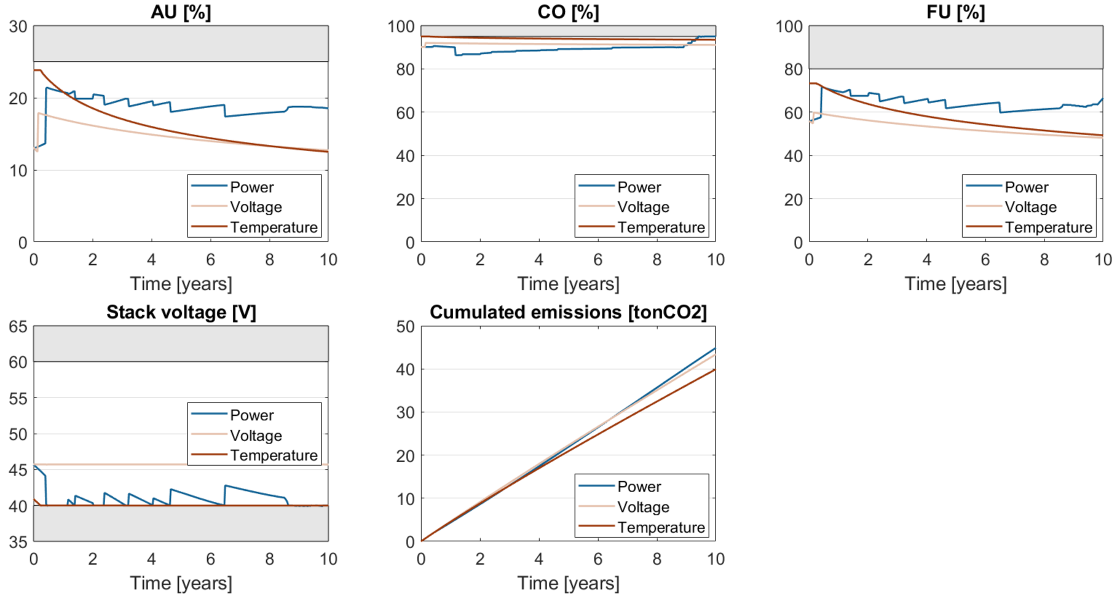

Figure A.26: Maximization of net operating income with fixed outputs, key indicators part 2.

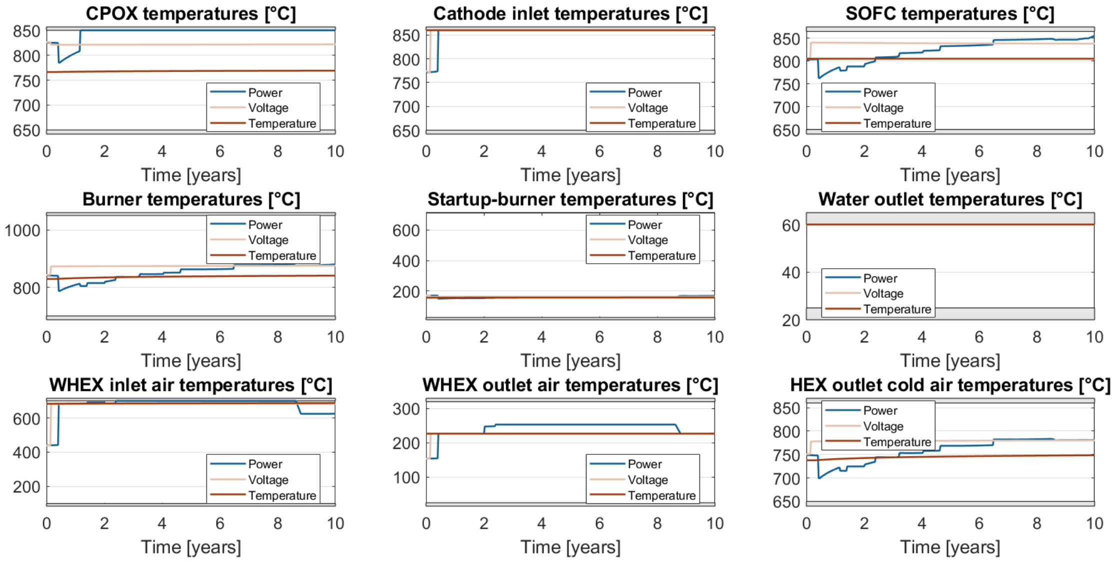

Figure A.27: Maximization of net operating income with fixed outputs, temperatures.

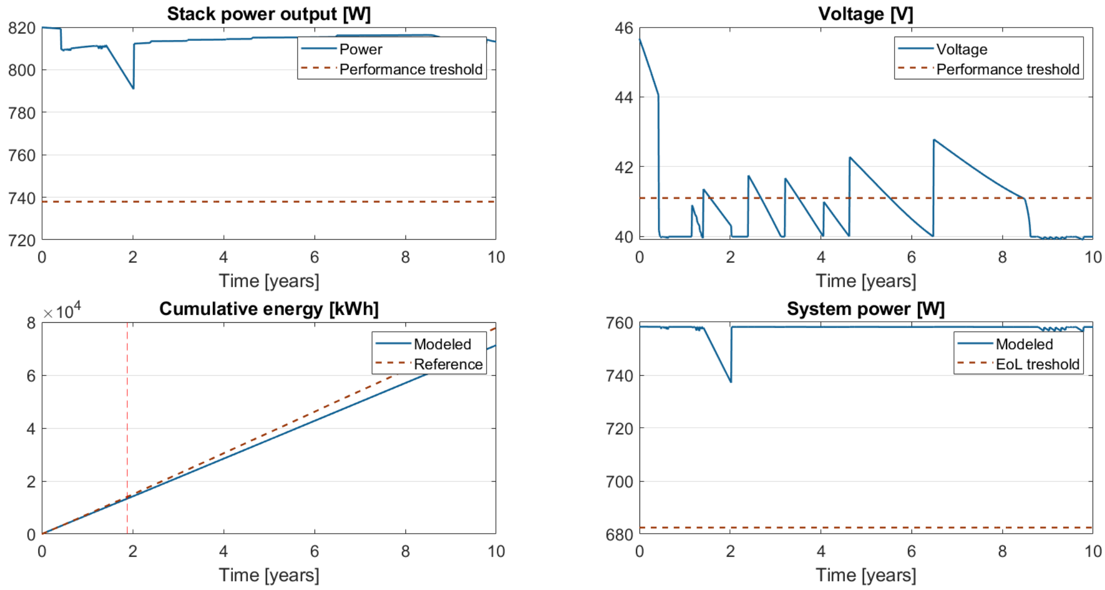

Figure A.28: Maximization of net operating income with fixed power, EoL evaluation.

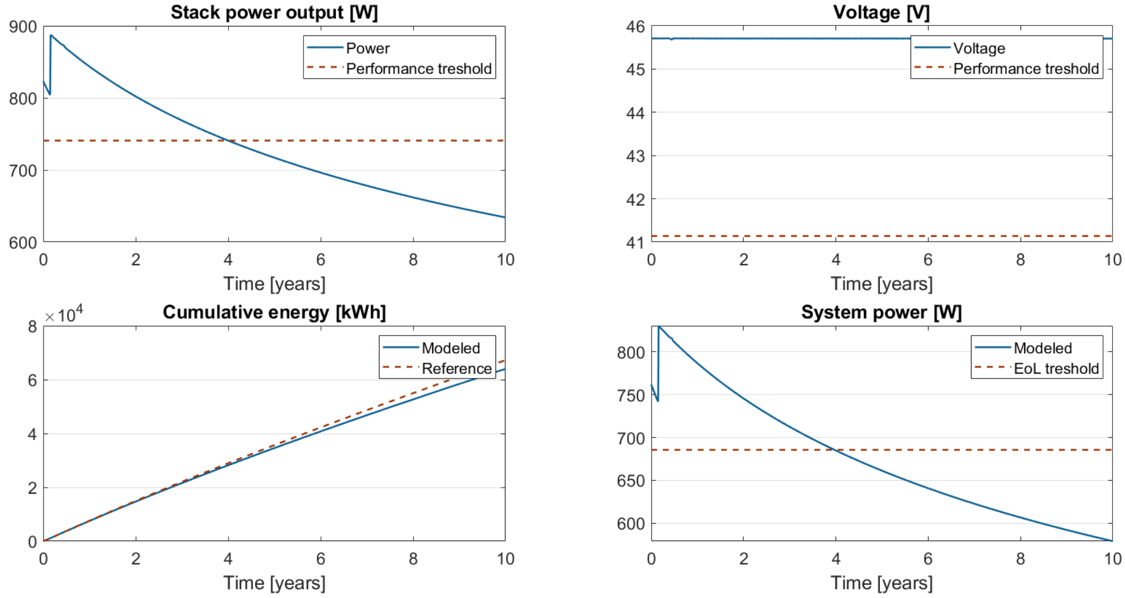

Figure A.29: Maximization of net operating income with fixed voltage, EoL evaluation.

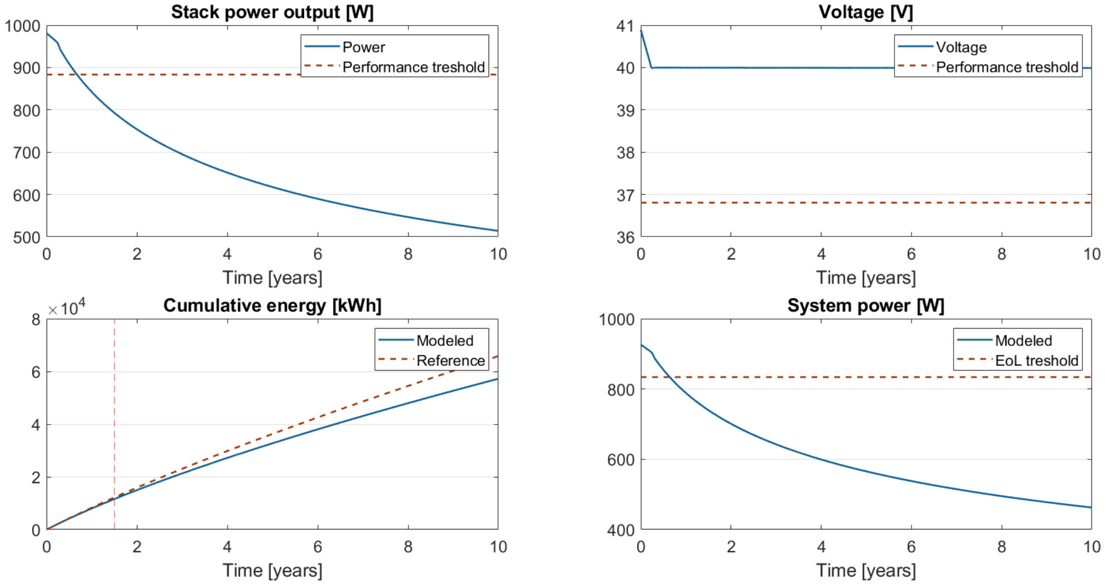

Figure A.30: Maximization of net operating income with fixed temperature, EoL evaluation.

A.7 Dynamic profile optimization results

All the missing results in the main analysis are plotted in the following figures.

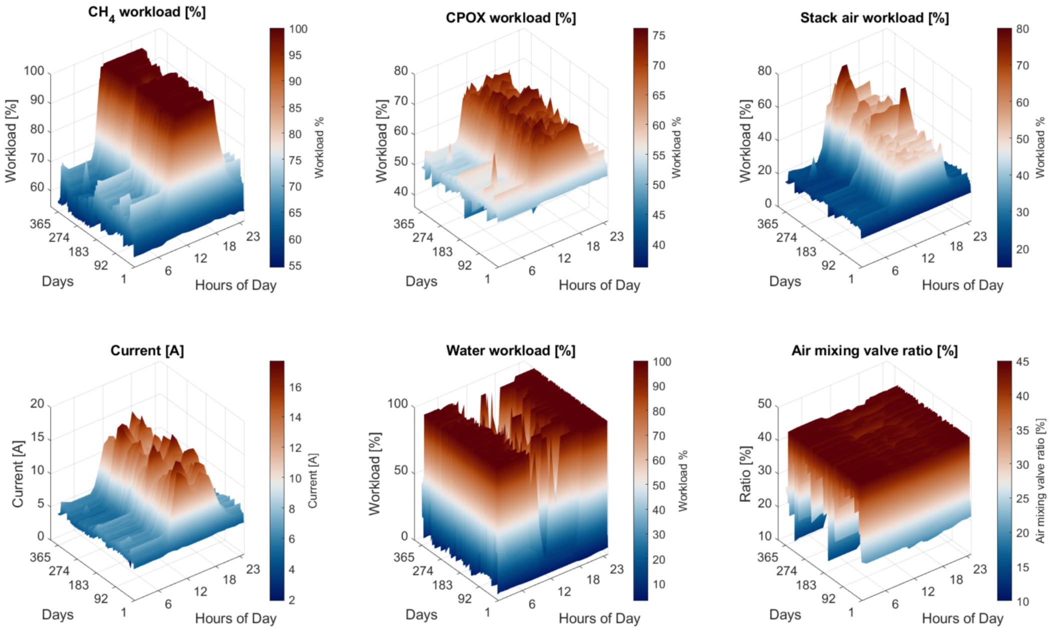

Figure A.31: Dynamic profile analysis minimizing degradation rate, inputs.

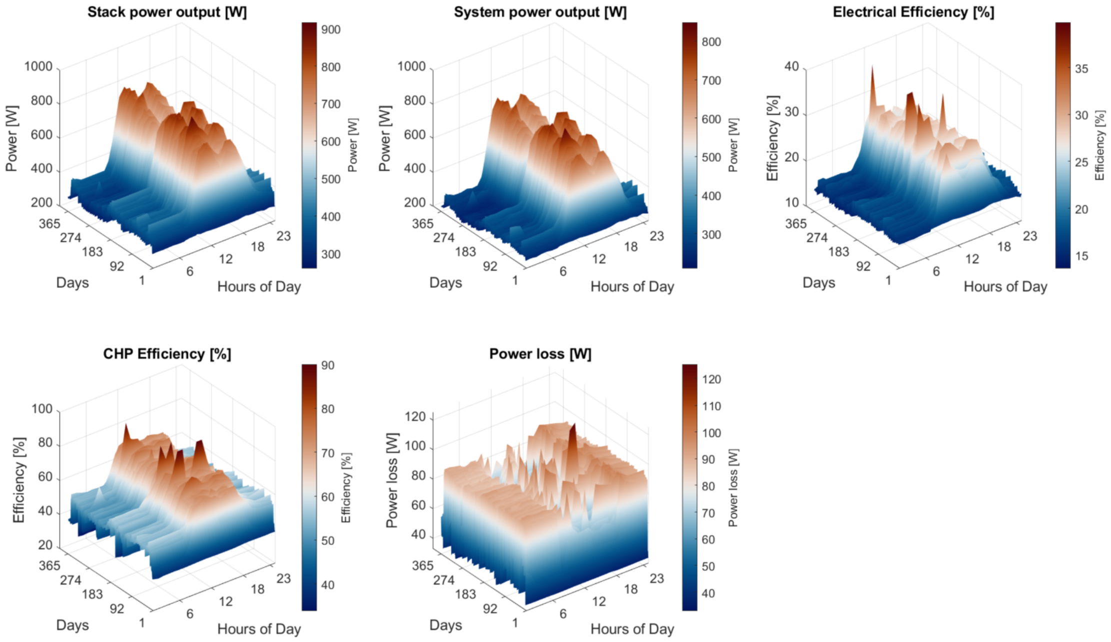

Figure A.32: Dynamic profile analysis minimizing degradation rate, key indicators 1.

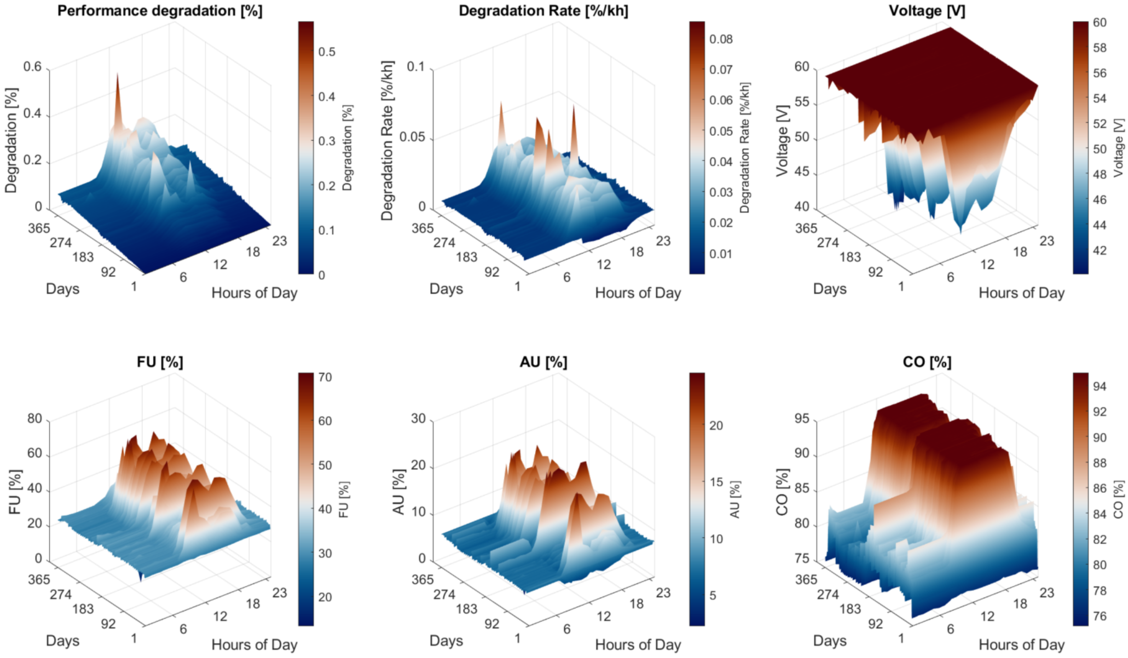

Figure A.33: Dynamic profile analysis minimizing degradation rate, key indicators 2.

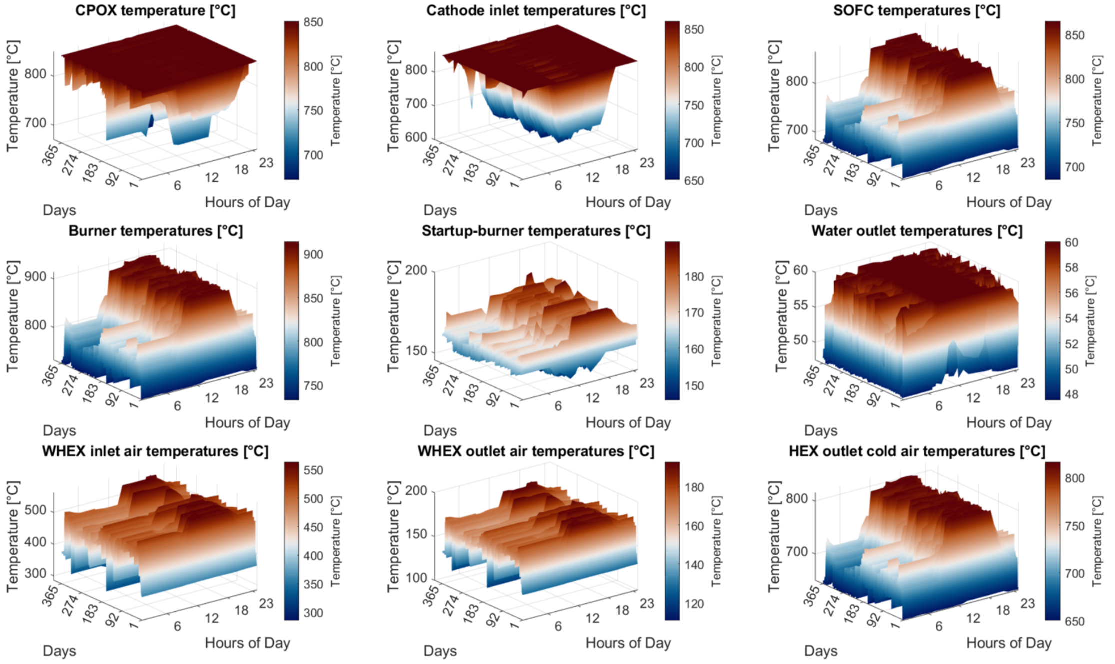

Figure A.34: Dynamic profile analysis minimizing degradation rate, temperatures.

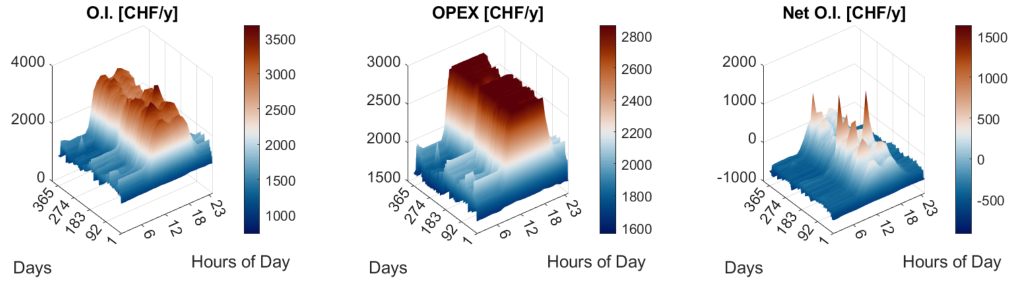

Figure A.35: Dynamic profile analysis minimizing degradation rate, techno-economics.

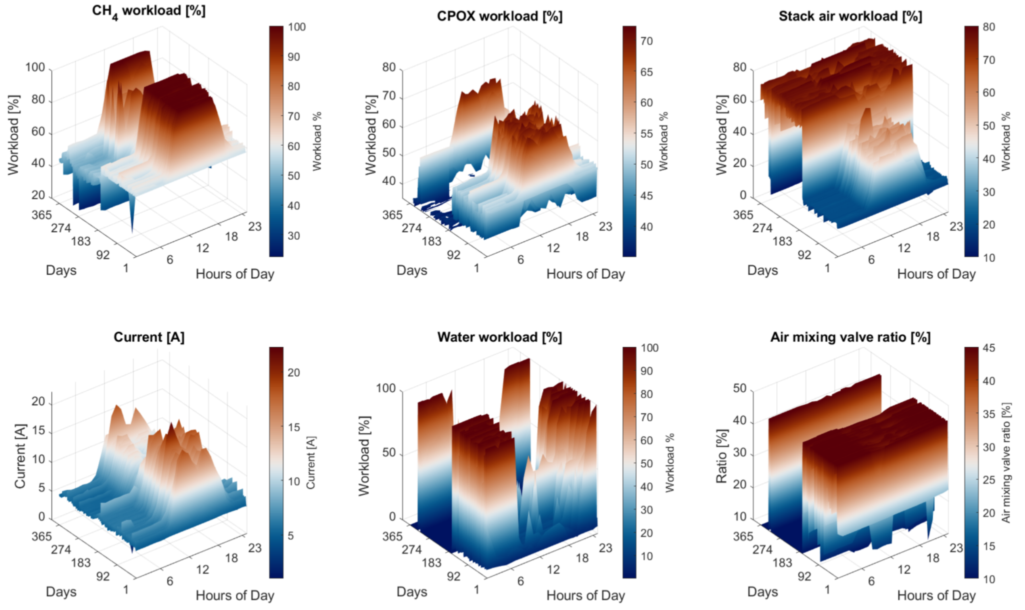

Figure A.36: Dynamic profile analysis maximizing electrical efficiency, inputs.

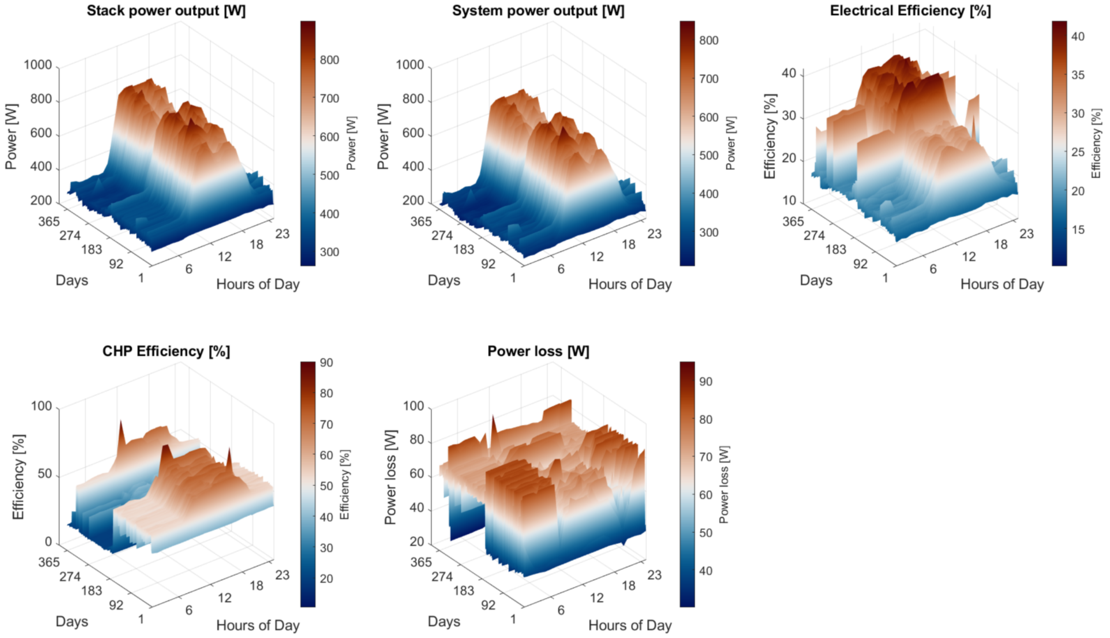

Figure A.37: Dynamic profile analysis maximizing electrical efficiency, key indicators 1.

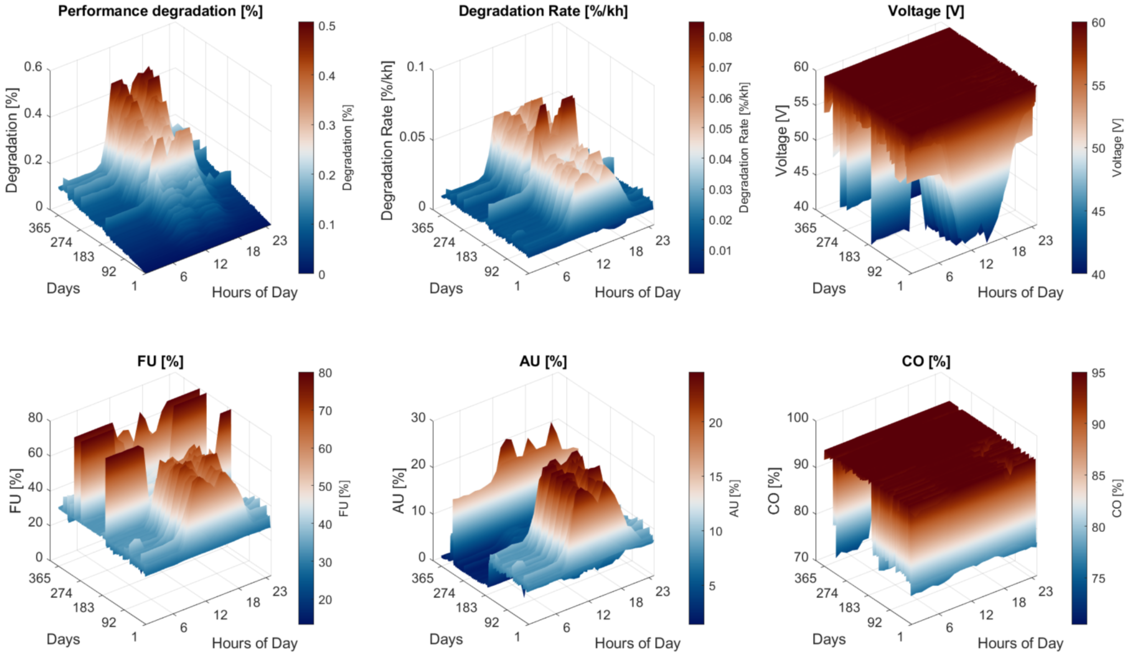

Figure A.38: Dynamic profile analysis maximizing electrical efficiency, key indicators 2.

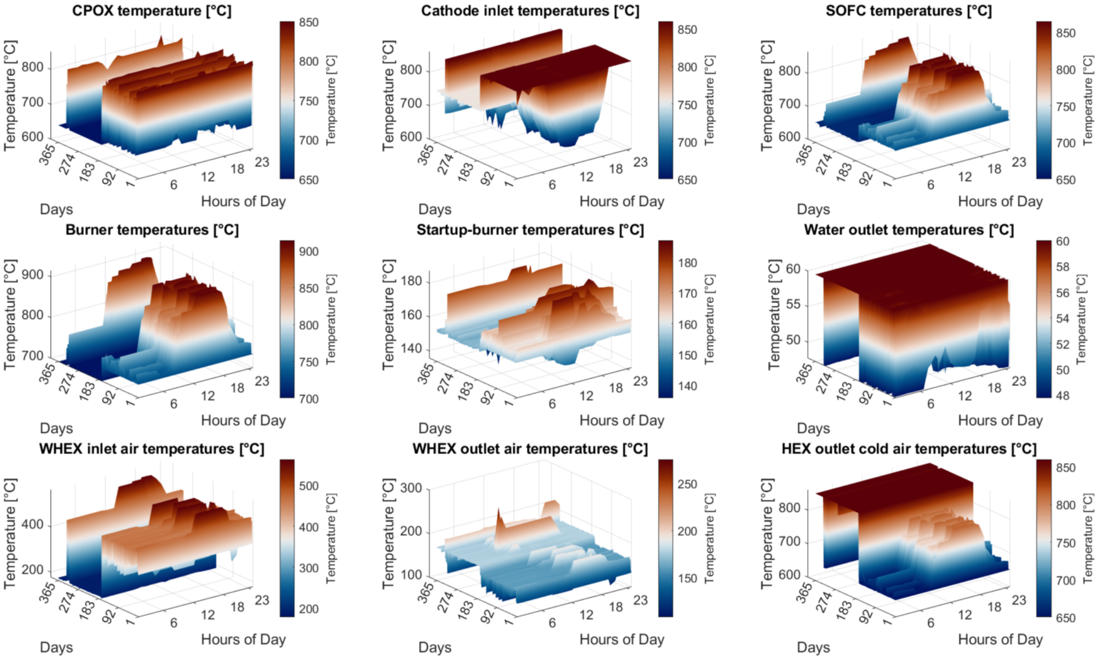

Figure A.39: Dynamic profile analysis maximizing electrical efficiency, key indicators 2.

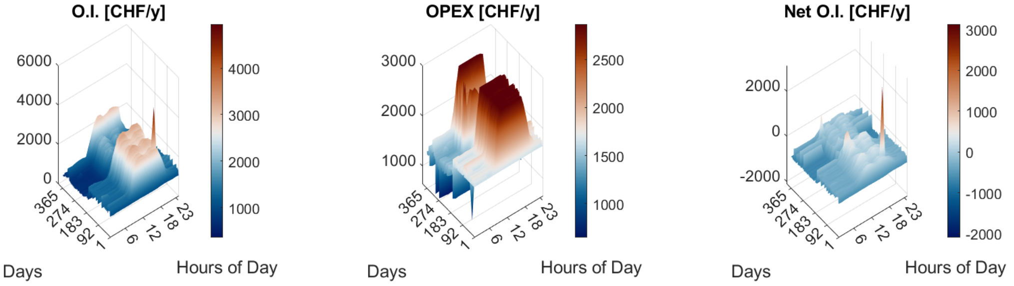

Figure A.40: Dynamic profile analysis maximizing electrical efficiency, techno-economics.

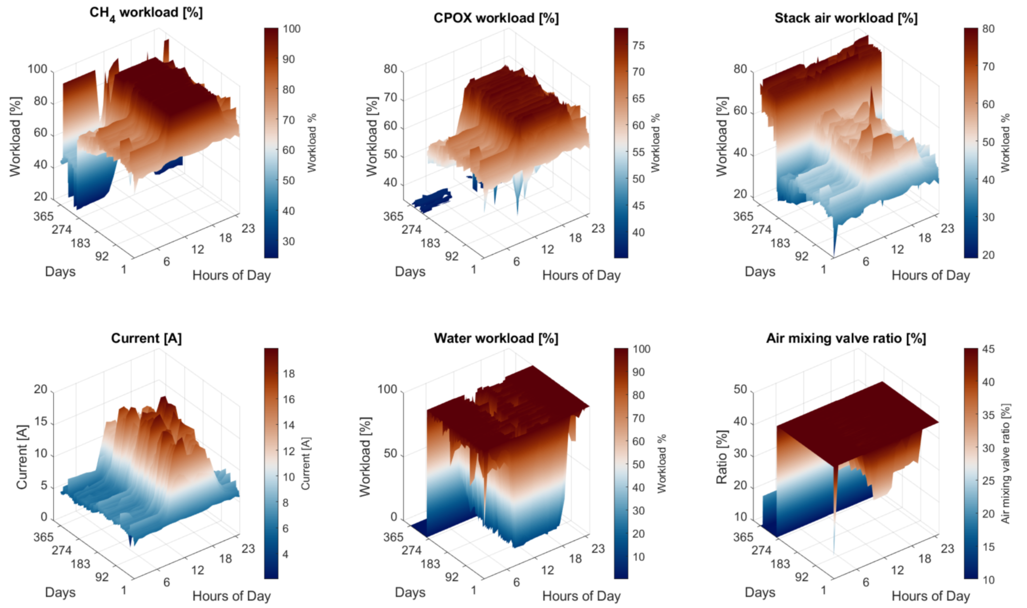

Figure A.41: Dynamic profile analysis maximizing net operating income, inputs.

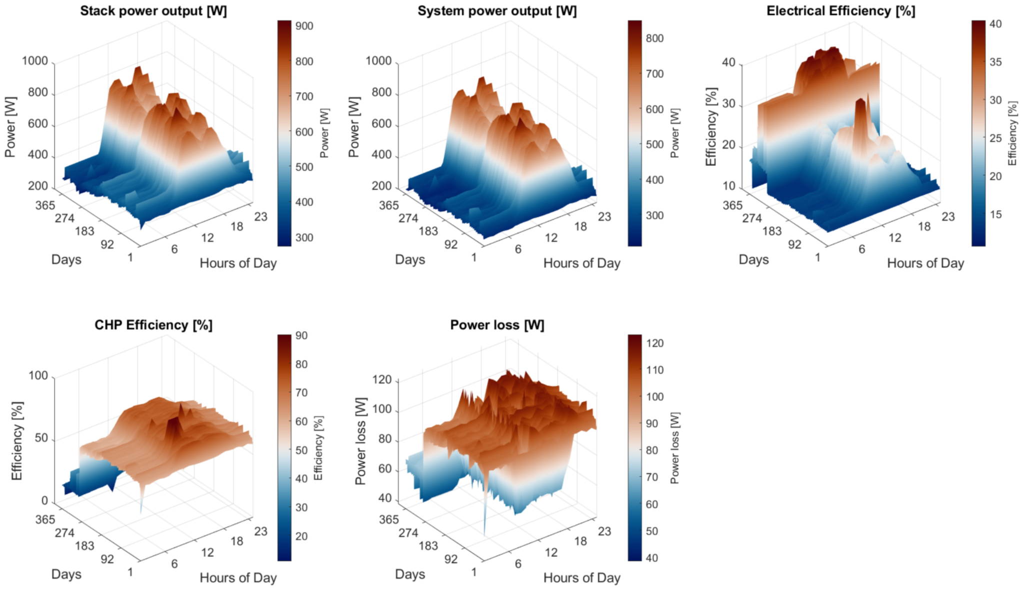

Figure A.42: Dynamic profile analysis maximizing net operating income, key indicators part 1.

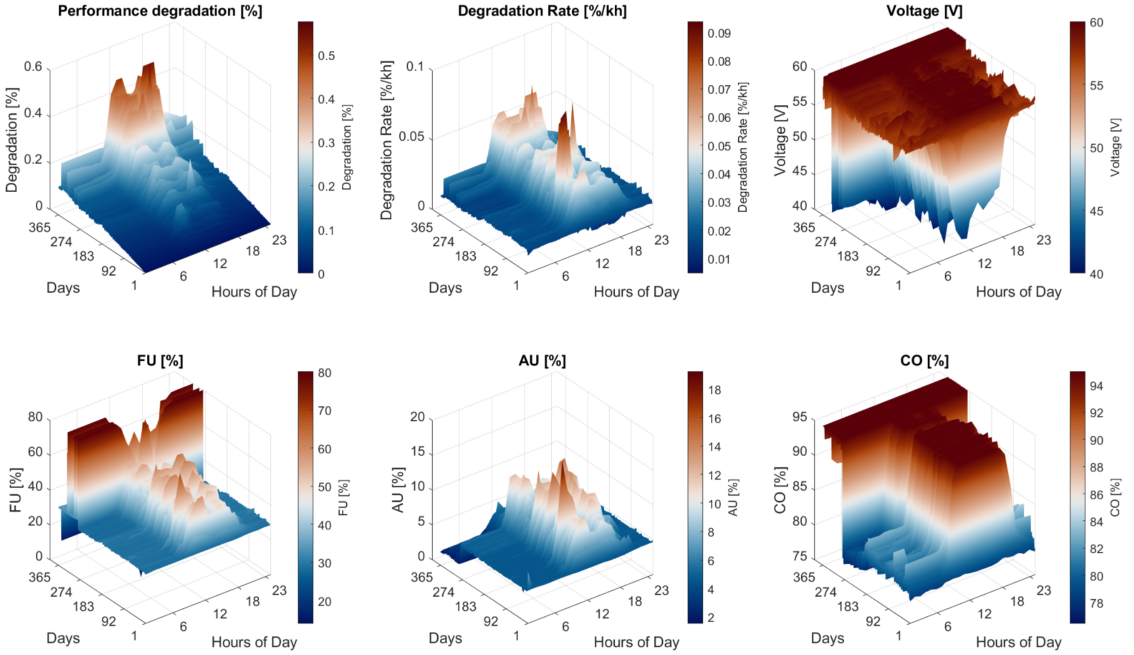

Figure A.43: Dynamic profile analysis maximizing net operating income, key indicators part 2.

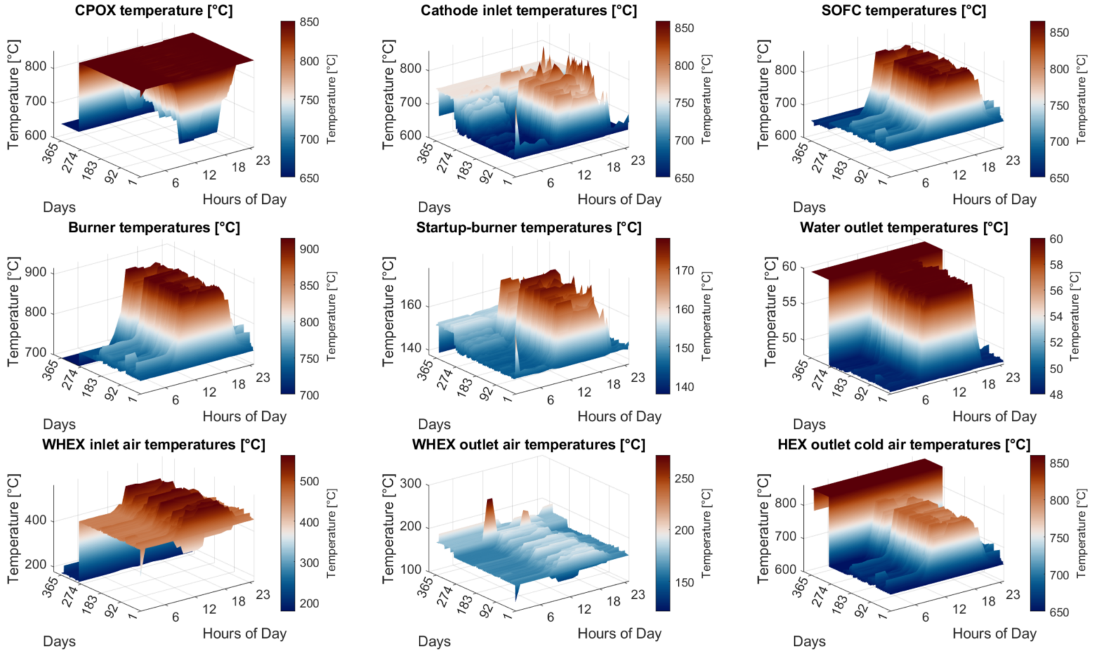

Figure A.44: Dynamic profile analysis maximizing net operating income, temperatures.

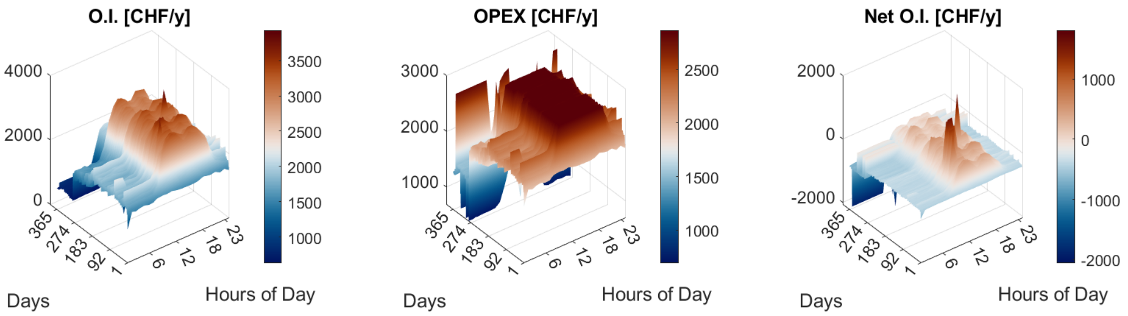

Figure A.45: Dynamic profile analysis maximizing net operating income, techno-economics.

Bibliography

[1] Ioannis Manisalidis et al. “Environmental and health impacts of air pollution: A review”. In: *Frontiers in Public Health* 8 (2020), p. 14. DOI: 10.3389/fpubh.2020.00014.

[2] United Nations Framework Convention on Climate Change. *Paris Agreement*. https://unfccc.int/sites/default/files/english_paris_agreement.pdf. Accessed: date-of-access. 2015.

[3] NASA and Potsdam Institute for Climate Impact Research. *Data collected via Climate Watch*. Provided by NASA; Potsdam Institute for Climate Impact Research via Climate Watch. 2023.

[4] International Energy Agency (IEA). *CO2 Emissions in 2022*. https://www.iea.org/reports/co2-emissions-in-2022. Licence: CC BY 4.0. Paris, 2023.

[5] World Economic Forum. “Solar and wind power are key to fighting climate change. Here’s how they can be expanded”. In: *World Economic Forum* (2022). URL: https://www.weforum.org/agenda/2022/03/solar-wind-power-renewable-energy-climate-change/.

[6] International Energy Agency (IEA). *Renewables 2023*. https://www.iea.org/reports/renewables-2023. Licence: CC BY 4.0. Paris, 2024.

[7] ERM Group Company - E4tech. *The Fuel Cell Industry Review 2021*. https://www.erm.com/globalassets/documents/fuel-cell-industry-review/thefuelcellindustryreview2021.pdf. Accessed: 2024-02-25. 2021.

[8] Mandeep Singh, Dario Zappa, and Elisabetta Comini. “Solid oxide fuel cell: Decade of progress, future perspectives and challenges”. In: *International Journal of Hydrogen Energy* 46.54 (2021), pp. 27643–27674. ISSN: 0360-3199. DOI: doi.org/10.1016/j.ijhydene.2021.06.020. URL: sciencedirect.com/science/article/pii/S0360319921021704.

[9] Kevin Huang and John B. Goodenough. *Solid Oxide Fuel Cell Technology: Principles, Performance, and Operations*. ID: ebk01:2510000000010548. 2009. ISBN: 9781845696511. URL: http://lib.ugent.be/catalog/ebk01:2510000000010548.

[10] S. Ali Saadabadi et al. “Solid Oxide Fuel Cells fuelled with biogas: Potential and constraints”. In: *Renewable Energy* 134 (2019), pp. 194–214. ISSN: 0960-1481. DOI: doi.org/10.1016/j.renene.2018.11.028. URL: sciencedirect.com/science/article/pii/S0960148118313478.

[11] Nikdalila Radenahmad et al. “A review on biomass derived syngas for SOFC based combined heat and power application”. In: *Renewable and Sustainable Energy Reviews* 119 (2020), p. 109560. ISSN: 1364-0321. DOI: doi.org/10.1016/j.rser.2019.109560. URL: sciencedirect.com/science/article/pii/S1364032119307683.

[12] Sanaz Zarabi Golkhatmi, Muhammad Imran Asghar, and Peter D. Lund. “A review on solid oxide fuel cell durability: Latest progress, mechanisms, and study tools”. In: *Renewable and Sustainable Energy Reviews* 161 (2022), p. 112339. ISSN: 1364-0321. DOI: doi.org/10.1016/j.rser.2022.112339. URL: sciencedirect.com/science/article/pii/S1364032122002520.

[13] Shahzad Hossain et al. “A review on proton conducting electrolytes for clean energy and intermediate temperature-solid oxide fuel cells”. In: *Renewable and Sustainable Energy Reviews* 79 (2017), pp. 750–764. ISSN: 1364-0321. DOI: doi.org/10.1016/j.rser.2017.05.147. URL: sciencedirect.com/science/article/pii/S1364032117308018.

[14] Tianyu Chen et al. “Highly efficient direct carbon solid oxide fuel cells operated with camellia oleifera biomass”. In: *Electrochimica Acta* 423 (2022), p. 140594. ISSN: 0013-4686. DOI: doi.org/10.1016/j.electacta.2022.140594. URL: sciencedirect.com/science/article/pii/S0013468622007538.

[15] Andre Weber. “Fuel flexibility of solid oxide fuel cells”. In: *Fuel Cells* 21.5 (Aug. 2021), pp. 440–452. ISSN: 1615-6854. DOI: 10.1002/fuce.202100037. URL: dx.doi.org/10.1002/fuce.202100037.

[16] David Bierschenk et al. “A Proposed Method for High Efficiency Electrical Energy Storage Using Solid Oxide Cells”. In: vol. 35. Apr. 2011, pp. 2969–2978. DOI: 10.1149/1.3570297.

[17] Christoph Peters. “Grain-size effects in nanoscaled electrolyte and cathode thin films for solid oxide fuel cells”. English. Dissertation. Karlsruhe: Karlsruhe Institute of Technology, 2009, pp. VIII, 155. ISBN: 978-3-86644-336-5. DOI: 10.5445/KSP/1000010126.

[18] Priscilla Caliandro. “Identification of Solid Oxide Cell Elementary Processes by Electrochemical Impedance Spectroscopy”. PhD Thesis. Sion: EPFL, Dec. 2018. URL: http://infoscience.epfl.ch/record/255087.

[19] Fritz Scholz, Allen J. Bard, and György Inzelt. *Electrochemical Dictionary*. Springer-Verlag Berlin Heidelberg, 2012. ISBN: 978-3-642-29550-8. DOI: 10.1007/978-3-642-29551-5.

[20] J.H. Song et al. “Title of the Article”. In: *J. Fuel Cell Sci. Technol.* 5 (2008), pp. 021003–1.

[21] Andrzej Lasia. *Electrochemical Impedance Spectroscopy and its Applications*. New York, NY: Springer, 2014. ISBN: 978-1-4614-8932-0.

[22] André Leonide. “SOFC modelling and parameter identification by means of impedance spectroscopy”. PhD thesis. Karlsruhe: Karlsruher Institut für Technologie (KIT), 2010. ISBN: 978-3-86644-538-3. DOI: 10.5445/KSP/1000019173. URL: https://publikationen.bibliothek.kit.edu/1000019173.

[23] Vanja Subotić and Christoph Hochenauer. "Analysis of solid oxide fuel and electrolysis cells operated in a real-system environment: State-of-the-health diagnostic, failure modes, degradation mitigation and performance regeneration". In: *Progress in Energy and Combustion Science* 93 (Nov. 2022), p. 101011. ISSN: 0360-1285. DOI: 10.1016/j.pecs.2022.101011. URL: dx.doi.org/10.1016/j.pecs.2022.101011.

[24] Zhan Gao et al. "A perspective on low-temperature solid oxide fuel cells". In: *Energy Environ. Sci.* 9 (2016), pp. 1602–1644. DOI: 10.1039/C5EE03858H.

[25] Ruth Knibbe et al. "Durability of Solid Oxide Cells". In: *Green* 1.4 (2011), pp. 1–15. DOI: 10.1515/green.2011.015.

[26] A. Nakajo et al. "Evolution of the Morphology Near Triple-Phase Boundaries in Ni–Yttria Stabilized Zirconia Electrodes Upon Cathodic Polarization". In: *ASME J. Electrochem. En. Conv. Stor.* 17.4 (Nov. 2020), p. 041004. DOI: 10.1115/1.4046478. URL: https://doi.org/10.1115/1.4046478.

[27] M.B. Mogensen et al. "Relation Between Ni Particle Shape Change and Ni Migration in Ni–YSZ Electrodes – a Hypothesis". In: *Fuel Cells* 17 (2017), pp. 434–441. DOI: 10.1002/fuce.201600222.

[28] Zhenjun Jiao et al. "Study on local morphological changes of nickel in solid oxide fuel cell anode using porous Ni pellet electrode". In: *Journal of Power Sources* 196 (3 2011), pp. 1019–1029. DOI: 10.1016/j.jpowsour.2010.08.047.

[29] F. Monaco et al. "Degradation of Ni-YSZ Electrodes in Solid Oxide Cells: Impact of Polarization and Initial Microstructure on the Ni Evolution". In: *Journal of The Electrochemical Society* 166.15 (2019), F1229. DOI: 10.1149/2.0281915jes.

[30] Yi Wang et al. "Degradation of solid oxide electrolysis cells: Phenomena, mechanisms, and emerging mitigation strategies—A review". In: *Journal of Materials Science & Technology* 55 (2020), pp. 35–55. ISSN: 1005-0302. DOI: 10.1016/j.jmst.2019.07.026.

[31] Y. Zheng et al. "Advanced Materials for Solid Oxide Fuel Cells". In: *Chemical Society Reviews* 46 (2017), pp. 1427–1463. DOI: 10.1039/C6CS00073J.

[32] C. Chatzichristodoulou et al. "Understanding Degradation Mechanisms in Electrolyte-Supported Solid Oxide Fuel Cells for Improved Cell Design". In: *Electrochimica Acta* 189 (2016), pp. 265–282. DOI: 10.1016/j.electacta.2015.12.176.

[33] N. Schrödl, E. Bucher, A. Egger, et al. "Long-Term Stability of the IT-SOFC Cathode Materials La0.6Sr0.4CoO3 - and La2NiO4 Against Combined Chromium and Silicon Poisoning". In: *Solid State Ionics* 276 (2015), pp. 62–71. DOI: 10.1016/j.ssi.2015.03.035.

[34] X. Yin, L. Bencze, V. Motalov, et al. "Thermodynamic Perspective of Sr-Related Degradation Issues in SOFCs". In: *International Journal of Applied Ceramic Technology* 15 (2018), pp. 380–390. DOI: 10.1111/ijac.12809.

[35] X. Chen et al. "Chromium Deposition and Poisoning in Dry and Humidified Air at (La0.8Sr0.2)0.9MnO3 Cathodes of Solid Oxide Fuel Cells". In: *International Journal of Hydrogen Energy* 35 (2010), pp. 2477–2485. DOI: 10.1016/j.ijhydene.2009.12.185.

[36] I. Sreedhar, B. Agarwal, P. Goyal, et al. “An Overview of Degradation in Solid Oxide Fuel Cells—Potential Clean Power Sources”. In: *Journal of Solid State Electrochemistry* 24 (2020), pp. 1239–1270. DOI: 10.1007/s10008-020-04584-4.

[37] Khalid Al-Khori et al. “Life Cycle Assessment for Integration of Solid Oxide Fuel Cells into Gas Processing Operations”. In: *Energies* 14.15 (Aug. 2021), p. 4668. ISSN: 1996-1073. DOI: 10.3390/en14154668. URL: http://dx.doi.org/10.3390/en14154668.

[38] Hilmi Hisyam Naimin et al. “Cleaner Power Generation: An In-depth Review of Life Cycle Assessment for Solid Oxide Fuel Cells”. In: *Jurnal Kejuruteraan* si6.2 (Dec. 2023), pp. 257–267. ISSN: 2289-7526. DOI: 10.17576/jkukm-2023-si6(2)-27. URL: http://dx.doi.org/10.17576/jkukm-2023-si6(2)-27.

[39] Marta Gandiglio et al. “Life Cycle Assessment of a Biogas-Fed Solid Oxide Fuel Cell (SOFC) Integrated in a Wastewater Treatment Plant”. In: *Energies* 12.9 (Apr. 2019), p. 1611. ISSN: 1996-1073. DOI: 10.3390/en12091611. URL: http://dx.doi.org/10.3390/en12091611.

[40] E. Ivers-Tiffée and A. V. Virkar. “Electrode Polarisations”. In: *High Temperature Solid Oxide Fuel Cells - Fundamentals, Design and Applications*. Ed. by S.C. Singhal and K. Kendall. Oxford, UK: Elsevier Ltd, 2003, pp. 229–260.

[41] Mohamed Derbeli, Oscar Barambones, and Lassaad Sbita. “A Robust Maximum Power Point Tracking Control Method for a PEM Fuel Cell Power System”. In: *Lied Sciences* (2018). Received: 2 November 2018; Accepted: 29 November 2018; Published: 1 December 2018.

[42] K. Wang et al. “A Review on solid oxide fuel cell models”. In: *International Journal of Hydrogen Energy* 36.12 (June 2011), pp. 7212–7228. ISSN: 0360-3199. DOI: 10.1016/j.ijhydene.2011.03.051. URL: http://dx.doi.org/10.1016/j.ijhydene.2011.03.051.

[43] V. Zaccaria, D. Tucker, and A. Traverso. “A distributed real-time model of degradation in a solid oxide fuel cell, part I: Model characterization”. In: *Journal of Power Sources* 311 (Apr. 2016), pp. 175–181. ISSN: 0378-7753. DOI: 10.1016/j.jpowsour.2016.02.040. URL: http://dx.doi.org/10.1016/j.jpowsour.2016.02.040.

[44] V. Zaccaria, D. Tucker, and A. Traverso. “A distributed real-time model of degradation in a solid oxide fuel cell, part II: Analysis of fuel cell performance and potential failures”. In: *Journal of Power Sources* 327 (Sept. 2016), pp. 736–742. ISSN: 0378-7753. DOI: 10.1016/j.jpowsour.2016.01.027. URL: http://dx.doi.org/10.1016/j.jpowsour.2016.01.027.

[45] WY Lee, D Wee, and AF Ghoniem. “An improved one-dimensional membrane-electrode assembly model to predict the performance of solid oxide fuel cell including the limiting current density”. In: *Journal of Power Sources* 186 (2009), pp. 417–427.

[46] P Aguiar, CS Adjiman, and NP Brandon. “Anode-supported intermediate temperature direct internal reforming solid oxide fuel cell. I: model-based steady-state performance”. In: *Journal of Power Sources* 138 (2004), pp. 120–136.

[47] Gyubin Min, Young Joon Park, and Jongsup Hong. “1D thermodynamic modeling for a solid oxide fuel cell stack and parametric study for its optimal operating conditions”. In: *Energy Conversion and Management* 209 (Apr. 2020), p. 112614. DOI: 10.1016/j.enconman.2020.112614.

[48] D.F. Cheddie and N.D.H. Munroe. "A dynamic 1D model of a solid oxide fuel cell for real time simulation". In: *Journal of Power Sources* 171 (2007), pp. 634–643.

[49] M. Sorrentino. "Development of a hierarchical structure of models for simulation and control of planar solid oxide fuel cells". PhD thesis. Italy: University of Salerno, 2006.

[50] W. Jiang et al. "Parameter setting and analysis of a dynamic tubular SOFC model". In: *Journal of Power Sources* 162 (2006), pp. 316–326.

[51] Hangyue Li et al. "Performance map and operating condition optimization of industrial-size SOFCs using a PINN surrogate model". In: *International Journal of Hydrogen Energy* 50 (Jan. 2024), pp. 1294–1307. ISSN: 0360-3199. DOI: 10.1016/j.ijhydene.2023.06.276. URL: http://dx.doi.org/10.1016/j.ijhydene.2023.06.276.

[52] Zewei Lyu et al. "Prediction of fuel cell performance degradation using a combined approach of machine learning and impedance spectroscopy". In: *Journal of Energy Chemistry* 87 (Dec. 2023), pp. 32–41. ISSN: 2095-4956. DOI: 10.1016/j.jechem.2023.08.028. URL: http://dx.doi.org/10.1016/j.jechem.2023.08.028.

[53] Ahmed M. Nassef et al. "Maximizing SOFC performance through optimal parameters identification by modern optimization algorithms". In: *Renewable Energy* 138 (Aug. 2019), pp. 458–464. ISSN: 0960-1481. DOI: 10.1016/j.renene.2019.01.072. URL: http://dx.doi.org/10.1016/j.renene.2019.01.072.

[54] Dario Marra et al. "A neural network estimator of Solid Oxide Fuel Cell performance for on-field diagnostics and prognostics applications". In: *Journal of Power Sources* 241 (Nov. 2013), pp. 320–329. ISSN: 0378-7753. DOI: 10.1016/j.jpowsour.2013.04.114. URL: http://dx.doi.org/10.1016/j.jpowsour.2013.04.114.

[55] P Costamagna, L Magistri, and AF Massardo. "Design and part-load performance of a hybrid system based on a solid oxide fuel cell reactor and a micro gas turbine". In: *Journal of Power Sources* 96 (2001), pp. 352–368.

[56] R Peters et al. "Efficiency analysis of a hydrogen-fueled solid oxide fuel cell system with anode off-gas recirculation". In: *Journal of Power Sources* 328 (2016), pp. 105–113.

[57] WL Becker et al. "Design and technoeconomic performance analysis of a 1MW solid oxide fuel cell polygeneration system for combined production of heat, hydrogen, and power". In: *Journal of Power Sources* 200 (2012), pp. 34–44.

[58] R Torii et al. "Anode gas recirculation for improving the performance and cost of a 5-kW solid oxide fuel cell system". In: *Journal of Power Sources* 325 (2016), pp. 229–237.

[59] S Campanari. "Thermodynamic model and parametric analysis of a tubular SOFC module". In: *Journal of Power Sources* 92 (2001), pp. 26–34.

[60] YJ Park, G Min, and J Hong. "Comparative study of solid oxide fuel cell-combined heat and power system designs for optimal thermal integration". In: *Energy Conversion and Management* 182 (2019), pp. 351–368.

[61] M Ni, DYC Leung, and MKH Leung. "Electrochemical modeling and parametric study of methane fed solid oxide fuel cells". In: *Energy Conversion and Management* 50 (2009), pp. 268–278.

[62] M Fallah, SMS Mahmoudi, and M Yari. “Advanced exergy analysis for an anode gas recirculation solid oxide fuel cell”. In: *Energy* 141 (2017), pp. 1097–112.

[63] M Rokni. “Addressing fuel recycling in solid oxide fuel cell systems fed by alternative fuels”. In: *Energy* 137 (2017), pp. 1013–1025.

[64] A Chitsaz, J Hosseinpour, and M Assadi. “Effect of recycling on the thermodynamic and thermoeconomic performances of SOFC based on trigeneration systems; A comparative study”. In: *Energy* 124 (2017), pp. 613–624.

[65] Jingxuan Peng et al. “Comprehensive Analysis of Solid Oxide Fuel Cell Performance Degradation Mechanism, Prediction, and Optimization Studies”. In: *Energies* 16.2 (Jan. 2023), p. 788. ISSN: 1996-1073. DOI: 10.3390/en16020788. URL: http://dx.doi.org/10.3390/en16020788.

[66] Xiao-long Wu et al. “Health state prediction and analysis of SOFC system based on the data-driven entire stage experiment”. In: *Applied Energy* 248 (2019), pp. 126–140. ISSN: 0306-2619. DOI: https://doi.org/10.1016/j.apenergy.2019.04.053. URL: https://www.sciencedirect.com/science/article/pii/S0306261919307007.

[67] Jingxuan Peng et al. “Generalized Spatial–Temporal Fault Location Method for Solid Oxide Fuel Cells Using LSTM and Causal Inference”. In: *IEEE Transactions on Transportation Electrification* 8 (Dec. 2022), pp. 1–1. DOI: 10.1109/TTE.2022.3187870.

[68] Boštjan Dolenc et al. “State of health estimation and remaining useful life prediction of solid oxide fuel cell stack”. In: *Energy Conversion and Management* 148 (Sept. 2017), pp. 993–1002. DOI: 10.1016/j.enconman.2017.06.041.

[69] Muhammad Zubair Khan et al. “Lifetime Prediction of Anode-Supported Solid Oxide Fuel Cell on the Basis of Individual Components Degradation”. In: *ECS Transactions* 91.1 (July 2019), pp. 621–627. ISSN: 1938-5862. DOI: 10.1149/09101.0621ecst. URL: http://dx.doi.org/10.1149/09101.0621ecst.

[70] Pengfei Zhu et al. “Ni coarsening and performance attenuation prediction of biomass syngas fueled SOFC by combining multi-physics field modeling and artificial neural network”. In: *Applied Energy* 322 (Sept. 2022), p. 119508. ISSN: 0306-2619. DOI: 10.1016/j.apenergy.2022.119508. URL: http://dx.doi.org/10.1016/j.apenergy.2022.119508.

[71] Mumin Rao et al. “Data-Driven State Prediction and Analysis of SOFC System Based on Deep Learning Method”. In: *Energies* 15.9 (Apr. 2022), p. 3099. ISSN: 1996-1073. DOI: 10.3390/en15093099. URL: http://dx.doi.org/10.3390/en15093099.

[72] Kaichuang Yang et al. “Machine-learning-assisted prediction of long-term performance degradation on solid oxide fuel cell cathodes induced by chromium poisoning”. In: *Journal of Materials Chemistry A* 10.44 (2022), pp. 23683–23690. ISSN: 2050-7496. DOI: 10.1039/d2ta03944c. URL: http://dx.doi.org/10.1039/D2TA03944C.

[73] A. Cuneo et al. “Probabilistic analysis of a fuel cell degradation model for solid oxide fuel cell and gas turbine hybrid systems”. In: *Energy* 141 (2017), pp. 2277–2287. ISSN: 0360-5442. DOI: https://doi.org/10.1016/j.energy.2017.12.002. URL: https://www.sciencedirect.com/science/article/pii/S0360544217320212.

[74] Maxim Ananyev et al. “SOFC Degradation Quantification Using Image Analysis”. In: June 2011.

[75] D Simwonis, F Tietz, and D Stöver. “Nickel coarsening in annealed Ni/8YSZ anode substrates for solid oxide fuel cells”. In: *Solid State Ionics* 132.3 (2000). Solid Oxide Fuel Cells dedicated to Prof. H. Tagawa, pp. 241–251. ISSN: 0167-2738. DOI: https://doi.org/10.1016/S0167-2738(00)00650-0. URL: https://www.sciencedirect.com/science/article/pii/S0167273800006500.

[76] Muhammad Zubair Khan et al. “A simplified approach to predict performance degradation of a solid oxide fuel cell anode”. In: *Journal of Power Sources* 391 (2018), pp. 94–105. ISSN: 0378-7753. DOI: https://doi.org/10.1016/j.jpowsour.2018.04.080. URL: https://www.sciencedirect.com/science/article/pii/S0378775318304294.

[77] Carlos Boigues Muñoz et al. “Performance Degradation Prediction of a Low-Temperature SOFC via Impedance Spectroscopy and CFD Modelling”. In: *ECS Transactions* 68.1 (June 2015), pp. 2227–2235. ISSN: 1938-6737. DOI: 10.1149/06801.2227ecst. URL: http://dx.doi.org/10.1149/06801.2227ecst.

[78] M. L. Ferrari. “Advanced control approach for hybrid systems based on solid oxide fuel cells”. In: *Applied Energy* 145 (2015), pp. 364–373. DOI: 10.1016/j.apenergy.2015.02.059.

[79] Jianzhong Zhu et al. “An Optimized Strategy for Fuel Cell Degradation Control in SOFC Power Systems”. In: *ECS Meeting Abstracts*. Vol. MA2021-03. 17th International Symposium on Solid Oxide Fuel Cells (SOFC-XVII), July 18, 2021 - July 23, 2021. The Electrochemical Society. 2021, p. 63. DOI: 10.1149/MA2021-03163mtgabs. URL: https://iopscience.iop.org/article/10.1149/MA2021-03163mtgabs.

[80] Christopher Graves et al. “Eliminating degradation in solid oxide electrochemical cells by reversible operation”. In: *Nature Materials* 14.1 (2015). Published online: 22 December 2014, pp. 239–244. DOI: 10.1038/nmat4165. URL: https://www.nature.com/articles/nmat4165.

[81] Theis Løye Skafte et al. “Electrothermally balanced operation of solid oxide electrolysis cells”. In: *Journal of Power Sources* 523 (Mar. 2022), p. 231040. ISSN: 0378-7753. DOI: 10.1016/j.jpowsour.2022.231040. URL: http://dx.doi.org/10.1016/j.jpowsour.2022.231040.

[82] P. Aguiar, C.S. Adjiman, and N.P. Brandon. “Anode-supported intermediate-temperature direct internal reforming solid oxide fuel cell”. In: *Journal of Power Sources* 147.1–2 (Sept. 2005), pp. 136–147. ISSN: 0378-7753. DOI: 10.1016/j.jpowsour.2005.01.017. URL: http://dx.doi.org/10.1016/j.jpowsour.2005.01.017.

[83] S.A. Hajimolana et al. “Thermal stress management of a solid oxide fuel cell using neural network predictive control”. In: *Energy* 62 (Dec. 2013), pp. 320–329. ISSN: 0360-5442. DOI: 10.1016/j.energy.2013.08.031. URL: http://dx.doi.org/10.1016/j.energy.2013.08.031.

[84] Benjamin J. Spivey and Thomas F. Edgar. “Dynamic modeling, simulation, and MIMO predictive control of a tubular solid oxide fuel cell”. In: *Journal of Process Control* 22.8 (Sept. 2012), pp. 1502–1520. ISSN: 0959-1524. DOI: 10.1016/j.jprocont.2012.01.015. URL: http://dx.doi.org/10.1016/j.jprocont.2012.01.015.

[85] V. Zaccaria, D. Tucker, and A. Traverso. “Operating strategies to minimize degradation in fuel cell gas turbine hybrids”. In: *Applied Energy* 192 (Apr. 2017), pp. 437–445. ISSN: 0306-2619. DOI: 10.1016/j.apenergy.2016.10.098. URL: http://dx.doi.org/10.1016/j.apenergy.2016.10.098.

[86] Lars Grüne and Jürgen Pannek. “Nonlinear Model Predictive Control”. In: *Nonlinear Model Predictive Control: Theory and Algorithms*. London: Springer London, 2011, pp. 43–66. ISBN: 978-0-85729-501-9. DOI: 10.1007/978-0-85729-501-9_3. URL: https://doi.org/10.1007/978-0-85729-501-9_3.

[87] Zhi-dan Zhong et al. “Adaptive maximum power point tracking control of fuel cell power plants”. In: *Journal of Power Sources* 176.1 (2008), pp. 259–269. ISSN: 0378-7753. DOI: https://doi.org/10.1016/j.jpowsour.2007.10.080. URL: https://www.sciencedirect.com/science/article/pii/S0378775307024172.

[88] Anke Hagen et al. “Degradation of Anode Supported SOFCs as a Function of Temperature and Current Load”. In: *Journal of The Electrochemical Society* 153.6 (2006), A1165. ISSN: 0013-4651. DOI: 10.1149/1.2193400. URL: http://dx.doi.org/10.1149/1.2193400.

[89] XiaoJuan Wu and Qianwen Ye. “Fault diagnosis and prognostic of solid oxide fuel cells”. In: *Journal of Power Sources* 321 (2016), pp. 47–56. ISSN: 0378-7753. DOI: https://doi.org/10.1016/j.jpowsour.2016.04.080. URL: https://www.sciencedirect.com/science/article/pii/S0378775316304232.

[90] Tarannom Parhizkar and Saeedreza Hafeznezami. “Degradation based operational optimization model to improve the productivity of energy systems, case study: Solid oxide fuel cell stacks”. In: *Energy Conversion and Management* 158 (Feb. 2018), pp. 81–91. DOI: 10.1016/j.enconman.2017.12.045.

[91] Xiaojuan Wu et al. “A prognostic-based dynamic optimization strategy for a degraded solid oxide fuel cell”. In: *Sustainable Energy Technologies and Assessments* 39 (June 2020). DOI: 10.1016/j.seta.2020.100682.

[92] RUBY PROJECT. *Real-time optimization unit*. Report – R D5.2. Grant Agreement No.: 875047. Related WP: WP5. Due date (in months): M39. Dissemination level: Confidential – CO. EPFL, HES-SO, Jan. 2020.

[93] Konrad W. Eichhorn Colombo et al. “Mathematical modeling and simulation of hydrogen-fueled solid oxide fuel cell system for micro-grid applications - Effect of failure and degradation on transient performance”. In: *Energy* 202 (July 2020), p. 117752. ISSN: 0360-5442. DOI: 10.1016/j.energy.2020.117752. URL: http://dx.doi.org/10.1016/j.energy.2020.117752.

[94] MathWorks Inc. *MATLAB version 9.13 (R2022b)*. 2022. URL: https://www.mathworks.com/products/matlab.html.

[95] A. Di Filippi. “Development and experimental validation of CPOx reforming dynamic model for fault detection and isolation in SOFC systems”. Doctoral Thesis. Salerno, Italy: Universita degli Studi di Salerno, 2015.

[96] National Institute of Standards and Technology. *NIST Chemistry WebBook, NIST Standard Reference Database Number 69*. Online. Available from the National Institute of Standards and Technology. 2024. URL: https://webbook.nist.gov/.

[97] Frank P. Incropera et al. *Fundamentals of Heat and Mass Transfer*. 6th. See Chapter 11 for the e-NTU method for heat exchangers. Hoboken, NJ: John Wiley & Sons, 2006. ISBN: 978-0471457282.

[98] Valentina Zaccaria, Alberto Traverso, and David Tucker. "A Real-Time Degradation Model for Hardware in the Loop Simulation of Fuel Cell Gas Turbine Hybrid Systems". In: *Volume 3: Coal, Biomass and Alternative Fuels; Cycle Innovations; Electric Power; Industrial and Cogeneration*. GT2015. American Society of Mechanical Engineers, June 2015. DOI: 10.1115/gt2015-43604. URL: http://dx.doi.org/10.1115/GT2015-43604.

[99] National Energy Technology Laboratory (NETL). *Cost and Performance Baseline for Fossil Energy Plants Volume 1: Bituminous Coal and Natural Gas to Electricity*. Report. Revision 3. Washington, D.C.: U.S. Department of Energy, 2015. URL: https://www.netl.doe.gov/.

[100] HEV Schweiz. *Energiepreise in der Schweiz*. https://www.hev-schweiz.ch/vermieten/statistiken/energiepreise/. Accessed: 2023-05-10. 2019.

[101] Banken, Versicherungen & Telekom. *Electricity Prices in Switzerland: A Comprehensive Guide*. https://www.moneyland.ch/en/electricity-switzerland-guide. Accessed: 2023-05-10. 2019.

[102] Bundesamt für Umwelt (BAFU). *CO2 Levy on Thermal Fuels*. https://www.bafu.admin.ch/bafu/en/home/topics/climate/info-specialists/reduction-measures/co2-levy.html. Accessed: 2023-05-10. 2022.

[103] U.S. Department of Energy. *Total Cost of Ownership Model for Solid Oxide Fuel Cells in Combined Heat and Power Applications*. https://www.energy.gov/eere/fuelcells/articles/total-cost-ownership-model-solid-oxide-fuel-cells-combined-heat-and-power. Accessed: 2023-05-10. 2023.

[104] Oiken. *Electricity Selling Prices*. https://oiken.ch/publications/2024/. Accessed: 2023-05-10. 2024.

[105] International Energy Agency (IEA). *Energy Efficiency 2023*. https://www.iea.org/reports/energy-efficiency-2023. Licence: CC BY 4.0. Paris, 2023.

[106] Xiaolong Wu et al. "Nonlinear Model Predictive Control (NMPC) for Solid Oxide Fuel Cells (SOFCs): Approaches and Applications". In: *Journal of Power Sources* 498 (2023), pp. 229–244.

[107] X.W. Zhang et al. "Nonlinear model predictive control based on the moving horizon state estimation for the solid oxide fuel cell". In: *International Journal of Hydrogen Energy* 33.9 (2008), pp. 2355–2366. ISSN: 0360-3199. DOI: https://doi.org/10.1016/j.ijhydene.2008.02.063.

[108] M. Schultze and J. Horn. "Nonlinear Model Predictive Control of PEM Fuel Cell Systems for Generation of Exhaust Gas with Low Oxygen Content". In: *IFAC Proceedings Volumes* 46.19 (2013). 19th IFAC Symposium on Automatic Control in Aerospace, pp. 470–475. ISSN: 1474-6670. DOI: https://doi.org/10.3182/20130902-5-DE-2040.00128.

[109] U.S. Department of Energy. *Hydrogen and Fuel Cell Technologies Office Multi-Year Program Plan*. Office of Energy Efficiency and Renewable Energy. 2024. URL: https://www.energy.gov/eere/fuelcells/hydrogen-and-fuel-cell-technologies-office-multi-year-program-plan.

[110] Marine Jouin et al. "Estimating the end-of-life of PEM fuel cells: Guidelines and metrics". In: *Applied Energy* 177 (Sept. 2016), pp. 87–97. ISSN: 0306-2619. DOI: 10.1016/j.apenergy.2016.05.076. URL: http://dx.doi.org/10.1016/j.apenergy.2016.05.076.

[111] Huicui Chen, Pucheng Pei, and Mancun Song. "Lifetime prediction and the economic lifetime of Proton Exchange Membrane fuel cells". In: *Applied Energy* 142 (Mar. 2015), pp. 154–163. ISSN: 0306-2619. DOI: 10.1016/j.apenergy.2014.12.062. URL: http://dx.doi.org/10.1016/j.apenergy.2014.12.062.

[112] Wood Mackenzie. *Europe Levelised Cost of Electricity (LCOE) 2023*. Accessed: 2024-06-05. 2023. URL: https://www.woodmac.com/reports/power-markets-europe-levelised-cost-of-electricity-lcoe-2023-150185487/.

[113] Swiss Energy. *Swiss Energy*. Accessed: 2024-06-05. 2024. URL: https://www.swissenergy.ch/.